THE INFLUENCE OF THERMAL AND MAGNETIC LAYERS ON SOLAR OSCILLATION FREQUENCIES

Mark Daniell

A Thesis Submitted for the Degree of PhD
at the
University of St Andrews

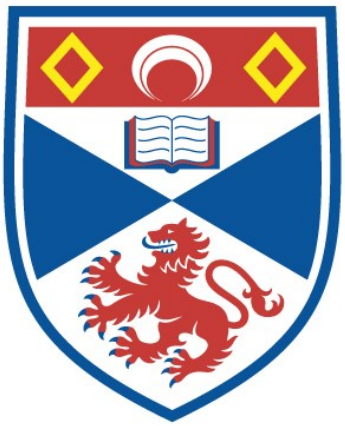

1998

The Influence of Thermal and Magnetic Layers on Solar Oscillation Frequencies

Mark Daniell

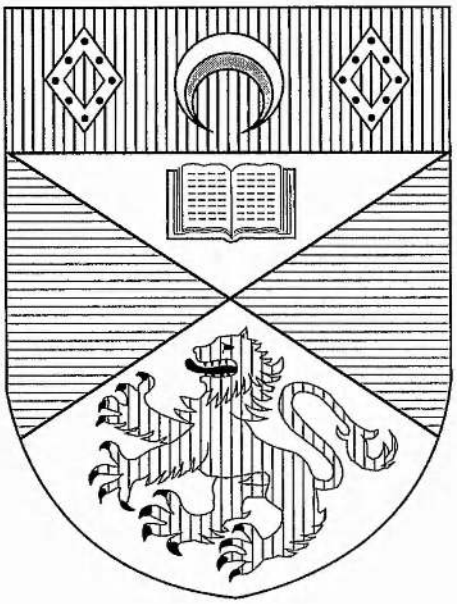

A thesis submitted for the Degree of Doctor of Philosophy

of the University of St. Andrews

17th July 1998

ProQuest LLC.
789 East Eisenhower Parkway
P.O. Box 1346
Ann Arbor, MI 48106 – 1346

TL 9146

Abstract

In this thesis, a study is made of the global solar oscillations known as $p-$modes, modelled by a plane-parallel stratified plasma, within which is embedded a horizontal layered magnetic field. A magnetohydrodynamic formalism is used to investigate the models. The main aim of the thesis is to model the turnover effect in the frequency shifts of the $p-$modes observed over the course of the solar cycle.

Radial oscillations (modes of degree zero) of the Sun are studied for several atmospheric temperature and magnetic field profiles. It is found that the turnover in frequency shifts may be obtained by an increase in the strength of the atmospheric horizontal magnetic field (assumed to be uniform), coupled with a simultaneous increase in atmospheric temperature.

The effect of a thin superadiabatic layer in the upper convection zone on $p-$mode frequencies is also considered. For this model we study modes of general degree, and find that the observed rise and subsequent downturn in the frequency shifts can be duplicated, in the absence of a magnetic field, by simultaneously steepening the temperature gradient of the superadiabatic layer and increasing the atmospheric temperature. In the presence of a magnetic field, where the atmosphere is permeated by a uniform horizontal magnetic field, turnover is reproduced by a combination of an increase in magnetic field strength, a steepening of the temperature gradient in the superadiabatic region, and an increase in atmospheric temperature. The unstable superadiabatic layer also gives rise to convective modes, which are considered briefly.

Finally, a model incorporating a magnetic layer residing at the base of the convection zone is constructed and its influence on the frequencies of $p-$modes assessed. By simply changing the magnetic field strength of this layer, we are unable to reproduce the observed solar cycle variations in $p-$mode frequencies.

The buried magnetic layer supports surface and body magnetoacoustic waves, and a brief study is made of their properties.

Declarations

1. I, Mark Daniell, hereby certify that this thesis, which is approximately 50,000 words in length, has been written by me, that it is the record of work carried out by me and that it has not been submitted in any previous application for a higher degree.

   Date: 17th July 1998 Signature of candidate: ..

2. I was admitted as a research student in October 1994 and as a candidate for the degree of Ph.D. in October 1995; the higher study for which this is a record was carried out in the University of St. Andrews between 1994 and 1998.

   Date: 17th July 1998 Signature of candidate: ..

3. I hereby certify that the candidate has fulfilled the conditions of the Resolution and Regulations appropriate for the degree of Ph.D. in the University of St. Andrews and that the candidate is qualified to submit this thesis in application for that degree.

   Date: 17 July 1998 Signature of supervisor: .

4. In submitting this thesis to the University of St. Andrews I understand that I am giving permission for it to be made available for use in accordance with the regulations of the University Library for the time being in force, subject to any copyright vested in the work not being affected thereby. I also understand that the title and abstract will be published, and that a copy of the work may be made and supplied to any *bona fide* library or research worker.

   Date: 17th July 1998 Signature of candidate: ..

Acknowledgements

I would like to express my greatest thanks to my supervisor, Bernard Roberts. Without his help and support, over and above the supervision of this thesis, I doubt if any of this work would have been completed.

I would also like to thank the members of the Solar Theory Group of St. Andrews for their relaxed and friendly attitude, especially the office mates that I have shared with over the last few years; namely Nick, Apollonia, Clare and Erwin.

Last, and certainly not least, I would like to thank my girlfriend Wendy for her continued support and patience throughout the last five years. As she knows, without her none of this would have been worthwhile.

Contents

Chapter 1

Introduction

1.1 The Sun and Solar Oscillations

Since man first began to try and understand the universe around him, the Sun has occupied a central position for his questioning. Ancient peoples worshipped the Sun as a god, and many cultures have used its motion as a way of forming a yearly calender; a basic understanding of its relative motion which we still rely on today. Since the invention of the telescope, the full splendour of the Sun has become apparent, furthering mankind's wish to understand it. Today, the Sun still commands central attention as it provides us with our very own 'stellar laboratory' from which to understand some of the most fundamental physical processes of the universe.

On a universal scale, the Sun is a very ordinary and unexceptional star, but it is the only one which we can resolve as a disc and hence observe in any great detail. As a result of its proximity we can observe the many surface features that it exhibits such as sunspots, prominences and flares. We can also make detailed measurements of its magnetic field and the stream of particles which this is responsible for, the *solar wind.*

The Sun consists of an ionised gas, which is compressible and therefore capable of supporting sound waves. The fact that it is strongly stratified by gravity and has an abundance of magnetic field configurations means that it may sustain waves associated with these forces.

For waves to occur, a restoring force is necessary. In the case of sound waves, the restoring force is pressure. Gravity gives rise to a restoring buoyancy force within the plasma, and magnetism adds restoring forces acting through magnetic pressure and

magnetic tension. Any study of waves on the Sun is necessarily complicated by the fact that more often than not all of these restoring forces are present at the same time.

The Sun is highly dynamic in nature and so waves are always present. For example, there are the *running penumbral waves* which are seen to propagate from the umbrae of sunspots; flares give rise to *Moreton waves* which travel across the solar disc at speeds of up to 250,000 miles per hour; and prominences are observed to contain a range of modes of oscillation. By attempting to understand the multitude of wave phenomena that occur on the Sun, we gain a clearer understanding of the forces which give rise to them, and the nature of the object in which the waves occur.

In this introductory chapter, we briefly describe the structure of the Sun (Section 1.2) and its magnetic field (Section 1.3). In Section 1.4 we introduce the basic equations used in the investigations that we undertake. The main interest of this thesis is in global solar oscillations and how magnetism influences them; this topic is introduced in Section 1.5. In Section 1.6 we describe a special type of wave phenomena, magnetic surface waves. Finally, Section 1.7 gives an outline of the thesis.

1.2 The Structure of the Sun

The Sun is a huge ball of ionised gas, a plasma, with a mass equal to 300,000 Earths and a radius over 100 times that of the Earth. It is composed primarily of hydrogen (90%) and helium (10%). Its interior is highly opaque and we see only its outer surface layers. As a result, the structure of the interior is inferred from mathematical models combined with highly accurate measurements of global oscillations detected at the solar surface; this is the subject of helioseismology.

Energy is generated in the *core* of the Sun where temperatures are in the region of 1.5×10^{7o}K. Almost 99% of the energy is generated in the core which contains approximately half of the mass of the Sun, and extends outwards to about a quarter of its radius.

The high energy photons produced in the core do not propagate away into space immediately, but are contained by the large opacities found at these depths. They are continually being absorbed and re-emitted by ions of lower temperatures as they make their outward progress from the core. The region in which this process occurs is known as the *radiative zone*, a stable region extending from the core to a distance of approximately 70% of the solar radius. It is estimated that it takes photons about 10^7 years to traverse the

radiative zone.

At the outer extremes of the radiative zone, radiation alone does not transport energy efficiently. The temperatures are such that the electrons begin to combine with other elements so that photons are absorbed more easily. As the radiative conductivity is reduced, the magnitude of the temperature gradient is increased until the temperature is decreasing so rapidly that convective instabilities occur. As a result, turbulent convection sets in giving rise to the bulk motion of plasma in a cellular pattern. Convection is the main process of energy transport in this region, known as the *convection zone*, extending from the radiative zone outwards for a further 200,000 km.

Above the convection zone, radiation may escape directly from the Sun and the material returns to convective stability. This region is where the bulk of the light that we see is emitted from, called the *photosphere*. The photosphere is thin with a width of only 500 km. At the top of the photosphere the temperature drops to a minimum at around 4170°K, refered to as the temperature minimum.

The region lying above the temperature minimum is known as the *chromosphere*, where the temperature begins to rise slowly. The chromosphere has a thickness of approximately 2000 km above which the temperature rises exceedingly quickly to several hundred thousand degrees Kelvin over what is known as the *transition region.*

Finally, above the transition region lies the *corona* where the temperature rises to several million degrees. The corona extends into space beyond the Earth. Near surface features of the corona are solar prominences, coronal loops and coronal holes.

For a fuller description of the solar structure, see Priest (1982).

1.3 The Solar Magnetic Field

Many of the features observed on the Sun owe their existence to its magnetic field. It may influence the plasma in many ways, some of which are passive while others are active. For example, it may passively channel the plasma in a flow, or act as a thermal blanket insulating one volume of plasma from a neighbouring, thermally different, volume. Alternatively, the magnetic field introduces forces which may actively manipulate the plasma to form various structures or may store energy and then suddenly, and violently, release it. Additionally, the magnetic field supports waves and drives instabilities.

The magnetic field and plasma of the solar atmosphere are very strongly inter-

dependent. There are several ways of gauging the relative importance of each in solar applications. Firstly, we have the magnetic Reynolds number R_m given by

$$R_m = \frac{uL}{\eta}, \tag{1.1}$$

where η ($=1/\mu_o\sigma$, where μ_o is the magnetic permeability of free space and σ the electrical conductivity) is the magnetic diffusivity, u is a characteristic flow speed of the plasma, and L is a characteristic length scale for changes in the field and in the flow. For most solar phenomena the length scales are large ($\sim$ 1Mm) and as a result R_m is enormous ($\approx 10^6 - 10^{12}$), so for most processes the magnetic field and the plasma act as if they are 'frozen' together. To determine which forces dominate however, a commonly used parameter is the plasma β, usually defined by the ratio of the plasma pressure to the magnetic pressure. In a low β plasma, the magnetic field is dominant, while in a high β plasma the fluid will dominate over the magnetic field. An example of a low β plasma is the corona where the relatively strong magnetic fields occupy a highly rarefied plasma, while in the interior of the Sun extremely high gas pressures serve to ensure dominance of the plasma over magnetic fields of even the highest strengths.

The solar magnetic field is believed to be generated in a shallow layer at the base of the convection zone. The field is thought to be generated by a dynamo action, perhaps in the form of *flux tubes* (self contained tubes of intense magnetic flux). The magnetic field is subject to instabilities which allow flux to break free from this reservoir. The flux tubes then rise under magnetic buoyancy and through the action of the turbulent forces of the convection zone to eventually emerge at the solar surface. At the surface, the cellular structure of the granules and supergranules serve to aggregate the flux at the cell boundaries. At these margins, features such as sub-telescopic intense magnetic flux tubes with field strengths of 1-2kG and the larger sunspots, with field strengths of around 3kG, are formed.

Above this, in the chromosphere, the flux tubes expand rapidly with height owing to the rapid decrease of the plasma pressure. As a result, the magnetic field begins to fill the entire atmosphere, whereas below this the atmosphere is largely devoid of magnetic flux (except in the intense flux tubes and sunspots). This gives rise to a magnetic field that is in the form of a magnetic canopy which is roughly horizontal in nature (Giovanelli 1980; Giovanelli and Jones 1982; Jones and Giovanelli 1983).

In the corona features such as coronal loops, prominences, flares and coronal mass

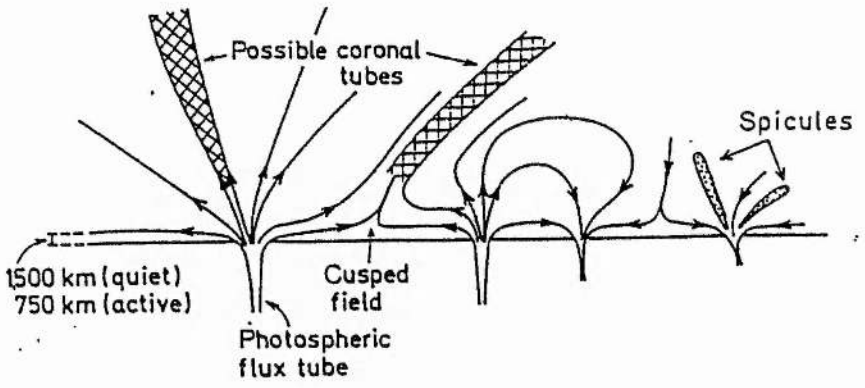

Figure 1.1: A schematic representation of the solar magnetic field from the photosphere outwards, taken from Spruit and Roberts (1983).

ejections are observed, all resulting from the presence of the magnetic field. The high temperature of the corona is also thought to result from the magnetic field through such processes as, for example, magnetic reconnection and the damping of Alfvén waves. A schematic representation of the solar magnetic field is given in Figure 1.1, taken from Spruit and Roberts (1983).

All of the magnetic features observed on the Sun tend to show a cyclic nature in their number, size and intensity. For some years the Sun will be *quiet*, with very few coronal features and few sunspots. Gradually, activity on the Sun will increase with more sunspots being observed, with the latitudes at which they emerge following a distinctive pattern. Also, prominences become more abundant and the occurrence of flares becomes more common. The activity will peak for a maximum period, when the Sun is highly *active*, after which the activity will decrease sharply. The process then begins once again. This pattern of behaviour is known as the *solar cycle*, with an average period of 11 years. The most recent maximum occurred in 1989, and at the time of writing we are again approaching this phase in the Sun's cycle.

For a more detailed description of the Sun's magnetic field and its variation with the solar cycle, see Priest (1982).

1.4 Basic Equations

Before introducing the theoretical work carried out on solar oscillations, we shall present the basic equations which describe the physical processes governing the motions of a plasma typically found in the Sun.

Within the Sun, the predominant forces likely to influence a plasma element are fluid and magnetic ones. As a result, the equations which describe the motion of such a plasma element arise from the combination of fluid mechanics and electromagnetism. The field studying the interaction between a plasma and a magnetic field, combining these two areas of physics, is known as magnetohydrodynamics, or MHD.

The field of magnetohydrodynamics relies upon various assumptions (see, for example, Priest 1982). Primarily, the plasma is taken to be a single continuous fluid, assumed to be in thermodynamic equilibrium. The plasma is assumed to be compressible and of infinite conductivity. Also, as most physical velocities found on the Sun are much less than the speed of light, relativistic effects are ignored. The basic equations are then formed by combining Maxwell's equations with the laws of fluid mechanics (for a more in depth discussion of the equations, see Priest 1982).

Let us consider a plasma with density ρ, pressure P, and temperature T, moving under the influence of gravity $\mathbf{g}$. Assume also that the plasma fluid is moving with a velocity $\mathbf{u}$, within a magnetic field $\mathbf{B}$. The plasma is governed by conservation of mass, i.e. no material is being destroyed or created in a control volume. This gives rise to the equation of mass continuity,

$$\frac{D\rho}{Dt} + \rho \nabla \cdot \mathbf{u} = 0. \tag{1.2}$$

The derivative D/Dt is the temporal rate of change as one moves with a fluid element. It is known as the advective (or convective) derivative:

$$\frac{D}{Dt} \equiv \frac{\partial}{\partial t} + \mathbf{u} \cdot \nabla. \tag{1.3}$$

When considering a plasma element, we also assume that there is no exchange of heat between the element and the surrounding plasma. We therefore have a simple adiabatic energy equation,

$$\frac{DP}{Dt} = \frac{\gamma P}{\rho} \frac{D\rho}{Dt}, \tag{1.4}$$

where γ is the adiabatic index of the plasma (γ is the ratio of the specific heat at constant pressure to the specific heat at constant volume).

A further assumption is that the plasma acts as an ideal gas, giving an equation of state of the form

$$P = R\rho T, \tag{1.5}$$

where R ($= k_B/m_{av}$, where k_B is Boltzmann's constant and m_{av} is the mean particle mass of the plasma) is the gas constant.

With the neglection of diffusivity in Maxwell's equations, we are able to derive an equation for the magnetic induction of the plasma of the form

$$\frac{\partial \mathbf{B}}{\partial t} = \nabla \times (\mathbf{u} \times \mathbf{B}). \tag{1.6}$$

With no diffusive term being present, this equation implies that the fluid and the magnetic field are effectively frozen together, a good approximation for most solar applications (as we have pointed out in Section 1.3).

The motion of the plasma is governed by the pressure, magnetic and gravitational forces acting upon it. We therefore have a momentum equation of the form

$$\rho \frac{D\mathbf{u}}{Dt} = -\nabla P + \rho \mathbf{g} + \mathbf{j} \times \mathbf{B}, \tag{1.7}$$

where $\mathbf{j}$ is the current density, given by Ampere's law

$$\mu \mathbf{j} = \nabla \times \mathbf{B}. \tag{1.8}$$

The $\mathbf{j} \times \mathbf{B}$ term arising in Equation (1.7) is known as the Lorentz force. It may be decomposed by means of a triple vector identity into the form

$$\mathbf{j} \times \mathbf{B} = \frac{1}{\mu}(\mathbf{B} \cdot \nabla)\mathbf{B} - \nabla \left(\frac{B^2}{2\mu} \right). \tag{1.9}$$

The first term on the right hand side of Equation (1.9) represents a tension force parallel to $\mathbf{B}$ (and hence anisotropic) which arises when the field lines are curved; the second term on the right hand side of Equation (1.9) represents the gradient of an isotropic pressure force. The component of the magnetic pressure parallel to the magnetic field must cancel with the corresponding component of tension as the Lorentz force is given by $\mathbf{j} \times \mathbf{B}$ and hence must be normal to $\mathbf{B}$.

Finally, the magnetic field is constrained by the condition that there are no sources or sinks of magnetic flux. Hence

$$\nabla \cdot \mathbf{B} = 0. \tag{1.10}$$

These are the basic equations that we shall use throughout this thesis.

1.5 Global Oscillations of the Sun

Almost forty years ago, it was discovered that the visible surface of the Sun did not behave in a random way but in fact exhibited a regular oscillatory motion. The oscillations were first seen in Doppler images of the Sun obtained at the Mount Wilson Observatory, with a dominant period of 5 minutes and with velocity amplitudes of 1 m s^{-1} (Leighton 1960; Leighton *et al.* 1962). The discovery of these oscillations was later confirmed by Evans and Michard (1962). Subsequently, several observational studies were made of the oscillations in order to determine their characteristics and their causes. However, observational data was hard to interpret at the time because of the restriction to a single dimension of power spectral analysis techniques. This problem was overcome with the application of two dimensional power spectra to the oscillations. A two dimensional power spectrum, also known as a diagnostic diagram, plots the observed power as a function of the frequency and the horizontal wavenumber of the wave. The first diagnostic diagram to be constructed from the observational data was presented by Deubner (1975), using data collected by the magnetograph of the Fraunhofer Institute attached to the domeless Coudé refractor in Anacapri. From an application of diagnostic diagrams to the solar oscillations, a much greater understanding of the waves was gained; for example the obvious spatial and temporal coherence of the waves, and the indication that the oscillations were evanescent in the chromosphere. Today, it is known that the surface of the Sun displays thousands of individual waves, each with its own distinct frequency (Libbrecht, Woodard and Kaufmann 1990; Elsworth *et al.* 1990).

1.5.1 Formation of the modes

The observation that the visible surface of the Sun oscillated in a regular manner posed an interesting problem for theoreticians. An initial model, for example, attempted

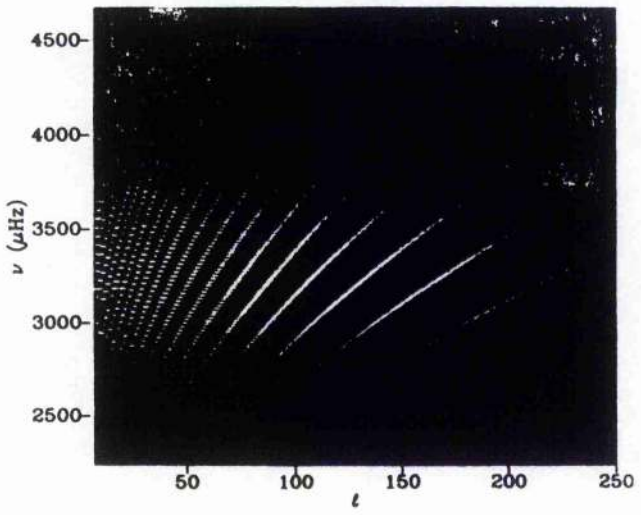

Figure 1.2: A diagnostic diagram showing the frequency ν of the $p-$modes versus degree l. Each Ridge corresponds to modes of different radial order, n. (Figure reproduced from Duvall *et al.* (1987)).

to explain the five minute oscillations as a response of the photosphere to convective overshooting of the granules: the theory of 'photospheric ringing' (Schmidt and Zirker 1963; Meyer and Schmidt 1967). There were several flaws to this model, however, as it predicted that the generated acoustic waves should propagate isotropically in the horizontal as well as the vertical direction. This model had to be ruled out therefore as observations had already shown that the 5 minute oscillations were mainly vertical motions. Also, observations showed that there was no correlation between the appearance of a granule and the onset of oscillations (Frazier 1968). Various other models have been applied to this problem, such as chromospheric gravity modes (Uchida 1965). All of these models were shown to be incorrect as they predicted a different power spectra in the diagnostic diagram to that observed.

The explanation for the 5-minute oscillations was finally provided by Ulrich (1970) and, independently, Leibacher and Stein (1971). These workers predicted that the observations displayed a visible indication of the trapping of acoustic waves in a resonant cavity beneath the photosphere. In a plot of frequency against horizontal wavenumber they produced very distinctive parabolic dispersion curves with separately spaced power ridges. The parabolic ridges were postulated to arise from the constructive interference of standing acoustic waves within the Sun. It was not until the observations of Deubner (1975), who was attempting to carry out better temporal and spatial analysis of the oscillations, which

showed clearly the separately spaced parabolic power ridges, was the theory of trapped modes beneath the photosphere accepted. A present day high quality diagnostic diagram is shown in Figure 1.2.

The formation of trapped modes in an acoustic cavity within the solar interior can be understood in the following way. A resonant cavity may be seen as a region in which waves can propagate, in a vertical direction say, but is bounded above and below by non-propagating regions effectively trapping the waves. If there is a disturbance at some position within the solar interior, acoustic waves will propagate outwards in all directions. A wave that is propagating towards the centre of the Sun at a non-zero angle to the vertical will encounter progressively higher temperatures and thus increasing sound speeds. As the wave is not propagating exactly vertically, the end of the wavefront nearer the centre of the Sun travels faster than the end nearer the surface. The effect of this is to turn the wave until at some depth it is propagating horizontally at which stage it begins to propagate outwards towards the solar surface, as shown in Figure 1.3. The depth at which the wave becomes horizontal defines the lower boundary of the cavity.

Through the process of refraction, the wave finds itself propagating outwards towards the solar surface, its direction becoming more vertical as it approaches the photosphere. At the surface, a rapid decrease in the plasma density is present. Specifically, at the temperature minimum the gas density decreases with height at a greater rate than at any other level of the Sun. A wave may behave in two different ways on encountering the solar surface. If the wave is above a certain frequency, the cutoff frequency (Lamb 1932), then it is free to propagate away into space and no cavity is formed. However, if the density scale height is such that it is less than the vertical wavelength of the wave, the photosphere acts as an effective density discontinuity reflecting the wave back into the solar interior and so forming the upper boundary of the acoustic cavity. The acoustic cutoff frequency that divides these two behaviours has a value of around 5.43 mHz at the temperature minimum.

These two conditions are not the only ones necessary for formation of a trapped wave within the cavity. The waves must also exhibit constructive interference; for certain waves, the repeated process of refraction and reflection bring them back to their original position. For constructive interference to occur the wave should return to its original starting point after an integral number of reflections at the solar surface. This introduces the integer l, called the *degree* of the wave, equivalent to the number of reflections the wave undergoes, and is essentially a measure of the horizontal wavelength. Also, the wave returning to the

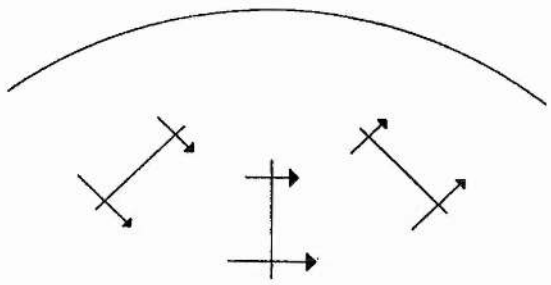

Figure 1.3: The refraction of a plane wave front propagating at a non-zero angle to the vertical (from Johnston 1994).

starting point should be in phase with the original wave. This final condition determines the frequency of the wave and its overtones. These are classified by the integer n, called the *radial order* of the wave. The radial order is simply the number of nodes the wave has on a radius of the Sun. These continued processes lead to a standing wave pattern being formed within the cavity. We call the particular configuration of the standing wave with respect to the cavity a *mode*.

Acoustic modes with large horizontal wavelengths (and hence low l) travel to great depths within the solar interior as they are refracted more gradually. As a result some standing waves cover the entire Sun while others are confined to the solar surface (Figure 1.3). The description of standing mode formation given above applies only for modes propagating at a non-zero angle to the vertical. However, there are also modes for which the whole surface of the Sun is oscillating in phase; these are modes of degree zero ($l = 0$). The wavefront of these modes is spherical and as such refraction is not felt by the modes and their cavities span the entire Sun. We investigate this special case of zero degree modes in Chapter 2.

The properties of cavity formation and the degree l serve to select the frequency of each mode. It was realised that through a diagnostic study of the frequencies of these modes the internal structure of the Sun could be determined. Through the process of inversion (see Deubner and Gough 1984), it is possible to use the measured frequencies to determine

the internal sound speed profile of the Sun and thus infer, for example, the temperature and density at various depths. Hence the field of *Helioseismology* was born, analogous to the study of the Earth's internal structure through the seismology of earthquake waves.

1.5.2 Spherical harmonics

For the Sun, three dimensional standing waves give rise to approaching and receding areas of the surface. The velocity pattern that appears for this can be divided into radial and angular parts. As mentioned earlier, the radial structure of the mode is described by the radial order n. The angular part, however, introduces two numbers owing to the sphericity of the Sun. Firstly, we have the spherical harmonic degree, l, described above, and secondly there is the azimuthal order m which, together with l, describes the spatial variation of the modes. The integer m is simply the number of nodal lines perpendicular to the solar equator. Ignoring the rotation of the Sun, m is not required because in a non-rotating sphere modes of the same l and n, but different m, have the same frequency. We mention briefly here that the small differences in measured frequencies between modes of different m is used to determine the internal rotational velocity of the Sun.

For the integers l, n and m, the radial component of a perturbation is described by the eigenfunction ξ in spherical co-ordinates (r, θ, ϕ), where r is the radius, θ the colatitude, and ϕ the longitude. The general solution of the radial displacement is then given by

$$\xi(l, m, n) = A_{ln}(r) Y_l^m(\theta, \phi) e^{i\omega_{mnl}t}, \tag{1.11}$$

where $A_{ln}(r)$ is the radial dependence of the eigenfunction of the mode. The spherical harmonic $Y_l^m(\theta, \phi) = P_l^m(\cos\theta)e^{im\phi}$, where $P_l^m(\cos\theta)$ is the associated Legendre function. The angular frequency ω_{mnl} depends in general on the values of l, m and n and is related to the cyclic frequency ν_{mnl} by $\omega_{mnl} = 2\pi\nu_{mnl}$. The measurement of ν_{mnl} provides the basic data of helioseismology, for use in the inversion process or for comparison with the calculated oscillation frequencies of solar models, for example. The degree l may take values 0,1,2,... while the value of m is restricted to be between $-l$ and $+l$, since $P_l^m(\cos\theta) = 0$ if $|m| > l$.

The spherical harmonic function displays a complicated behaviour for general values of l and m. If $m = 0$, there are no nodal lines perpendicular to the equator and the mode is termed *zonal*. If $l = m$ the mode is *sectoral*, and if $l > m$ we have what is known as a *tesseral* harmonic.

The function $A = A_{ln}(r)$ is determined by an ordinary differential equation in r, the solution of which, under suitable boundary conditions, gives the eigenmodes and eigenfrequencies of the system. For a spherically symmetric model, where the modes are independent of m, the radial equation for adiabatic oscillations, ignoring any perturbation to the gravitational potential, is given by (see, for example, Deubner and Gough 1984)

$$\frac{d^2\Psi}{dr^2} + \left[\frac{\omega^2 - \omega_a^2}{c_s^2} - \frac{l(l+1)}{r^2}\left(1 - \frac{\omega_g^2}{\omega^2}\right)\right]\Psi = 0, \tag{1.12}$$

where

$$\Psi = c_s^2 \rho_o^{\frac{1}{2}} \mathrm{div} A, \qquad \omega_a^2 = \frac{c_s^2}{4H^2}(1 - 2H'), \qquad H = \frac{\rho_o}{\rho_o'}, \qquad \omega_g^2 = g\left(\frac{1}{H} - \frac{g}{c_s^2}\right). \tag{1.13}$$

The parameters appearing in Equation (1.13) are the density scale height H, the buoyancy (or Brunt-Väisälä) frequency ω_g, and a generalisation of the acoustic cutoff frequency ω_a (Lamb 1908). The prime $'$ denotes differentiation with respect to r. The Brunt-Väisälä frequency, like the acoustic cutoff frequency, describes different types of mode behaviour. If $\omega_g^2 > 0$, ω_g is the natural frequency for buoyancy driven oscillations, but if $\omega_g^2 < 0$, then ω_g represents the complex growth rate of unstable convective modes (see Chapter 3). In a gravitationally stratified atmosphere, marginal stability to convective motions is obtained when $\omega_g^2 = 0$.

In this thesis, we shall not be concerned with spherical effects but will instead adopt an approach which uses a plane-parallel stratified model. This approximation is not valid for low-l modes. Under this assumption the equivalent form of Equation (1.12) is given by

$$\frac{d^2\Psi}{dx^2} + \left[\frac{\omega^2 - \omega_a^2}{c_s^2} - k_x^2\left(1 - \frac{\omega_g^2}{\omega^2}\right)\right]\Psi = 0, \tag{1.14}$$

where x is the coordinate in a horizontal direction and k_x is the horizontal wavenumber. Comparison of Equations (1.12) and (1.14) shows that equivalent modes are being considered when

$$k_x = \frac{\sqrt{l(l+1)}}{R_{sun}}, \tag{1.15}$$

where R_{sun} is the solar radius (R_{sun}=6.96 $\times$ 10^5km). The horizontal wavelength of the wave is then given by $\lambda_x = 2\pi/k_x$.

1.5.3 Helioseismology

In Section 1.5.1 we have described the existence of the 5-minute oscillations as standing acoustic waves in a cavity in the solar interior, and introduced their mathematical description in terms of spherical harmonics in Section 1.5.2. The oscillations formed by this process are termed $p-$modes with pressure being the dominant restoring force. This notation was first introduced by Cowling (1941). As mentioned earlier, the value of the Brunt-Väisälä frequency gives rise to other fluid motions when $\omega_g^2 \neq 0$. These modes have buoyancy as the restoring force on a displaced plasma element: these are termed gravity modes ($g-$modes) for an atmosphere where $\omega_g^2 > 0$, whereas if $\omega_g^2 < 0$ they are convective modes (see Chapter 3, where we have termed them g^--modes). Finally, a third global oscillation is the *fundamental* or $f-$mode. It lies between the $p-$modes and $g-$modes in a dispersion diagram and is analogous to an interfacial surface gravity wave on deep water, with the dispersion relation $\omega^2 = gk_x$. The fluid motions associated with this mode are incompressible and the mode is effectively independent of the thermal structure of the Sun. Its energy is concentrated around the photosphere and is channelled horizontally, having no vertical propagation.

Possibly the greatest value of the $p-$mode frequencies in helioseismology has been in their use to determine the internal structure of the Sun. Modes of different horizontal wavenumbers reside in cavities of different depths, hence a spectrum of frequencies provides information on the internal structure at all levels. For example, low l modes reside throughout almost the whole of the solar interior while high l modes are confined to layers near the surface and as such are only dependent on the structure of these depths. At present, helioseismology is one of only two methods capable of inferring the interior structure of the Sun. The other method is the measurement of solar neutrinos which emanate from the nuclear reactions in the solar core. However, the observed neutrino flux is only about one third of that predicted by standard solar models (Davis, Evans and Cleveland 1978).

Not only are helioseismological data sets used to infer the variation of, say, the sound speed within the solar interior, but the measured frequencies also provide a perfect benchmark against which to test the various models of solar structure. In a majority of models of the structure of the Sun, the model is derived from standard stellar evolution theory and then calibrated to the luminosity and the surface abundance of elements seen on the Sun. For these models the frequencies of their oscillations may be obtained numerically.

For simplicity the standard solar model calculations assume that the Sun is spherically symmetric, that the oscillations are adiabatic and linear, and that magnetism and convection are negligible (Christensen-Dalsgaard 1986).

Standard solar models predict frequencies that are very close to those observed, but there are errors which are greater than the observational accuracy. This implies that something is missing from these models. A number of candidates that may possibly rectify these discrepancies have been suggested. For example, modifications to the equation of state may be necessary, the addition of convection and turbulence would be of benefit, and the inclusion of other particles such as WIMPs in the solar core. Also, Christensen-Dalsgaard *et al.* (1988) have reported that by using a sophisticated equation of state, the errors increase with increasing l. This might indicate the position of the problem since high l modes reside near the surface. In fact, the superadiabatic layer of the outer convection zone is poorly understood owing to partial ionisation of the material there. It is also the place of transition from optically thick to optically thin radiation, and from high β to low β plasmas. From this we may see that much work remains in modelling and understanding the interior of the Sun. For a description of helioseismological techniques see the review by Deubner and Gough (1984).

1.5.4 Solar cycle variations in $p-$mode frequencies

The frequencies of the $p-$modes are measured to such an accuracy that the error is only about one part in ten thousand. The precision in these measurements has allowed observers to notice small but systematic changes in the $p-$mode frequencies over the solar cycle.

Figure 1.4 displays the measured frequency shift as a function of mode frequency, averaged over all observed modes. Figure 1.4 is reproduced from Libbrecht and Woodard (1991) and compares observational data sets obtained in 1986, 1988 and 1989. Frequency differences between 1986 and 1988 are shown as circles, while the squares show differences between 1986 and 1989. The results of Figure 1.4 show that with an increase in solar activity (1986 was solar minimum and 1989 was on the rise phase towards solar maximum) there is a rise in $p-$mode frequencies up to frequencies of about 3.9 mHz. Above this frequency, some effect seems to stop the frequency increase, and the frequency shift falls steeply. The observed effect at about 3.9 mHz is called the 'turnover'. The main aim of this thesis is to

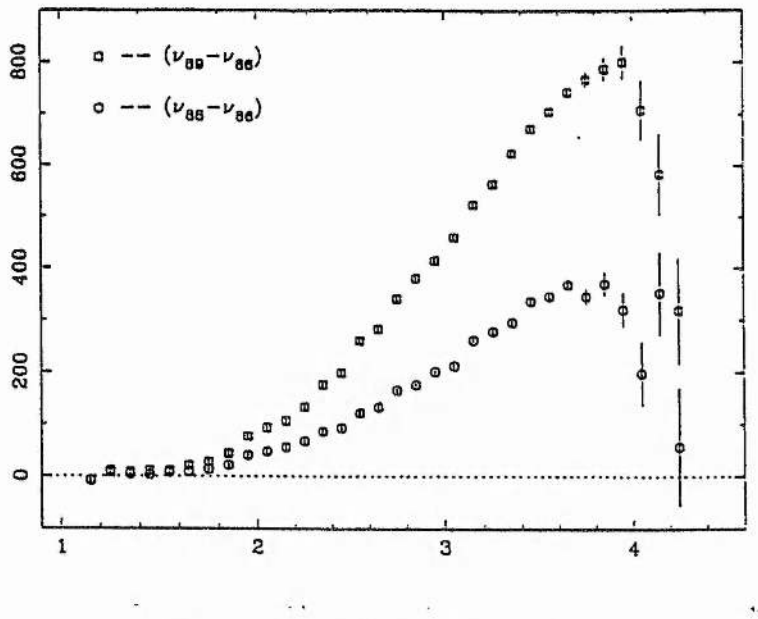

Figure 1.4: The observed frequency shift (in nHz), averaged over l, plotted against the original mode frequencies (in mHz). The circles represent the observed changes between 1986 and 1988 while the squares represent the changes between 1986 and 1989; error bars are represented by the vertical lines. (Reproduced from Libbrecht and Woodard (1991)).

attempt to pinpoint the physical processes occurring over the solar cycle which give rise to this distinctive behaviour.

The most well documented and observed global variation of the solar cycle is that of the magnetic field. Three magnetic regions have been investigated to explain the modification of mode frequencies with this in mind: the strong fields believed to reside in the convective overshoot region at the base of the convection zone; the fibril fields of the photosphere; and the canopy fields of the chromosphere.

The effect of a magnetic field at the base of the convection zone on low l $p-$mode frequencies has been considered by Roberts and Campbell (1986) and Campbell and Roberts (1986). They suggested that the frequency changes over the solar cycle observed by Woodard and Noyes (1985) could be explained by variations in the strength of the field. Their work implied a peak field strength of $5\times10^5 - 10^6$G in the field at the base of the convection zone, which is large for dynamo theories but is not unrealistic in view of the high gas pressures at that depth. We take up this problem in Chapter 4.

Other models have addressed the problem of the interaction of fibril fields beneath the photosphere with acoustic waves (e.g. Bogdan and Zweibel 1985; Zweibel and Bogdan 1986; Bogdan and Cattaneo 1989; Zweibel and Däppen 1989; and Rosenthal 1995). The

approach used in these models is to consider a population of scatterers (magnetic flux tubes) whose scattering properties are known and average the effect these have on acoustic wave frequencies. Zweibel and Bogdan (1986) found that frequency changes of the order 0.1%-0.3% were possible and Rosenthal (1995) was able to produce results in broad agreement with the observations with frequency shifts of the order 1 part in 10^4. Another study of photospheric fields and their influence on the frequencies of the $p-$modes has been carried out by Goldreich *et al.* (1991). They suggested that the positive component of the frequency shift was induced by a rise in strength of the photospheric magnetic field to an rms value of 200 G from solar minimum to maximum, and that the observed drop at high frequency was due to the increase in temperature of the chromosphere combined with a chromospheric resonant cavity.

The importance of a chromospheric canopy field on influencing $p-$mode frequencies has been investigated by Campbell and Roberts (1989), Evans and Roberts (1990, 1992), Jain and Roberts (1994, 1996), Johnston (1994), and Johnston *et al.* (1994). A canopy type field confined to the chromosphere will affect most strongly modes trapped near the surface (i.e. intermediate and high l modes). As a result it is sufficient to consider modes with short horizontal wavelengths, allowing plane-parallel models to be used. Campbell and Roberts (1989) used a model consisting of a field-free convection zone, with a stably stratified linear temperature profile, overlain by an isothermal atmosphere permeated by a horizontal magnetic field. The field is structured in such a way as to provide a constant Alfvén speed in the atmosphere, taken to represent the canopy field of the chromosphere. Campbell and Roberts (1989) showed that an increase in magnetic field strength decreased the $p-$mode frequencies but admitted that their model underestimated the effect of a magnetic canopy.

Evans and Roberts (1990) and Jain and Roberts (1994) used the same interior profile of Campbell and Roberts (1989) but included a uniform magnetic field in the atmosphere. In a model chromosphere of this kind, the Alfvén speed increases exponentially (with height) without bound and is at the other extreme of the magnetic field profile used by Campbell and Roberts (1989). Evans and Roberts (1990) were concerned with investigating the changes in mode frequency brought about by changes in magnetic field strength. They showed that the frequencies of the $p-$modes increased with an increase in magnetic field strength, but this alone could not produce the observed turnover in the frequency shifts. Jain and Roberts (1994) combined increasing the magnetic field strength of the atmosphere with increasing temperature in the same region. Through this they were able

to reproduce qualitatively the observed solar cycle variation in $p-$mode frequencies, but found that they required unrealistically large changes in chromospheric temperature to do so ($\triangle T \approx 1500^{o}$K).

In this thesis, we continue the investigation into possible explanations for the observed solar cycle variations in $p-$mode frequencies.

1.6 Magnetoacoustic Waves

In an astrophysical plasma such as that found in the Sun, the magnetic field tends to give structure to the medium within which it resides. The magnetic structuring of the Sun is particularly evident from the surface outwards in features such as sunspots, intense flux tubes in the photosphere, prominences and spicules. Where the plasma is bounded in this fashion, surrounded by plasma of different properties, we find surfaces rather than a uniform medium. Also, the presence of gravity adds an extra complication through stratification of the plasma; this is of great importance beneath the photosphere although its effect is less pronounced in the corona. The magnetic field and gravity thus create *inhomogeneity* in the solar atmosphere which greatly influences the properties of solar oscillations. As mentioned, the magnetic field serves to give rise to surfaces, but stratification introduces several additional effects. Firstly, gravity may serve to amplify or dampen the amplitude of propagating waves. Secondly, it may cause evanescence in waves in some regions which are oscillatory in others; a good example of this behaviour is the $p-$modes studied in the subsequent chapters.

The formation of interfaces through magnetic fields (or gravity) gives rise to the existence of surface waves, waves which exist on a strong discontinuity but which spatially decay away from the interface. Surface waves exist alongside the body waves of the plasma which are also modified by the presence of a sharp change in physical conditions. The body waves are the main form of communication between different regions. Before discussing of surface wave phenomena, we present briefly the results describing the body waves of a *uniform medium.*

In all wave analysis, an equilibrium plasma structure is perturbed and the resulting disturbance is investigated to see if it propagates as a wave. Consider an infinite equilibrium containing uniform gas pressure P_o, density ρ_o, temperature T_o, and magnetic field $\mathbf{B_o} =$

$(0, 0, B_o)$. Gravity is ignored. A perturbation in, say, pressure of the form

$$P(x, y, z, t) = P_o + P\exp\left[i(\omega t - \mathbf{K} \cdot \mathbf{r})\right], \tag{1.16}$$

where P_o is the equilibrium pressure, P the amplitude of the disturbance, ω the angular frequency, and $\mathbf{K}$ $(= (k_x, k_y, k_z))$ the wavevector, applied to Equations (1.2)-(1.10), gives the dispersion relation (see, for example, Roberts 1985):

$$(\omega^2 - k_z^2 v_a^2)[\omega^4 - (c_s^2 + v_a^2)K^2\omega^2 + K^2 k_z^2 c_s^2 v_a^2] = 0, \tag{1.17}$$

where $K = |\mathbf{K}|$, c_s is the sound speed and v_a the Alfvén speed.

Three forms of wave are present in the dispersion relation given by Equation (1.17). Firstly, there is an Alfvén wave, travelling along the magnetic field (and hence anisotropically) at the Alfvén speed, given by the round bracketed term in Equation (1.17). Additionally, there are two magnetoacoustic waves known as the fast and slow magnetoacoustic waves. These waves have associated fast speed c_f $(= (c_s^2 + v_a^2)^{\frac{1}{2}})$ and slow cusp speed c_t $(= c_s^{\frac{1}{2}} v_a^{\frac{1}{2}}/c_f)$, and can be seen to be hybrids of magnetic and sound waves. The fast magnetoacoustic wave is close in character to a sound wave whereas the slow wave is similar in nature to an Alfvén wave. However, as we have mentioned, the assumption of uniformity is rarely appropriate in the solar atmosphere. The sharp transitions present in density, pressure and magnetic field modify the waves described above and *magnetoacoustic surface waves* propagate along the surfaces produced by such structures.

There are many candidates for surface waves. For example, there is the running penumbral wave seen to emanate from the umbrae of sunspots and which propagates between the penumbra and the underlying, generally field-free, plasma. These have been modelled as magnetoacoustic-gravity modes by Nye and Thomas (1974, 1976*b*) and as fast magnetoacoustic surface waves by Small and Roberts (1984). Also, there is the $f-$mode, a buoyancy driven mode analogous to deep water waves.

1.7 Outline of the Remaining Chapters

In this opening chapter, we have given a brief description of the Sun, with regards to the large diversity of oscillations that it may sustain, its structure, and its magnetic field. In particular, we have introduced and described the main area of interest in this thesis, the global solar oscillations known as $p-$modes and the variation of their frequencies over the

solar cycle. The basic models presented are designed such that analytical methods may be used throughout. Through these models, we attempt to determine the physical changes which give rise to the observed variations in $p-$mode frequencies, particularly the turnover seen at 3.9mHz (Figure 1.4).

In Chapter 2, we consider a model specifically constructed to investigate modes of degree zero, where $l = 0$. The model is used to analyse the effect of an overlying chromosphere on the frequencies of these modes. We do this by applying different magnetic field profiles and temperatures in the chromosphere. The dispersion relations obtained are solved numerically and the results are compared to observational data for low degree modes.

In Chapter 3 we turn our attention to modes of general degree ($l \neq 0$) and investigate another potential surface layer which may be the site of the physical changes responsible for $p-$mode frequency variations. The region investigated is the thin superadiabatic layer of the upper convection zone. A three layer model is used to include this layer and a complicated dispersion relation is derived. We solve the dispersion relation numerically and evaluate the frequency shifts brought about by varying the temperature profile of the superadiabatic layer and the temperature of the photosphere above it. We also investigate the effects of magnetic fields present in the atmosphere but, for analytical convenience, use the somewhat crude profile of a uniform horizontal magnetic field. The inclusion of a superadiabatic layer in the model gives rise to convective modes associated with this layer. In this chapter we also consider their sensitivity to the physical variations applied to the $p-$modes. Again, the results are compared to the relevant observations.

In Chapter 4 we move deeper into the Sun and develop a model which allows us to calculate frequency changes in the $p-$modes brought about by a magnetic layer at the base of the convection zone. Again, a complicated dispersion relation is obtained which is solved numerically for different sub-convective magnetic field strengths. The main focus of attention is on general degree modes, but we also adapt the model of Chapter 2 to analyse the effect that this layer has on the radial modes.

The presence of a magnetic layer below the convection zone gives rise to the surface and body modes associated with it. In Chapter 5 we make a brief investigation of their properties. A detailed study of compressible magnetoacoustic surface modes in the presence of gravity is, to our knowledge, still to be undertaken.

Finally, in Chapter 6 we summarise the main results of the thesis and present some suggestions for further investigations.

Chapter 2

Modes of Degree Zero

2.1 Introduction

In Chapter 1, we discussed how the solar $p-$modes are formed by the trapping of acoustic waves within a cavity in the Sun's interior. The cavity is formed at its lower boundary by the increase of the sound speed with depth, leading to the process of acoustic refraction, and at its upper boundary by the somewhat more complicated reflective properties of the photosphere and chromosphere.

The detailed structure of the solar atmosphere above the photosphere may be of prime importance in bringing about the slight changes in $p-$mode frequencies that are observed over the solar cycle. This is because the rate of evanescence in the modes, i.e. the rapidity with which the eigenmodes decay, is determined in this region. One would expect frequency shifts for low degree modes to be slight as these modes are very deeply penetrating, but the upper boundary does dictate the fine structure of the modes. By way of illustration, we may consider two extreme cases of an upper boundary: firstly, we may have a rigid wall as an upper boundary which implies an infinite rate of evanescence, i.e. all modes are trapped; or, at the other extreme, there may be an open upper boundary, analogous to the open end of an organ pipe, where there is zero rate of evanescence.

So then, with these two physical processes trapping acoustic waves in a cavity in the solar interior, we should expect to see many modes of different degree, radial order and frequency superimposed upon each other at any one time. However, there is one particular class of oscillation that stands out from the others, at least from a theoretical viewpoint, namely modes of degree zero ($l = 0$).

Why are zero degree modes unique? The answer lies in that these modes are purely radial in nature and as a result no refraction takes place within the solar interior. The entire surface of the sun is oscillating in phase for this mode, with no nodal lines being present, and reflection is the only physical process forming a standing wave cavity.

To gain some insight into these modes, consider again the wavefront picture described in Section 1.5.1. At any point in the sun, we will encounter a spherical wavefront, every point of which is moving towards the centre of the sun with the same phase speed. As no part of the wavefront is deeper than any other, the wave is not refracted by the increasing temperature. This wave front will eventually pass through the centre of the sun and expand outwards again until it is reflected by the solar surface.

So, in terms of wave motion, we simply have a wave that is propagating radially towards or away from the centre of the sun. The wave does not undergo refraction but it is constrained by the reflective properties of the outer atmospheric layers. As a result the cavity for the standing waves formed is the entire sun.

How do we model such modes mathematically? Generally low-l modes are difficult to treat because they are deeply penetrating and as such are sensitive to spherical effects. With $l = 0$ modes we may progress more readily. First of all, the radial nature of the modes allows us to write any disturbance in terms of just one variable, the depth, z. Also, to form standing waves, disturbances must be symmetrical about the centre of the sun. This simplifies the problem by letting us consider just one half of a waves transit across a solar diameter and also allows a plane-parallel model to be used as a good approximation.

Therefore, we may model the convection zone and below as a polytropic fluid with a temperature that increases linearly with depth, the gradient of which is chosen to give marginal stability to convective motions (i.e. we assume that the lower region is adiabatically stratified with the Brunt-Väisälä or buoyancy frequency, ω_g, zero). The interior is similar to that considered in previous work on general degree $p-$modes (Campbell and Roberts 1989; Evans and Roberts 1990,1991; Jain and Roberts 1994) except for one detail. In the earlier work, the convection zone and below was modelled as being semi-infinite. This was because those models were derived to study higher degree modes which are confined close to the solar surface. For our model we consider a finite range of z on $[0, z_d]$, where z_d is some finite depth. This is purely because of the symmetrical nature of the modes about the centre of the sun.

In the atmosphere above the convective region we impose an isothermal chromo-

sphere within which is embedded a horizontal magnetic field, **B**. The temperature, T_{at}, of the atmosphere and the magnetic field strength B are allowed to vary so that their effect on mode frequencies can be investigated.

The chapter is organised as follows. In the following section (Section 2.2), we summarise the observational results concerning low degree modes and the evidence for solar cycle variations in mode frequencies. In Section 2.3, we introduce the equilibrium structure of the model and derive the equations governing motions. Section 2.4 will be concerned with the investigation of the simplest case that the model allows. This section furnishes us with a set of base frequencies that we may use as a standard to measure frequency shifts against. This topic is pursued in section 2.5, where we consider the calculation of frequency differences arising from a variation in the physical parameters of the chromosphere. Section 2.5 discusses changes in mode frequency due to a change in atmospheric temperature alone (Section 2.5.1). We allow for two extremes of chromospheric magnetic field profile, namely that of a canopy field that provides either a constant Alfvén speed (Section 2.5.2) or a *uniform* magnetic field (Section 2.5.3). Section 2.6 shows how we may manipulate the dispersion relations found and, finally, in Section 2.7 we discuss the results obtained.

2.2 The Observed Properties of Low Degree Modes

The search for the frequencies of the radial oscillations of the Sun was initiated by Isaak and co-workers at the University of Birmingham. It was soon realised that better observing sites were required and in 1974 the apparatus was relocated to the Pic du Midi observatory in the French Pyrenees. They very quickly began collecting good quality data from their instruments (see, for example, Claverie *et al.* (1979)). The BISON (Birmingham Solar Oscillation Network) now has six observing stations around the globe including sites in Chile, South Africa and Australia, providing 24 hour data collection. As a result, the BISON group probably boast the highest quality observational data with accuracies in the measurement of the frequencies approaching one part in 100000.

The frequencies of low degree oscillations were first measured from space by the ACRIM (Active Cavity Radiometer Irradiance Monitor) instrument on board the Solar Maximum Mission (SMM) satellite. The collection of data was undertaken during two periods in the early 1980's; the first observations were made during 1980 (near solar maximum) and the second during 1984 (at a time near solar minimum).

The first analysis of the data from these two observation windows was carried out by Woodard and Noyes (1985). The timing of the observations allowed them to analyse the ACRIM data with regards to finding any significant changes in the frequencies of $l = 0$ and $l = 1$ modes over the 11 year solar cycle. By taking frequencies in the five-minute band and calculating the difference

$$\triangle\nu = \nu(1980) - \nu(1984), \tag{2.1}$$

Woodard and Noyes (1985) were able to show a frequency *decrease* in low degree $p-$modes from solar maximum to solar minimum. In fact, the mean frequency difference from 1980 to 1984 was found to be

$$\triangle\nu = 0.42 \pm 0.14 \ \mu\text{Hz}. \tag{2.2}$$

Since then, the sparsity of data points in the modes measured by ACRIM coupled with a break in the monitoring of the Sun by the SMM satellite has prompted many workers into attempting to reproduce or refute the solar cycle dependency of mode frequency claimed by Woodard and Noyes (1985). The first to follow up on this work were Pallé *et al.* (1986), using Tenerife data from 1977 to 1984. For low l and high radial order n ($17 \leq n \leq 30$), they found no conclusive evidence for frequency variations over the solar cycle.

Woodard (1987) extended the data analysis of Woodard and Noyes (1985), taking additional ACRIM data from 1985 and 1986. Assuming the frequency shift to be independent of radial order, Woodard (1987) showed a frequency decrease for low l modes between 1980 and 1985/86 of 0.41 ± 0.24 μHz, thus reinforcing the claims of Woodard and Noyes (1985).

In a similar study, Fossat *et al.* (1987) used ACRIM data for the period around the solar maximum along with full disk velocity measurements taken from the South Pole during November 1984 to February 1985. Comparing the two sets of data, they also claimed a *decrease* in frequency, of 0.39 ± 0.04 μHz, between the two periods, strengthening the results of Woodard and Noyes (1985) and Woodard (1987).

However, the evidence for a solar cycle dependence of the low l $p-$mode frequencies remained inconclusive. Later work carried out by Jefferies *et al.* (1988) on data taken from the Observatorio del Teide between 1977 and 1985 showed no frequency variation over the period of observation. In contradiction to this, Pallé *et al.* (1989), extending the data from their previous work, were now able to show a decrease in the frequencies of low degree

modes of 0.37±0.04 μHz over the course of the solar cycle. Specifically, for modes of degree zero they showed a mean decrease of 0.18±0.003 μHz from solar maximum to minimum.

The evidence for the solar cycle dependence of low l $p-$mode frequencies was further strengthened by Elsworth *et al.* (1990). Using modes of high radial orders, they discovered a drop in frequency of 0.46±0.06 μHz from solar maximum to solar minimum. Also, Anguera Gubau *et al.* (1992), using data collected between 1980-1989, showed relative variations in $p-$mode frequencies comparable to the earlier observations.

Recently, Régulo *et al.* (1994) give a trend in frequency changes with the solar cycle of around 0.52±0.02 μHz for low degree modes ($0 < l < 3$) in the frequency range 2.5-3.7 mHz, and Elsworth *et al.* (1994) have added to the results given in Elsworth *et al.* (1990) by taking the BISON data up to early 1994.

Finally, the results of Chaplin *et al.* (1998) not only display a variation in the low l $p-$mode frequencies over the course of the solar cycle, but also show evidence for a steep downturn in frequency shifts for modes with frequencies above 3.7-3.9 mHz, indicating that the low l modes behave in a similar fashion to intermediate degree modes (see Libbrecht and Woodard (1991) and the discussion in Chapter 1).

2.3 The Model and Governing Equations

The model we use consists of two layers of fluid, the lower one representing the convection zone and below of the solar interior and the upper one the chromosphere. The lower region extends in depth z from 0 to z_d; the upper region ($z < 0$) is semi-infinite in extent. The profile of equilibrium temperature, $T_o(z)$, is taken to increase linearly with depth within $[0, z_d]$, and to be constant in $z < 0$.

Specifically, we consider a temperature profile of the form

$$T_o(z) = \begin{cases} T_{oL}(1 + \frac{z}{z_o}), & 0 < z < z_d, \\ T_{at}, & z < 0. \end{cases} \tag{2.3}$$

Here, T_{oL} is the temperature at the top ($z = 0$) of the convection zone and T_{at} is the uniform temperature within the chromosphere. The temperature scale height at the top of the convection zone is denoted by z_o. We shall discuss the value given to z_o later.

The solar plasma is assumed to be an ideal, perfectly conducting plasma, threaded by a structured horizontal magnetic field of the form $\mathbf{B} = B(z)\hat{\mathbf{x}}$. The entire medium is

gravitationally stratified in depth z. The unperturbed state is one of magnetohydrostatic equilibrium satisfying

$$\frac{d}{dz}\left(P_o + \frac{B^2}{2\mu}\right) = \rho_o g \tag{2.4}$$

with

$$P_o(z) = R\rho_o(z)T_o(z); \tag{2.5}$$

here $P_o(z)$ and $\rho_o(z)$ are the equilibrium gas pressure and density respectively, g is the gravitational acceleration (assumed constant), μ ($= 4\pi \times 10^{-7}$ Henry m^{-1}) is the magnetic permeability and $R{=}k_B/m_{av}$ where k_B is Boltzmann's constant and m_{av} is the mean particle mass of the plasma. Equation (2.4) holds both in the atmosphere $z < 0$ and in the field-free ($B = 0$) interior $[0, z_d]$.

Equations (2.4) and (2.5) may be solved simultaneously to give the equilibrium gas pressure and density for specific magnetic field profiles.

Let us also consider conditions pertaining across the interface $z = 0$ between the two regions. We do not demand that the temperature is continuous across the interface at $z = 0$. This enables the temperature at the top of the convection zone, T_{oL}, to be held fixed whilst varying the atmospheric temperature, T_{at}. Also, it is preferable to keep the interior of the model the same throughout all of the calculations so that the changes in atmospheric conditions alone are purely responsible for any changes in mode frequency that we may find.

The condition imposed at the interface is that the total (gas plus magnetic) pressure be continuous across $z = 0$. Therefore, the gas pressure at the top of the convection zone, P_{oL}, is related to the total (gas plus magnetic) pressure in the atmosphere by

$$P_{oL} = P_{at} + \frac{B_o^2}{2\mu}, \tag{2.6}$$

where P_{at} and $B_o^2/2\mu$ are the gas and magnetic pressures at the base of the chromosphere; the magnetic field strength at the base $z = 0$ of the chromosphere is taken to be B_o ($=B(z = 0)$).

Equation (2.5) and Equation (2.6) combine to give a relation between the plasma density ρ_{at} at the base of the chromosphere to the density ρ_{oL} at the top of the convection zone:

$$\rho_{at}c_{at}^2 = \rho_{oL}c_{oL}^2 - \frac{\gamma}{2\mu}B_o^2. \tag{2.7}$$

Here, $c_{oL} = (\gamma P_{oL}/\rho_{oL})^{\frac{1}{2}}$ is the sound speed at the top of the convection zone, $c_{at} = (\gamma P_{at}/\rho_{at})^{\frac{1}{2}}$ is the constant sound speed in the atmosphere, and γ denotes the adiabatic index.

From Equation (2.7) we may obtain the interfacial density ratio:

$$\frac{\rho_{at}}{\rho_{oL}} = \frac{c_{oL}^2}{(c_{at}^2 + \frac{\gamma}{2}v_{ao}^2)}. \tag{2.8}$$

The Alfvén speed at the base of the chromosphere is denoted by $v_{ao}(= (B_o^2/\mu\rho_{at})^{\frac{1}{2}})$. We may also see from Equation (2.7) that restrictions must be placed on the strength of the magnetic field in order to maintain $\rho_{at} > 0$. We shall discuss this when we consider the effects of a chromospheric magnetic field in Section 2.5.2.

The equations governing the motion are:
the equation of mass continuity

$$\frac{\partial \rho}{\partial t} + \nabla \cdot (\rho \mathbf{u}) = 0, \tag{2.9}$$

the momentum equation

$$\rho \frac{D\mathbf{u}}{Dt} = -\nabla P + \rho \mathbf{g} + \mathbf{j} \times \mathbf{B}, \tag{2.10}$$

the induction equation (with no diffusion),

$$\frac{\partial \mathbf{B}}{\partial t} = \nabla \times (\mathbf{u} \times \mathbf{B}), \tag{2.11}$$

and an adiabatic energy equation of the form

$$\frac{DP}{Dt} = \frac{\gamma P}{\rho}\frac{D\rho}{Dt}. \tag{2.12}$$

The current density, $\mathbf{j}$, is given by Ampere's law

$$\mu \mathbf{j} = \nabla \times \mathbf{B}, \tag{2.13}$$

and the advective derivative is denoted by

$$\frac{D}{Dt} \equiv \frac{\partial}{\partial t} + \mathbf{u} \cdot \nabla. \tag{2.14}$$

Finally, the magnetic field satisfies the solenoidal constraint:

$$\nabla \cdot \mathbf{B} = 0. \tag{2.15}$$

The relative amplitudes of solar oscillations are known to be small compared to the local sound speed (see, for example, Christensen-Dalsgaard (1986)). As a result a

linear analysis may be used on the system of Equations (2.9)-(2.15). Taking a velocity perturbation of the form

$$\mathbf{u} = (0, 0, u_z(z))e^{i\omega t}, \tag{2.16}$$

where ω is the angular frequency of the disturbance, and applying it to Equations (2.9)-(2.15) leads to a linearised momentum equation of the form

$$\rho_o \frac{\partial \mathbf{u}}{\partial t} = \rho_1 g \hat{\mathbf{z}} - \nabla P_1 - \nabla \left(\frac{B_o(z) b_x}{\mu} \right), \tag{2.17}$$

where the equilibrium quantities are denoted with the subscript o and the perturbed pressure and density by the subscript 1. The $x-$component of the perturbed magnetic field $\mathbf{B}$ is b_x. As there are no horizontal motions, we may take the $z-$component of Equation (2.17) and differentiate it with respect to time to give

$$\rho_o \frac{\partial^2 u_z}{\partial t^2} = g \frac{\partial \rho_1}{\partial t} - \frac{\partial}{\partial z} \left(\frac{\partial P_1}{\partial t} + \frac{B_o(z)}{\mu} \frac{\partial b_x}{\partial t} \right). \tag{2.18}$$

The perturbations ρ_1, P_1 and b_x may be eliminated by using the linearised forms of Equations (2.9), (2.11) and (2.12):

$$\frac{\partial \rho_1}{\partial t} = - \left(u_z \frac{\partial \rho_o}{\partial z} + \rho_o \frac{\partial u_z}{\partial z} \right), \tag{2.19}$$

$$\frac{\partial P_1}{\partial t} = - \left(c_s^2(z) \rho_o \frac{\partial u_z}{\partial z} + u_z \frac{\partial P_o}{\partial z} \right), \tag{2.20}$$

and

$$\frac{B_o(z)}{\mu} \frac{\partial b_x}{\partial t} = - \left(v_a^2(z) \rho_o \frac{\partial u_z}{\partial z} + u_z \frac{\partial}{\partial z} \left[\frac{B_o^2(z)}{2\mu} \right] \right). \tag{2.21}$$

Applying Equations (2.19)-(2.21) to Equation (2.18) gives

$$\rho_o \frac{\partial^2 u_z}{\partial t^2} = \frac{\partial}{\partial z} \left[c_s^2 \rho_o \frac{\partial u_z}{\partial z} + u_z \frac{\partial}{\partial z} \left(P_o + \frac{B_o^2(z)}{2\mu} \right) + \frac{B_o^2(z)}{\mu} \frac{\partial u_z}{\partial z} \right] - g \left(\rho_o \frac{\partial u_z}{\partial z} + u_z \frac{\partial \rho_o}{\partial z} \right). \tag{2.22}$$

Finally, manipulation of Equation (2.22) using Equation (2.4) gives rise to the wave equation for perturbations u_z to the equilibrium (2.4):

$$\rho_o \frac{\partial^2 u_z}{\partial t^2} = \frac{\partial}{\partial z} \left[\rho_o (c_s^2(z) + v_a^2(z)) \frac{\partial u_z}{\partial z} \right]. \tag{2.23}$$

In the above, $c_s(z) = (\gamma P_o(z)/\rho_o(z))^{\frac{1}{2}}$ is the local sound speed and $v_a(z) = (B_o^2(z)/\mu\rho_o(z))^{\frac{1}{2}}$ is the local Alfvén speed within the medium. With the time dependence for $u_z(z)$ given by

Equation (2.16) we may immediately gain the governing equation for the vertical velocity component:

$$\frac{d}{dz}\left[\rho_o(z)[c_s^2(z)+v_a^2(z)]\frac{du_z}{dz}\right]+\rho_o(z)\omega^2 u_z=0. \tag{2.24}$$

Equation (2.24) is the governing equation for a stratified fluid permeated by a horizontal magnetic field undergoing a purely one dimensional perturbation. It is applicable to both layers of the model when the specific equilibrium density, sound and Alfvén speeds are substituted. More general models have been considered which reduce to Equation (2.24) (see, for example Goedbloed 1971; Adam 1977; Roberts 1985). Equation (2.24) is simple in form because of our assumption of one dimensionality (the horizontal wavenumber $k_x = 0$).

We consider the solution of Equation (2.24) for different equilibria and use these solutions to determine mode frequencies through a derived dispersion relation. As we have already stated, some form of base frequencies are required to measure frequency shifts against and we shall turn to this now.

2.4 Mode Frequencies

The main incentive behind this work is an interest in whether physical changes in the outer atmospheric layers of the sun may produce the shifts in p–mode frequencies that are observed over the solar cycle (see Chapter 1 and Section 2.2). In order to consider frequency shifts, we first calculate some base frequencies for the model. To do this we consider the simplest case that the model allows.

The most basic of situations is where we take the temperature to be continuous across the interface at $z = 0$, so that $T_{oL} = T_{at}$, and the atmosphere is assumed to be field-free ($B_o = 0$). In this section we derive a dispersion relation for this situation and use the frequencies that it gives as the base ones for other cases. Frequencies may then be found for different chromospheric parameters (temperature and magnetic field strength) and compared to the calculated base frequencies. The temperature at the reference level $z = 0$ will be taken to be the solar temperature minimum, $T_{at} = 4170°\mathrm{K}$.

In the *absence* of a magnetic field equilibrium condition (2.4) reduces to

$$\frac{dP_o}{dz}=\rho_o g, \tag{2.25}$$

applicable in both regions ($z < 0$ and $0 \leq z \leq z_d$), and pressure condition (2.8) across the interface simplifies to

$$\frac{\rho_{at}}{\rho_{oL}} = 1, \tag{2.26}$$

given that $T_{oL} = T_{at}$.

On substituting the temperature profile (2.3), with the constraints given above, the hydrostatic condition (2.25) can be solved to give the equilibrium pressure distribution:

$$P_o(z) = \begin{cases} P_{oL}(1 + \frac{z}{z_o})^{m+1}, & 0 < z < z_d, \\ P_{at} e^{\frac{z}{H}}, & z < 0, \end{cases} \tag{2.27}$$

where

$$m = \frac{g z_o}{R T_{oL}} - 1 \qquad \text{and} \qquad H \equiv \frac{R T_{at}}{g} = \frac{c_{at}^2}{g\gamma} \tag{2.28}$$

are the polytropic index of the convection zone and the density scale height of the chromosphere respectively. Note that we have retained the subscript at to denote parameters of the atmosphere, such as the pressure P_{at} at the base of the chromosphere. Here $P_{oL} = P_{at}$, but retaining the distinguishing notation that will be used later helps avoid confusion.

It is from the polytropic index of the gas m that we obtain the temperature scale height z_o for the lower region. In choosing the interior to be marginally stable to convective motions, the Brunt-Väisälä frequency, defined by

$$\omega_g^2 = g\left[\frac{1}{\rho_o(z)}\frac{d\rho_o(z)}{dz} - \frac{g}{c_s^2(z)}\right], \tag{2.29}$$

is zero. For the model presented here, $\rho_o(z) \propto (1 + z/z_o)^m$ and $c_s^2(z) \propto (1 + z/z_o)$. For the profiles of equilibrium density and sound speed squared for the model, the Brunt-Väisälä is given by

$$\omega_g^2 = \left[m - \frac{(m+1)}{\gamma}\right]\frac{g}{z + z_o}. \tag{2.30}$$

Therefore m is related to the adiabatic exponent γ by $m = 1/(\gamma - 1)$. For an adiabatic exponent of $\gamma = 5/3$, we obtain $m = 3/2$, and this gives a temperature scale height $z_o = 244.5$ km at the temperature minimum.

The lower region of this fluid, which we shall call the interior, will be kept the same for all chromospheric variations that are to be considered. Let us look for a solution

of Equation (2.24) in this zone where the temperature profile is given by (2.3). Firstly, note that the sound speed squared $c_s^2(z)$ in this region is of the form

$$c_o(z)^2 = c_{oL}^2(1 + \frac{z}{z_o}), \qquad 0 < z < z_d. \tag{2.31}$$

The sound speed c_{oL} at the top ($z = 0$) of the convection zone ($c_{oL} = (\gamma R T_{oL})^{\frac{1}{2}}$) is taken to be the sound speed at the temperature minimum in our calculations, as mentioned earlier. Substituting Equation (2.31) into Equation (2.24) with $v_a = 0$ leads to

$$\frac{d^2u_z}{dz^2} + \frac{m+1}{z_o(1+\frac{z}{z_o})}\frac{du_z}{dz} + \frac{\omega^2}{c_{oL}^2(1+\frac{z}{z_o})}u_z = 0. \tag{2.32}$$

To solve this equation it is convenient to introduce a number of transformations. Setting

$$s = 1 + \frac{z}{z_o}, \qquad 0 \leq z \leq z_d \tag{2.33}$$

yields

$$s\frac{d^2u_z}{ds^2} + (m+1)\frac{du_z}{ds} + \frac{\omega^2 z_o^2}{c_{oL}^2}u_z = 0. \tag{2.34}$$

If now we introduce

$$r = \frac{2\omega z_o}{c_{oL}}s^{\frac{1}{2}}, \tag{2.35}$$

then Equation (2.34) becomes

$$r^2\frac{d^2u_z}{dr^2} + (2m+1)r\frac{du_z}{dr} + r^2u_z = 0. \tag{2.36}$$

Finally, setting

$$u_z = r^{-m}X, \tag{2.37}$$

we obtain Bessel's equation for functions of order m (Abramowitz and Stegun, 1965: 9.1.1):

$$r^2\frac{d^2X}{dr^2} + r\frac{dX}{dr} + (r^2 - m^2)X = 0. \tag{2.38}$$

The general solution to Equation (2.38) is

$$X = c_1 J_m(r) + c_2 Y_m(r). \tag{2.39}$$

The Bessel functions of the first and second kind are denoted by $J_m(r)$ and $Y_m(r)$ whilst the constants of integration are given by c_1 and c_2.

The amplitude of the vertical disturbance in plasma velocity in $[0, z_d]$ is therefore given by:

$$u_z = r^{-m}\left[c_1 J_m(r) + c_2 Y_m(r)\right], \qquad 0 \le z \le z_d, \tag{2.40}$$

with

$$r = \frac{2\omega z_o}{c_{oL}}\left(1 + \frac{z}{z_o}\right)^{\frac{1}{2}}. \tag{2.41}$$

From the relations (Abramowitz and Stegun 1965; 9.1.30)

$$\frac{d}{dz}\left[z^{-m} J_m(z)\right] = -z^{-m} J_{m+1}(z) \tag{2.42}$$

and

$$\frac{d}{dz}\left[z^{-m} Y_m(z)\right] = -z^{-m} Y_{m+1}(z), \tag{2.43}$$

and noting that

$$\frac{dr}{dz} = \frac{2\omega^2 z_o}{c_{oL}^2}\frac{1}{r}, \tag{2.44}$$

we obtain

$$\frac{du_z}{dz} = -\frac{2\omega^2 z_o}{c_{oL}^2} r^{-(m+1)}\left[c_1 J_{m+1}(r) + c_2 Y_{m+1}(r)\right]. \tag{2.45}$$

We now turn to the semi-infinite upper region $z < 0$, which we take to represent the chromosphere. In this region Equation (2.24) reduces to

$$\frac{d^2 u_z}{dz^2} + \frac{1}{H}\frac{du_z}{dz} + \frac{\omega^2}{c_{at}^2} u_z = 0, \qquad z < 0. \tag{2.46}$$

Equation (2.46) has solutions of the form

$$u_z = \mathcal{A} e^{\lambda z}, \qquad z < 0, \tag{2.47}$$

where

$$2H\lambda = -1 \pm \left(1 - \frac{4\omega^2 H^2}{c_{at}^2}\right)^{\frac{1}{2}}. \tag{2.48}$$

Combined with the solution for the velocity profile found in the interior (Equation (2.40)), we obtain the velocity distribution:

$$u_z = \begin{cases} \mathcal{A} e^{\lambda z}, & z < 0, \\ r^{-m}\left[c_1 J_m(r) + c_2 Y_m(r)\right], & 0 < z < z_d, \end{cases} \tag{2.49}$$

where r is defined by (2.41). Also,

$$\frac{du_z}{dz} = \begin{cases} \lambda \mathcal{A} e^{\lambda z}, & z < 0, \\ -(2\omega^2 z_o / c_{oL}^2) r^{-(m+1)} \left[c_1 J_{m+1}(r) + c_2 Y_{m+1}(r) \right], & 0 < z < z_d. \end{cases} \tag{2.50}$$

There are two points of interest in solution (2.47) that we require comment on here. Firstly, a specific boundary condition must be applied in order to determine which sign of the square root is required in Equation (2.47) and, secondly, the square root itself. What do we understand by this? We know that perturbations in the atmosphere ($z < 0$) are either propagatory or evanescent and that for modes to be trapped in a bounded cavity it is the evanescent solutions that are of interest. Those solutions where the square root becomes complex imply that no cavity exists, i.e. the modes are propagating away from the interface; these are called leaky modes and will not be discussed here. As a result of this restriction on the square root, we see that to form the type of modes required the frequency of the modes must be less than a critical frequency ω_{ac} determined by the physical structure of the atmosphere. Thus we require $\omega < \omega_{ac}$, where

$$\omega_{ac}^2 \equiv \frac{c_{at}^2}{4H^2} = \frac{g^2 \gamma^2}{4 c_{at}^2}; \tag{2.51}$$

ω_{ac} is the acoustic cut-off frequency for an isothermal atmosphere (Lamb 1908). As an example, in this section we are taking the temperature of the atmosphere to be the same as that at the temperature minimum, i.e. $T_{at} = T_{oL} = 4170°\text{K}$. This gives us a cyclic cut-off frequency, $\nu_{ac} (\equiv \omega_{ac}/2\pi)$, of approximately 5.43 mHz. This cut-off frequency is constant throughout the atmosphere and is a global quantity owing to the isothermal nature of the region.

So, for the range of frequencies $\omega < \omega_{ac}$ we may now apply additional boundary conditions to solutions (2.49) and (2.50) in order to match the solutions in the two regions and so obtain a dispersion relation. We accomplish this by considering conditions as we move a long distance from the interface into the atmosphere ($z \to -\infty$), together with the conditions at the interface itself and the constraint that the rigid wall at $z = z_d$ imposes.

As a first condition, let us return to choosing the sign of the square root in Equation (2.47). We demand that the kinetic energy density of the modes, $\frac{1}{2}\rho_o u_z^2$, declines to zero as we move further away from the interface into the atmosphere. Thus,

$$u_z(z) e^{\frac{z}{2H}} \to 0 \qquad \text{as} \qquad z \to -\infty. \tag{2.52}$$

Inspection of Equation (2.47) with this condition indicates that it is the positive sign that we require, and then λ is determined by

$$2H\lambda = -1 + \left(1 - \frac{4\omega^2 H^2}{c_{at}^2}\right)^{\frac{1}{2}} = -1 + \left(1 - \frac{\omega^2}{\omega_{ac}^2}\right)^{\frac{1}{2}}, \tag{2.53}$$

with $\omega < \omega_{ac}$.

At the base of the model, we have placed a rigid wall at $z = z_d$ and this implies that

$$u_z = 0 \qquad \text{at} \qquad z = z_d, \tag{2.54}$$

giving

$$c_2 = -c_1 \frac{J_m(r_d)}{Y_m(r_d)}. \tag{2.55}$$

Across the interface, we require that the velocity perturbation $u_z(z)$ remain continuous, i.e.

$$u_z \quad \text{is} \quad \text{continuous} \quad \text{across} \quad z = 0. \tag{2.56}$$

The final boundary condition is somewhat more complicated. We require pressure balance to be maintained and so the total pressure perturbation across the interface must be continuous. To do this we demand continuity of the time derivative of the Lagrangian pressure perturbation, P_{LT}, defined by

$$\frac{\partial P_{LT}}{\partial t} = \frac{\partial P_T}{\partial t} + u_z \rho_o g \tag{2.57}$$

where P_T $(= P + \frac{1}{\mu}(\mathbf{B_o} \cdot \mathbf{b}))$ is the perturbation in the total pressure (gas plus magnetic). Substituting for P_T in Equation (2.57) gives

$$\frac{\partial P_{LT}}{\partial t} = \frac{\partial}{\partial t}\left[P_1 + \frac{\mathbf{B_o} \cdot \mathbf{b}}{\mu}\right] + \rho_o u_z g, \tag{2.58}$$

where $\mathbf{b}$ is the perturbed magnetic field. The equilibrium magnetic field $\mathbf{B_o}$ is aligned in the $x-$direction, so

$$\mathbf{B_o} \cdot \mathbf{b} = B_o(z) b_x \tag{2.59}$$

and hence

$$\frac{\partial P_{LT}}{\partial t} = \frac{\partial P_1}{\partial t} + \frac{B_o(z)}{\mu}\frac{\partial b_x}{\partial t} + \rho_o u_z g. \tag{2.60}$$

We may then use Equations (2.20) and (2.21) to replace perturbed quantities with equilibrium ones. Along with Equation (2.4), we gain an expression for the Lagrangian pressure perturbation:

$$\frac{\partial P_{LT}}{\partial t} = -\rho_o(z)(c_s^2(z) + v_a^2(z))\frac{du_z}{dz}. \tag{2.61}$$

Hence

$$\rho_o(z)(c_s^2(z) + v_a^2(z))\frac{du_z}{dz} \quad \text{is continuous across the interface.} \tag{2.62}$$

In the absence of a magnetic field, condition (2.62) implies that

$$\rho_o c_s^2(z)\frac{du_z}{dz} \quad \text{is continuous across} \quad z = 0. \tag{2.63}$$

This is the fourth and final boundary condition that we require.

Application of conditions (2.52), (2.54), (2.56) and (2.63), combined with the reduced equilibrium interfacial density condition (2.26), leads to the dispersion relation for the base frequencies of this model:

$$\frac{1}{\omega}\left[(\omega_{ac}^2 - \omega^2)^{\frac{1}{2}} + \omega_{ac}\right] \quad [J_{m+1}(r_o)Y_m(r_d) - Y_{m+1}(r_o)J_m(r_d)]$$
$$= [J_m(r_o)Y_m(r_d) - Y_m(r_o)J_m(r_d)], \tag{2.64}$$

where

$$r_o = \frac{2\omega z_o}{c_{oL}} \tag{2.65}$$

and

$$r_d = \frac{2\omega z_o}{c_{oL}}\left(1 + \frac{z_d}{z_o}\right)^{\frac{1}{2}}. \tag{2.66}$$

Equation (2.64) is the dispersion relation for a polytropic layer of fluid overlain by an isothermal atmosphere, the temperature profile being continuous across the interface between the two layers. The lower region is taken to be bounded by a rigid wall at $z = z_d$, and represents the convection zone and below, whilst the upper region is semi-infinite in extent and is assumed to represent the chromosphere.

The dispersion relation (2.64) may be solved numerically to give the base oscillation frequencies of the model. In order to do this, the parameters we use are taken to have typical solar values, displayed in Table 2.1. The values shown in Table 2.1 have been chosen to best approximate the atmospheric structure of the sun, given the simple nature of our model. In

Parameter	Value
T_{oL}	4170^o K
P_{oL}	86.82 kg m^{-1} s^{-2}
z_o	244.5 km
R	6425.97 $m^2 s^{-2} K^{-1}$
$z_d (= R_{sun})$	6.96×10^8 m
c_{oL}	6.6829 km s^{-1}
γ	5/3
g	274.0 m s^{-2}
m	3/2
ν_{ac}	5.43 mHz

Table 2.1: Typical solar values that used as parameters for the calculation of base frequencies for the model.

choosing the parameters of our model, recall that in Section 2.3 the equilibrium magnetic field was taken to be horizontal and dependent on height, i.e. $\mathbf{B}_o = B(z)\hat{\mathbf{x}}$. The magnetic field models a canopy type structure. From the observations of Giovanelli and Jones (1982), the emerging magnetic flux takes on a canopy form around 500 km above the photosphere. This places it at around the temperature minimum. As a result, the values that we shall take for T_{oL}, P_{oL}, etc. correspond with conditions at the temperature minimum. The values given in Table 2.1 are taken from The Harvard Smithsonian Reference Atmosphere (H.S.R.A) (Gingerich *et al.* 1971). The overall depth of the interior is taken to be the solar radius.

From the dispersion relation (2.64) we may obtain a set of discrete solutions which we recognise as forming a range of modes of integer order, n. This sequence of solutions is displayed in Figure 2.1 with n ranging from zero to 40. The cyclic frequencies $\nu (\equiv \frac{\omega}{2\pi})$ are in mHz and are plotted against radial order, n. As a comparison, observed frequencies for the $l = 0$ modes are also plotted. The crosses (+++) are taken from the observations of Libbrecht *et al.* (1990) and the stars (***) are from Elsworth *et al.* (1994). The frequencies given by Libbrecht *et al.* (1990) cover radial orders from 12 to 33 and those taken from Elsworth *et al.* (1994) cover orders 12-26. Note that the stars overlap the first 15 crosses. We see from Figure 2.1 that for even a simple model such as considered here there is good agreement with the observations.

It is apparent from Figure 2.1 that there is a linear dependence between mode

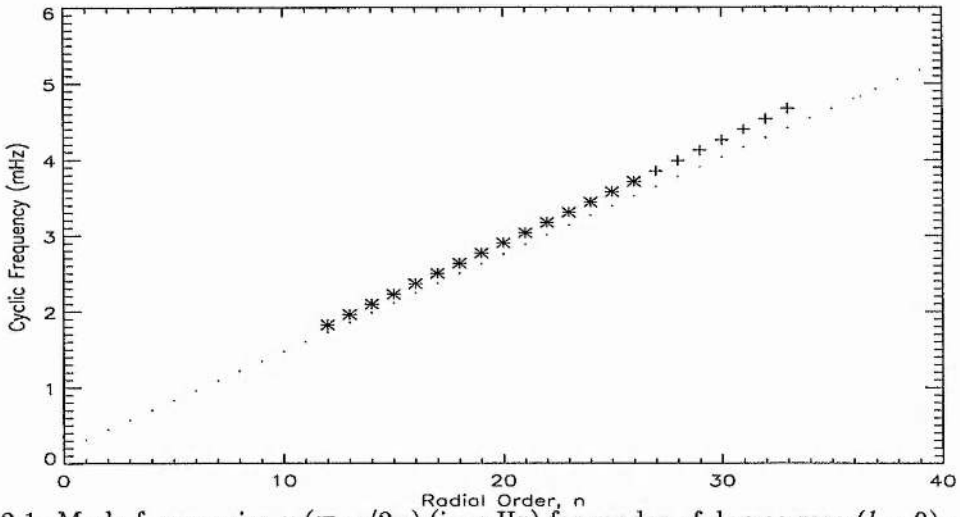

Figure 2.1: Mode frequencies ν ($\equiv \omega/2\pi$) (in mHz) for modes of degree zero ($l = 0$) against radial order, n. The calculated mode frequencies for the model are shown as dots (...) and the observed frequencies are shown as either crosses (+) or stars (*). The crosses are taken from Libbrecht *et al.* (1990) and the stars from Elsworth *et al.* (1994). Note that the stars overlap the first 15 crosses.

frequency and radial order. This differs from the well known observed and theoretical $p-$mode spectra for $l \neq 0$ modes where the dependence of mode frequency on radial order is approximately $\propto n^{\frac{1}{2}}$. How are we to understand this? We must remember that for this model, the cavity depth is the same for all modes. For the general order $p-$modes, the behaviour is different because the depth of the cavity is itself dependent upon the frequency of the mode. The resultant effect for these modes is that for any specific degree, l, the depth of the cavity increases with mode frequency and thus we see the parabolic scaling $\omega \propto n^{\frac{1}{2}}$. A simple physical analogy that we may draw with this model is that of a guitar string of finite length fixed at both ends. It is well known that for a guitar string, the mode frequency will be proportional to the overtone number, or order, n. Remembering that the cavity depth is the same for all radial oscillations, the similarity is clear.

Therefore, we see that this simple plane-parallel model of a polytropic region bounded at one extreme by a rigid wall and overlain at the other by a field-free, isothermal atmosphere will reproduce the observed frequencies of the $l = 0$ modes with a reasonable accuracy. The frequencies found for this simple case will be used as the base ones to measure any frequency shifts against. If we assume that these frequencies are determined

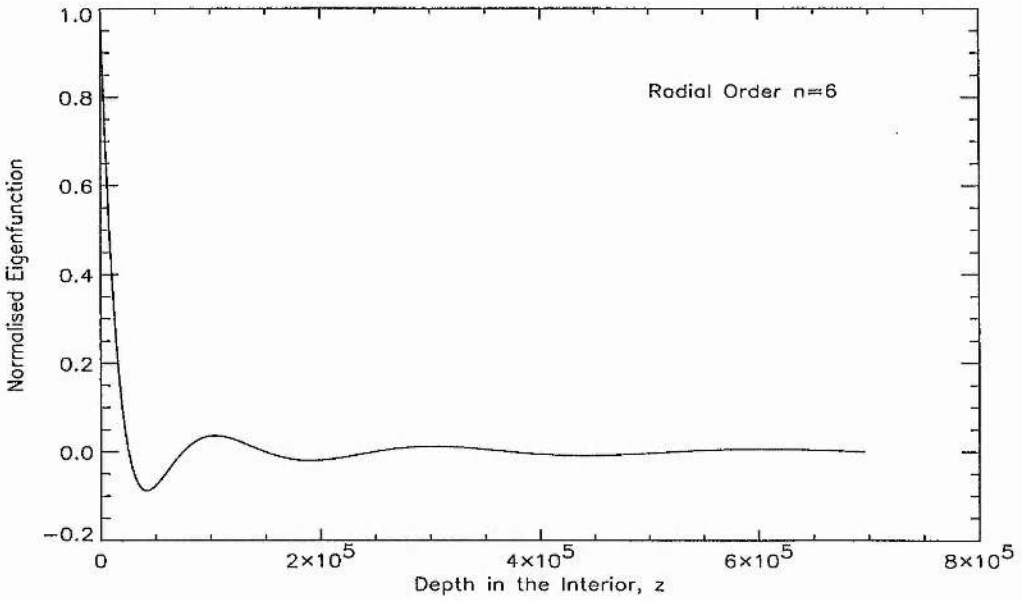

Figure 2.2: The normalised vertical velocity component, $u_z(z)/u_z(z=0)$, plotted against depth for the $n=6$ $p-$mode. The curve stops where we have placed the rigid wall (at the solar radius).

for conditions that are representative of conditions at solar minimum, then we may vary the structure of the chromosphere, in a mimicry of the solar activity cycle, in order to investigate the observed changes in mode frequency. We consider this problem in Section 2.5 by studying three specific chromospheric models each of which allows an analytical approach to the problem.

The mode frequencies found from Equation (2.64) may be used to calculate the eigenfunctions defined by Equation (2.49). In Figure 2.2 we have displayed the normalised eigenfunction $u_z(z)/u_z(z=0)$ as a function of depth z, for the $n=6$ mode. Note that

$$\frac{u_z(z)}{u_z(z=0)} = \frac{r^{-m}[J_m(r)Y_m(r_d) - Y_m(r)J_m(r_d)]}{r_o^{-m}[J_m(r_o)Y_m(r_d) - Y_m(r_o)J_m(r_d)]}. \tag{2.67}$$

It can be seen that the amplitude of the mode falls very quickly to zero. In fact, the amplitude of all the modes compared to their amplitude at the surface is diminished considerably by 200000 km into the interior.

2.5 Frequency Shifts Imposed by Changes in Chromospheric Parameters

2.5.1 Thermal changes ($T_{at} \neq T_{oL}, B_o = 0$)

Now that we have obtained a set of base frequencies for the model, we turn to a study of how mode frequencies may be changed over a solar cycle. In order to do this, we shall allow the parameters governing the structure of the atmosphere to vary whilst the interior of the model is kept unchanged. The first step in addressing this problem is to consider an isothermal atmosphere that is field-free, but allow the temperature of the atmosphere to vary. In this case, the temperature profile given by Equation (2.3) is no longer continuous across the interface at $z = 0$, as it was in Section 2.4. This comes from the expectation of an increase in the mean chromospheric temperature over the solar cycle, induced by a rise in magnetic field strength. To begin with, however, we consider frequency shifts in the absence of a magnetic field; this allows some insight into the full problem once we allow for the presence of a magnetic field in the atmosphere.

The velocity perturbation u_z and its gradient du_z/dz are again given by Equations (2.49) and (2.50), except that now $c_{at} \neq c_{oL}$. Also, the equilibrium condition on pressure balance at the interface now gives an interfacial density ratio of the form

$$\frac{\rho_{at}}{\rho_{oL}} = \frac{c_{oL}^2}{c_{at}^2}. \tag{2.68}$$

Note that the cyclic cut-off frequency $\nu_{ac} \equiv \frac{\omega_{ac}}{2\pi}$, although still a global quantity, *decreases* with an increase in atmospheric temperature (see Table 2.2).

In finding the dispersion relation for this model, boundary conditions (2.52), (2.54), (2.56) and (2.63) are used once more and so the dispersion relation is readily obtained. The result is

$$\begin{aligned}\frac{1}{\omega}\frac{c_{at}}{c_{oL}}\left[(\omega_{ac}^2 - \omega^2)^{\frac{1}{2}} + \omega_{ac}\right]&\left[J_{m+1}(r_o)Y_m(r_d) - Y_{m+1}(r_o)J_m(r_d)\right] \\ &= \left[J_m(r_o)Y_m(r_d) - Y_m(r_o)J_m(r_d)\right]\end{aligned} \tag{2.69}$$

with r_o and r_d again given by Equations (2.65) and (2.66).

Equation (2.69) is the dispersion relation for modes formed in a polytropic region, extending from $z = 0$ to a wall at $z = z_d$, overlain by an isothermal atmosphere. Note that Equation (2.69) reduces to Equation (2.64) when $c_{at} = c_{oL}$. Table 2.2 presents the

Parameter	Value
$c_{at}(T_{at} = 4500°\text{K})$	6.94224 km s^{-1}
$c_{at}(T_{at} = 5000°\text{K})$	7.31776 km s^{-1}
$c_{at}(T_{at} = 5500°\text{K})$	7.67494 km s^{-1}
$c_{at}(T_{at} = 6000°\text{K})$	8.01621 km s^{-1}
$\nu_{ac}(T_{at} = 4500°\text{K})$	5.234 mHz
$\nu_{ac}(T_{at} = 5000°\text{K})$	4.966 mHz
$\nu_{ac}(T_{at} = 5500°\text{K})$	4.735 mHz
$\nu_{ac}(T_{at} = 6000°\text{K})$	4.533 mHz

Table 2.2: Sound speeds c_{at} and cyclic cut-off frequencies ν_{ac} for the different atmospheric temperatures T_{at} used in the numerical calculations of Section 2.4.1.

atmospheric parameters to be used in the numerical calculations. The parameters relating to the lower region are given earlier in Table 2.1.

What of the changes in mode frequency that are brought about by a change in chromospheric temperature, T_{at}? Figure 2.3 shows the change in cyclic frequency $\nu \equiv \omega/2\pi$ induced by an increase in atmospheric temperature, T_{at}. The change in mode frequency $\triangle\nu$ is calculated by

$$\triangle\nu = \nu(T_{at}) - \nu(4170°\text{K}), \tag{2.70}$$

where $\nu(T_{at})$ is the mode frequency found for a raised chromospheric temperature T_{at} and $\nu(4170°\text{K})$ is the base frequency for a chromospheric temperature of 4170°K; the base frequency was calculated in Section 2.4. Chromospheric temperatures of T_{at} =4170°K, 4500°K, 5000°K, 5500°K and 6000°K are taken. Figure 2.3 shows that an *increase* in atmospheric temperature leads to a *decrease* in mode frequency, the greater shifts occurring for the higher temperatures. The change in frequency is negligible for modes of low frequency (and hence low radial order) and becomes increasingly larger and negative for higher frequencies. To calculate the curves associated with these frequency shifts, we have allowed n to vary from 0 to the highest possible value such that the frequency of a mode is less than the acoustic cut-off frequency for that specific chromospheric temperature. Frequency changes are then plotted against the base frequencies determined in Section 2.4 for an atmospheric temperature of 4170°K.

The effect of increasing the atmospheric temperature is identical in form to that found in previous studies of non-radial modes (see, for example, Evans 1990 and Jain 1994)

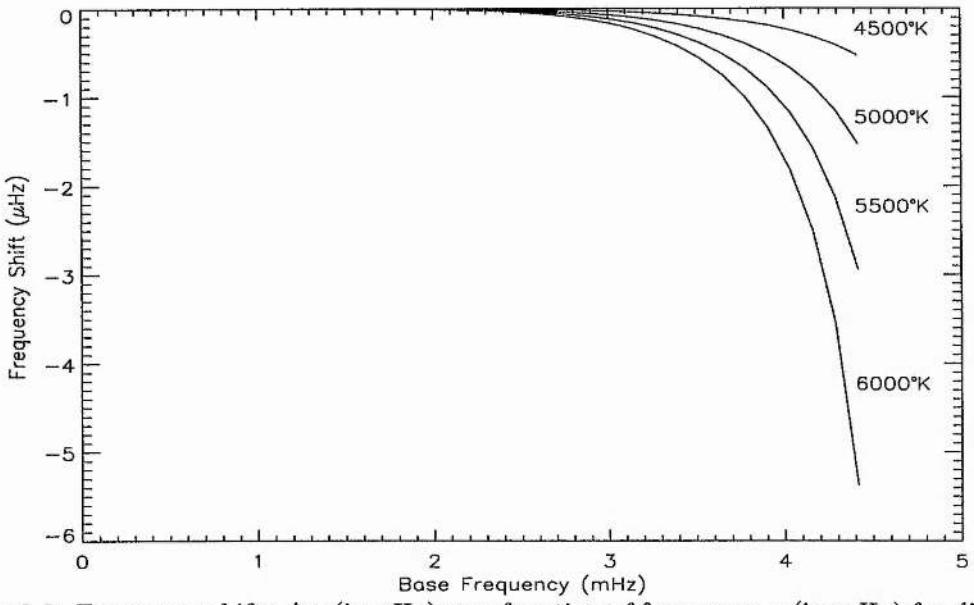

Figure 2.3: Frequency shifts $\triangle\nu$ (in μHz) as a function of frequency ν (in mHz) for different atmospheric temperatures. The shifts are plotted against the frequencies found for an atmosphere with a temperature of $4170°K$. The curves shown are for atmospheric temperatures of 4500°K, 5000°K, 5500°K, and 6000°K. Note the magnitude of the shifts.

but, as we would expect, the magnitude of the frequency decreases is smaller for $l = 0$ modes. However, changes in frequency are not zero as given in Evans and Roberts (1990) and Jain and Roberts (1994), where $\triangle\nu \propto l$, but it must be remembered that earlier models were not applicable at low degree and, as a result, neither were any asymptotic expansions approximating frequency shifts.

We conclude from this section that an increase in the temperature of the chromosphere leads to a decrease in the mode frequencies of radial $p-$modes.

How are the eigenfunctions modified by a change in atmospheric temperature? From Figure 2.3 it can be seen that the difference in frequency between each mode is extremely small. Consequently, the spacing between eigenfunctions is also minimal and it proves to be more instructive to calculate the difference in eigenfunctions. To do this we calculate $\triangle u_z$ where

$$\triangle u_z = \left(\frac{u_z(z)}{u_z(z=0)}\right)_{T_{at}} - \left(\frac{u_z(z)}{u_z(z=0)}\right)_{T_{at}=4170°K}. \tag{2.71}$$

The first term on the right hand side of Equation (2.71) is the normalised eigenfunction for a raised atmospheric temperature whereas the second term is that calculated for the base

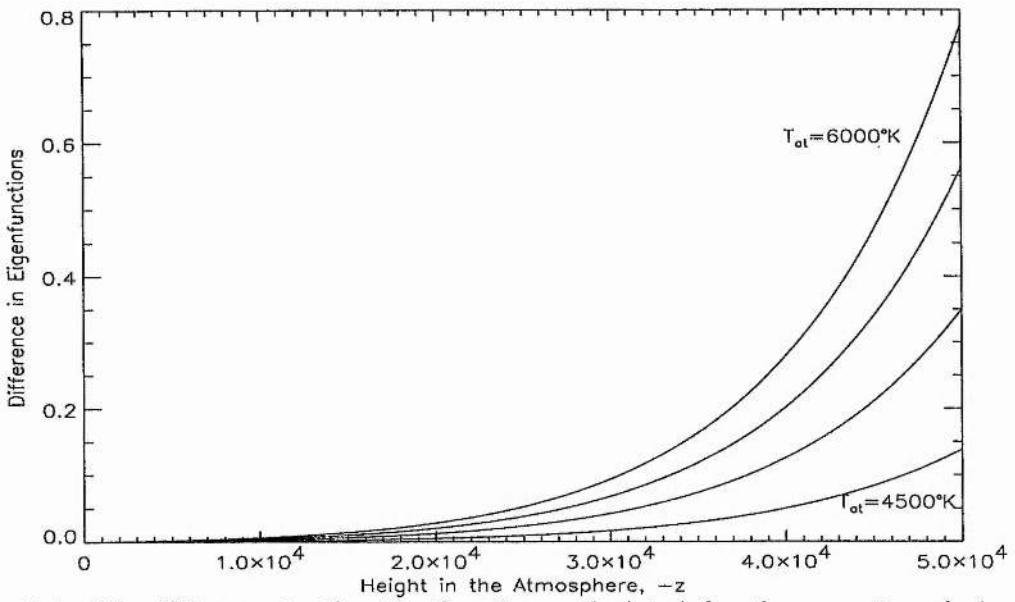

Figure 2.4: The difference in the eigenfunctions calculated for the $n = 6$ mode in the atmosphere. The atmospheric temperatures taken are those used in the calculation of the frequency shifts in Figure 2.3.

model of Section 2.4.

Figure 2.4 displays the results of this calculation. We have again used atmospheric temperatures of T_{at} =4500°K, 5000°K, 5500°K and 6000°K. Figure 2.4 indicates that the vertical velocity u_z increases more rapidly with height at higher temperatures.

We have seen then that a rise in chromospheric temperature produces curves that are similar in form to those found for general degree $p-$modes but are much smaller in magnitude. We now apply a magnetic field to the atmosphere and consider its influence on mode structure.

2.5.2 Constant Alfvén speed in the atmosphere ($T_{at} = T_{oL}, B_o \neq 0$)

The very fact that the chromosphere of the sun is dominated by the presence of a roughly horizontal, canopy magnetic field (Giovanelli 1980) implies that it must have some influence on the nature of the solar $p-$modes. In fact, the influence of this magnetic field is likely to be most marked on the oscillation frequencies in this region of the atmosphere where the plasma beta is small. However, although the magnetic field will vary from location to location and from time to time, long term variations with the solar cycle are also to be expected. We attempt to mimic the evolution of the magnetic field with the solar cycle

by investigating a simple equilibrium magnetic field profile that produces an Alfvén speed that is constant in height in the atmosphere. The specific choice of magnetic field profile, which we introduce more fully below, allows an exact treatment of the problem (Yu 1965; Thomas 1983; Campbell and Roberts 1989) but, as we shall see later, we must proceed with some caution. As in Section 2.5.1, we shall investigate whether a change in chromospheric parameters, in this case the field strength at the base of the chromosphere, induces a change in the oscillation frequencies that are comparable to the changes reported in observations.

In order to carry this out, we model the magnetic chromosphere in $z < 0$ as an isothermal region with a temperature equal to that at the top of the convection zone, i.e. $T_{at} = T_{oL}$. This allows us to determine the effects that are imposed by the magnetic field alone. Thus the sound speed is constant across the interface but, as in Section 2.5.1, there is a density jump across $z = 0$, the ratio of the densities at the boundary being given by Equation (2.8) with $c_{at} = c_{oL}$.

Inspection of Equation (2.8) with $c_{at} = c_{oL}$ shows that the magnetic field alone must be responsible for the density discontinuity that is present at $z = 0$. It imposes this density jump by the additional pressure that the magnetic field applies in the atmosphere. If we consider the pressure balance Equation (2.6), then we see that for an increase in magnetic field strength, a decrease in atmospheric pressure, P_{at}, is required if the gas pressure at the top of the convection zone, P_{oL}, is kept constant. However, because the temperature of the atmosphere is to be maintained no matter what the magnetic field strength in that region, Equation (2.5) implies that there must be a drop in the atmospheric plasma density, ρ_{at}. Therefore, an evacuation of the atmospheric plasma takes place and hence the density jump implied by Equation (2.8) arises.

This simple matter of the pressure balance of our equilibrium places some limitations on our work. There must obviously be a finite positive gas pressure in the atmosphere, and in order to satisfy this, Equation (2.6) implies that there is a limiting value to the strength of magnetic field that we may apply. The upper limit to the field strength is found when the gas density drops to zero in the upper region; for the parameters given in Table 2.1 (for around the temperature minimum), the upper limit on the atmospheric magnetic field strength is approximately 147 G.

The specific magnetic field profile that supplies us with a constant Alfvén speed is found by solving the magneto-hydrostatic condition (2.4) along with the ideal gas law

(2.5). Solving these two conditions gives an equilibrium magnetic field profile of the form

$$B(z) = B_o e^{\frac{z}{2H_B}}, \qquad z < 0, \tag{2.72}$$

where

$$H_B = \frac{c_{at}^2}{g\Gamma} \qquad \text{and} \qquad \Gamma = \frac{2\beta\gamma}{2\beta+\gamma} \tag{2.73}$$

are the magnetically modified density scale height and adiabatic exponent, respectively. We have introduced the ratio of the sound and Alfvén speeds squared given by

$$\beta = \frac{c_{at}^2}{v_{ao}^2}. \tag{2.74}$$

The β used here differs from the usual plasma beta defined to be the ratio of the gas and magnetic pressures (plasma beta$= 2\mu P/B^2 = 2c_s^2/\gamma v_{ao}^2$). The Alfvén speed v_{ao} is given by $v_{ao} = B_o/(\mu\rho_{at})^{\frac{1}{2}}$. Thus, the equilibrium magnetic field profile $B(z)$ is given by

$$B(z) = \begin{cases} B_o e^{\frac{z}{2H_B}}, & z < 0, \\ 0, & 0 < z < z_d. \end{cases} \tag{2.75}$$

A solution for the velocity perturbation in the interior of the model has already been provided, namely Equation (2.40), and so now we need only study the magnetically permeated atmosphere. For the magnetic field profile (2.75), Equation (2.24) reduces, under our assumptions of constant sound speed and Alfvén speed, to

$$\frac{d^2u_z}{dz^2} + \frac{1}{H_B}\frac{du_z}{dz} + \frac{\omega^2}{(c_{at}^2+v_{ao}^2)}u_z = 0, \qquad z < 0. \tag{2.76}$$

Note that Equation (2.76) reduces to Equation (2.46) in the absence of a magnetic field.

Equation (2.76) has solutions similar in form to Equation (2.46). Specifically,

$$u_z = \mathcal{B}e^{\tau z}, \qquad z < 0, \tag{2.77}$$

where

$$\tau = \frac{1}{2H_B}\left[-1 \pm \left(1 - \frac{4\omega^2 H_B^2}{(c_{at}^2+v_{ao}^2)}\right)^{\frac{1}{2}}\right] \tag{2.78}$$

and $\mathcal{B}$ is a constant of integration. Combining Equation (2.77) with the solution for the interior (Equation (2.40)) gives a velocity distribution of the form

$$u_z = \begin{cases} \mathcal{B}e^{\tau z}, & z < 0, \\ r^{-m}\left[c_1 J_m(r) + c_2 Y_m(r)\right], & 0 < z < z_d, \end{cases} \tag{2.79}$$

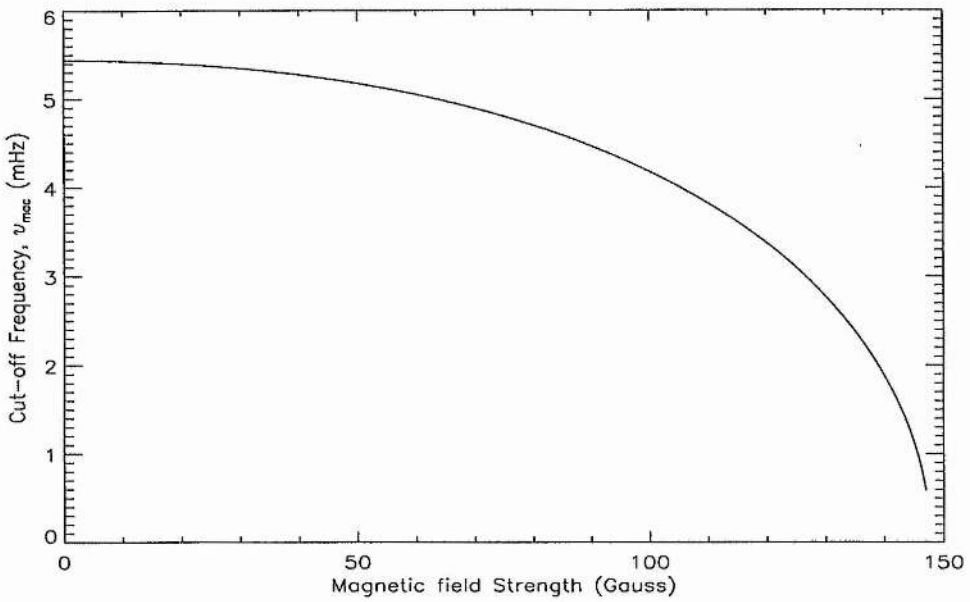

Figure 2.5: The cyclic magnetoacoustic cut-off frequency, ν_{mac}, for a magnetic field profile that gives a constant Alfvén speed. Note that ν_{mac} approaches zero as the upper atmosphere becomes fully evacuated.

where r is defined by (2.41). Also, the compressibility of the atmosphere, $\nabla \cdot \mathbf{u}$ ($\equiv \frac{du_z}{dz}$), is given by

$$\frac{du_z}{dz} = \begin{cases} \tau \mathcal{B} e^{\tau z}, & z < 0, \\ -(2\omega^2 z_o / c_{oL}^2) r^{-(m+1)} \left[c_1 J_{m+1}(r) + c_2 Y_{m+1}(r) \right], & 0 < z < z_d. \end{cases} \tag{2.80}$$

Note that the parameter τ in Equation (2.78) once again introduces a cut-off frequency into the atmosphere that serves to trap the modes. More importantly, the cut-off frequency is modified by the presence of a magnetic field and this magnetoacoustic cut-off frequency, ω_{mac}, is defined by

$$\omega_{mac}^2 = \frac{(c_{at}^2 + v_{ao}^2)}{4H_B^2} = \frac{(c_{at}^2 + v_{ao}^2) g^2 \Gamma^2}{4 c_{at}^4}. \tag{2.81}$$

On inspection of Equation (2.81), it is clear that the assumption of constant sound and Alfvén speeds in the atmosphere maintains the global nature of this frequency. The influence of a magnetic field on the cyclic magnetoacoustic cut-off frequency, $\nu_{mac} (\equiv \omega_{mac}/2\pi)$, leads to a rapid decrease in ν_{mac} with an increase in field strength, as shown in Figure 2.5. A point of interest in Figure 2.5 is that ν_{mac} approaches zero as the magnetic

field reaches its limiting strength. This is expected because of the evacuation of the atmosphere induced by the magnetic field. The net result is that we have an effectively open boundary at $z = 0$ when the magnetic field totally evacuates the upper atmosphere and no trapping of the modes takes place.

We note that ω_{mac} is identical to that found by Campbell and Roberts (1989) in their expansion for small horizontal wavenumber of a more complicated expression for the magnetically modified cut-off frequency in their study of non-radial modes.

Once again, we have arrived at the stage where all that is required to provide us with the relevant dispersion relation is the application of appropriate boundary conditions. We require that the kinetic energy density of the modes vanish as $z \to -\infty$ and hence condition (2.52) is required, with the density scale height replaced by its magnetically modified counterpart. This condition tells us that it is the positive sign in solution (2.77) that is the appropriate one to choose. Thus, τ is defined by

$$\tau = \frac{1}{2H_B}\left[-1 + \left(1 - \frac{4\omega^2 H_B^2}{(c_{at}^2 + v_{ao}^2)}\right)^{\frac{1}{2}}\right]. \tag{2.82}$$

Also, the presence of a rigid wall at $z = z_d$ and the necessity of avoiding a discontinuity in the velocity profile across the interface implies that boundary conditions (2.54) and (2.56) are again applicable.

Finally, we require the Lagrangian pressure perturbation to be continuous across the interface at $z = 0$, but now allowing that the added magnetic pressure exerts an influence. With this taken into consideration, Equation (2.62) tells us that

$$\rho_o(z)(c_s^2(z) + v_{ao}^2)\frac{du_z}{dz} \quad \text{is continuous across the interface.} \tag{2.83}$$

Condition (2.83) reduces to the non-magnetic perturbed pressure condition (2.63) in the absence of a magnetic field.

With these considerations taken into account and applied to solutions (2.79) and (2.80), the dispersion relation is found to be

$$\frac{1}{\omega}\frac{\gamma}{\Gamma}\frac{c_T}{v_{ao}}\left[(\omega_{mac}^2 - \omega^2)^{\frac{1}{2}} + \omega_{mac}\right] \quad [J_{m+1}(r_o)Y_m(r_d) - Y_{m+1}(r_o)J_m(r_d)]$$
$$= [J_m(r_o)Y_m(r_d) - Y_m(r_o)J_m(r_d)]. \tag{2.84}$$

Here c_T is the chromospheric tube (or cusp) speed, defined by

$$c_T = \frac{c_{at}v_{ao}}{(c_{at}^2 + v_{ao}^2)^{\frac{1}{2}}}. \tag{2.85}$$

Parameter	Value
$v_{ao}(B_o = 10G)$	0.4967 km s^{-1}
$v_{ao}(B_o = 30G)$	1.5184 km s^{-1}
$v_{ao}(B_o = 100G)$	6.7335 km s^{-1}
$\beta(B_o = 10G)$	181.02
$\beta(B_o = 30G)$	19.37
$\beta(B_o = 100G)$	0.985

Table 2.3: The Alfvén speed and β for various magnetic field strengths used in the numerical calculations.

Equation (2.84) is the dispersion relation for a field-free polytrope that is bounded at depth $z = z_d$ by a rigid wall and over which lies an isothermal atmosphere that contains a magnetic field which provides a constant Alfvén speed.

We wish to calculate changes in mode frequency that are due to the magnetic canopy alone. In order to do this, we shall follow the same procedure as used in Section 2.5.1, but the parameter that we shall vary now is the field strength B_o at the base of the chromosphere. We are therefore calculating frequency shifts, $\triangle\nu$, according to

$$\triangle\nu = \nu(B_o) - \nu(0), \tag{2.86}$$

where $\nu(B_o)$ is the frequency of the mode for a specific chromospheric field of strength B_o at the chromospheric base, and $\nu(0)$ is the mode of a corresponding radial order determined in the absence of a magnetic field (see Section 2.4).

To calculate the frequency shifts according to Equation (2.86), we apply three magnetic field strengths at the base of the chromosphere, namely B_o =10G, 30G and 100G. The Alfvén speeds and plasma betas, β, that these field strengths provide are shown in Table 2.3, the relevant parameters for the interior being used from Table 2.1 once more. Again we have allowed n to vary from 0 to the highest frequency such that $\omega < \omega_{mac}$.

The results of these calculations are shown in Figure 2.6 and we may see from this that the introduction of a magnetic field of this form leads to a reduction in mode frequency for all modes. Figure 2.6 also shows that this decrease in mode frequency is made more pronounced by an increase in the magnetic field strength, B_o. However, these reductions in mode frequency are far smaller than those brought about by purely thermal changes (see Section 2.5.1).

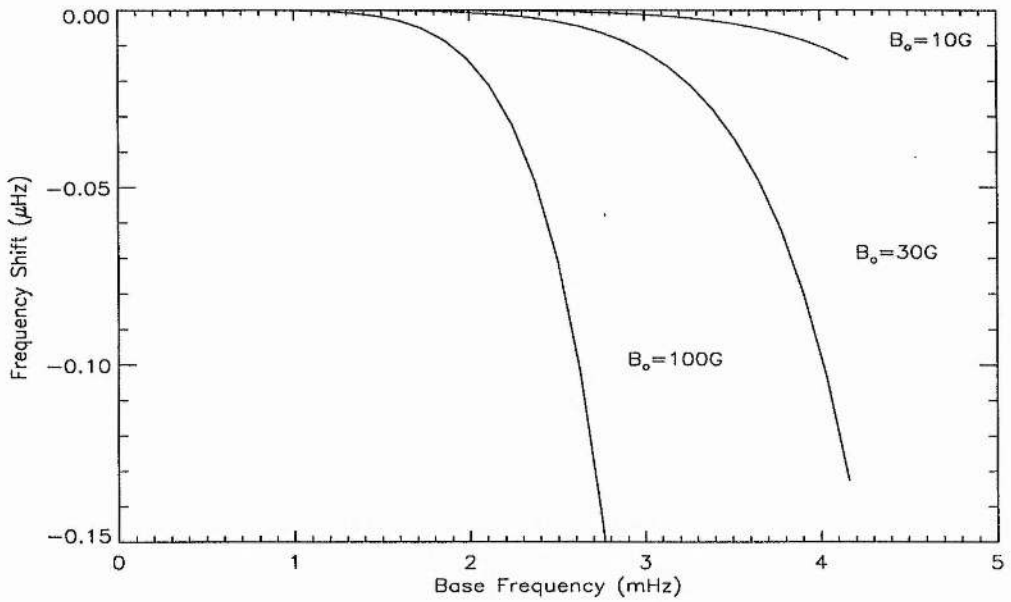

Figure 2.6: Frequency shifts (in μHz) as a function of frequency (in mHz) found for different field strengths B_o at the base of the chromosphere. The shifts are plotted against the base frequencies determined in the absence of a magnetic field (see Section 2.4). Note that the magnitude of the frequency shifts is much smaller than those found in Section 2.5.1.

The curves shown in Figure 2.6 are qualitatively similar to those found by Campbell and Roberts (1989) but qualitative comparison is difficult; firstly because the model of Campbell and Roberts (1989) was inapplicable at low l and, secondly, because they only produced curves for the frequency changes found for low radial orders. However, we may conclude that the expected behaviour of radial modes interacting with an exponentially decaying magnetic field is to show a *decrease* in frequency.

As in Section 2.5.1 the difference in the eigenfunctions will be displayed rather than the eigenfunctions themselves. We calculate a difference of the same form of Equation (2.71):

$$\triangle u_z = \left(\frac{u_z(z)}{u_z(z=0)}\right)_{B_o} - \left(\frac{u_z(z)}{u_z(z=0)}\right)_{B_o=0}, \tag{2.87}$$

where B_o takes on the values used in the calculation of Figure 2.6. The results of this are shown in Figure 2.7. We can see from Figure 2.7 that u_z increases less rapidly with height in a magnetic atmosphere than a field-free one. This is readily explained by considering the parameters λ and τ from Equations (2.53) and (2.82). Firstly, a comparison of the density scale heights in the atmosphere tells us that $H_B > H$. Also, the cut-off frequencies for the

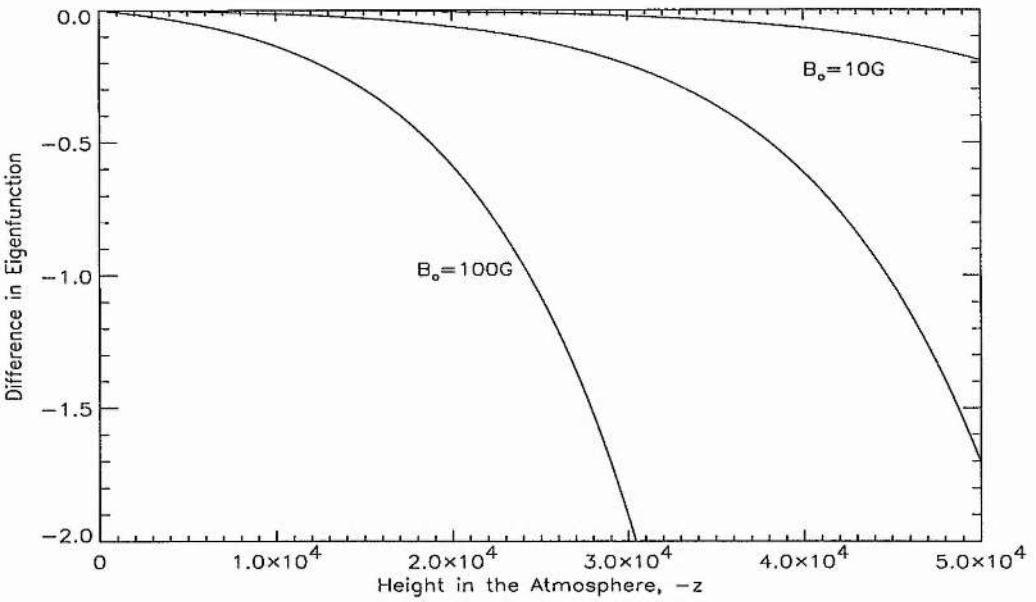

Figure 2.7: Difference in eigenfunctions, as in Figure 2.4. Here we see that the eigenmodes grow more slowly when a magnetic field is present than in a field-free atmosphere.

two models, ω_{ac} and ω_{mac}, have the property $\omega_{ac} > \omega_{mac}$. Hence $\lambda > \tau$ and the results shown in Figure 2.7 are evident.

2.5.3 Uniform magnetic field in the atmosphere

As a final study for this Chapter, we consider another extreme for the equilibrium magnetic field profile, that of a horizontal canopy field which is *uniform* throughout the atmosphere; $\mathbf{B}(z) = B_o\hat{\mathbf{x}}$ in $z < 0$. We shall allow too that the atmospheric temperature is not in general equal to that at the top of the convection zone. Hence Equation (2.3) is the required temperature equilibrium with $T_{at} \neq T_{oL}$. The influence of both the magnetic field and variations in the atmospheric temperature can then be investigated either independently or jointly.

This model is analogous to the equilibrium used in previous studies of general degree modes (Evans and Roberts 1990, 1992; Jain and Roberts 1994) except that the lower region in this study is contained by a rigid wall at a depth $z = z_d$.

We may solve the magneto-hydrostatic equation (2.4) together with the ideal gas law (2.5) to obtain the equilibrium pressure distribution, to be combined with the equilibrium pressure found for the interior (Section 2.4). Altogether, we obtain an equilibrium

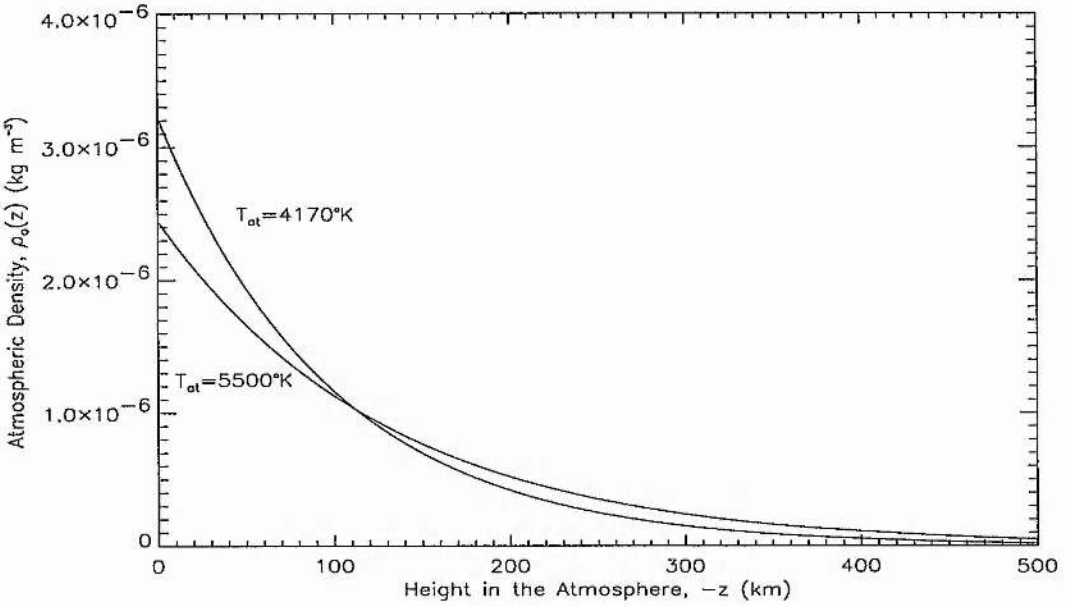

Figure 2.8: The equilibrium density profiles for an atmosphere that contains a uniform magnetic field of strength 10G. Atmospheric temperatures of 4170°K and 5500°K are taken. Note that although the plasma evacuation is more pronounced at the interface, at higher atmospheric temperatures the density falls off more slowly.

pressure profile of the form

$$P_o(z) = \begin{cases} P_{oL}(1+\frac{z}{z_o})^{m+1}, & 0 < z < z_d, \\ P_{at}e^{\frac{z}{H}}, & z < 0, \end{cases} \tag{2.88}$$

where m is the polytropic index and H is the density scale height given by Equation (2.28). Note that the presence of a uniform magnetic field does not alter the thermal equilibrium structure of the atmosphere, i.e. H is not modified by the magnetic field. This may be understood by inspection of the magneto-hydrostatic equation, Equation (2.4). A uniform magnetic field makes no contribution to this equation and hence no effect is felt by the scale height H. However, the gas pressure at the base of the magnetic atmosphere is P_{at}, related to the magnetic pressure $B_o^2/2\mu$ and the gas pressure P_{oL} the top of the convection zone by the pressure balance condition (2.6) such that P_{at} decreases as B_o increases.

The atmospheric equilibrium is matched to the lower region by Equation (2.6) and hence the ratio of densities across the interface is given by Equation (2.8). However, from pressure balance, we see that the atmospheric pressure and also the density at the base of the chromosphere, ρ_{at}, decline for an increase in magnetic field strength, as we have seen in

Section 2.5.2. This effect is accentuated when an increase in the chromospheric temperature also occurs.

The choice of magnetic field profile implies that the Alfvén speed in the atmosphere is now a function of height, $-z$. Specifically, the profile of the Alfvén speed $v_a(z) \equiv B(z)/(\mu\rho(z))^{\frac{1}{2}}$ is given by

$$v_a(z) = v_{ao}e^{\frac{-z}{2H}}, \qquad z < 0; \tag{2.89}$$

thus $v_a(z)$ increases with height in the atmosphere.

Note that the Alfvén speed $v_a(z)$ is indirectly dependent upon the atmospheric temperature, T_{at}. This dependence arises in Equation (2.89) because of the dependence of the density scale height H of the atmosphere on T_{at}. When the chromospheric temperature is raised, H *increases* as can be seen from Equation (2.28), but the density at the base of the chromosphere $\rho_{at}(= P_{at}/RT_{at})$ is *decreased*. For a hotter atmosphere, we therefore obtain an equilibrium density profile that is lower at the interface but declines more slowly than that for a cooler atmosphere owing to the increase in H. Figure 2.8 displays two equilibrium density profiles for the atmospheric temperatures of 4170°K and 5500°K. The scale heights for the two temperatures used in Figure 2.8 are approximately 98 km for $T_{at} = 4170^{o}K$ and 128 km for $T_{at} = 5500^{o}K$.

As we have mentioned above, a rise in atmospheric temperature leads to an increase in the density scale height H. However, H is also increased by the magnetic field alone through a reduction in the plasma density ρ_{at}. The overall effect on the Alfvén speed profile $v_a(z)$ is that for higher chromospheric temperatures we see a higher value for v_{ao} because of the reduction in ρ_{at} in the presence of a magnetic field, but the Alfvén speed increases more slowly with height than it does for cooler atmospheres because of the increase in H. This is displayed in Figure 2.9.

With the equilibrium structure specified, we may now determine the velocity perturbation $u_z(z)$. With a uniform magnetic field, Equation (2.24) becomes

$$\left(1 + \frac{c_{at}^2}{v_{ao}^2}e^{\frac{z}{H}}\right)\frac{d^2u_z}{dz^2} + \frac{1}{H}\frac{c_{at}^2}{v_{ao}^2}e^{\frac{z}{H}}\frac{du_z}{dz} + \frac{\omega^2}{v_{ao}^2}e^{\frac{z}{H}}u_z = 0. \tag{2.90}$$

To solve Equation (2.90), we apply the transformation (Adam 1975; Nye and Thomas 1976*a*; Evans and Roberts 1990)

$$\xi = -\frac{c_{at}^2}{v_{ao}^2}e^{\frac{z}{H}}, \tag{2.91}$$

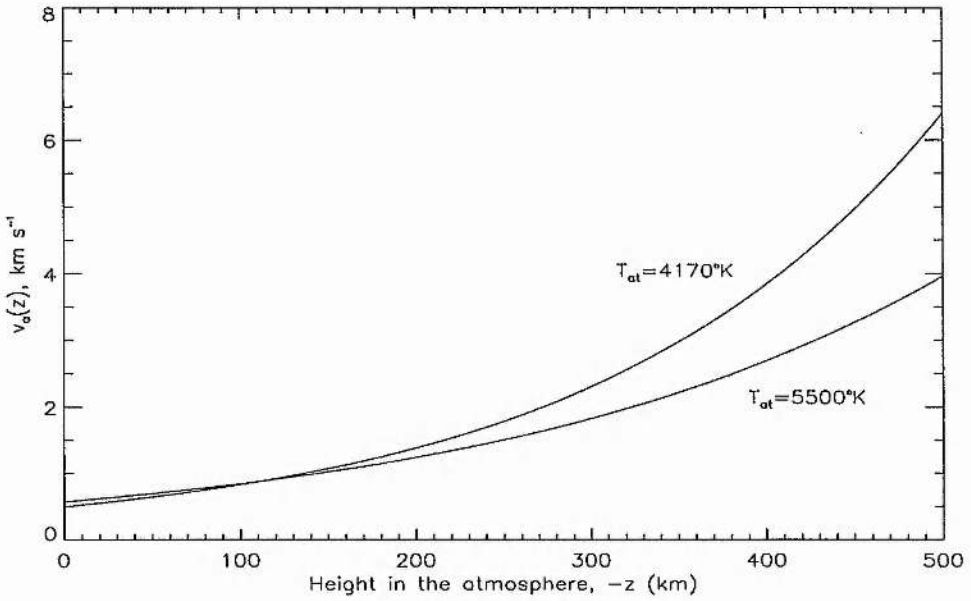

Figure 2.9: The Alfvén speed profile for a magnetic field of strength 10G and two choices of atmospheric temperature T_{at}. The temperature of the atmosphere is raised from 4170°K to 5500°K. Note the less rapid increase of $v_a(z)$ with height for a hotter atmosphere, although v_{ao} is increased.

which provides us with the hypergeometric equation (Abramowitz and Stegun 1965; Chapter 15)

$$\xi(1-\xi)\frac{d^2u_z}{d\xi^2} + [1-(p+q+1)\xi]\frac{du_z}{d\xi} - pqu_z = 0, \tag{2.92}$$

where

$$p+q=1, \qquad pq = \frac{\omega^2 H^2}{c_{at}^2}. \tag{2.93}$$

The parameters p and q are easily obtainable from Equation (2.93):

$$p = \frac{1}{2}\left[1 \pm \left(1 - \frac{4\omega^2 H^2}{c_{at}^2}\right)^{\frac{1}{2}}\right] \qquad \text{and} \qquad q = 1-p. \tag{2.94}$$

The fact that we have two possible solutions for each of the parameters p and q in Equation (2.94) does not present us with any problem. The hypergeometric function is symmetrical in p and q (Abramowitz and Stegun 1965; 15.1.1):

$$F(p,q;1;z) = F(q,p;1;z), \tag{2.95}$$

and so we may arbitrarily choose the sign in front of the square root. We take

$$p = \frac{1}{2}\left[1 + \left(1 - \frac{4\omega^2 H^2}{c_{at}^2}\right)^{\frac{1}{2}}\right] \qquad \text{and} \qquad q = 1 - p. \tag{2.96}$$

Equation (2.92) is solvable around the singular point $\xi = 0$ but the solution is made more complicated because one of the parameters in the hypergeometric equation is equal to one. The general solution of Equation (2.92) is (Abramowitz and Stegun 1965; 15.5.16 and 15.5.17)

$$\begin{aligned} u_z \qquad &= \alpha_1 F(p,q;1;\xi) + \alpha_2 \left\{ F(p,q;1;\xi)\ln\xi + \textstyle\sum_{n=1}^{\infty} \frac{(p)_n (q)_n}{(n!)^2}\xi^n \right. \\ &\left. \times[\psi(p+n) - \psi(p) - \psi(q+n) - \psi(q) - 2\psi(n+1) + 2\psi(1)]\right\}, |\xi| < 1, \end{aligned} \tag{2.97}$$

where $\psi(x)$ is the digamma function (Abramowitz and Stegun 1965: 6.3.1), defined by

$$\psi(x) = \frac{d}{dx}[\ln\Gamma(x)] \tag{2.98}$$

with $\Gamma(x)$ being the standard gamma function, and $(p)_n$ is given by

$$(p)_n = p(p+1)(p+2)\ldots(p+n-1), \qquad (p)_0 = 1. \tag{2.99}$$

In the previous sections, it was sufficient to demand that the kinetic energy density of the perturbation decays as $z \to -\infty$. For the case of a uniform magnetic field, however, we must also demand that the magnetic energy density disappears as $z \to -\infty$. The magnetic energy density of the disturbance E_B is given by

$$E_B = \frac{(\mathbf{B_o} + \mathbf{b})(\mathbf{B_o} + \mathbf{b})}{\mu} - \frac{\mathbf{B_o}^2}{2\mu} \tag{2.100}$$

which, upon linearisation, yields

$$E_B = \frac{b_x B_o}{\mu}. \tag{2.101}$$

From the linearised form of the induction equation, Equation (2.21), the horizontal component of the magnetic field perturbation b_x is given by

$$i\omega b_x = -B_o \frac{du_z}{dz}, \tag{2.102}$$

and hence the magnetic energy density is

$$E_B = \frac{i}{\omega}\frac{B_o^2}{\mu}\frac{du_z}{dz}. \tag{2.103}$$

To find the behaviour of E_B, and hence which solution we require from Equation (2.97), it is convenient to rewrite u_z as

$$u_z = F(p,q;1;\xi)(\alpha_1 + \alpha_2 \ln \xi) + \alpha_2 \times$$
$$\sum_{n=1}^{\infty} \frac{(p)_n (q)_n}{(n!)^2} \xi^n [\psi(p+n) - \psi(p) - \psi(q+n) - \psi(q) - 2\psi(n+1) + 2\psi(1)]. \quad (2.104)$$

Using the result (Abramowitz and Stegun 1965: 15.2.1)

$$\frac{d}{dz} F(a,b;c;z) = \frac{ab}{c} F(a+1, b+1; c+1; z) \quad (2.105)$$

and knowing that

$$\frac{d\xi}{dz} = -\frac{\beta}{H} e^{\frac{z}{H}}, \quad (2.106)$$

leads to

$$\frac{du_z}{dz} = -\frac{pq\beta e^{\frac{z}{H}}}{H} F(p+1, q+1; 2; -\beta e^{\frac{z}{H}}) \left[\alpha_1 + \alpha_2 \ln(-\beta e^{\frac{z}{H}})\right]$$
$$-\frac{\alpha_2 e^{\frac{-z}{H}}}{\beta} F(p,q;1;-\beta e^{\frac{z}{H}}) - \frac{\beta}{H} e^{\frac{z}{H}} \alpha_2 \sum_{n=2}^{\infty} \frac{(p)_n (q)_n}{(n!)^2} n(-\beta e^{\frac{z}{H}})^{(n-1)}$$
$$\times [\psi(p+n) - \psi(p) - \psi(q+n) - \psi(q) - 2\psi(n+1) + 2\psi(1)]. \quad (2.107)$$

With this result, we now have an expression for the magnetic energy density given by Equation (2.103). On inspection of Equation (2.107), it may be seen that the second term on the right hand side increases exponentially as we move higher into the atmosphere. To satisfy the boundary condition indicated by Equation (2.103) we must therefore take $\alpha_2 = 0$. Hence the velocity on $z < 0$ is given by

$$u_z = \alpha_1 F(p,q;1;-\beta e^{\frac{z}{H}}). \quad (2.108)$$

This result also satisfies the requirement of the kinetic energy density remaining finite as we move further away from the interface.

This allows us to write the velocity distribution for this model as

$$u_z = \begin{cases} \alpha_1 F(p,q;1;-\beta e^{\frac{z}{H}}), & z < 0, \\ r^{-m} \left[c_1 J_m(r) + c_2 Y_m(r)\right], & 0 < z < z_d, \end{cases} \quad (2.109)$$

and its derivative as

$$\frac{du_z}{dz} = \begin{cases} -\alpha_1 pq \frac{\beta}{H} e^{\frac{z}{H}} F(p+1, q+1; 2; -\beta e^{\frac{z}{H}}), & z < 0, \\ -(2\omega^2 z_o / c_{oL}^2) r^{-(m+1)} \left[c_1 J_{m+1}(r) + c_2 Y_{m+1}(r)\right], & 0 < z < z_d, \end{cases} \quad (2.110)$$

which provides us with the required information to obtain a dispersion relation.

The final three boundary conditions are exactly those used in Section 2.5.2 and need not be presented again. Application of these boundary conditions yields the dispersion relation:

$$\frac{\gamma}{\Gamma}\frac{g\gamma v_{ao}^2}{c_{oL}\omega(c_{at}^2+v_{ao}^2)}[J_{m+1}(r_o)Y_m(r_d)-Y_{m+1}(r_o)J_m(r_d)]F(p,q;1;-\beta)$$
$$=[J_m(r_o)Y_m(r_d)-Y_m(r_o)J_m(r_d)]F(p+1,q+1;2;-\beta). \quad (2.111)$$

Equation (2.111) is the dispersion relation describing modes for an isothermal atmosphere permeated by a horizontal magnetic field which resides over a field-free medium containing a linear temperature profile.

We may recover the dispersion relation for the field-free case of Section 2.5.1 by allowing $\beta \to \infty$ in Equation (2.111). In order to do this, we use the transformation (Abramowitz and Stegun 1965; 15.3.7)

$$F(p,q;r;z)=\frac{\Gamma(r)\Gamma(q-p)}{\Gamma(q)\Gamma(r-p)}(-z)^{-p}F(p,1-r+p;1-q+p;\frac{1}{z})$$
$$+\frac{\Gamma(r)\Gamma(p-q)}{\Gamma(p)\Gamma(r-q)}(-z)^{-q}F(q,1-r+q;1-p+q;\frac{1}{z}), \quad (2.112)$$

which allows us to write Equation (2.111) as

$$\frac{\gamma}{\Gamma}\frac{g\gamma v_{ao}^2\beta\mathcal{D}_1}{c_{oL}\omega(c_{at}^2+v_{ao}^2)}\left[\frac{\Gamma(1-2p)}{\Gamma^2(1-p)\beta^{2p-1}}F(p,p;2p;-\frac{1}{\beta})\right.$$
$$\left.+\frac{\Gamma(2p-1)}{\Gamma^2(p)}F(1-p,1-p;2(1-p);-\frac{1}{\beta})\right]$$
$$=\mathcal{D}_2\left[\frac{\Gamma(1-2p)}{\Gamma(2-p)\Gamma(1-p)\beta^{2p-1}}F(p+1,p;2p;\frac{1}{\beta})\right.$$
$$\left.+\frac{\Gamma(2p-1)}{\Gamma(p+1)\Gamma(p)}F(2-p,1-p;2(1-p);\frac{1}{\beta})\right], \quad (2.113)$$

where

$$\mathcal{D}_1=J_{m+1}(r_o)Y_m(r_d)-Y_{m+1}(r_o)J_m(r_d) \quad (2.114)$$

and

$$\mathcal{D}_2=J_m(r_o)Y_m(r_d)-Y_m(r_o)J_m(r_d). \quad (2.115)$$

As $\beta \to \infty$ the hypergeometric functions may be reduced by the knowledge that

$$F(p,q;r;0)=1, \qquad \forall \qquad p,q,r. \quad (2.116)$$

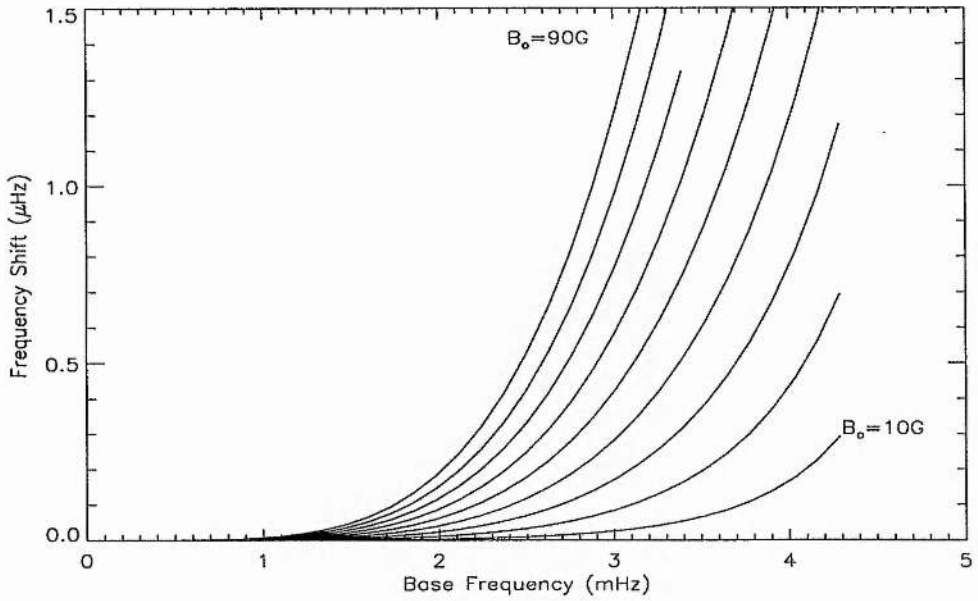

Figure 2.10: Frequency shifts induced by a uniform magnetic field. Changes in mode frequency are plotted against base frequencies (see Section 2.4). Field strengths ranging from 10G to 90G in 10G steps have been used. Note the scale of the shifts is in μHz.

This allows us to simplify Equation (2.113) to

$$\mathcal{D}_1 \frac{g\gamma}{c_{oL}\omega} \frac{\Gamma(p+1)}{\Gamma(p)} - \mathcal{D}_2 = 0 \tag{2.117}$$

Substituting for $\mathcal{D}_1$ and $\mathcal{D}_2$ from Equations (2.114) and (2.115) and using

$$\frac{\Gamma(p+1)}{\Gamma(p)} = p \tag{2.118}$$

recovers dispersion relation (2.69) for the field-free case:

$$\frac{g\gamma}{2c_{oL}\omega}\left[1+\left(1-\frac{4\omega^2 c_{at}^2}{g^2\gamma^2}\right)^{\frac{1}{2}}\right]\left[J_{m+1}(r_o)Y_m(r_d) - Y_{m+1}(r_o)J_m(r_d)\right] = J_m(r_o)Y_m(r_d) - Y_m(r_o)J_m(r_d). \tag{2.119}$$

The numerical treatment applied to Equation (2.111) will be analogous to that used in Sections 2.5.1 and 2.5.2, but the combined effects of variations in both magnetic field strength and atmospheric temperature will now be considered. However, note that the argument β appearing in Equation (2.111) is usually greater than 1 and hence we have used transformation (2.112) in our numerical code to calculate the hypergeometric equation.

As a first consideration, we shall calculate mode frequencies for a magnetised atmosphere which has a temperature equal to that at the top of the lower region, i.e. $T_{at} = T_{oL} = 4170°\mathrm{K}$. This enables the influence of the uniform magnetic field alone to be treated, and the frequencies found for this magnetic atmosphere will then be compared with those for the field-free case of Section 2.4. The comparison again takes the form of a frequency difference, namely

$$\triangle\nu = \nu(B_o, T_{at} = 4170°\mathrm{K}) - \nu(B_o = 0, T_{at} = 4170°\mathrm{K}). \tag{2.120}$$

Figure 2.10 displays the changes in mode frequency found from Equations (2.120) and (2.111). The magnetic field has been allowed to increase in strength from 10G to 90G in intervals of 10G. Figure 2.10 shows that all modes experience an increase in frequency with an increase in magnetic field strength. The effect is larger for stronger magnetic field strengths. This result is comparable to Evans and Roberts (1990) but note that the magnitude of the shift is smaller in this model, as we would expect.

In Figure 2.10, the curves extend in base frequencies only up to approximately 4.3 mHz. This is not due to the effect of a magnetoacoustic cut-off frequency, as in Section 2.5.2, but is simply to avoid computational difficulties in the calculations. We may see the reason for this if we consider the parameters p and q of the hypergeometric function, presented in Equation (2.94). For an angular frequency ω above a certain critical value, the parameters p and q become complex in nature. The condition for them to be real is that the expression within the square root be positive. This is exactly the same condition found in Section 2.4 for modes to be trapped in the interior and evanescent in the atmosphere (see Equation (2.48)). As the purpose of our calculations is to compare the mode frequencies of a magnetic atmosphere against its field-free counterpart, we do not consider frequencies for which p and q become complex, because we have no field-free reference frequency to measure against. In fact, there is no cut-off frequency for an atmosphere containing a uniform magnetic field; for any mode frequency, the perturbation u_z becomes evanescent at sufficient heights in the atmosphere (see Evans (1990) for a fuller discussion).

As a way of combining thermal and magnetic influences, the temperature of the upper atmosphere is now raised to $T_{at} = 5500°\mathrm{K}$ and the difference

$$\triangle\nu = \nu(B_o, 5500°\mathrm{K}) - \nu(0, 4170°\mathrm{K}) \tag{2.121}$$

calculated. Figure 2.11 shows the results. An immediate difference between this case and the previous one may be noted: In Figure 2.11, for the lowest magnetic field strengths, a

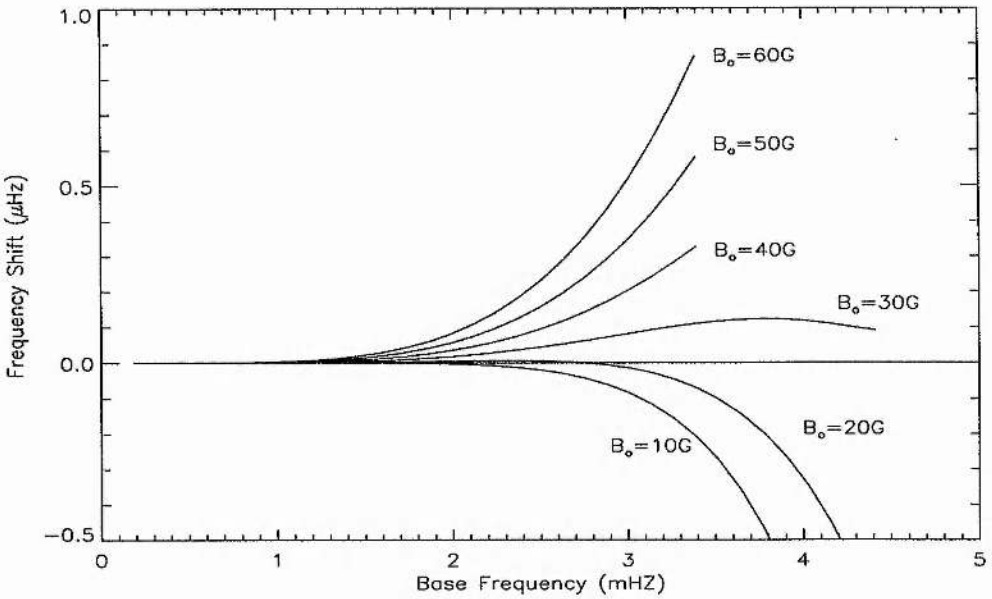

Figure 2.11: As Figure 2.10 except that the atmospheric temperature has been raised to 5500°K. The higher atmospheric temperature induces a negative frequency shift for lower magnetic field strengths.

reversal in the sign of the frequency shift has taken place. For higher magnetic fields, the positive shifts in frequency are of comparable magnitudes to those of Figure 2.10. This displays the competing effects of magnetism and temperature. The effect of the magnetic field is to raise the frequency but the temperature increase leads to a reduction in mode frequency that outweighs the influence of the magnetic field at low field strengths.

An encouraging result here is the change in frequency found for a field strength of 30G with $T_{at} = 5500°$K. This, qualitatively at least, reproduces the observed behaviour seen over the solar cycle; a rise in frequency up to around 3.9 mHz followed by a drop in the frequency increase for frequencies above this value. The result we have here agrees with that found by Jain and Roberts (1994) who produce curves that are qualitatively similar to the observations with the characteristic rise and subsequent sharp drop. Again, of course, the curves we produce display smaller shifts than for non-radial modes. This shall be discussed in Section 2.7.

To illustrate more clearly how thermal effects begin to dominate over magnetic ones, we now consider the case of keeping the magnetic field in the atmosphere constant and allow the atmospheric temperature to rise. We choose a field strength of 30G as the

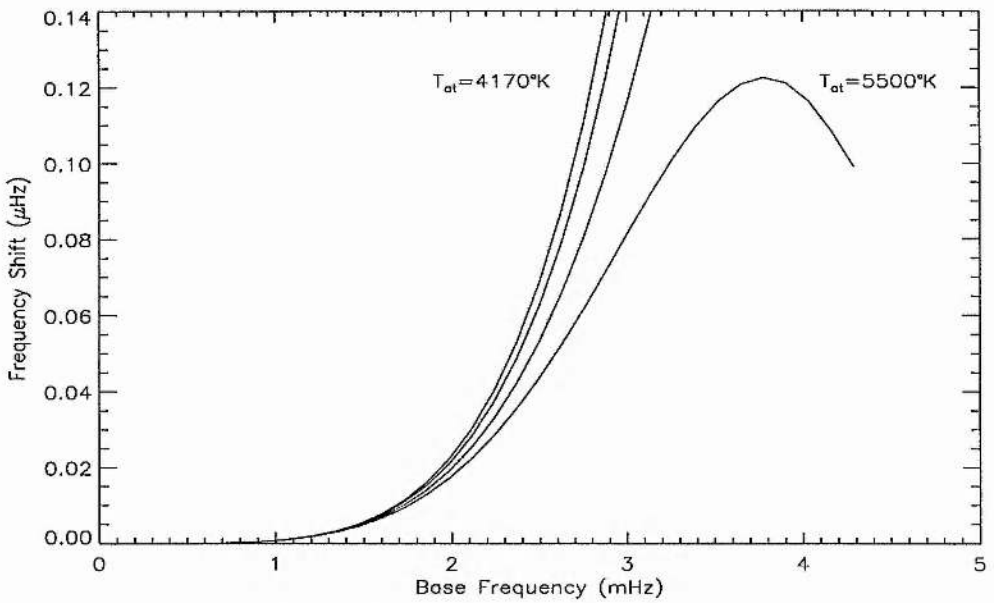

Figure 2.12: Frequency changes of a magnetic atmosphere over its field-free counterpart when the chromospheric field is kept constant but the atmospheric temperature is increased. We have chosen a magnetic field of strength $B_o = 30$G, and considered atmospheric temperatures $T_{at} = 4170°$K, 4500°K, 5000°K and 5500°K. It is apparent that at lower temperatures, magnetic effects dominate but as the temperature increases, thermal effects begin to appear and a turnover in the frequency shift is apparent.

field strength and calculate the difference

$$\triangle\nu = \nu(30\text{G}, T_{at}) - \nu(0, 4170°\text{K}). \tag{2.122}$$

Figure 2.12 shows the frequency shift curves calculated according to Equation (2.122). Atmospheric temperatures of 4170°K, 4500°K, 5000°K and 5500°K are taken. It may be seen that for an atmosphere in which the magnetic field strength does not vary but which undergoes a rise in temperature, the magnetic effects are reduced. In fact, for a particular combination of atmospheric conditions, in this case a rise in magnetic field strength from 0 to 30G and T_{at} increasing from 4170°K to 5500°K, the increase in frequency brought about by a rise in magnetic field strength and the decrease in frequency brought about by a rise in atmospheric temperature is balanced to give a sharp frequency rise up to frequencies of around 3.8 mHz, followed by a turnover and rapid decline in the frequency increase above 3.8 mHz. Therefore an increase in magnetic field strength coupled with a rise in chromospheric temperature reproduces the observed frequency variations in the low

l $p-$modes. However we do require rather extreme variations in T_{at} ($\triangle T_{at} \approx 1500°$K). We shall discuss this in Section 2.7.

2.6 An Alternative Approach to the Dispersion Relations

In all of the dispersion relations obtained in this chapter, the Bessel functions have always appeared in the same combinations, defined here as $\mathcal{D}_1$ and $\mathcal{D}_2$ such that

$$\mathcal{D}_1 = J_{m+1}(r_o)Y_m(r_d) - Y_{m+1}(r_o)J_m(r_d) \tag{2.123}$$

and

$$\mathcal{D}_2 = J_m(r_o)Y_m(r_d) - Y_m(r_o)J_m(r_d). \tag{2.124}$$

This is because these functions form the solution to the interior of our model and this lower region is not changed throughout the calculations. Also, the boundary conditions used to match the two regions together are unaltered apart from the sound speed being replaced by the fast magnetoacoustic speed in the Lagrangian pressure perturbation.

This observation alone is not of any particular interest. What is of interest, however, is the *order* of these functions. Note that the order of the functions in each case is either the polytropic index m, or $m+1$. In the numerical calculations we have taken m to be $3/2$, corresponding to a convectively neutral medium with adiabatic index $\gamma = 5/3$. This particular choice of the polytropic index allows us to rewrite the Bessel functions in terms of spherical Bessel functions by using the relations (Abramowitz and Stegun 1965: 10.1.1)

$$j_n(z) = \left(\frac{\pi}{2z}\right)^{\frac{1}{2}} J_{n+\frac{1}{2}}(z) \tag{2.125}$$

and

$$y_n(z) = \left(\frac{\pi}{2z}\right)^{\frac{1}{2}} Y_{n+\frac{1}{2}}(z). \tag{2.126}$$

A straight replacement of one function for another is of no use, but we may reduce $j_n(z)$ and $y_n(z)$ greatly by noting that the order of these functions is either 1 or 2. As a result of this, we are able to write these functions very simply in terms of sines and cosines by using the relations (Abramowitz and Stegun 1965: 10.1.11 and 10.1.12)

$$j_1(z) = \frac{\sin z}{z^2} - \frac{\cos z}{z}, \tag{2.127}$$

$$j_2(z) = \left(\frac{3}{z^3} - \frac{1}{z}\right)\sin z - \frac{3}{z^2}\cos z, \tag{2.128}$$

$$y_1(z) = -\frac{\cos z}{z^2} - \frac{\sin z}{z}, \tag{2.129}$$

and

$$y_2(z) = \left(-\frac{3}{z^3} + \frac{1}{z}\right)\cos z - \frac{3}{z^2}\sin z. \tag{2.130}$$

Application of Equations (2.125)-(2.130) to Equations (2.123) and (2.124) leads to trigonometrical representations of $\mathcal{D}_1$ and $\mathcal{D}_2$; after much algebra, we obtain

$$\mathcal{D}_1 = \frac{2}{(r_o r_d)^{\frac{1}{2}}\pi}\left[\left(\frac{3}{r_o} + \frac{3}{r_d r_o^2} - \frac{1}{r_d}\right)\sin(r_d - r_o) + \left(1 - \frac{3}{r_o^2} + \frac{3}{r_d r_o}\right)\cos(r_d - r_o)\right], \tag{2.131}$$

and

$$\mathcal{D}_2 = \frac{2}{(r_o r_d)^{\frac{1}{2}}\pi}\left[\left(\frac{1}{r_d} - \frac{1}{r_o}\right)\cos(r_d - r_o) + \left(\frac{1}{r_o r_d} + 1\right)\sin(r_d - r_o)\right]. \tag{2.132}$$

Instead of working in terms of r_o and r_d, we find it convenient to introduce the variable Ω and the parameter α such that

$$\Omega = r_o = \frac{2\omega z_o}{c_{oL}} \qquad \text{and} \qquad \alpha = (1 + \frac{z_d}{z_o})^{\frac{1}{2}} - 1. \tag{2.133}$$

This choice of parameters allows us to write the arguments of the trigonometric functions as

$$r_d - r_o = \alpha\Omega, \tag{2.134}$$

and Equations (2.131) and (2.132) reduce to

$$\mathcal{D}_1 = \frac{1}{(\alpha+1)\Omega^3}\left[((2+3\alpha)\Omega^2 + 3)\sin\alpha\Omega + ((\alpha+1)\Omega^2 - 3\alpha)\Omega\cos\alpha\Omega\right] \tag{2.135}$$

and

$$\mathcal{D}_2 = \frac{1}{(\alpha+1)\Omega^2}\left[((\alpha+1)\Omega^2 + 1)\sin\alpha\Omega - \alpha\Omega\cos\alpha\Omega\right]. \tag{2.136}$$

As an example of the procedure that we have followed above, let us look once again at the dispersion relation for a field-free atmosphere, Equation (2.69). This dispersion relation reads

$$\frac{1}{\omega}\frac{c_{at}}{c_{oL}}\left[(\omega_{ac}^2 - \omega^2)^{\frac{1}{2}} + \omega_{ac}\right]\left[J_{m+1}(r_o)Y_m(r_d) - Y_{m+1}(r_o)J_m(r_d)\right] = \left[J_m(r_o)Y_m(r_d) - Y_m(r_o)J_m(r_d)\right]. \tag{2.137}$$

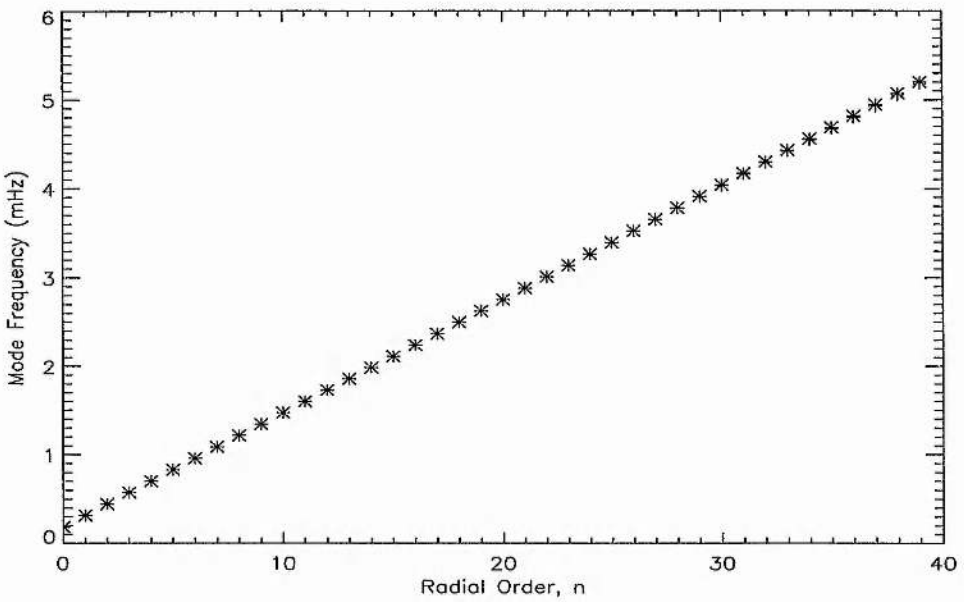

Figure 2.13: A comparison of the calculated mode frequencies from Equations (2.137) and (2.138). The results for the original dispersion relation are presented as crosses (+++) and those for the reduced one as stars (***). Within the numerical accuracy employed, there is no difference between the two sets of results.

Application of the above transformations leads to

$$\frac{2c_{at}z_o}{c_{oL}^2\Omega}\left[\left(\omega_{ac}^2-\frac{c_{oL}^2\Omega^2}{4z_o^2}\right)^{\frac{1}{2}}+\omega_{ac}\right]\left[((2+3\alpha)\Omega^2+3)\sin\alpha\Omega\right.$$
$$\left.+((\alpha+1)\Omega^2-3\alpha)\Omega\cos\alpha\Omega\right]$$
$$=\Omega\left[((\alpha+1)\Omega^2+1)\sin\alpha\Omega-\alpha\Omega\cos\alpha\Omega\right]. \qquad (2.138)$$

We may now solve Equation (2.138) in terms of Ω and make a comparison with the results of Section 2.4. Figure 2.13 displays the mode frequencies found from both dispersion relations plotted against equivalent radial orders from the two sets of data. Of course, there is negligible difference between the two sets of data.

2.7 Discussion

A simple plane-parallel, two layer model has been used in an attempt to understand the observed solar cycle behaviour of the radial modes of oscillation of the Sun. The model consists of a lower field-free region which is bounded at depth and within which

the temperature increases linearly with depth; above this zone is an upper atmosphere, extending to infinity, permeated by a horizontal magnetic field.

From this model we have been able to reproduce mode frequencies that are close to those observed (Libbrecht and Woodard 1990; Elsworth *et al.* 1994), the frequencies displaying a linear dependence on radial order, n. This initial result is an encouraging introduction to the main focus of this chapter, namely the nature of changes in mode frequency brought about by changes in chromospheric conditions. The $l = 0$ mode penetrates to the core of the Sun and as such holds a unique position in determining the role (if any) of the outer layers of the Sun in $p-$mode solar cycle changes. If the deepest layers of the sun varied over the activity cycle, the $l = 0$ modes would be the most likely to respond to these changes. Also, as a diagnostic tool, the $l = 0$ modes may hold key information about the solar cycle in their unique position of having no angular structure.

What we have in mind through a study of this kind is the effect the outer atmospheric layers of the sun have on its oscillation frequencies over the course of the solar cycle. Also, changes in the chromosphere brought about by the birth and death of active regions can be considered. We have examined changing two parameters in the chromosphere, the atmospheric temperature, T_{at}, and the strength of the magnetic field, B_o. As we have noted, it is in fact the presence of a magnetic field that is responsible for an increase in the temperature of the atmosphere, but it is of interest to study the two effects separately.

The frequency shifts we find are simply a response to changes in the upper atmosphere. The presence of the magnetic field has two important physical effects. Firstly, the evanescent modes in the atmosphere are of fast magnetoacoustic type because the velocity perturbation is transverse to the magnetic field. As the characteristic speed of this mode is the fast magnetoacoustic speed, $(c_s^2 + v_a^2)^{\frac{1}{2}}$, the transit time in the magnetic field is reduced as the fast speed increases with field strength. This serves to increase the mode frequency. Also, the magnetic field adds support to the atmosphere because of the increase of the magnetically modified scale height, H_B, with increasing field strength. The mode frequencies tend to to be reduced by this effect because of the extra inertia added to the system.

Initially, we restricted our attention to changing the thermal properties of the atmosphere (Section 2.5.1). In the absence of a magnetic field, raising the chromospheric temperature led to a decrease in mode frequency for all radial orders. This result has been known for sometime (Lamb 1932) for a general two layer atmosphere and has also been shown in models studying general degree modes (Evans and Roberts 1990; Jain and

Roberts 1994). By a similar argument to the above, we would expect frequency shifts to be negative: the effect of increasing the atmospheric temperature, T_{at}, is to raise the density scale height H of the atmosphere. The extra inertia that this supplies gives rise to a frequency decrease. The changes that we find at the highest frequencies range from a drop of approximately 0.5 μHz with a raise in chromospheric temperature to 4500°K, to approximately 5 μHz with a temperature of 6000°K. Changes in atmospheric temperature therefore have a large effect on the mode frequencies for this model, and moreover they fail to reproduce the observed solar cycle variations of the $l = 0$ modes (see Section 2.2).

For the constant Alfvén speed model we have used an atmosphere analogous to that employed by Campbell and Roberts (1989). Our results are comparable with theirs, with all modes showing a frequency decrease. However, they find that the $n = 1$ p–mode suffers a frequency increase; this does not happen for the $l = 0$ modes here. The magnitude of the shifts is approximately 0.01 μHz for the weakest fields to 1 μHz for stronger fields, much smaller in magnitude than the frequency shifts seen in Section 2.5.1. However, the assumption of a constant Alfvén speed underestimates the influence of the magnetic field. This is because the magnetic field strength $B_o(z)$ decreases proportionally to $\rho_o^{\frac{1}{2}}$, giving a magnetic scale height that is smaller than to be expected. In reality, the magnetic scale height of the atmosphere would be larger, implying that magnetic effects are more significant.

The sign of the frequency changes can be further examined by studying the decrements λ and τ arising in solutions (2.47) and (2.77). These solutions are of the same form, implying that the magnetic field chosen simply mimics changes in atmospheric temperature (*cf.* Section 2.5.1). An exponentially decaying magnetic field has little rigidity. Hence, for an atmosphere with constant Alfvén speed, the reduction in gas density due to the presence of the magnetic field is the dominant effect. This is directly analogous to the reduction in atmospheric density associated with a rise in chromospheric temperature in the field-free case and explains why one case is a mimicry of the other.

The final case that we have considered, that of a uniform magnetic field, provides us with some interesting results. Considering an atmosphere for which $T_{oL} = T_{at}$ (as explored by Evans and Roberts (1990)), we find an increase in mode frequency for all modes. Again, the shifts are very small, ranging at the highest frequencies from 0.2 μHz for a 10G field to over 1 μHz for higher strength fields. These results compare well with Evans and Roberts (1990), with the shifts here being much smaller. For example, Evans and Roberts (1990)

find that for degree $l = 100$ and mode $n = 20$, a drop in canopy field strength from 10G to 0 causes a frequency fall of approximately 1 μHz. For the same radial order and magnetic field reduction, we find that modes of degree zero suffer a drop in frequency that is 20% that of the $l = 100$ modes. Our results agree well with the observations of Isaak *et al.* (1986) and Elsworth *et al.* (1994). Also, from the condition on the transit time decreasing for an increase in magnetic field strength, our results are understandable.

Finally, by considering the combined influences of an increase in magnetic field strength with a corresponding rise in chromospheric temperature, some encouraging results are found. By raising the atmospheric temperature to 5500°K we are able to produce a downturn in the frequency shifts. For low changes in magnetic field strength, a somewhat unrealistic change to T_{at} even changes the sign of the frequency shifts (compare Figures 2.10 and 2.11). For certain specific changes in B_o and T_{at}, however, we are able to produce a steep rise in $\triangle\nu$ up to frequencies of around 3.8 mHz, followed by a downturn for frequencies above this value (see Figure 2.12). Qualitatively, the results of Figure 2.12 are similar to the observed solar cycle variations of intermediate degree $p-$modes, but the magnitude of the changes is much smaller. Quantitatively, the peak in Figure 2.12 is in good agreement with the variation in the $l = 0$ mode frequencies given by Pallé *et al.* (1989).

A previous study of the frequency shifts suffered by radial modes was carried out by Goldreich *et al.* (1991). They found results that agreed very well with observations and suggested that the observed frequency shifts could be divided into two components; a positive component (where the frequency shifts increase as the frequency increases) and a negative component which causes the frequency shift to drop sharply at frequencies above $\approx$ 4 mHz. They concluded that changes in the photospheric magnetic field strength are responsible for the positive component in the frequency shifts, and that an increase in the chromospheric temperature over the solar cycle, combined with a chromospheric resonance gives rise to the sharp drop in frequency shift. Our results agree reasonably well, but of course we have considered magnetic fields in the chromosphere rather than the photosphere, and our model does not allow for the presence of a chromospheric resonance. Also, Goldreich *et al.* do not put a figure on the rise in chromospheric temperature necessary to give the correct shape to their curves making comparison difficult; we find that very large changes in chromospheric temperature are required ($\triangle T_{at} \approx 1500$°K).

The findings of this chapter add further weight to the argument that it is changes to the outer layers of the sun over the solar cycle that are responsible for the observed variation

in the $p-$mode frequencies (see, for example, Campbell and Roberts 1989; Libbrecht and Woodard 1990; Evans and Roberts 1990; Woodard *et al.* 1991; Shibahashi 1991; Jain and Roberts 1994; Bachmann *et al.* 1994; Nishizawa and Shibahashi 1994). Here, we have seen that the $l = 0$ mode responds to changes in the chromosphere in a similar fashion to those found earlier for modes of non-zero degree. It is particularly interesting to note that this result agrees exceptionally well with the recent observations of Chaplin *et al.* (1998) who find that modes of degree zero display a rise phase followed by evidence of a turnover.

Chapter 3

The Upper Convection Zone and its Effect on P-Mode Frequencies

3.1 Introduction

Numerical simulations of convection applied to solar models and models of convection solved with solar values as parameters infer that the main bulk of the solar convection zone is very nearly adiabatically stratified (see, for example, Christensen-Dalsgaard *et al.* (1991)). In fact, below a depth of approximately 3000 km, measured from the photosphere, the actual temperature gradient ∇ ($\equiv \partial \ln T / \partial \ln p$) exceeds the adiabatic temperature gradient, ∇_{ad}, by only about one part in a million (Demarque *et al.* 1997).

Over most of the convection zone of the Sun, the convective efficiency η ($\equiv$ convective flux/reference flux, where the reference flux is, for example, the radiative flux or the magnetic flux) is very high ($\eta >> 1$), but near the solar surface the plasma density drops off so rapidly that convection becomes an inefficient process ($\eta \sim 1$) and the temperature gradient becomes strongly superadiabatic in order to maintain effective energy transport.

The superadiabatic layer in the upper part of the solar convection zone forms a thin transitional layer between the mildly superadiabatic ($\nabla \approx \nabla_{ad}$) deep convection zone and the outer, optically thin, atmospheric layers of the Sun where radiative transfer of energy dominates ($\nabla - \nabla_{ad} \sim 1$). Physically, this thin layer may be understood as a region unstable to convective motions accompanied by a zone of partial ionisation of hydrogen (Smeyers 1970; Kim *et al.* 1996). A convective element travelling upwards through a layer of this kind frees ionisation energy which is converted to thermal energy. This increases the

buoyancy of the convective element, causing it to continue in its upward journey. The net effect of this is a substantial deviation of the temperature gradient from its adiabatic value. This joint energy process, of radiative and convective transport of energy, is decoupled in the deep convection zone where radiative transfer is negligible (Kim *et al.* 1995).

Several models have been proposed to more accurately describe the structure of the superadiabatic layer, usually with a view to reconciling the discrepancies between the calculated oscillation frequencies of solar models and the actual observed frequencies of the Sun (Monteiro *et al.* 1996; Kim *et al.* 1996; Demarque *et al.* 1997). Our interest in this chapter is based upon the possibility that solar cycle changes in $p-$modes may be influenced by changes in the superadiabaticity of the upper convection zone. We note that it is primarily alterations in the structure of the superadiabatic layer which are believed responsible for the measured fluctuations in solar luminosity over the solar cycle (Dearborn and Blake 1980; Endal *et al.* 1985). The variation in solar luminosity has been measured by Willson and Hudson (1988) using ACRIM data from the solar maximum mission. They found that between 1980 (solar maximum) and 1986 (solar minimum) the total solar irradiance fell by 0.03%, following which the luminosity began to rise once more. This long term variation suggests a correlation between solar luminosity and the solar cycle.

By perturbing the ratio α of the mixing length L of a convective element to the local pressure scale height Λ, a change in the convective energy transport efficiency may be modelled (an increase in α leads to an increase in the convective efficiency η, and vice versa). An increase in α allows energy to flow more freely by convection and brings the local temperature gradient required to sustain the energy flow closer to the adiabatic gradient. Dearborn and Blake (1980) showed that small changes in α lead to a rapid adjustment of the superadiabatic layer on a time scale of about 1 day. To maintain hydrostatic equilibrium, the rest of the convection zone adjusts rapidly ($\sim$ 1 hour) to the new hydrostatic structure and this is followed by a slow relaxation to the new thermal equilibrium state.

Dearborn and Blake (1980) argue that the net effect of this is that if α increases, the convection zone begins contracting, converting potential energy to thermal energy; energy changes take place on a time scale of $\sim 10^5$ years, leading to a temporary but immediate increase in luminosity. The luminosity change lasts only while the convection zone adjusts itself to the new thermal equilibrium which in fact is not reached before another disturbance to the hydrostatic structure, because of the large time scale ($\sim 10^5$ years) required.

Only large perturbations to the mixing length L in the deep convection zone have a

significant effect on the luminosity and radius of models (Endal *et al.* 1985). The immediate response (~1 day for readjustments to a new thermal equilibrium) of the superadiabatic region to changes in convective efficiency, however, lead to substantial luminosity changes: Endal *et al.* (1985) report a 0.3% change in luminosity for a 1% change in L. In fact, Dearborn and Blake (1980) claim that 90% of the observed luminosity variation is caused by changes in convective efficiency as small as 1% in the superadiabatic layer. These luminosity variations are most likely to be seen as changes in the effective surface temperature, T_{eff}. Changes in T_{eff} have been reported by Livingston (1978) who claimed to measure a cooling of approximately 6°K of the photospheric surface temperature as the Sun approached solar maximum.

Although convection operates in the superadiabatic layer, a significant fraction of energy flows by radiation ($\eta \sim 1$ in the superadiabatic zone). As a result the superadiabatic layer does not react to an increase in convective efficiency by contracting, but rather as a radiative region would by expanding (Dearborn and Blake 1980).

Overall the convective efficiency of the Sun would appear to be at its greatest at solar minimum, when the Sun is at its most luminous, and R_{sun} and T_{eff} are at a maximum. A decrease in the efficiency of convection within the superadiabatic layer as solar maximum is approached, perhaps by magnetic fields inhibiting convection, would then lead to a contraction of the superadiabatic region, giving a change in solar radius, lowering the effective surface temperature and thus decreasing the overall solar luminosity.

Changes to the superadiabatic layer can be expected to have an influence on $p-$mode frequencies over the course of the solar cycle; we wish to model this effect. We model the bulk of the convection zone (and below) as being marginally stable to convective motions with a temperature profile that increases linearly with depth. By stable to convective motions we mean that the polytropic index m of the plasma is related to the adiabatic exponent γ by the relation

$$m = \frac{1}{\gamma - 1}, \tag{3.1}$$

thus producing a buoyancy (Brunt-Väisälä) frequency, defined by

$$\omega_g^2 = \frac{-g}{T_s(z)} \left[\nabla - \nabla_{ad}\right], \tag{3.2}$$

that is exactly zero. The assumption that $\omega_g^2 = 0$ excludes both convective instability and g-modes.

Above the neutral convection zone, we impose a thin layer taken to model the superadiabatic region. Again, for analytical simplicity, we impose a linear temperature profile, but one that is steeper than that of the neutral convection zone beneath it. Superadiabaticity ($\omega_g^2 < 0$) in this layer requires that

$$m < \frac{1}{\gamma - 1}. \tag{3.3}$$

In the superadiabatic layer convective motions (with $\omega^2 < 0$) may occur.

Finally, in the atmosphere above the superadiabatic layer we impose an isothermal layer representing the photosphere and above, within which may reside a horizontal magnetic field $\mathbf{B}$ (see Section 3.6).

At the time of writing this chapter, a piece of work similar in spirit to this investigation has appeared (Vanlommel and Cadez (1998)). They were interested in the effect of various temperature profiles on the acoustic eigenfrequencies, concentrating their attention on the chromosphere-corona transition region. However, they also investigated the effect of varying the temperature gradient of the main bulk of the convection zone away from an adiabatic gradient to more superadiabatic profiles. They found that the frequency of the $f-$mode could be increased by several hundred μHz by varying the temperature gradient of the convection zone by up to twice the adiabatic gradient. The large shifts in frequency found by Vanlommel and Cadez (1998) would further indicate that the main bulk of the convection zone does not alter its structure over the solar cycle.

We have organised the chapter as follows: in the next section (Section 3.2) we introduce in detail the equilibrium model and obtain various equilibrium profiles of thermodynamic variables. In Section 3.3 we consider perturbations to this equilibrium and solve the differential equations governing plasma motions. In section 3.4 we derive a dispersion relation for the model in the absence of a magnetic field. In Section 3.5, the effects of changing thermal conditions of the model on the $p-$mode frequencies and convective mode growth times are investigated. A horizontal magnetic field is added to the atmosphere in Section 3.6 and its additional effects considered. Finally, in Section 3.7 we discuss the results found.

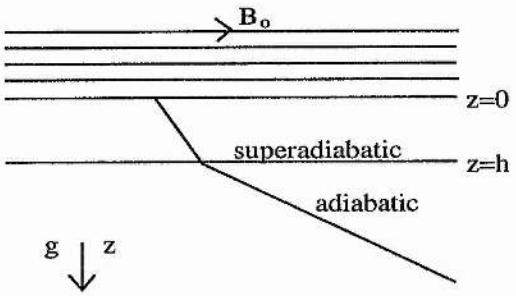

Figure 3.1: The model used to assess the effect on $p-$mode frequencies of a strongly superadiabatic layer at the top of the convection zone. The atmosphere overlying the superadiabatic layer is assumed to be isothermal and embedded with a non-uniform horizontal magnetic field.

3.2 The Equilibrium Model

3.2.1 Overall equilibrium

A simple three layer model is used to include the thin superadiabatic region of the upper convection zone. This model may therefore be viewed as a simple extension to the models of Campbell and Roberts (1989), Evans and Roberts (1990, 1992) and Jain and Roberts (1994). The equilibrium state is displayed in Figure 3.1. The reference level $z = 0$ is chosen to correspond to the top of the superadiabatic layer which extends to a depth of $z = h$. Beneath the superadiabatic layer, at depths $z > h$, the medium is assumed to be marginally stable to convective motions ($\omega_g^2 = 0$). The temperature profiles of these two regions, which collectively we shall call the interior ($z > 0$), are taken to be linear, but with a steeper gradient in $0 < z < h$. The unbounded isothermal atmosphere in $z < 0$ is taken to model the photosphere and above and may be permeated by a horizontal magnetic field $\mathbf{B} = B(z)\hat{\mathbf{x}}$ of strength $B(z)$ which varies with height.

In general, the plasma is assumed to be an ideal, inviscid and perfectly conducting; gravity g acts in the positive $z-$direction. The unperturbed plasma pressure $P_o(z)$, density $\rho_o(z)$ and magnetic field distribution $B(z)$ satisfy the equation of magnetohydrostatic

balance:

$$\frac{d}{dz}\left(P_o(z)+\frac{B^2(z)}{2\mu}\right)=\rho_o(z)g, \tag{3.4}$$

where μ ($=4\pi\times10^{-7}$ Henry m^{-1}) is the magnetic permeability. The plasma pressure and density are related to the temperature profile by the ideal gas law:

$$P_o(z)=R\rho_o(z)T_o(z), \tag{3.5}$$

where R is taken to be k_B/m_{av} (k_B is Boltzmann's constant and m_{av} is the mean particle mass of the plasma).

The equilibrium temperature profile is taken to be

$$T_o(z)=\begin{cases} T_{at}, & z<0,\\ T_s(1+\frac{z}{z_{ou}}), & 0<z<h,\\ T_h(1+\frac{z-h}{z_{ol}}), & z>h. \end{cases} \tag{3.6}$$

The temperature of the isothermal atmosphere is given by T_{at}, that at the top of the superadiabatic region by T_s and the temperature at the top of the adiabatic layer is taken to be T_h, chosen such that the temperature is continuous at $z=h$, i.e. $T_h=T_s(1+h/z_{ou})$. The temperature may be discontinuous at $z=0$. In all subsequent numerical calculations T_h will be kept fixed. The temperature scale height of the superadiabatic layer is given by z_{ou} and that of the convectively stable layer to be z_{ol}. In order to maintain a temperature gradient T_s/z_{ou} in $0<z<h$ that is steeper than the adiabatic gradient T_h/z_{ol} in $z>h$, we require that

$$z_{ol}>z_{ou}+h. \tag{3.7}$$

In order to more accurately model the superadiabatic zone, the exponent γ used for this layer is taken to be different from the exponent elsewhere in the medium, as suggested by standard solar models such as Guenther *et al.* (1992). Specifically, the chosen profile for $\gamma(z)$ is

$$\gamma(z)=\begin{cases} \gamma_{ad}, & z<0,\\ \gamma_{sa}, & 0<z<h,\\ \gamma_{ad}, & z>h, \end{cases} \tag{3.8}$$

with $\gamma_{sa}<\gamma_{ad}$. The adiabatic exponent of the atmosphere and the neutral convection zone is γ_{ad}, and the superadiabatic region has exponent γ_{sa}. The choice of an adiabatic exponent

which has a piece-wise constant variation with depth gives a sound speed squared, $c_s^2(z)$, of the form

$$c_s^2(z) = \begin{cases} c_{at}^2, & z < 0, \\ c_s^2(1 + \frac{z}{z_{ou}}), & 0 < z < h, \\ c_h^2(1 + \frac{z-h}{z_{ol}}), & z > h. \end{cases} \tag{3.9}$$

The sound speed of the atmosphere is $c_{at}(= (\gamma_{ad} R T_{at})^{\frac{1}{2}})$, in general different from the sound speed at the top of the central layer $c_s(= (\gamma_{sa} R T_s)^{\frac{1}{2}})$ because of the differing adiabatic exponents. Similarly, the sound speed at the base of the superadiabatic layer ($c_{h-} = c_s(1 + h/z_{ou})^{\frac{1}{2}}$) and that at the top of the lower region $c_h(= (\gamma_{ad} R T_h)^{\frac{1}{2}})$ are also different. Hence we have two discontinuities in the sound speed profile for our model, one at $z = 0$ and the other at $z = h$.

In the non-magnetic medium, Equation (3.4) reduces to

$$\frac{dP_o}{dz} = \rho_o g. \tag{3.10}$$

Application of the temperature profile (3.6) to the magnetostatic balance (Equations (3.4) or (3.10)), along with the ideal gas equation (3.5), gives the equilibrium pressure distribution $P_o(z)$:

$$P_o(z) = \begin{cases} P_{at} e^{\frac{z}{H}}, & z < 0, \\ P_s(1 + \frac{z}{z_{ou}})^{m_u+1}, & 0 < z < h, \\ P_h(1 + \frac{z-h}{z_{ol}})^{m_l+1}, & z > h. \end{cases} \tag{3.11}$$

The plasma pressure at the base of the atmosphere is denoted by P_{at} and that at the top of the superadiabatic layer by P_s. The pressure at $z = h$ is P_h and that at $z = 0$ is P_s.

The parameters H, m_u and m_l appearing in Equation (3.11) are defined by

$$H = \frac{c_{at}^2}{g\gamma_{ad}}, \qquad m_u = \frac{g z_{ou}}{R T_s} - 1, \qquad \text{and} \qquad m_l = \frac{g z_{ol}}{R T_h} - 1, \tag{3.12}$$

where H is the pressure scale height of the isothermal atmosphere, and m_u is the polytropic index of the superadiabatic layer and m_l is the polytropic index in the adiabatic region.

To maintain static equilibrium, pressure balance must be satisfied at both $z = 0$ and $z = h$. The requirement at $z = h$ leads to

$$P_h = P_s(1 + h/z_{ou})^{m_u+1} \qquad \text{and} \qquad \gamma_{ad} c_{h-}^2 = \gamma_{sa} c_h^2. \tag{3.13}$$

To maintain pressure continuity at $z = 0$ we require that P_{at}, P_s and B_o, the magnetic field strength at the base of the atmosphere, are related by

$$P_s = P_{at} + \frac{B_o^2}{2\mu}. \tag{3.14}$$

This places a limit on the size of B_o before the magnetic field evacuates the atmosphere.

Using Equation (3.14) along with Equation (3.5), pressure balance may be expressed in terms of an interfacial density ratio

$$\frac{\rho_{at}}{\rho_s} = \frac{\gamma_{ad} c_s^2}{\gamma_{sa}(c_{at}^2 + \frac{1}{2}\gamma_{ad} v_{ao}^2)}, \tag{3.15}$$

where ρ_{at} is the plasma density at the base of the photosphere and ρ_s is the plasma density at the top of the central layer. Here, v_{ao} is the Alfvén speed at the base of the atmosphere, defined by

$$v_{ao} = \frac{B_o}{(\mu\rho_{at})^{\frac{1}{2}}}. \tag{3.16}$$

3.2.2 Constraints on temperature and sound speed gradients

The temperature gradient in the upper superadiabatic region is taken to be greater than that of the adiabatically stratified convection zone (inequality (3.7)). For the lower convection zone we choose $\gamma_{ad} = 5/3$, giving $m_l = 3/2$ from Equation (3.1). From the standard solar model of Guenther *et al.* (1992) which displays a variable γ, we select an average value of the exponent for the superadiabatic layer of $\gamma_{sa} = 1.2$. From the requirement of superadiabaticity (Equation (3.3)) this requires that $m_u < 5$; $m_u = 5$ is the value for the upper layer of the model to be neutrally stable, i.e. if $m_u = 1/(\gamma_{sa} - 1)$. However, from Equation (3.12), z_{ou} and z_{ol} are seen to be related by

$$z_{ol} = \frac{(m_l + 1)}{(m_u + 1)}(z_{ou} + h), \tag{3.17}$$

indicating the tighter constraint that for this model $m_u < m_l$. This constraint also proves to be somewhat loose if we wish to be as realistic as the model allows us. The actual run of the sound speed squared in the standard solar model departs strongly from a linear behaviour in the outermost layers of the Sun. Modelling this is beyond the range of our study, but it should be noted that the gradient of the sound speed is generally steeper in the upper layers than it is at depth. Demanding that the gradient of the square of the sound speed is greater in the superadiabatic region than that in the adiabatic lower region, we find that

$$m_u < \frac{\gamma_{sa}}{\gamma_{ad}}(m_l + 1) - 1. \tag{3.18}$$

For our choice of parameters given above, $\gamma_{sa} = 1.2$, $\gamma_{ad} = 5/3$ and $m_l = 3/2$, we require that

$$m_u < 0.8. \tag{3.19}$$

We are interested here in how small changes in m_u influence the frequencies of the $p-$modes and growth-times of convective modes (g^-−modes) confined to the superadiabatic layer; the precise value of m_u is not our concern. In the numerical illustrations given below, we choose $m_u = 0.75$ as representative of the value of m_u at solar minimum.

3.3 Perturbations

The equations governing plasma motions are as follows (see Chapter 1):
the equation of mass continuity

$$\frac{\partial \rho}{\partial t} + \nabla \cdot (\rho \mathbf{u}) = 0; \tag{3.20}$$

the momentum equation

$$\rho \frac{D\mathbf{u}}{Dt} = -\nabla P + \rho \mathbf{g} + \mathbf{j} \times \mathbf{B}; \tag{3.21}$$

the adiabatic energy equation

$$\frac{DP}{Dt} = \frac{\gamma P}{\rho} \frac{D\rho}{Dt}; \tag{3.22}$$

the induction equation with no diffusion

$$\frac{\partial \mathbf{B}}{\partial t} = \nabla \times (\mathbf{u} \times \mathbf{B}). \tag{3.23}$$

Here, the convective derivative is denoted by

$$\frac{D}{Dt} \equiv \frac{\partial}{\partial t} + \mathbf{u} \cdot \nabla, \tag{3.24}$$

while the current density $\mathbf{j}$ is given by

$$\mu \mathbf{j} = \nabla \times \mathbf{B}, \tag{3.25}$$

and the magnetic field satisfies the solenoidal constraint

$$\nabla \cdot \mathbf{B} = 0. \tag{3.26}$$

The equilibrium of Section 3.2 is perturbed by a two dimensional velocity field of the form

$$\mathbf{u} = (u_x(z), 0, u_z(z))\exp\left[i(\omega t - k_x x)\right], \tag{3.27}$$

where ω is the angular frequency of the disturbance and k_x the horizontal wavenumber. The system of Equations (3.20)-(3.26) may then be linearised for the perturbation (3.27) leading to the governing equations describing the velocity components. The governing equations are obtained and solved in each of the three layers separately.

3.3.1 The interior ($z > 0$)

Within the non-magnetic interior of the model, it proves useful to introduce the compression $\triangle(\equiv \nabla \cdot \mathbf{u})$ as a convenient variable to work with. Equations (3.20)-(3.26) determine the relationship between the vertical velocity u_z and the compression $\triangle$ as

$$\frac{du_z}{dz} = \left[1 - \frac{k_x^2 c_s^2(z)}{\omega^2}\right]\triangle - \frac{gk_x^2}{\omega^2}u_z \tag{3.28}$$

and

$$(\omega^4 - g^2k_x^2)u_z = g[k_x^2c_s^2(z) - \gamma(z)\omega^2]\triangle - \omega^2 c_s^2(z)\frac{d\triangle}{dz}. \tag{3.29}$$

Assuming that $\omega^2 \neq gk_x$, u_z may be eliminated between Equations (3.28) and (3.29) to obtain the governing differential equation for $\triangle$ (Lamb 1932):

$$c_s^2(z)\frac{d^2\triangle}{dz^2} + \left[g\gamma(z) + c_s^2(z)'\right]\frac{d\triangle}{dz} + \left\{\omega^2 - k_x^2c_s^2(z) + \frac{gk_x^2}{\omega^2}\left[(\gamma(z)-1)g - c_s^2(z)'\right]\right\}\triangle = 0, \tag{3.30}$$

with the prime $'$ denoting the derivative with respect to depth z. We now look for the solution of Equation (3.30) in each of the two layers of the interior.

The superadiabatic layer ($0 < z < h$)

In order to solve Equation (3.30) in the superadiabatic layer of the interior, where the adiabatic exponent is $\gamma = \gamma_{sa}$ and where the sound speed squared is $c_s^2(z) = c_s^2(1+z/z_{ou})$, we set

$$\triangle = e^{-k_x(z+z_{ou})}f(z), \tag{3.31}$$

where $f(z)$ is to be found. After some algebra we obtain the solution for $\triangle$ first given by Lamb (1932):

$$\triangle = e^{-k_x(z+z_{ou})}\left[A_1 M(-a_u, m_u+2, 2k_x(z+z_{ou})) + B_1 U(-a_u, m_u+2, 2k_x(z+z_{ou}))\right], \qquad 0<z<h, \tag{3.32}$$

where A_1 and B_1 are arbitrary constants, and M and U are confluent hypergeometric functions (Abramowitz and Stegun 1965; Chapter 13). The parameter a_u is given by

$$2a_u = \frac{(m_u+1)}{\gamma_{sa}}\Omega^2 + \left[\frac{(m_u+1)}{\gamma_{sa}}(\gamma_{sa}-1)-1\right]\frac{1}{\Omega^2} - (m_u+2), \tag{3.33}$$

where we have introduced the dimensionless frequency Ω through

$$\Omega^2 = \frac{\omega^2}{gk_x}. \tag{3.34}$$

The component of the vertical velocity u_z is then given by Equation (3.29).

The adiabatic convection zone $(z > h)$

Following a similar procedure to that used for the superadiabatic layer, but now setting

$$\triangle = e^{-k_x(z+z_{ol}-h)}g(z), \tag{3.35}$$

yields the solution

$$\triangle = e^{-k_x(z+z_{ol}-h)}\left[A_2 M(-a_l, m_l+2, 2k_x(z+z_{ol}-h)) + B_2 U(-a_l, m_l+2, 2k_x(z+z_{ol}-h))\right], \tag{3.36}$$

where A_2 and B_2 are arbitrary constants and

$$2a_l = m_l\Omega^2 - (m_l+2). \tag{3.37}$$

The simpler form of a_l compared with a_u arises from our assumption that $m_l = 1/(\gamma_{ad}-1)$, corresponding to the lower convection zone being convectively neutral.

At this point, it is convenient to introduce the first boundary condition to be used in our model. We impose the condition that the kinetic energy density of the disturbance should vanish as $z \to +\infty$. Specifically, we require that $\rho_o(z)u_z^2(z) \to 0$ as $z \to +\infty$. From the properties of confluent hypergeometric functions as z becomes large, we see that to satisfy this condition we must set $A_2 = 0$. Hence

$$\triangle = B_2 e^{-k_x(z+z_{ol}-h)}U(-a_l, m_l+2, 2k_x(z+z_{ol}-h)), \qquad z>h, \tag{3.38}$$

in the neutrally stable convection zone.

3.3.2 The atmosphere ($z < 0$)

In the magnetised atmosphere it is preferable to work directly in terms of u_z. The velocity perturbation u_z (with Fourier form (3.27)) satisfies the second order differential equation (Goedbloed 1971; Adam 1977; Roberts 1985)

$$\frac{d}{dz}\left[\frac{\rho_o(c_s^2+v_a^2)(\omega^2-k_x^2c_T^2)}{(\omega^2-k_x^2c_s^2)}\frac{du_z}{dz}\right] = \left[\frac{\rho_o g^2 k_x^2}{(\omega^2-k_x^2c_s^2)} - \rho_o(\omega^2-k_x^2v_a^2) - gk_x^2\frac{d}{dz}\left(\frac{\rho_o c_s^2}{(\omega^2-k_x^2c_s^2)}\right)\right]u_z. \tag{3.39}$$

Here, $c_s(z)$ and $v_a(z)$ denote the sound speed and Alfvén speed in the atmosphere, which at this stage may be non-isothermal. In addition to these speeds it is convenient to introduce the magnetohydrodynamic cusp (or slow mode) speed $c_T(z)$ defined by

$$c_T(z) = \frac{c_s v_a}{(c_s^2+v_a^2)^{\frac{1}{2}}}. \tag{3.40}$$

As a first study we assume that the atmosphere, like the interior, is field-free. Then Equation (3.39) with $v_a = 0$ reduces to

$$\frac{d}{dz}\left[\frac{\rho_o c_s^2\omega^2}{(\omega^2-k_x^2c_s^2)}\frac{du_z}{dz}\right] = \left[\frac{\rho_o g^2 k_x^2}{(\omega^2-k_x^2c_s^2)} - \rho_o\omega^2 - gk_x^2\frac{d}{dz}\left(\frac{\rho_o c_s^2}{(\omega^2-k_x^2c_s^2)}\right)\right]u_z. \tag{3.41}$$

Under the assumption of an *isothermal* atmosphere, Equation (3.41) further reduces to

$$\frac{d^2u_z}{dz^2} + \frac{1}{H}\frac{du_z}{dz} + A_o u_z = 0, \tag{3.42}$$

where

$$A_o = \frac{k_x\left[\Omega^2(g\Omega^2 - k_x c_{at}^2) + g(\gamma_{ad}-1)\right]}{c_{at}^2\Omega^2} \tag{3.43}$$

and H is the scale height of the atmosphere ($H = c_{at}^2/(g\gamma_{ad})$).

Equation (3.42) possesses solutions of the form

$$u_z = F_1 e^{\lambda z}, \qquad z < 0, \tag{3.44}$$

where

$$2H\lambda = -1 \pm (1 - 4A_oH^2)^{\frac{1}{2}}. \tag{3.45}$$

We make the assumption that $4A_oH^2 < 1$, for which λ is real. This introduces a cutoff frequency in the isothermal atmosphere; modes whose frequency satisfies this condition are evanescent in the atmosphere and are thus trapped in the interior of the model.

Modes which do not satisfy $4A_oH^2 < 1$ are free to propagate out of (or leak from) the atmosphere; they will not be discussed in this work.

Inspection of $4A_oH^2 = 1$ shows that the cutoff frequency $\omega = \omega_{co}$ is given by a quadratic in ω_{co}^2:

$$\omega_{co}^4 - (\omega_{ac}^2 + k_x^2 c_{at}^2)\omega_{co}^2 + g^2 k_x^2(\gamma_{ad} - 1) = 0. \tag{3.46}$$

The cutoff frequency is thus defined by

$$2\omega_{co}^2 = (\omega_{ac}^2 + k_x^2 c_{at}^2) \pm \left[(\omega_{ac}^2 + k_x^2 c_{at}^2)^2 - 4g^2 k_x^2(\gamma_{ad} - 1)\right]^{\frac{1}{2}}, \tag{3.47}$$

where ω_{ac} is the acoustic cutoff frequency for an isothermal atmosphere (Lamb 1932), given by

$$\omega_{ac}^2 = \frac{c_{at}^2}{4H^2}. \tag{3.48}$$

The choice of the sign in front of the square root in Equation (3.44) is obtained by the demand that the kinetic energy density, $\frac{1}{2}\rho_o u_z^2$, decays as $z \to -\infty$. Inspection of Equation (3.44) under this condition tells us that it is the plus sign in the parameter λ of Equation (3.45) that we require and thus

$$2H\lambda = -1 + (1 - 4A_oH^2)^{\frac{1}{2}}. \tag{3.49}$$

Now that we are equipped with the solutions for the velocity disturbance, we may apply boundary conditions across each of the interfaces at $z = 0$ and $z = h$ in order to obtain the dispersion relation relating frequencies ω and horizontal wavenumbers k_x.

3.4 The Field-Free Dispersion Relation

In Section 3.3 the boundary conditions as $z \to \pm\infty$ were applied early, for ease of presentation of the solutions. There are four remaining boundary conditions to apply and it is to those which we now turn.

The first two of the remaining conditions are simply that the vertical velocity perturbation $u_z(z)$ is continuous across each interface, i.e.

$$u_z \quad \text{is} \quad \text{continuous} \quad \text{at} \quad z = 0 \quad \text{and} \quad z = h. \tag{3.50}$$

Also, the total pressure perturbation must be continuous across $z = 0$ and $z = h$. This is equivalent to continuity of

$$\frac{\rho_o c_s^2 \omega^2}{(\omega^2 - k_x^2 c_s^2)} \frac{du_z}{dz} + \left(\frac{g k_x^2 \rho_o c_s^2}{(\omega^2 - k_x^2 c_s^2)} \right) u_z. \tag{3.51}$$

Inspection of the relation between $\triangle$ and u_z given by Equation (3.28) shows that condition (3.51) implies continuity of

$$\rho_o(z) c_s^2(z) \triangle(z) \qquad \text{at} \qquad z = h, \tag{3.52}$$

and that

$$\rho_o(z_o^+) c_s^2(z_o^+) \triangle(z_o^+) = \frac{\rho_o(z_o^-) c_s^2(z_o^-)}{(\omega^2 - k_x^2 c_s^2)} (\omega^2 \lambda + g k_x^2) u_z(z_o^-); \tag{3.53}$$

here z_o^+ is the limit as $z \to 0$ from the superadiabatic layer and z_o^- is the limit as $z \to 0$ from the atmosphere.

Application of Equations (3.50)-(3.53) to Equations (3.36), (3.38) and (3.44) leads, after much algebra, to the dispersion relation for the field-free version of this model:

$$2 k_x \Omega^2 c_s^2 a_u \gamma_{ad} (\Omega^2 \lambda + k_x) \Phi = \left[\alpha \gamma_{ad} (\Omega^2 \lambda + k_x) - \gamma_{sa} k_x (g \Omega^2 - k_x c_{at}^2)(\Omega^4 - 1) \right] \Psi, \tag{3.54}$$

where

$$\alpha = k_x c_s^2 (\Omega^2 + 1) - g \gamma_{sa} \Omega^2, \tag{3.55}$$

$$\Psi = \epsilon M(-a_u, m_u + 2, 2 k_x z_{ou}) + \delta U(-a_u, m_u + 2, 2 k_x z_{ou}), \tag{3.56}$$

$$\Phi = \delta U(1 - a_u, m_u + 3, 2 k_x z_{ou}) - \frac{\epsilon}{m_u + 2} M(1 - a_u, m_u + 3, 2 k_x z_{ou}), \tag{3.57}$$

$$\delta = \chi M(-a_u, m_u + 2, 2 k_x (h + z_{ou})) + \frac{\tau}{m_u + 2} M(1 - a_u, m_u + 3, 2 k_x (h + z_{ou})), \tag{3.58}$$

$$\epsilon = \tau U(1 - a_u, m_u + 3, 2 k_x (h + z_{ou})) - \chi U(-a_u, m_u + 2, 2 k_x (h + z_{ou})), \tag{3.59}$$

$$\tau = a_u U(-a_l, m_l + 2, 2 k_x z_{ol}) \qquad \text{and} \qquad \chi = a_l U(1 - a_l, m_l + 3, 2 k_x z_{ol}). \tag{3.60}$$

Dispersion relation (3.54) is somewhat complicated in its nature. It is the dispersion relation for a three layer model, the lower region of which supports a linear, adiabatic temperature profile over which is a thin superadiabatic region unstable to convective motions. Above the superadiabatic layer lies an isothermal atmosphere. The medium supports

not only $p-$mode solutions, but also convective modes with $\Omega^2 < 0$, which we label as $g^- - modes$. The convective modes are largely confined to the superadiabatic layer.

In the next section we shall solve Equation (3.54) for the $p-$ and g^-−modes and determine the change in their behaviour brought about by conditions changing within the superadiabatic region and the atmosphere.

3.4.1 Reduction to the purely adiabatic case

In the limit of equal temperature gradients over the two internal layers we are able to retrieve the zero-field dispersion relation for such models as investigated by Campbell and Roberts (1989), Evans and Roberts (1990) and Jain and Roberts (1994). In order to demonstrate this we set the adiabatic exponents equal in $z > 0$, i.e. $\gamma_{sa} = \gamma_{ad} = \gamma$, along with equality of the polytropic indices ($m_u = m_l = m$) and the parameter a entering the confluent hypergeometric functions ($a_u = a_l = a$).

Under this assumption, Ψ and Φ become

$$\begin{aligned}\Psi = \tau[U(e,f,Y)M(c,d,Z) + \frac{1}{d}M(e,f,Y)U(c,d,Z)] \\ +\chi[U(c,d,Z)M(c,d,Y) - U(c,d,Y)M(c,d,Z)]\end{aligned} \tag{3.61}$$

and

$$\begin{aligned}\Phi = \frac{\tau}{d}[M(e,f,Y)U(e,f,Z) - U(e,f,Y)M(e,f,Z)] \\ +\chi[M(c,d,Y)U(e,f,Z) + \frac{1}{d}U(c,d,Y)M(e,f,Z)]\end{aligned} \tag{3.62}$$

where we have set

$$\begin{aligned} c = -a, \qquad d = m+2, \qquad Z = 2k_x z_{ou} \\ e = 1-a, \qquad f = m+3, \qquad Y = 2k_x(z_{ou}+h). \end{aligned} \tag{3.63}$$

With the temperature gradients in the two layers equal, the depth of the upper layer h becomes arbitrary and hence may be set equal to zero. Then $Y = Z$ and Ψ and Φ reduce to

$$\Psi = \tau[U(e,f,Z)M(c,d,Z) + \frac{1}{d}M(e,f,Z)U(c,d,Z)] \tag{3.64}$$

and

$$\Phi = \chi[U(e,f,Z)M(c,d,Z) + \frac{1}{d}M(e,f,Z)U(c,d,Z)]. \tag{3.65}$$

From Abramowitz and Stegun (1965; 13.4.8 and 13.4.21)

$$M'(a,b,z) = \frac{a}{b}M(a+1,b+1,z) \tag{3.66}$$

and

$$U'(a,b,z) = -aU(a+1,b+1,z). \tag{3.67}$$

Equations (3.64) and (3.65) then become

$$\Psi = -\frac{\tau}{c}[M(c,d,Z)U'(c,d,Z) - U(c,d,Z)M'(c,d,Z)] \tag{3.68}$$

and

$$\Phi = -\frac{\chi}{c}[M(c,d,Z)U'(c,d,Z) - U(c,d,Z)M'(c,d,Z)]. \tag{3.69}$$

Inspection of Equations (3.68) and (3.69) indicates that Ψ and Φ are now represented by the Wronskian of the confluent hypergeometric functions. The solutions that we have are the solutions 1 and 5 of the eight presented by Abramowitz and Stegun (Abramowitz and Stegun 1965; 13.1.12 and 13.1.5). The Wronskian of these two solutions is defined by $W\{1,5\}$ given by (Abramowitz and Stegun 1965; 13.1.22):

$$W\{1,5\} = -\frac{\Gamma(d)Z^{-d}e^{Z}}{\Gamma(c)} \tag{3.70}$$

for the parameters c, d and Z defined above.

Hence we finally simplify Ψ and Φ to

$$\Psi = \frac{\tau}{c}\frac{\Gamma(d)Z^{-d}e^{Z}}{\Gamma(c)} \tag{3.71}$$

and

$$\Phi = \frac{\chi}{c}\frac{\Gamma(d)Z^{-d}e^{Z}}{\Gamma(c)}. \tag{3.72}$$

The dispersion relation (3.54) now becomes

$$\eta(\Omega^2\lambda + k_x)\chi = [\alpha(\Omega^2\lambda + k_x) - k_x(g\Omega^2 - k_x c_{at}^2)(\Omega^4 - 1)]\tau \tag{3.73}$$

where

$$\alpha = k_x c_s^2(\Omega^2 + 1) - g\gamma\Omega^2, \qquad \eta = 2k_x\Omega^2 c_s^2 a, \tag{3.74}$$

$$\tau = U(-a, m+2, 2k_x z_o) \quad \text{and} \quad \chi = U(1-a, m+3, 2k_x z_o). \tag{3.75}$$

Finally, rearranging Equation (3.73) into the form

$$\eta\frac{\chi}{\tau} = \alpha - \frac{k_x(g\Omega^2 - k_x c_{at}^2)(\Omega^4 - 1)}{(\Omega^2\lambda + k_x)} \tag{3.76}$$

provides us with the dispersion relations of Campbell and Roberts (1989), Evans and Roberts (1990) and Jain and Roberts (1994) in the zero field limit.

Parameter	Value
$T_s = T_{at}$	6500° K
T_h	30865.4° K
P_s	9000 kg m^{-1} s^{-2}
γ_{ad}	5/3
m_l	3/2
γ_{sa}	1.2
m_u	0.75
R	6425.97 $m^2 s^{-2} K^{-1}$
g	274.0 m s^{-2}
ν_{ac}	4.35 mHz
h	1000 km
z_{ou}	266.8 km
z_{ol}	1809.7 km

Table 3.1: Typical solar values used as parameters for the calculation of base frequencies and growth times in our model.

3.5 Numerical Solution of the Field-Free Dispersion Relation

The dispersion relation (3.54) may be solved numerically subject to the constraint $4A_oH^2 < 1$. As in the previous chapter, we wish to obtain a set of base frequencies for the model against which any subsequent changes in mode frequency, as a response to changing physical conditions, may be measured. Additionally, we calculate convective growth times σ (or $e-$folding times) for the unstable modes, and their sensitivity to model parameters may also be considered. To choose the parameters relevant to conditions at solar minimum we have referred to the model of Guenther *et al.* (1992), selecting for the reference levels of our model the parameter values displayed in Table 3.1.

Note from Table 3.1 that the temperature T_s that we have used is the temperature just below the photosphere, rather than that at the temperature minimum as used in the models of Campbell and Roberts (1989), Evans and Roberts (1990) and Jain and Roberts (1994). We have made this choice in an attempt to model the extent of the superadiabatic layer which does not reach as far as the temperature minimum. From the model of Guenther *et al.* (1992) we note that the Brunt-Väisälä frequency squared changes sign from negative to positive as we move upwards through the Sun at about the photospheric level, hence our choice of T_s. The choice of T_s and P_s are taken to approximate reasonably well conditions

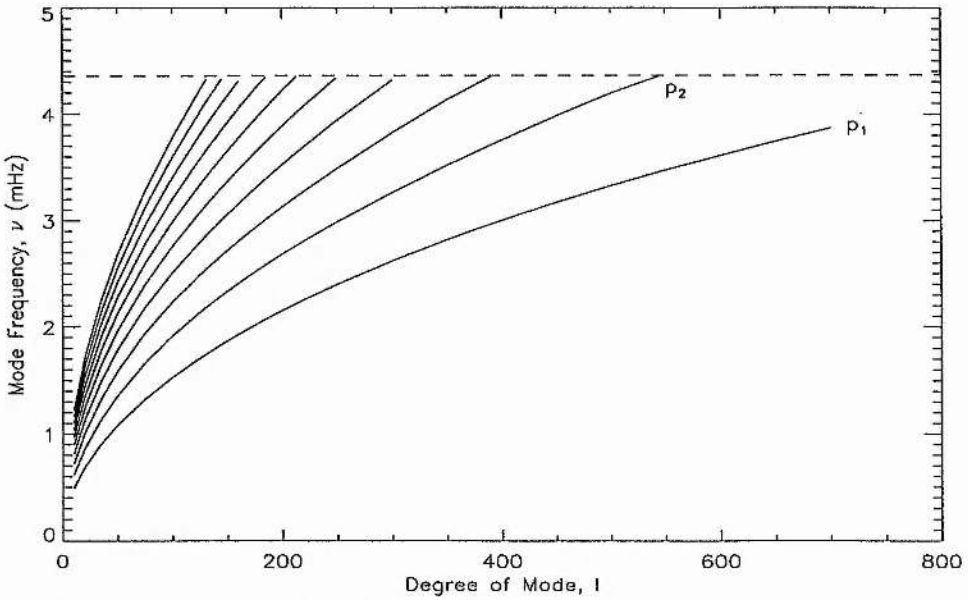

Figure 3.2: Cyclic frequency ν (in mHz) versus degree $l = 10 - 700$ for the first 10 $p-$modes. The cut-off frequency given by Equation (3.47) is shown as a dashed curve.

at this level of the atmosphere. Note also the value of T_h presented in Table 3.1. This is calculated from $T_h = T_s(1 + h/z_{ou})$ for the values of z_{ou} and h given in Table 3.1, for conditions pertaining to the solar minimum. We shall keep T_h constant while allowing the nature of the superadiabatic layer to vary through changes in m_u, T_s, z_{ou} and h.

From this base set of parameters we allow our model to evolve, in representation of the solar cycle, in the following way: as the Sun approaches its maximum, the convective efficiency of the superadiabatic layer appears to decrease by $\sim 1\%$, i.e. the region becomes more superadiabatic, with its temperature gradient moving further away from the adiabatic value. We model this effect by a *decrease* in the value of m_u. Also, following Livingston's (1978) observation that the effective photospheric temperature of the Sun falls by 6°K as the Sun approaches maximum, we allow T_s to fall by the same amount when calculating frequencies and growth rates for the model at its 'maximum'. Rewriting Equation (3.12) as

$$z_{ou} = \frac{RT_s}{g}(m_u + 1), \tag{3.77}$$

we see that a reduction in z_{ou} gives a steeper temperature profile, as required. Writing h in terms of T_s, T_h and z_{ou},

$$h = z_{ou}\left(\frac{T_h}{T_s} - 1\right), \tag{3.78}$$

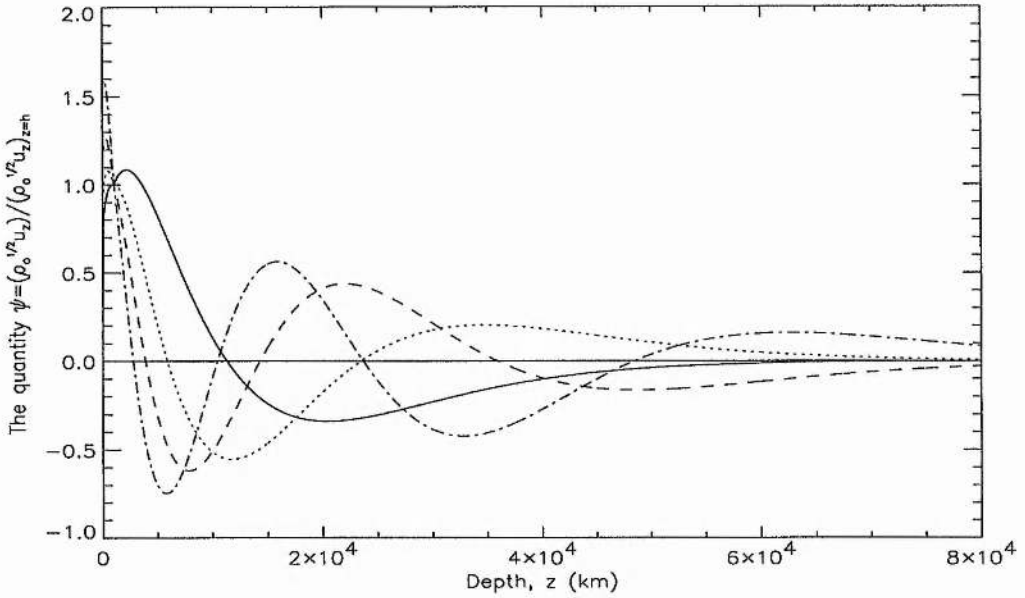

Figure 3.3: The quantity $\psi(z)$ versus depth z (in km) for the first four $p-$modes of degree $l = 100$. The $n = 1$ mode, p_1, is shown as a solid line, p_2 as a dotted line, p_3 as a dashed line and p_4 as a dot-dashed line.

it is clear that a decrease in z_{ou} leads to a thinner superadiabatic layer, representing the contraction of the superadiabatic layer at solar maximum. To investigate the above situations we study the $p-$modes and the g^-−modes separately.

3.5.1 The $p-$modes

Figure 3.2 shows the behaviour of the first ten $p-$modes calculated from Equation (3.54) for the parameters given in Table 3.1. Frequencies extend up to the cut-off frequency defined in Equation (3.47), shown as a dashed (- - - -) curve. Above the cut-off frequency modes are free to propagate into the photosphere and above and as such leak energy into that region. We confine our study to trapped modes. The curves are plotted in a continuous fashion although only integral l has any physical meaning for a sphere, of course. The standard notation n is used to label the modes; n corresponds to the number of nodes that the vertical velocity has in the vertical direction.

To illustrate the behaviour of the $p-$modes within the interior we have plotted the

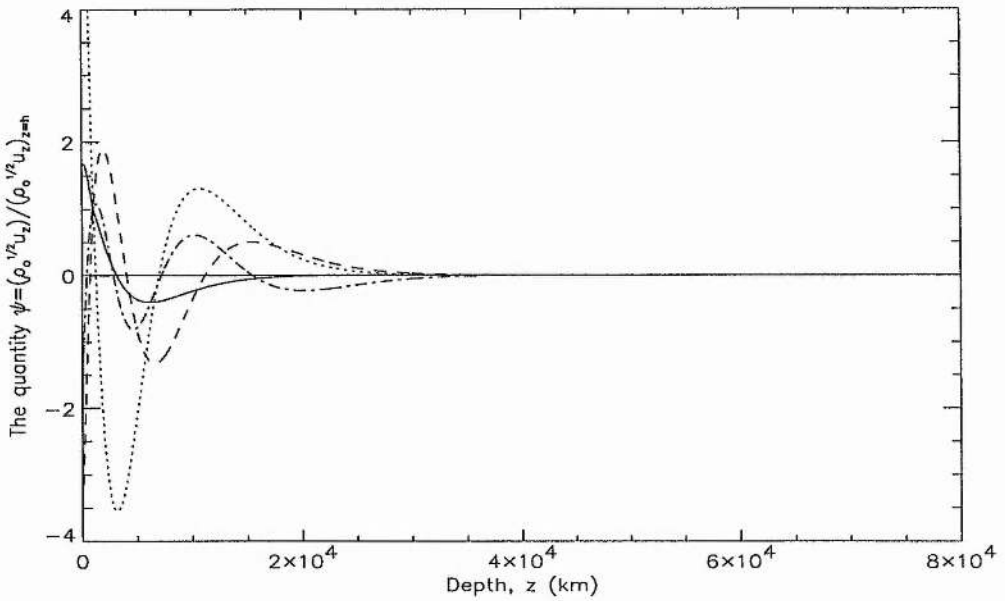

Figure 3.4: The quantity $\psi(z)$ versus depth z (in km) for the first four $p-$modes of degree $l = 300$. The $n = 1$ mode, p_1, is shown as a solid line, p_2 as a dotted line, p_3 as a dashed line and p_4 as a dot-dashed line. Note the change in scale on the vertical axis.

quantity ψ defined by

$$\psi(z) = \frac{\rho_o^{\frac{1}{2}}(z)u_z(z)}{(\rho_o^{\frac{1}{2}}u_z)_{z=h}}; \tag{3.79}$$

ψ is normalised to be unity at the level $z = h$. The quantity ψ is related to the energy density of mode, the energy density of vertical motions being $\frac{1}{2}\rho_o(z)u_z^2$ (and so $\propto \psi^2$). We consider the first four $p-$modes of degrees $l = 100$ and $l = 300$. Figure 3.3 shows ψ as a function of depth z for the $l = 100$ $p-$modes and Figure 3.4 gives the corresponding results for $p-$modes of degree $l = 300$. Modes with one radial node are displayed as solid lines and those with two radial nodes as dotted lines; modes with three radial nodes are shown as dashed lines and those with four radial nodes as dot-dashed lines. As expected, modes of degree $l = 100$ penetrate somewhat further into the solar interior than those with $l = 300$. The level at which the curves begin to show an asymptotic decay in ψ is the depth at which the modes are beginning to be strongly refracted by the increase in sound speed and are turned back towards the solar surface.

With the set of frequencies obtained for modes of various degrees l and vertical (or radial) orders n, we now turn to a study of changes in the frequencies of these modes,

m_u	h
0.74625	998 km
0.7425	996 km
0.73875	994 km
0.735	992 km

Table 3.2: The reduced values of the polytropic index m_u corresponding to a steepening of the temperature gradient in the superadiabatic layer, and the resultant thickness h of that region.

as a response to changes within the superadiabatic layer and the isothermal atmosphere.

Changes in the superadiabatic layer only

As the Sun approaches its activity maximum, the superadiabatic layer is expected to show a decrease in its convective efficiency and respond to this by contracting (Dearborn and Blake 1980). This is accompanied by a reduction in the surface temperature as energy release is somewhat inhibited. To model this and related possible changes in the superadiabatic layer we reset the temperature T_s at the surface of the model to 6494°K, 6°K cooler than the previous value for T_s, and allow the polytropic index m_u to decrease by $0.5\% - 2\%$ in steps of 0.5%. In doing this we are steepening the temperature gradient of the superadiabatic region, i.e moving it further away from the adiabatic value. The corresponding change in thickness to the superadiabatic region as a consequence of these changes is shown in Table 3.2. For the moment we are interested in variations of the superadiabatic layer only, and so the atmospheric temperature will be maintained at $T_{at} = 6500°\mathrm{K}$.

Figure 3.5 shows the effect on $p-$mode frequencies of changing m_u by the amounts given in Table 3.2, plotted against the base frequencies of Section 3.5.1. The frequency difference is calculated by

$$\triangle\nu = \nu(m_u, T_s = 6494°\mathrm{K}) - \nu(m_u = 0.75, T_s = 6500°\mathrm{K}), \tag{3.80}$$

where $\nu(m_u, T_s = 6494°\mathrm{K})$ is the frequency calculated for a decrease in convective efficiency while $\nu(m_u = 0.75, T_s = 6500°\mathrm{K})$ is the mode of corresponding radial order calculated as in Section 3.5.1. The degree l is set equal to 100. From Figure 3.5 we may see that all modes suffer a frequency *increase* as a response to the increased superadiabaticity of

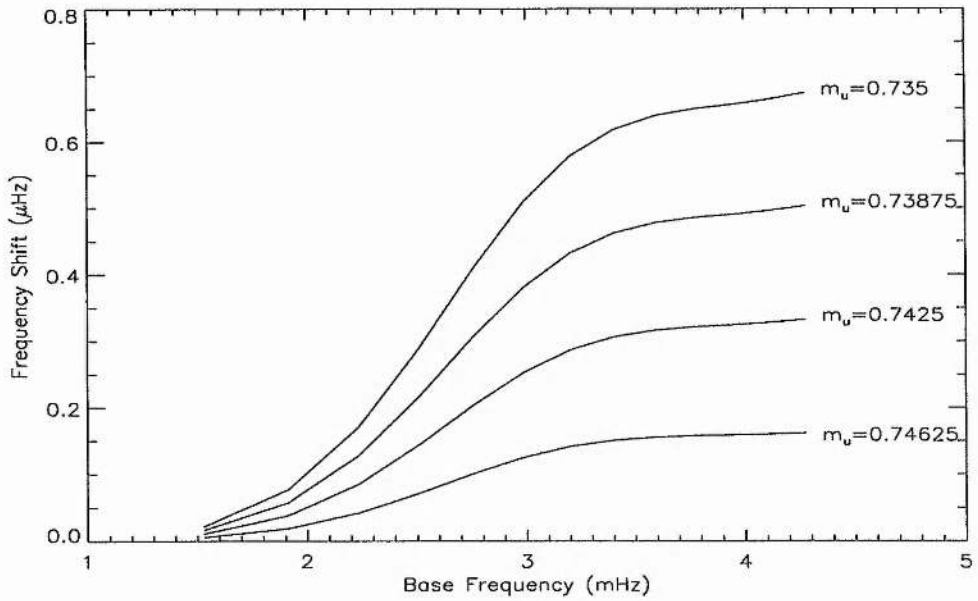

Figure 3.5: The frequency shift $\Delta\nu$ as a function of $p-$mode frequency as determined by Equation (3.80) for different values of the polytropic index m_u of the superadiabatic layer and surface temperature change from $T_s = 6500°$K to $T_s = 6494°$K.. The degree l is set equal to 100.

the convectively unstable layer. The frequency increase shows a steep rise for modes with frequencies between approximately 2-3 mHz and then levels out at frequencies above 3.4 mHz. The levelling out of the frequency increase would appear to be less pronounced with larger changes to m_u, with the curve even starting to turn slightly upwards again at around 4-4.2 mHz. The curves in Figure 3.5 extend as far as the cut-off frequency of the atmosphere, at about 4.35 mHz. Also, from Figure 3.5 we may see that an increase in the temperature gradient of the central layer gives rise to larger frequency increases the steeper it becomes.

We have also calculated the frequency difference $\Delta\nu$, by Equation (3.80), for various degrees l. For this calculation we have chosen just one reduced value of m_u, namely $m_u = 0.7425$, corresponding to a 1% increase in the temperature gradient of the superadiabatic layer. Figure 3.6 shows that for all values of l there is an increase in mode frequency with $\Delta\nu$ increasing with increasing ν. The effect is larger with increasing l. The flattening out of the frequency increase, however, begins to take effect at higher ν for higher l.

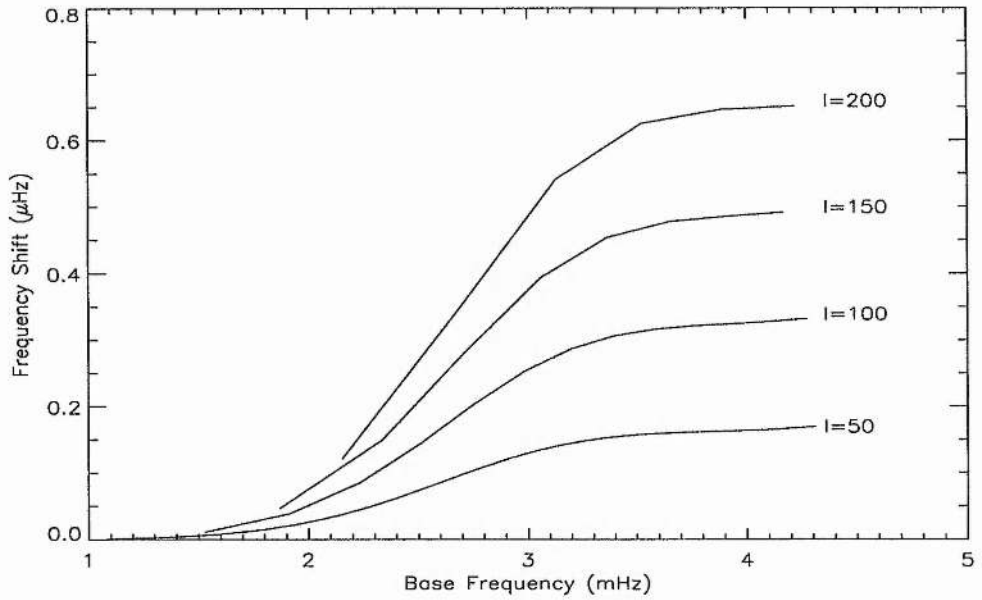

Figure 3.6: The frequency shift $\Delta\nu$ as a function of $p-$mode frequency ν as determined by Equation (3.80) for modes of degree $l = 50$, 100, 150 and 200.

Atmospheric changes coupled with steepening temperature gradients

We have described in Section 3.2 how the Sun is believed to cool slightly at the surface and to contract marginally as it reaches its activity maximum and therefore show a decrease in luminosity. However, although the Sun reacts very rapidly to the new hydrostatic equilibrium that these changes dictate it takes much longer to reach the new thermal equilibrium involved. How can we apply this to the model presented here? With the plane-parallel model that we are using which is infinite in extent it is obviously not possible to model a reduction of the solar radius but we may mimic this somewhat by allowing the superadiabatic layer to contract, supposing that this is the only part of the Sun to alter its structure and give a measurable change. How does the atmosphere behave though?

Imagine a spherical Sun with the properties of our model and assume that there is no fluid movement across the interface at $z = 0$ and that the gas pressure is continuous at this level. Then a decrease in radius will require a higher plasma density in the interior, and as a response, from Equation (3.5) there will be a decrease in the temperature to maintain the same gas pressure. The plasma in the layers above this level, however, finds itself more rarefied. In order to maintain hydrostatic balance, therefore, the temperature of the outer layers must increase by a certain amount.

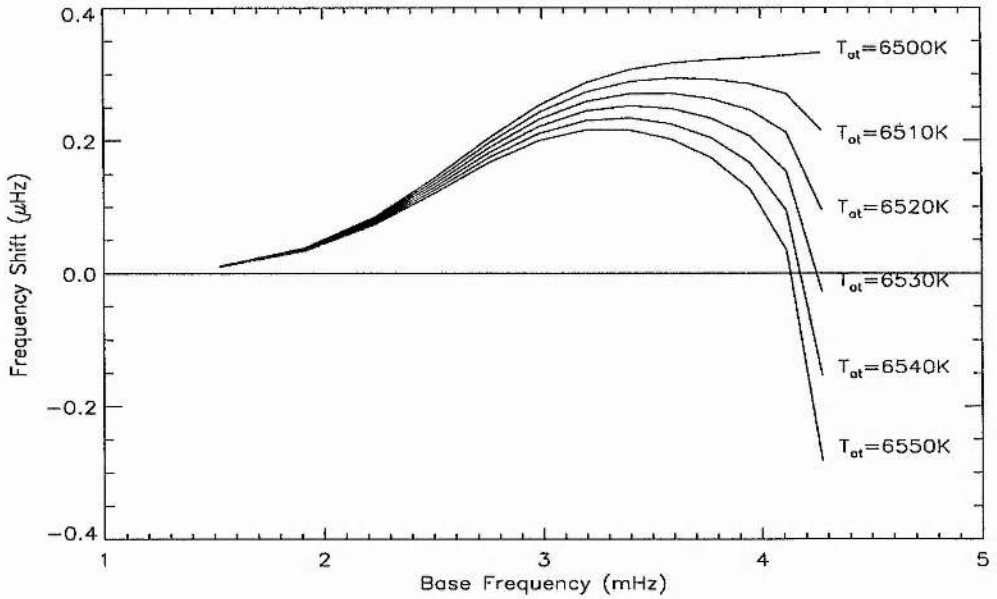

Figure 3.7: The frequency shift $\Delta\nu$ given by Equation (3.81) as a function of base mode frequency ν. The value of the polytropic index of the superadiabatic layer is decreased by 1% while the temperature of the atmosphere T_{at} is increased.

Obviously, the real Sun does not suddenly contract and expand in this way, but as an attempt to model such possible effects we now introduce increases in atmospheric temperature to accompany the changes in the superadiabatic layer discussed earlier. We consider frequency shifts $\Delta\nu$ determined by

$$\Delta\nu = \nu(m_u = 0.7425, T_s = 6494^{\circ}\mathrm{K}, T_{at}) - \nu(m_u = 0.75, T_s = 6500^{\circ}\mathrm{K} = T_{at}) \qquad (3.81)$$

where $\nu(m_u = 0.7425, T_s = 6494^{\circ}\mathrm{K}, T_{at})$ is the mode frequency calculated for a decrease in convective efficiency coupled with a rise in atmospheric temperature T_{at} and $\nu(m_u = 0.75, T_s = 6500^{\circ}\mathrm{K}, T_{at} = 6500^{\circ}\mathrm{K})$ are the base frequencies determined for modes of an equivalent radial order (as found in Section 3.5.1). Atmospheric temperatures of 6510°K, 6520°K, 6530°K, 6540°K, and 6550°K are taken. Figure 3.7 displays $\Delta\nu$ plotted against $\nu(m_u = 0.75, T_s = 6500^{\circ}\mathrm{K}, T_{at} = 6500^{\circ}\mathrm{K})$. Figure 3.7 shows that there is a steep initial increase in mode frequency up to frequencies of around 3.3 mHz followed by a downturn in $\Delta\nu$ for frequencies above this value. The rise in frequency is inhibited by increasing atmospheric temperatures while the plunge in frequency shift is felt more strongly. In fact, above frequencies of 4 mHz some modes suffer a frequency decrease for a certain increase in T_{at}. Again, the curves extend as far as the cut-off frequency for the model. A discussion

of these results will be presented in Section 3.7.

3.5.2 The convective modes (g^-−modes)

With the introduction of a superadiabatic layer into the model we have allowed for the possibility of convective modes to occur, owing to the unstable nature of this region. Modes of this type are found as solutions to Equation (3.54) with $\Omega^2 < 0$. Figure 3.8 shows the results of solving Equation (3.54) for $\Omega^2 < 0$, for horizontal wavenumber k_x ranging from 0.14-2.9 Mm^{-1} (corresponding to l ranging from 100 to 2000). From Figure 3.8 we see that a family of convective modes is present with very small squared angular frequencies. The modes form an anti-Sturmian sequence: $|\omega_1^2| > |\omega_2^2| > ... > |\omega_n^2| > |\omega_{n+1}^2|$, where n is the radial order of the mode and the sequence has the property that $|\omega_n^2| \to 0$ as $n \to \infty$ for a given k_x. Also, we may see that for a given radial order n, $|\omega^2|$ increases as k_x increases. As $k_x \to 0$, $\omega^2 \to 0$ which is to be expected as it is known that no disturbance with buoyancy as its restoring force may operate in a purely radial direction (Lamb 1932). We have used the notation g_m^- to describe the mode order of the convective modes, with the number of convective rolls within the superadiabatic zone being m (and the number of nodes measured in the vertical direction of the vertical flow, is $n = m - 1$).

The spectra of frequencies given in Figure 3.8 correspond to growth times (or e−folding times) σ ($\sigma = 1/(i\omega * 60)$ for σ in minutes) for each of these modes. The e−folding time is the time it takes for a disturbance to grow by a factor of e. The growth times σ associated with the angular frequencies of Figure 3.8 are shown in Figure 3.9. Growth times (in minutes) are plotted against horizontal wavenumber k_x (Mm^{-1}). From Figure 3.9 we see that for a given k_x, the growth time σ increases for increasing radial order n. For a specific mode of convection, g_n^-, the growth time decreases as k_x increases and as $k_x \to 0$, $\sigma \to \infty$ for all g_n^-.

It is of interest to examine the behaviour of these modes within the interior of the model. In order to achieve this, we once again plot ψ (related to the normalised radial energy density of the modes), given by Equation (3.79). Figure 3.10 shows ψ plotted against depth, z. The horizontal wavenumber k_x is approximately 0.14 Mm^{-1} (corresponding to $l = 100$) and the first three convective modes are displayed. The solid line represents the g_1^-−mode, the dotted line the g_2^-−mode and the dashed line denotes the g_3^-−mode. The turnover motion of the modes is largely confined to the superadiabatic layer, i.e. the first

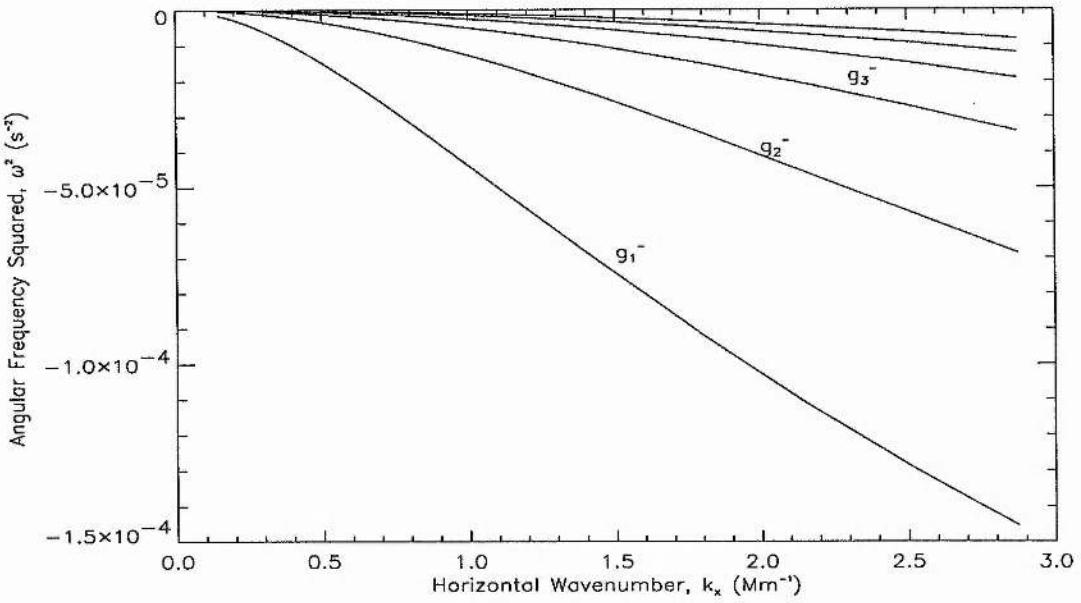

Figure 3.8: The angular frequency squared ω^2 (s^{-2}) plotted against horizontal wavenumber k_x (Mm^{-1}) for the first six modes of convection produced by the superadiabatic layer. The notation used corresponds to the order of the modes, m. The number of nodes in the vertical velocity component is given by $n = m - 1$.

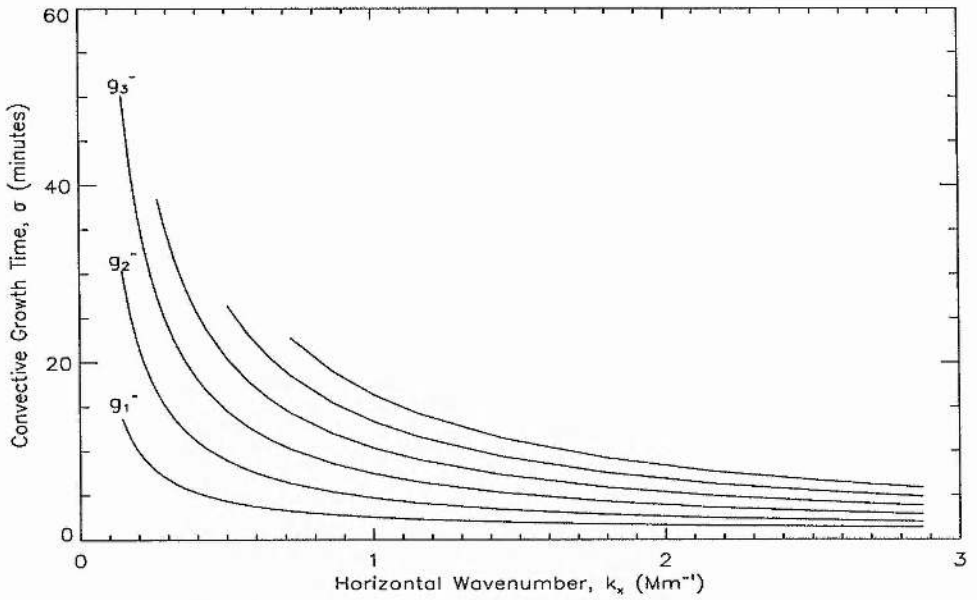

Figure 3.9: The growth times σ (in minutes) associated with the angular frequencies presented in Figure 3.8 plotted against horizontal wavenumber k_x.

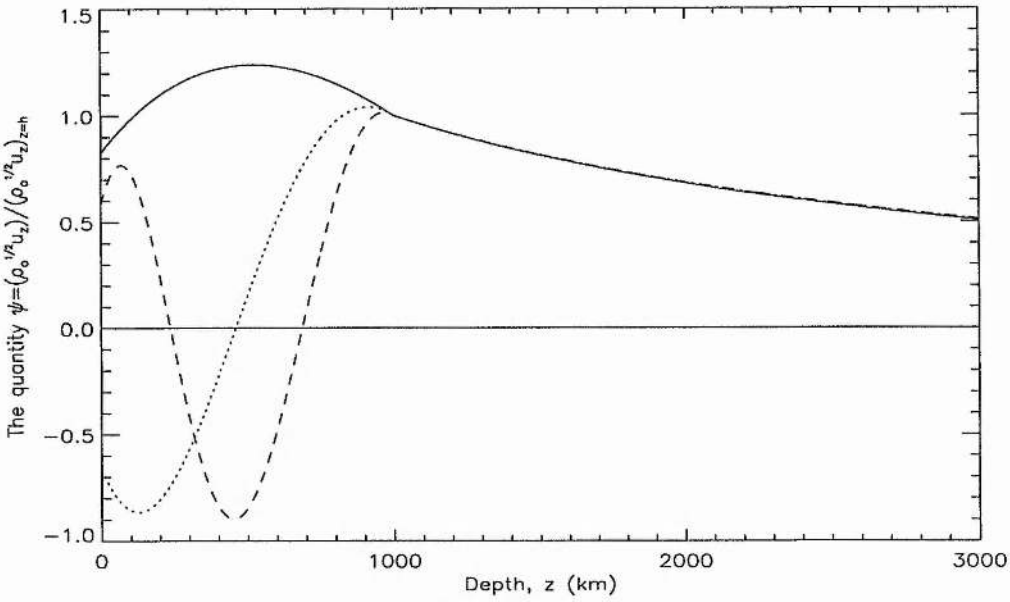

Figure 3.10: A plot of ψ against depth z. The first three unstable modes are shown for a horizontal wavenumber $k_x = 0.14$ Mm^{-1}. The g_1^-−mode is denoted by a solid line, the g_2^-−mode as a dotted line and the g_3^-−mode as a dashed line.

1000 km, with an approximately exponential decay of the energy density below this depth. From Figure 3.10 we see that the decay of the energy density (which is proportional to ψ^2) appears to be at the same rate for all modes in the stable bulk of the convection zone.

From Figure 3.10 we may view the nodes in ψ (and so in the radial energy density of vertical motions) as being the depth at which a turnover in the direction of the convective rolls takes place, i.e. where motions are purely horizontal. Note the abrupt change in the behaviour of the modes at the boundary between the two regions. This discontinuity in the gradient of ψ is understandable because both ρ_o and u_z, although continuous at $z = h$, do not have continuous gradients at this point.

To compare with Figure 3.10 we have also plotted ψ for convective modes of horizontal wavenumbers $k_x \approx 1$ Mm^{-1} and 2 Mm^{-1} (corresponding to $l = 700$ and $l = 1500$, respectively). Figure 3.11 shows ψ plotted against depth z for $k_x \approx 1$ Mm^{-1} and Figure 3.12 the same quantity for modes with $k_x \approx 2$ Mm^{-1}. Again the g_1^-, g_2^-, and g_3^-−modes are denoted by solid, dotted and dashed lines, respectively, but in Figures 3.11 and 3.12 we have also plotted the g_4^-−mode (as a dot-dashed line). Note the change in vertical scale between the two figures. From Figures 3.11 and 3.12 we may see that the general behaviour of the

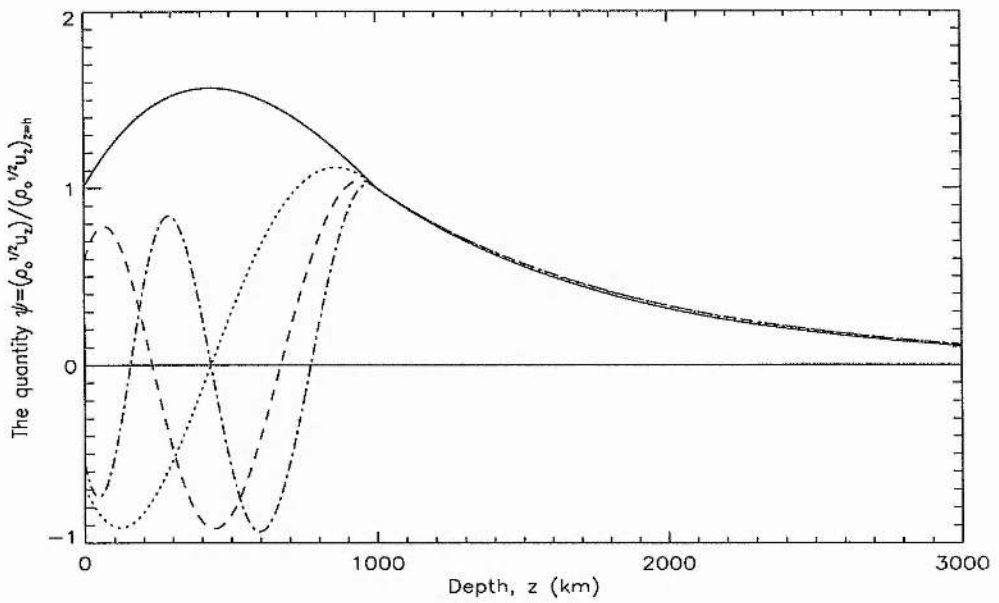

Figure 3.11: As in Figure 3.10 but with $k_x = 1$ Mm^{-1}. Also, the g_4^-−mode has been plotted as a dot-dashed line. Note the change in vertical scale.

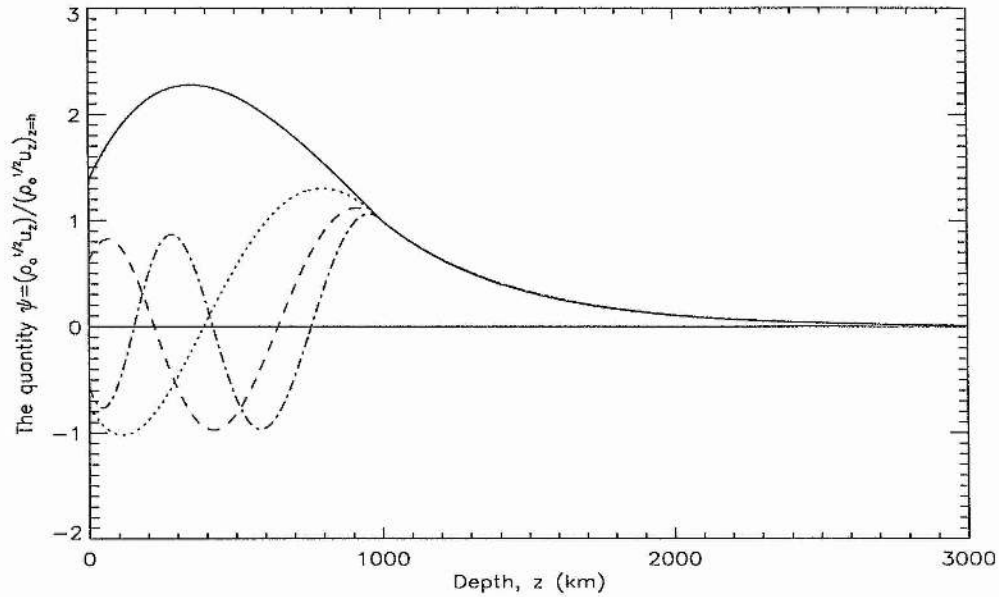

Figure 3.12: As in Figure 3.11 but with $k_x = 2.15$ Mm^{-1}. Note the change of scale along the vertical axis.

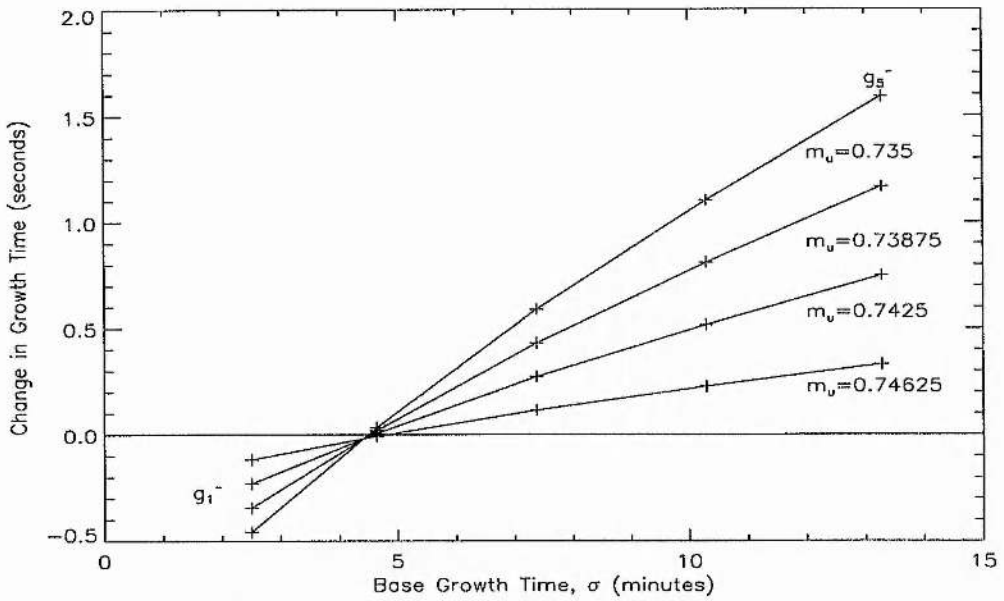

Figure 3.13: The change in convective growth time, $\triangle\sigma$ (in seconds), plotted against the base growth time σ (in minutes), as given by Equation (3.82). The horizontal wavenumber is set to 1 Mm^{-1} and $\triangle\sigma$ is shown for g_n^-, $n = 1 - 5$. Note that the specific modes are indicated by crosses (+).

modes for various k_x is qualitatively similar. Of interest though is that for larger horizontal wavenumber k_x (corresponding to smaller horizontal wavelength), we would expect a higher ratio of the energy density to be contained in the superadiabatic layer. However, only the g_1^-−modes display any great change in the magnitude of ψ in the upper region, while the overtones show only a marginal increase in ψ as k_x increases.

Finally, note in Figures 3.10-3.12 that the nodes of ψ, i.e. the position of purely horizontal plasma motion, are positioned almost exactly equally for each g_n^-, independent of wavenumber k_x. Hence the depth of penetration for each convective element with a specific order n is the same regardless of the horizontal structure of the mode. A similar result has also been noted by Smeyers (1970) in a numerical study of the convective modes of the outer solar envelope.

Changes to the superadiabatic layer

In a treatment similar to that used for the p−modes, it is of interest to investigate the response of the convective growth times σ to changes in various physical parameters

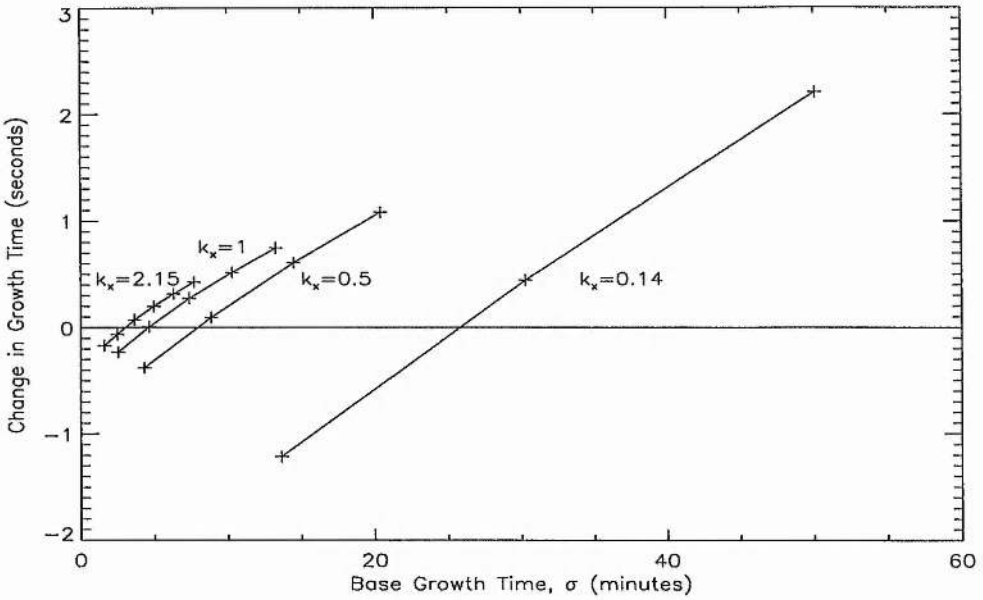

Figure 3.14: Changes in convective growth times (in seconds) plotted as a function of base growth times (in minutes) for a 1% decrease in m_u. The values of k_x used are 0.14 Mm^{-1} (three modes shown), 0.5 Mm^{-1} (four modes shown), 1 Mm^{-1} (five modes shown) and 2.15 Mm^{-1} (six modes shown). The specific modes are shown as crosses (+).

in the model, chosen to represent the evolution of the Sun over its cycle. Initially we vary the value of the polytropic index m_u of the superadiabatic layer, in order to change the temperature gradient of that region; specifically, steepening the temperature gradient in the upper layer of the interior by lowering m_u by $0.5\% - 2\%$, in order to reduce the convective efficiency of the layer. At the same time, the surface temperature T_s at $z = 0$ will be lowered by 6^oK, in accordance with the observations of Livingston (1978). No alterations to the structure of the atmosphere will be made at this point. We may then compare the growth times found for these conditions with the base growth times found earlier. The values of m_u used in this section, along with the resultant thickness of the superadiabatic layer, are displayed in Table 3.2.

Figure 3.13 presents the results of the calculated change in growth time $\triangle\sigma$ for modes with $k_x \approx 1$ Mm^{-1}, where

$$\triangle\sigma = \sigma(m_u, T_s = 6494^o\mathrm{K}) - \sigma(m_u = 0.75, T_s = 6500^o\mathrm{K}). \tag{3.82}$$

The growth time of modes for the model representing solar minimum are given by $\sigma(m_u = 0.75, T_s = 6500^o\mathrm{K})$ and those representing growth times at solar maximum by $\sigma(m_u, T_s =$

6494°K). In Figure 3.13, $\triangle\sigma$ (in seconds) is plotted against $\sigma(m_u = 0.75, T_s = 6500°\text{K})$ (in minutes) and the first five convective modes are illustrated, the specific modes being indicated by crosses (+). The horizontal wavenumber $k_x = 1$ Mm^{-1} (corresponding to $l = 700$). Changes to m_u are taken in 0.5% intervals, ranging from 0.5% to 2%. Figure 3.13 shows that the magnitude of the change in growth time is greater for a larger variance of m_u. Of most interest though is that while the g_3^- to g_5^-−modes display an increase to their respective growth times, the g_1^-−mode displays a decrease in the time of its growth of up to half a second. Also, the g_2^-−mode displays a decrease in its growth time for small changes to m_u, changing to an increase in σ as m_u is further reduced For the g_3^- to g_5^-−modes the suppression of their e−folding time is what we would expect as the convective efficiency of the superadiabatic region has been reduced but as to why the growth time of the g_1^-−mode should be quickened remains unclear.

Also, the change in growth time given by Equation (3.82) has been calculated for a range of horizontal wavenumbers. For this calculation we have chosen a 1% steepening of the temperature gradient of the superadiabatic layer. We have taken k_x equal to 0.14 Mm^{-1}, 0.5 Mm^{-1}, 1 Mm^{-1} and 2.15 Mm^{-1}, and the results are plotted in Figure 3.14. Figure 3.14 shows that some modes experience a suppression of their growth times whilst others show an enhancement. Also, the range of $\triangle\sigma$ is narrowed with increasing k_x and we have illustrated this further by showing in Figure 3.14 $\triangle\sigma$ for the first three modes for $k_x = 0.14$ Mm^{-1}, the first four modes for $k_x = 0.5$ Mm^{-1}, the first five modes for $k_x = 1$ Mm^{-1} and the first six modes for $k_x = 2.15$ Mm^{-1}.

Additional effects from T_{at} changes

As a final study into purely thermal effects on g^-−mode growth times we now allow the temperature of the atmosphere T_{at} to vary along with the changes made to the superadiabatic layer (as discussed above). Figure 3.15 shows the results of calculating the change in convective growth times $\triangle\sigma$ given by

$$\triangle\sigma = \sigma(m_u, T_s = 6494°\text{K}, T_{at}) - \sigma(m_u = 0.75, T_s = 6500°\text{K} = T_{at}), \tag{3.83}$$

where $\sigma(m_u, T_s = 6494°\text{K}, T_{at})$ is the growth time of a mode at solar maximum coupled with a rise in atmospheric temperature and $\sigma(m_u = 0.75, T_s = 6500°\text{K} = T_{at})$ is the corresponding mode at solar minimum. The results in Figure 3.15 are plotted against $\sigma(m_u = 0.75, T_s = 6500°\text{K} = T_{at})$ with $k_x = 1$ Mm^{-1}. Atmospheric temperatures of

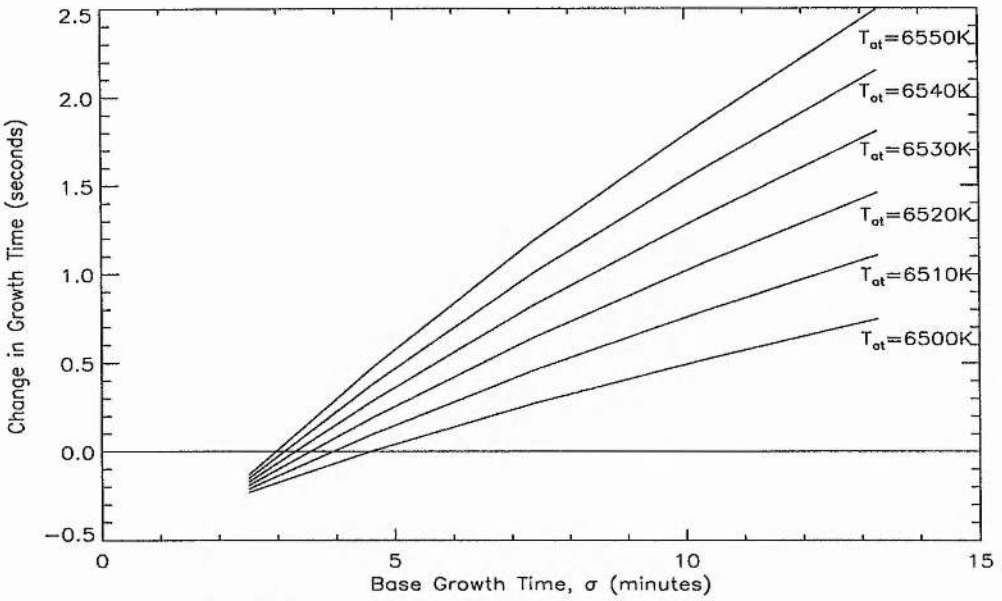

Figure 3.15: The values of $\triangle\sigma$ plotted against σ as calculated from Equation (3.83). The horizontal wavenumber $k_x = 1$ Mm^{-1} and the atmospheric temperature T_{at} is allowed to rise from 6500°K to 6550°K in intervals of 10°K.

6510°K, 6520°K, 6530°K, 6540°K and 6550°K are taken. Figure 3.15 shows that the effect of additionally raising T_{at} once again gives a *decrease* in the growth time of the g_1^-−mode and an *increase* to the growth time of higher order modes but the overall effect is somewhat different to only altering the properties of the superadiabatic layer. Whereas in Figure 3.13 the magnitude of $\triangle\sigma$ increased for all modes with decreasing m_u, Figure 3.15 displays an higher increase to the growth time of the overtones with higher atmospheric temperatures and a *decrease* to the quickening of the growth time of the g_1^-−mode.

3.5.3 Summary of thermal effects

We have seen that a steepening of the temperature gradient in the superadiabatic layer combined with a cooling of the surface temperature T_s by 6°K leads to an *increase* in the p−mode frequencies. The rise in frequency is shallow for low frequencies, steepening through the mid-range of frequencies and finally levelling off at high frequencies (above 3.3 mHz). The frequency increase is enlarged as the convective efficiency of the superadiabatic layer is decreased, and higher l modes are influenced more than those of lower l. When an increase in atmospheric temperature T_{at} is also applied the same behaviour is seen with

regards to a slow increase at low frequencies and the steep rise in the mid-range, but we now see the observed maximum of the frequency increase followed by a steep downturn at high frequency. The shifts at high frequency may even become negative for sufficiently high atmospheric temperatures.

The g^-−modes show different responses to changes in model parameters. With a steepening temperature gradient in the superadiabatic layer and $T_s = 6494^o$K, the g_1^-−mode shows an enhancement of its growth time, with σ getting smaller as m_u is decreased. The overtones, however, all show a suppression of their motions, with a sufficient decrease in m_u, with their growth times being increased. When these changes are combined with a rise in T_{at} the same qualitative behaviour of the g^-−modes is observed except that for higher atmospheric temperatures the enhancement of the g_1^-−mode is *lessened* and the overtones are suppressed further. The overall effect is magnified with higher atmospheric temperatures.

3.6 Additional Effects of a Magnetic Atmosphere

With the fact that magnetic activity increases on the Sun as it approaches maximum, it is obviously of interest to investigate the additional changes to ν and σ imposed by a magnetic field. We assume the interior of the model is entirely free of magnetic fields. The reference level $z = 0$ has been chosen to represent conditions just below the photosphere. We follow the work of Evans and Roberts (1990) and Jain and Roberts (1994) in applying a uniform *horizontal* magnetic field in the atmosphere. We appreciate that this is only a crude representation of the effects of magnetic fields at this level in the atmosphere.

We therefore model a horizontal uniform magnetic field of the form $\mathbf{B_o} = B_o\hat{\mathbf{x}}$ as an equilibrium which implies an Alfvén speed that grows exponentially with height. The rather extreme effects of a magnetic field configuration of this type will be considered for both the p−modes and g^-−modes.

3.6.1 The dispersion relation

Under the velocity disturbance given by Equation (3.27), the magnetohydrodynamic equations, Equations (3.20)-(3.26), provide us with the governing differential equa-

tion for u_z, namely Equation (3.39):

$$\frac{d}{dz}\left[\frac{\rho_o(c_s^2+v_a^2)(\omega^2-k_x^2c_T^2)}{(\omega^2-k_x^2c_s^2)}\frac{du_z}{dz}\right]$$
$$=\left[\frac{\rho_o g^2k_x^2}{(\omega^2-k_x^2c_s^2)}-\rho_o(\omega^2-k_x^2v_a^2)-gk_x^2\frac{d}{dz}\left(\frac{\rho_o c_s^2}{(\omega^2-k_x^2c_s^2)}\right)\right]u_z. \tag{3.84}$$

For an atmosphere which is isothermal, stratified under gravity and permeated by a horizontal magnetic field, the Alfvén speed squared is given by

$$v_a^2(z)=v_{ao}^2e^{\frac{-z}{H}}, \tag{3.85}$$

where $v_{ao}^2(\equiv\frac{B_o^2}{\mu\rho_{at}})$ is the square of the Alfvén speed at the base of the atmosphere. With the form of the Alfvén speed squared given by Equation (3.85), along with the constant sound speed of the atmosphere, c_{at}, Equation (3.84) reduces to

$$[A_1+A_2\exp(-A_3z)]\frac{d^2u_z}{dz^2}+A_1A_3\frac{du_z}{dz}+\left[A_4-k_x^2A_2\exp(-A_3z)\right]u_z=0, \tag{3.86}$$

where

$$A_1=\omega^2c_{at}^2, \qquad A_2=v_{ao}^2(\omega^2-k_x^2c_{at}^2), \qquad A_3=H^{-1},$$
$$A_4=(\gamma_{ad}-1)g^2k_x^2+\omega^2(\omega^2-k_x^2c_{at}^2). \tag{3.87}$$

Under the transformation (Adam 1975; Nye and Thomas 1976a)

$$\zeta=\frac{-A_1}{A_2}\exp(A_3z), \qquad V=u_z\zeta^{\frac{-k_x}{A_3}}, \tag{3.88}$$

Equation (3.84) may be recast in the form of a hypergeometric equation:

$$\zeta(1-\zeta)\frac{d^2V}{d\zeta^2}+[r-(p+q+1)\zeta]\frac{dV}{d\zeta}-pqV=0, \tag{3.89}$$

where

$$p+q=\frac{2k_x}{A_3}+1, \qquad pq=\frac{k_x}{A_3}\left(\frac{k_x}{A_3}+1\right)+\frac{A_4}{A_1A_3^2}, \qquad r=p+q=\frac{2k_x}{A_3}+1. \tag{3.90}$$

Around the point $\zeta=0$, the general solution to Equation (3.89) is (Abramowitz and Stegun; 15.5.3 and 15.5.4)

$$V=C_1F(p,q;r;\zeta)+C_2\zeta^{1-r}F(p-r+1,q-r+1;2-r;\zeta), \tag{3.91}$$

where C_1 and C_2 are arbitrary constants and F is the hypergeometric function.

In terms of the original variables, the solutions to Equation (3.91) may be written as

$$u_z = C_1 e^{k_x z} F(p, q; r; \frac{-A_1}{A_2} e^{A_3 z}) + C_2 e^{-k_x z} F(p - r + 1, q - r + 1; 2 - r; \frac{-A_1}{A_2} e^{A_3 z}). \tag{3.92}$$

Once again, it is the trapped modes of the system that we are interested in, and as such both the kinetic and magnetic energy densities must vanish as $z \to -\infty$ ($\zeta \to 0$). The magnetic energy density, E_B, of the perturbation is given by

$$E_B = \frac{(\mathbf{B_o} + \mathbf{b})(\mathbf{B_o} + \mathbf{b})}{\mu} - \frac{\mathbf{B_o}^2}{2\mu}, \tag{3.93}$$

which, when linearised, reduces to

$$E_B = \frac{b_x B_o}{\mu}. \tag{3.94}$$

From the induction equation, Equation (3.23), the horizontal component of the magnetic field perturbation b_x is given by

$$i\omega b_x = -B_o \frac{du_z}{dz}; \tag{3.95}$$

hence the magnetic energy is defined by

$$E_B = \frac{i}{\omega} \frac{B_o^2}{\mu} \frac{du_z}{dz}. \tag{3.96}$$

Then, using the result (Abramowitz and Stegun 1965; 15.2.1)

$$\frac{d}{dz} F(a, b; c; z) = \frac{ab}{c} F(a + 1, b + 1; c + 1; z) \tag{3.97}$$

it is easy to show that E_B vanishes as $z \to -\infty$ only if $C_2 = 0$. Therefore

$$u_z = C_1 e^{k_x z} F(p, q; r; \frac{-A_1}{A_2} e^{A_3 z}). \tag{3.98}$$

The solution given by Equation (3.98) may now be matched onto the solutions for the interior given by Equations (3.32) and (3.38). To accomplish this, the boundary conditions given by Equations (3.50) and (3.52) are applicable once more but in order for the total pressure perturbation P_T to be continuous at $z = 0$ we demand the continuity of

$$\frac{\rho_o (c_s^2 + v_a^2)(\omega^2 - k_x^2 c_T^2)}{(\omega^2 - k_x^2 c_s^2)} \frac{du_z}{dz} + \left(\frac{\rho_o g k_x^2 c_s^2}{\omega^2 - k_x^2 c_s^2} \right) u_z \qquad \text{across} \qquad z = 0. \tag{3.99}$$

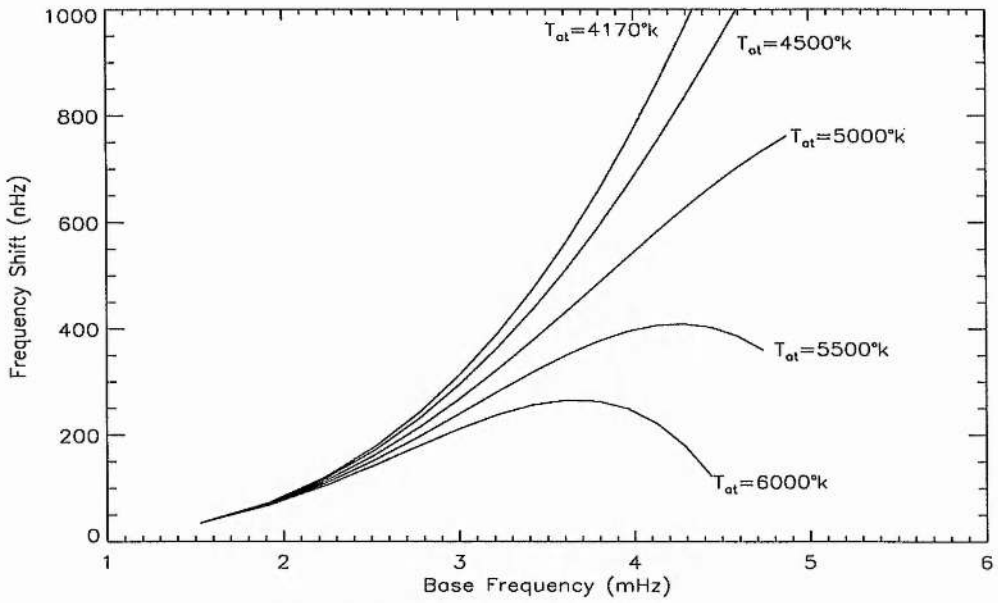

Figure 3.16: Frequency shifts $\triangle\nu$ (in nHz) for atmospheric field changes from 40G to 50G accompanied by simultaneous atmospheric temperature increases from 4170°K to T_{at} = 4170°K, 4500°K, 5000°K, 5500°K and 6000°K. The adiabatic indices γ_{sa} and $\gamma_{ad} = 5/3$ and $m_u = m_l = 3/2$. The degree $l = 100$. We recover the results given in Figure 3.7 of Jain (1994) for conditions corresponding to those at the temperature minimum at $z = 0$.

Application of Equations (3.50), (3.52) and (3.99) provides us with the dispersion relation for the model:

$$\sigma\Gamma_{ad}\left[1+\frac{(1+\beta)}{g\beta}(g\Omega^2-k_xc_{To}^2)Z_{01}\right]\Phi$$
$$=\left\{\alpha\Gamma_{ad}\left[1+\frac{(1+\beta)}{g\beta}(g\Omega^2-k_xc_{To}^2)Z_{01}\right]-\gamma_{sa}(\Omega^4-1)(g\Omega^2-k_xc_{at}^2)\right\}\Psi, \qquad (3.100)$$

where

$$\Gamma_{ad}=\frac{2\beta\gamma_{ad}}{2\beta+\gamma_{ad}}, \qquad (3.101)$$

$$Z_{01}=1-\frac{1}{k_x}\frac{pq}{r}\frac{A_1A_3}{A_2}\frac{F(p+1,q+1;r+1;\frac{-A_1}{A_2})}{F(p,q;r;\frac{-A_1}{A_2})}, \qquad (3.102)$$

and Ψ and Φ are defined by Equations (3.56) and (3.57), respectively.

Equation (3.100) is the dispersion relation for a model consisting of three layers of fluid stratified under gravity. The lower region is thermally stratified in such a way so as to maintain convective stability, while the layer above this contains a steeper temperature

gradient in order to make the fluid convectively unstable. The uppermost plasma layer is isothermal and permeated by a horizontal uniform magnetic field. A numerical study of dispersion relation (3.100) is now undertaken to investigate the additional changes incurred by the presence of a magnetic atmosphere.

3.6.2 Magnetic effects on the p–modes

To set the scene for our investigation it is convenient to examine the case of the interior layer being entirely stable to convective motions. In this way we expect to reproduce the results of Jain (1994) and Jain and Roberts (1994). To accomplish this it is necessary to set $\gamma_{sa} = \gamma_{ad} = 5/3$ and $m_u = m_l = 3/2$. Additionally, at the reference level $z = 0$ we set conditions equal to those at the temperature minimum, i.e. $T_s = 4170°\mathrm{K}$ and $P_s = 86.82$ kg m^{-1} s^{-2}. These are the conditions considered by Jain and Roberts (1994). Frequency changes $\triangle\nu$ imposed by a magnetic atmosphere are then calculated according to

$$\triangle\nu = \nu(B_o = 50\mathrm{G}, T_{at}) - \nu(B_o = 40\mathrm{G}, T_{at} = 4170°\mathrm{K}), \tag{3.103}$$

where $\nu(B_o = 40\mathrm{G})$ is the mode frequency calculated for a field strength of 40G and an atmospheric temperature equal to that at the temperature minimum and $\nu(B_o = 50\mathrm{G}, T_{at})$ is the corresponding mode frequency with the magnetic field strength increased to 50G and atmospheric temperatures T_{at} of 4170°K, 4500°K, 5000°K, 5500°K and 6000°K are considered.

The results of solving Equation (3.103) are shown in Figure 3.16 where we have plotted $\triangle\nu$ against $\nu(B_o = 40\mathrm{G}, T_{at} = 4170°\mathrm{K})$. The degree of the modes is set equal to 100. Figure 3.16 is identical in form to Figure 3.7 of Jain (1994) and qualitatively similar to the results of Jain and Roberts (1994), showing an increase in frequency of the modes at all frequencies with the characteristic maximum and subsequent downturn when higher chromospheric temperatures are applied.

We now reset the parameters for the interior of the model back to those given in Table 3.1 so that we may consider the combination of the effects of a magnetic atmosphere with variations in the superadiabatic layer.

To begin this investigation we consider the effect of an evolving magnetic field at conditions appropriate as a representation of the 'solar maximum'. We assume that the temperature gradient of the superadiabatic layer has already steepened by 1% over the

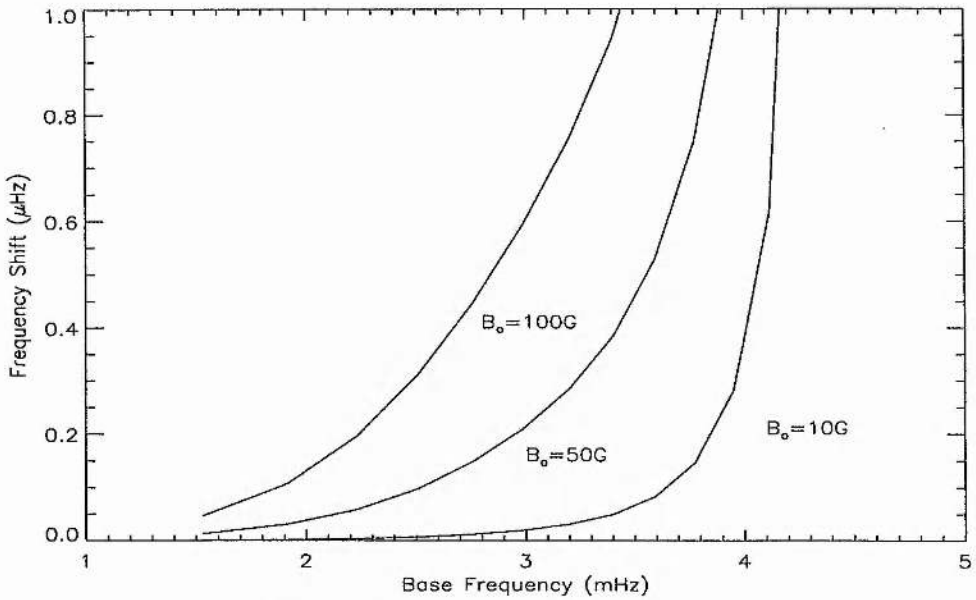

Figure 3.17: The change in $p-$mode frequencies for modes of degree $l = 100$, according to Equation (3.103). Magnetic field strengths of 10G, 50G and 100G are used. The base frequencies against which $\triangle\nu$ is plotted are calculated for $B_o = 0$ but with parameters of the superadiabatic layer at the model 'maximum' ($m_u = 0.7425, T_s = 6494°\mathrm{K}$).

'minimum' value and that the surface temperature has dropped by 6°K. To begin with we consider magnetic effects only, keeping the atmospheric temperature T_{at} fixed at 6500°K.

We are therefore interested in frequency shifts $\triangle\nu$ given by

$$\triangle\nu = \nu(B_o, m_u = 0.7425, T_s = 6494°\mathrm{K}) - \nu(B_o = 0, m_u = 0.7425, T_s = 6494°\mathrm{K}), \quad (3.104)$$

where $\nu(B_o = 0, m_u = 0.7425, T_s = 6494°\mathrm{K})$ is the mode frequency calculated at 'solar maximum' for a field-free atmosphere and $\nu(B_o, m_u = 0.7425, T_s = 6494°\mathrm{K})$ is the equivalent mode frequency under an applied magnetic field B_o in the atmosphere. Figure 3.17 shows the changes in mode frequency found from Equation (3.104). The change in mode frequency $\triangle\nu$ is plotted against $\nu(B_o = 0, m_u = 0.7425, T_s = 6494°\mathrm{K})$, and the degree l is set equal to 100. The magnetic field increases from zero to 10G, or 50G, or 100G. Figure 3.17 shows that all modes experience an increase in frequency with an increase in magnetic field strength. This result is comparable with the results of Evans and Roberts (1990) and Jain and Roberts (1994), except that here we find that the magnitude of the frequency shifts is *less* at low ν

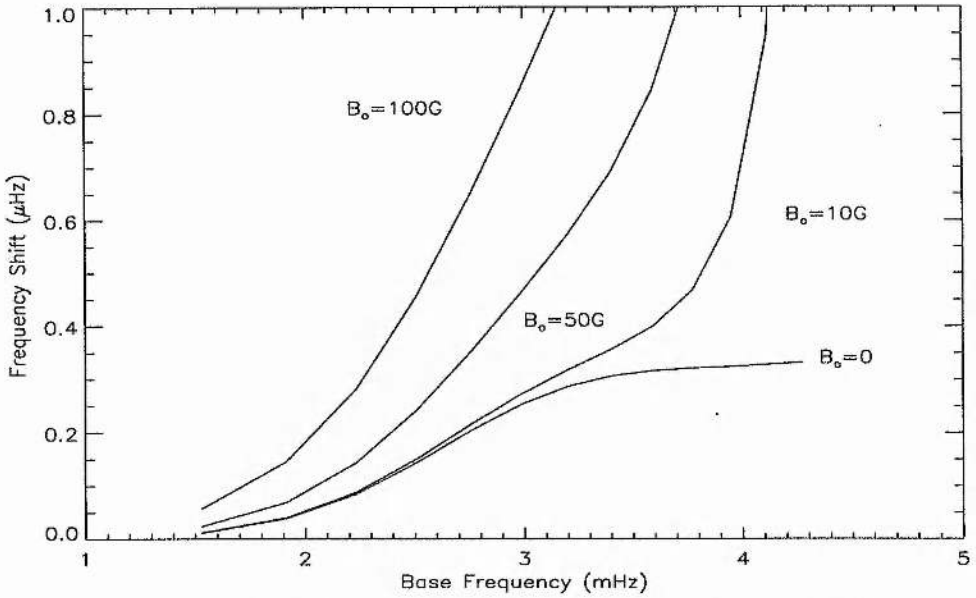

Figure 3.18: Frequency shifts $\Delta\nu$ as a consequence of atmospheric field changes together with a steepening of the temperature gradient of the superadiabatic layer. The results according to Equation (3.105) are plotted against the base frequencies of Section 3.5.1. The degree $l = 100$.

than those found in the previous works. We shall discuss this in Section 3.7.

As a next step we turn to a consideration of an evolution of the superadiabatic layer over the solar cycle, coupled with an increase in magnetic activity. We follow a similar procedure to that used in Section 3.5 by setting conditions for calculation of the base frequencies from Table 3.1. We then calculate frequencies for the model with a 1% steeper temperature gradient in the superadiabatic layer, along with a cooling of 6°K of T_s. Also, we now allow for an evolution of the magnetic field in the atmosphere.

Figure 3.18 shows the results of calculating the frequency change $\Delta\nu$, where

$$\Delta\nu = \nu(B_o, m_u = 0.7425, T_s = 6494^\circ\mathrm{K}) - \nu(B_o = 0, m_u = 0.75, T_s = 6500^\circ\mathrm{K}). \quad (3.105)$$

The frequency taken to represent the base frequency of the model 'minimum' is given by $\nu(B_o = 0, m_u = 0.75, T_s = 6500^\circ\mathrm{K})$ while the corresponding frequency of the model 'maximum' is given by $\nu(B_o, m_u = 0.7425, T_s = 6494^\circ\mathrm{K})$. Figure 3.18 shows the results for modes of degree l equal to 100 and field strengths of 10G, 50G and 100G. We have also included the curve for $B_o = 0$, showing the frequency changes imposed by altering the parameters of the superadiabatic layer only. From Figure 3.18 we see that the joint effect of

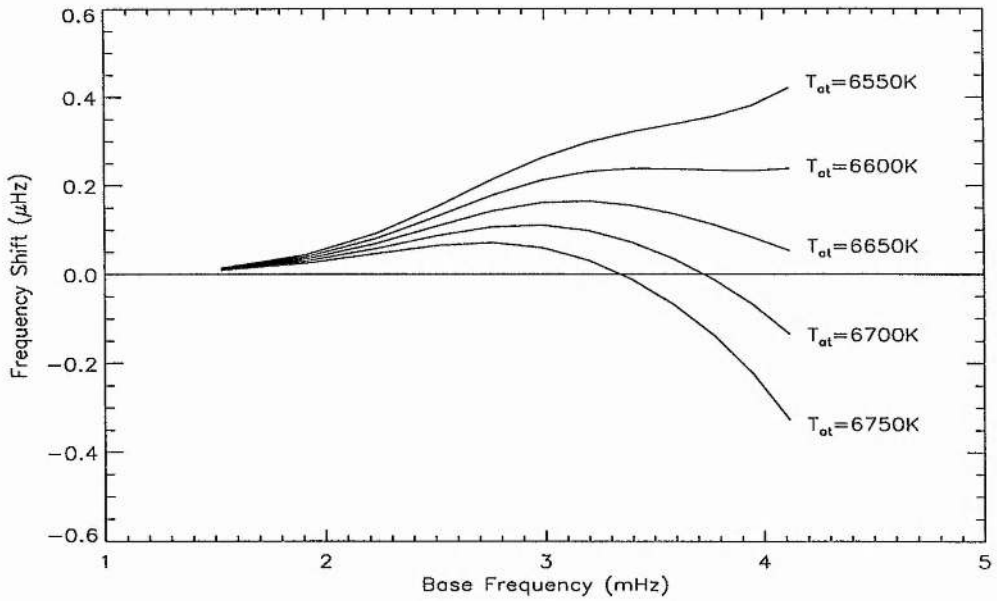

Figure 3.19: The combined effect of magnetic field strength increases, steepening temperature gradients and atmospheric temperature changes on $p-$mode frequencies of degree $l = 100$. The base frequencies used are $\nu(B_o = 40\text{G}, m_u = 0.75, T_s = 6500°\text{K}, T_{at} = 6500°\text{K})$ and atmospheric temperatures of 6550°K, 6600°K, 6650°K, 6700°K and 6750°K are considered.

a decrease in convective efficiency coupled with an increase in magnetic field is to increase mode frequencies over their base value. However, the results are quantitatively different to those of Figure 3.17. In Figure 3.18 we can see that the changes to mode frequency made by variations in the superadiabatic layer are much larger at low frequency than purely magnetic effects, especially when we look at the frequency shift curve for the case $B_o = 0$ compared to Figure 3.17. At high frequency though, magnetic effects dominate with the curves rising steeply above the thermal changes. The net effect of this joint evolution is that changes in the superadiabatic layer provide a 'boost' to the frequency increases at low frequency, especially for low magnetic field strengths. However, for high frequency modes, magnetic effects are dominant.

As a final study of the $p-$modes, we now alter the atmospheric temperature T_{at} along with the magnetic field strength and convective efficiency, and calculate the frequency difference $\triangle\nu$ according to

$$\triangle\nu = \nu(B_o = 50\text{G}, m_u = 0.7425, T_s = 6494°\text{K}, T_{at})$$

$$-\nu(B_o = 40\mathrm{G}, m_u = 0.75, T_s = 6500^o\mathrm{K}, T_{at} = 6500^o\mathrm{K}). \quad (3.106)$$

Here $\nu(B_o = 50\mathrm{G}, m_u = 0.7425, T_s = 6494^o\mathrm{K}, T_{at})$ is the frequency calculated for a raised atmospheric temperature and $\nu(B_o = 40\mathrm{G}, m_u = 0.75, T_s = 6500^o\mathrm{K}, T_{at} = 6500^o\mathrm{K})$ is the corresponding frequency for the model 'minimum', taken to be the base frequency. We have used an increase in magnetic field strength of 10G. Figure 3.19 displays the results. Frequency shifts are similar in form to those displayed in Figure 3.15 but note that in Figure 3.19 much larger increases in atmospheric temperature have had to be used to produce curves of the same shape. We have used atmospheric temperatures of 6550°K, 6600°K, 6650°K, 6700°K and 6750°K. This has been necessary because of the very large positive frequency shifts seen at high frequency for even small changes to magnetic field strength B_o (Figures 3.17 and 3.18).

3.6.3 Magnetic effects on the convective modes

Finally, we are left with the question of how the growth times of the convective modes are modified by a magnetic field. To examine this, we use the base model parameters from Table 3.1 and allow B_o to increase. We calculate changes in growth time $\triangle\sigma$ according to

$$\triangle\sigma = \sigma(B_o) - \sigma(B_o = 0), \quad (3.107)$$

where $\sigma(B_o)$ is the calculated growth time of the modes with a magnetic atmosphere of strength B_o and $\sigma(B_o = 0)$ is the equivalent base growth time found for field-free conditions (see Section 3.5.2).

In Figures 3.20 and 3.21 the shift $\triangle\sigma$ (in seconds) is plotted against the base growth time. In both cases the horizontal wavenumber k_x is set equal to 1 Mm^{-1}. From Figure 3.20 we see that an increase in magnetic field strength leads to an increase in the $e-$folding time of the convective mode, i.e. there is a suppression of the convective mode under the influence of a magnetic atmosphere. We have used magnetic field strengths of 10G, 35G, 60G and 85G. For these field strengths, the change in growth time is small and increases as the base growth time increases.

For larger magnetic field strengths the results are somewhat different. In Figure 3.21 magnetic field strengths of 150G, 350G, 550G and 750G have been used. Although each convective mode shows an increase in its $e-$folding time under these high field strengths,

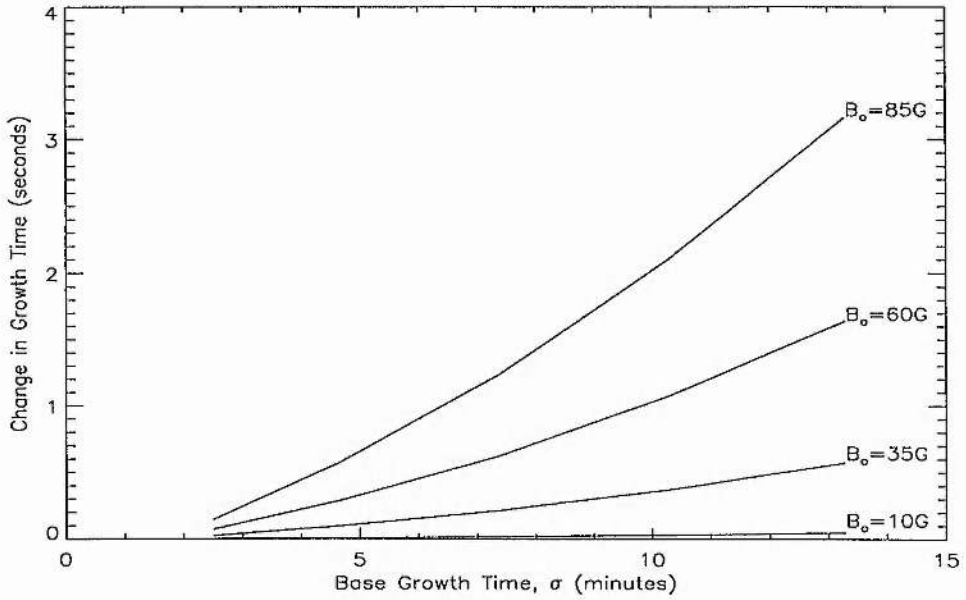

Figure 3.20: The change in growth time $\Delta\sigma$ (in seconds) as a function of base growth time σ (in minutes) as a consequence of magnetic field changes according to Equation (3.107). The horizontal wavenumber $k_x = 1$ Mm^{-1}. Magnetic field strengths of 10G, 35G, 60G and 85G are used. The base growth times are for a field-free medium (as found in Section 3.5.2).

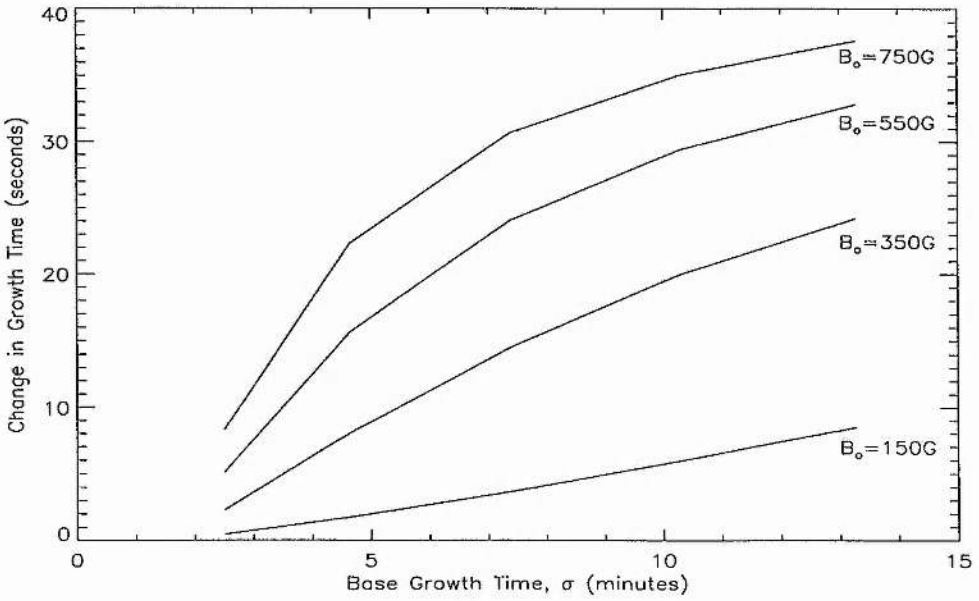

Figure 3.21: As in Figure 3.20 but using field strengths of 150G, 350G, 550G and 750G. Note the change of scale on the vertical axis.

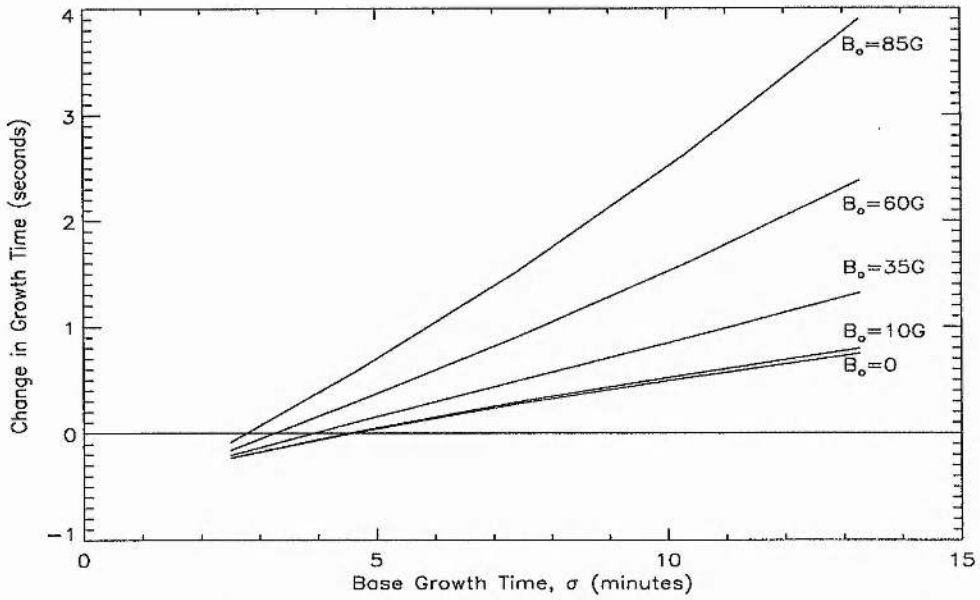

Figure 3.22: The combined effect of all the physical changes we have applied to the model on the g^-−modes. The results are plotted against the field-free base growth times (Section 3.5.2). The horizontal wavenumber $k_x = 1$ Mm^{-1} and field strengths of 0G, 10G, 35G, 60G and 85G are used.

the effect becomes more pronounced at lower base growth times and begins to level off as higher base growth times are reached.

Our final investigation is concerned with steepening the temperature gradient of the superadiabatic layer along with increasing B_o. We calculate growth time changes $\triangle\sigma$ given by

$$\triangle\sigma = \sigma(B_o, m_u = 0.7425, T_s = 6494°\text{K}) - \sigma(B_o = 0, m_u = 0.75, T_s = 6500°\text{K}), \quad (3.108)$$

where $\sigma(B_o, m_u = 0.7425, T_s = 6494°\text{K})$ is the base growth time calculated for model 'maximum' and $\sigma(B_o = 0, m_u = 0.75, T_s = 6500°\text{K})$ is the corresponding growth time given from Section 3.5.2.

Figure 3.22 gives the results for $k_x = 1$ Mm^{-1}. Magnetic field strengths of 0G, 10G, 35G, 60G and 85G are used. The results are similar to those of Section 3.5.2 in that the g_1^-−mode is actually enhanced by the steepening temperature gradient whilst all other modes are suppressed. The net effect of an additional magnetic field is to *decrease* the enhancement of the g_1^-−mode and to further the suppression of the higher order modes.

3.6.4 Summary of magnetic effects

When a horizontal magnetic field is introduced into the atmosphere the overall effect is an *increase* in $p-$mode frequencies. Under purely magnetic changes, the modes show a slight increase at low frequency, rapidly steepening at higher frequencies. The magnitude of the frequency increase is larger for stronger magnetic fields. Adding the changing convective efficiency of the superadiabatic layer to this situation we now observe a steeper rate to the increase in frequency at lower frequencies but no levelling out of the frequency increase at higher frequencies. The turnover which is observed in the actual modes of the Sun can be reproduced when we raise T_{at}, but larger changes to the atmosphere are required than in the field-free case (Section 3.5.1).

The convective modes all show an increase to their growth times when only the magnetic field strength of the atmosphere is changed. However, at low field strengths, the increase in σ is concave in form, whereas for large field strengths the changes to σ are convex in form with a steep rise in $\triangle\sigma$ for low base growth times with the curves levelling of as σ increases.

Finally, when atmospheric and superadiabatic changes are made, similarities with the thermal effects may be seen. The g_1^-−mode still shows a *decrease* in its growth time but as the field strength increases this decrease is lessened. The overtones, however, show an increase to their growth times, the effect being greater as the magnetic field grows.

3.7 Discussion

We have used a three layer, plane-parallel, model to examine the response of $p-$mode frequencies and g^-−mode growth times to variations in the thin superadiabatic region of the outer convection zone. We have combined the effects of changes to the superadiabatic layer with the addition of a horizontal magnetic field in the isothermal atmosphere. The lower region of fluid in the model contains a linear temperature profile, the gradient of which is maintained at marginal stability to convective motions. Above the marginally stable layer resides a thin layer of fluid, again with a linear temperature profile, but now with a steeper gradient than the fluid below. These two layers model the convection zone. Above the convective layers, we place a semi-infinite isothermal atmosphere representing the low photosphere and above. This atmosphere may be permeated by a horizontal magnetic

field.

We are especially interested in the upper convection zone for a number of reasons. There are three main properties of the Sun that are sensitive to the solar cycle and act as indicators of it: the surface magnetic field, the solar luminosity, and the acoustic eigenfrequencies. The increase in magnetic activity as the Sun approaches maximum has been known for a considerable amount of time but recently luminosity variations over the solar cycle have been measured and are possibly connected with changes in the superadiabatic region (see, for example, Endal *et al.* 1985) rather than deeper layers of the Sun. Observations of $p-$mode frequencies and their dependence on the solar cycle have indicated that it is probably changes to the outer layers of the Sun, below the photosphere, which give rise to frequency variations over the cycle (Libbrecht 1988; Libbrecht and Woodard 1990; Woodard and Libbrecht 1991). Observations also indicate that the overall level of surface magnetic activity could be the dominant mechanism for changes in mode frequencies (Woodard *et al.* 1991). From a theoretical point of view, Shibahashi (1991) has claimed that it is only possible to localise the source of the frequency shifts to that volume of the Sun located above the second helium ionisation zone (the outermost 14000 km of the solar interior). In fact, Nishizawa and Shibahashi (1994), from an analysis of the acoustic radii of the modes applied to the data of Libbrecht and Woodard (1991), confine the changes to solar structure responsible for $p-$mode frequency shifts to a depth of 200km below the photosphere. Moreover, Rhodes *et al.* (1994) compared the data of Libbrecht and Woodard (1990) to the results of Shibahashi (1991) and found the correlation between the results to be so good that they concluded that the source of the frequency shifts is much closer to the solar surface than the second helium ionisation zone. These aspects provide good indicators that the influence of the superadiabatic layer on $p-$mode frequencies requires careful examination.

The model presented here provides two separate spectra of frequencies: the distinctive and well observed parabolae of the $p-$modes with $\omega \propto k_x^{\frac{1}{2}}$, and the convective modes (g^--modes) which result from the complex buoyancy frequency of the superadiabatic layer.

The changes to the superadiabatic layer that we have implemented are a steepening of the temperature gradient of that region. Coupled to this, we have included a cooling of the surface temperature T_s by 6°K, consistent with the measurements of Livingston (1978). The atmospheric temperature T_{at} is also allowed to vary. As well as considering thermal variations (Section 3.5), we have combined these effects with the influence of a horizontal

uniform magnetic field (Section 3.6).

For the purely thermal changes (Section 3.5), we find that decreasing the convective efficiency of the superadiabatic layer by 0.5-2% *increases* the frequencies of the $p-$modes over their base values (Figure 3.5). The frequency shift curves in the range 2-3 mHz show a steep rise in frequency, with the curves levelling out at higher frequencies. For mode frequencies of 3.3 mHz we see a rise in mode frequency of 0.15 μHz for a decrease in convective efficiency of 0.5%, rising to 0.6 μHz for a 2% steepening of the temperature gradient. The effect is larger for larger values of l (Figure 3.6). The frequency increases incurred by steepening the temperature gradient of the superadiabatic layer are simply a response to the decrease in the transit time of the modes across the layer. The frequency $\omega \propto 1/T$, where T is the transit time of the mode; hence a reduction in T leads to an increase in ω and vice versa. However, simply varying the temperature gradient of the superadiabatic layer does not reproduce the distinctive downturn in frequency shifts at about 3.9 mHz as seen in observations. We are able to recreate this by simultaneously raising the atmospheric temperature T_{at} (Figure 3.7). The frequency changes that we calculate compare well to the data of Libbrecht and Woodard (1991). However, the peak frequency change in our model occurs at the somewhat lower base value of 3.4 mHz, compared with the value 3.9 mHz indicated by the observations. This discrepancy is perhaps acceptable given the relative simplicity of our model. Also, we find that by considering the low photosphere we require far smaller changes in T_{at} to produce the observed turnover in the frequency shifts than models which concentrated attention on the atmosphere above the temperature minimum. For example, Jain and Roberts (1994) found that they could reproduce the turnover in frequency shifts only by raising the chromospheric temperature by about 1500°K along with increasing the magnetic field strength by 10G. We are able to produce qualitatively similar results by increases in T_{at} ranging from 10°K to 50°K, which is not an entirely inconceivable increase.

With the introduction of a magnetic field into the atmosphere, we see that the effect of increasing the field strength alone serves to increase mode frequencies (Figure 3.17), as found by Evans and Roberts (1990). However, we see that for the model presented here the magnitude of the shifts is much smaller, especially at low frequencies. This is simply related to the different layer of the atmosphere that we are considering. The plasma pressure at the temperature minimum is some 100 times less than the region just below the photosphere that we use as a reference level. Hence for magnetic fields of the same strength

the plasma beta is significantly higher at our reference level than it is at the temperature minimum. Consequently the magnetic field has less influence then it does in the models of Evans and Roberts (1990) and Jain and Roberts (1994). However, the frequency shifts are changed to show a steep rise in the frequency range 2-3 mHz, when we combine magnetic field increases with variations in the superadiabatic layer (Figure 3.18). Finally, a downturn in the frequency shifts occurs when we combine the previous magnetic changes with raising T_{at} (Figure 3.19). Much larger increases in atmospheric temperature are required than the thermal changes of Section 3.5 with temperature increases of 50°K-250°K being necessary. This can be explained by the decrease in mode frequency induced by raising T_{at} now having to compete with the combined effects of magnetism and increasing temperature gradients. Also, we see from Figure 3.17 that magnetic effects are felt much more strongly at high frequencies, whereas the curves have levelled out at these frequencies for purely thermal variations, leading to the larger temperature changes necessary to produce the downturns.

In this chapter we have also investigated the effects that the same variations in physical parameters have on the convective modes of the superadiabatic layer. By simply changing the value of m_u to give a steeper temperature gradient, we saw that the g_1^-−mode actually quickened in its e−folding time while the overtones all suffered an increase in their growth rates (Figure 3.13) for a large enough decrease in m_u. The changes recorded for a base growth time of 10 minutes ranged from 0.2 seconds for a 0.5% change to m_u to 1.2 seconds for a 2% change. When an increase in T_{at} is also applied the results of Figure 3.15 show that the decrease in σ felt by the g_1^-−mode is lessened while the increase of σ for the overtones is raised further. We have fixed the value of T_h and have allowed T_s to take on two values only. Hence, when we decrease m_u only the scale height of the superadiabatic layer, z_{ou}, and the thickness of the region h vary; both of them in fact decreasing as m_u decreases. The increase in σ for the overtones can be understood by the decrease in the convective efficiency within the layer, with the modes having to work against a steeper temperature gradient. But why should the g_1^-−mode quicken in this case? An explanation may be that this mode feels the reduction in the thickness of the superadiabatic layer more strongly than it feels the variation in the temperature gradient. The further suppression of the modes when T_{at} is increased is probably due to the increase in the density scale height of the atmosphere. The extra inertia that this supplies reduces the rate at which energy may be fed into the atmosphere. Finally, we see that introducing a magnetic field into the atmosphere causes σ to increase for all modes if the parameters of the superadiabatic layer

are left unaltered. Again, this can be understood by the extra inertia that a magnetic field adds to the atmosphere.

In this chapter we have seen that the observed changes in $p-$mode frequencies over the solar cycle may be reproduced by increasing the temperature gradient of the superadiabatic layer while simultaneously raising the temperature of the low photosphere. When a surface magnetic field is also applied, greater changes to T_{at} are required to reproduce the observed shifts.

These results add further weight to the argument that it is the near surface layers of the Sun which undergo the greatest changes over the course of the solar cycle, indicating that the temperature gradient of the superadiabatic layer might change by as much as 1-2% over this time. Obviously, our model of the superadiabatic layer is simple but more sophisticated models of this region may hold key information to aid our understanding of the mechanism of the solar cycle and its influence on mode frequencies.

Chapter 4

The Dependence of the $P-$mode Frequencies on the Magnetic Field at the Base of the Convection Zone

4.1 Introduction

At and above the surface of the Sun, the magnetic field is observed to exist in a variety of different structures. For example, at the photosphere the magnetic fields are seen to be mostly in the form of intense flux tubes with field strengths ranging from 1.5 kG in the smaller pores to 3 kG in sunspots (Spruit and Roberts 1983; Roberts 1984). In the chromosphere the magnetic field begins to fan out to form a horizontal canopy field (Giovanelli 1980), due to the rapid decrease of the plasma pressure with height, and in the corona complex features such as prominences, loops and coronal holes are observed.

These phenomena are a surface manifestation of a global magnetic field located, stored and manipulated somewhere within the solar interior. The field is presumed to be generated by a dynamo action over the eleven year cycle and is subjected to instabilities causing magnetic flux to break free from the reservoir and rise to the surface under magnetic buoyancy.

The field which emerges at the solar surface in sunspot pairs obeys what is known as Joy's Law (Hale *et al.* 1919) which states that the line joining two spots makes an angle with the latitude of the spots, the tilt angle, which increases with increasing latitude. This feature indicates a certain ratio between the buoyancy rise time of a flux tube and the

Coriolis force acting on the tube. The coherent nature of the emergent flux indicates that the field has not been deformed by turbulent forces while rising through the convection zone. This implies that the internal magnetic field of the Sun is toroidal in nature and strong enough to withstand deformation from turbulent pressures at its location. Simply speaking, the magnetic pressure of the field, $B^2/2\mu$, is at least comparable to the local dynamical pressure, $\frac{1}{2}\rho v^2$, where ρ and v are the local density and flow speed, respectively. At the base of the convection zone this gives a field strength of at least 10^4 G while in the upper layers of the convection zone a field strength of 500 G is sufficient (Spruit 1974).

The position and strength of the toroidal field are open to debate. For the solar dynamo to operate, turbulent diffusion is necessary. However, if the dynamo were to operate in the bulk of the convection zone then magnetic buoyancy instabilities would rapidly sweep away magnetic fields of the above strength in a small fraction of the solar cycle (Parker 1979).

The solar dynamo problem has led to two suggestions for the position of the toroidal field. Firstly, the top of the radiative zone is stable enough to anchor fields for time periods comparable with the solar cycle and greater (Parker 1975; van Ballegooijen 1982a). However, the radiative zone is *too* stable to give the instabilities causing flux to rise upwards. Also, the stability of this region raises serious problems on how the dynamo can operate here, because the interaction of convection with the magnetic field is severely inhibited.

However, there is a shallow convective overshoot layer at the base of the convection zone which many authors have suggested as being the possible site of the solar dynamo (Spiegel and Weiss 1980; Galloway and Weiss 1980; van Ballegooijen 1982a,b; Rüdiger and Brandenberg 1995). At the base of the convection zone is a region of transition for the temperature gradient and internal rotation. The rotation changes from being differential in nature to being nearly solid body rotation across this region, known as the tachocline (Basu 1997), and it is natural to believe that the solar dynamo will operate where the rotation rate shows strong gradients (Weiss 1994). Also, convective and radiative energy transport compete here and the layer is likely to become unstable (van Ballegooijen 1982b). Hence, magnetic flux tubes in the overshoot region are not subjected to deformation by strong vertical flows and the field may be stored here, provided that magnetic buoyancy instabilities do not lead to a rapid loss of flux. The thickness of this layer is estimated to be a few tenths of the pressure scale height at that depth, approximately 10,000-20,000 km.

The strength of the magnetic field is not known. A lower limit may be put on the

field strength from the argument that the field must be strong enough to resist deformation from convective flows. Hence the field strength B must be such that the magnetic pressure $B^2/2\mu$ is at least comparable to the local dynamical pressure $\frac{1}{2}\rho v^2$, giving a lower bound of 10^4G in the convective overshoot layer. At the other extreme, it is unlikely that the magnetic field reaches a strength which brings it into equipartition with the plasma pressure. From the model of Guenther *et al.* (1992), this places an upper bound on the magnetic field of approximately 36 MG.

At the lower extreme, Rüdiger and Brandenberg (1995) have estimated that a field strength of 5 kG is consistent with the observed surface magnetic flux of 10^{24} Mx. Alternatively, van Ballegooijen (1982a) has suggested that a field strength of at least 2.10^4G is necessary to produce the observed magnetic flux in large active regions and to give the correct observational limits on the drift velocity of these regions. However, van Ballegooijen (1982b) has also argued that high fields would probably show up as a rapid drifting apart of tubes of opposite polarity in the photosphere, implying that a field strength of less than 10^5G should be found. At the other extreme, Basu (1997) in her investigation into the properties of the tachocline has put an upper limit of 0.3 MG on the sub-convective magnetic field. Also, Roberts and Campbell (1986) and Campbell and Roberts (1986) have suggested that to produce an observable change in the p-mode frequencies a field strength of at least 1 MG is required. Additionally, Dziembowski and Goode (1989) use the data of Libbrecht (1989) to estimate an axisymmetric quadrupole field of 2 ± 1 MG near the base of the convection zone.

D'Silva and Choudhuri (1993) and D'Silva (1993) have attempted to put a limit on the field strength by adding the Coriolis force to magnetic buoyancy, to reproduce the observed tilt of bipolar magnetic regions. In their studies they found field strengths of between 60 kG and 160 kG fitted the observed tilt angles but expressed some concerns over field strengths of this size due to difficulties of generation by the dynamo.

Finally, Lydon *et al.* (1996) have postulated that the observed variation in the frequency of the $p-$modes may be explained by a decrease in field strength of a (locally) horizontal field located approximately 320 km below the solar surface. Although they admit that with our current understanding of the stability criteria of magnetic fields it is impossible to store a field at this depth over the solar cycle, their results fit very well, quantitatively as well as qualitatively, with the observations, adding yet more questions to the problem.

As we can see, the magnitude of the magnetic field at the base of the convection

zone is not known. However, not only is it important to know the field strength for a clearer understanding of the solar dynamo mechanism but it is also important in the determination of the internal distribution of the angular velocity (see, for example, Schou and Brown 1994; Kosovichev 1996a,b; Basu 1997).

In this chapter we incorporate a sub-convective zone magnetic field into a model of the solar interior. We wish to find the changes in the frequencies of the $p-$modes brought about by changes to the field strength of this layer. In Section 4.2 we introduce the equilibrium model to be used in this investigation, and we then apply a two dimensional velocity perturbation to the equilibrium (Section 4.3). The dispersion relation for the model is presented in Section 4.4. We then examine in Section 4.5 the effect that changing certain parameters in the model has on mode frequencies before considering what effect the magnetic layer has on the structure of the modes (Section 4.7). In Section 4.8 we look at the special case of modes of degree zero and examine how they respond to changes in the magnetic layer. Finally, in Section 4.9, we discuss our results.

4.2 The Model

As a first attempt to include a layer of magnetic flux at the base of the convection zone, we consider the following model: To model the interior of the Sun, we consider a semi-infinite region of fluid, ranging in depth z from $z = 0$ to $z = +\infty$, within which there are three separate plasma layers. The temperature in the two field-free zones is taken to be linear in z. Between the field-free layers, a layer of magnetic flux resides (in $z_{uc} < z < z_{lc}$) within which the temperature is assumed to be isothermal. A rigid wall is placed at $z = 0$ (so as to remove atmospheric effects) and the entire medium is gravitationally stratified. The linear temperature profiles are chosen so as to be marginally stable to convective motions and the temperature is taken to be continuous across each interface, giving an equilibrium temperature profile of the form

$$T_o(z) = \begin{cases} T_s(1 + \frac{z}{z_{ou}}), & 0 < z < z_{uc}, \\ T_c, & z_{uc} < z < z_{lc}, \\ T_c(1 + \frac{z - z_{lc}}{z_{ou} + z_{uc}}), & z > z_{lc}. \end{cases} \tag{4.1}$$

Here, T_s is the temperature at $z = 0$, where the temperature scale height is z_{ou}; T_c is the temperature in the isothermal layer, taken to be $T_c = T_s(1 + z_{uc}/z_{ou})$ in order to provide a continuous temperature profile.

The distribution of the plasma pressure $P_o(z)$ and density $\rho_o(z)$ in the equilibrium state are related by the requirement of magnetostatic pressure balance, *viz.*

$$\frac{d}{dz}\left(P_o(z)+\frac{B_o^2(z)}{2\mu}\right)=g\rho_o(z), \tag{4.2}$$

to be coupled with the ideal gas law

$$P_o(z)=R\rho_o(z)T_o(z). \tag{4.3}$$

We are interested in the presence of a thin layer of magnetic flux within the convection zone and its influence on the modes of oscillation of the system. For mathematical simplicity, we suppose that the equilibrium horizontal magnetic field $B_o(z)\hat{\mathbf{x}}$ has strength which varies exponentially with depth z, the field being confined to the layer $z_{uc}<z<z_{lc}$. The magnetic layer is assumed to be isothermal. Then,

$$B_o(z)=\begin{cases} 0, & 0<z<z_{uc}, \\ B_{lc}e^{\frac{z-z_{lc}}{2H_c}}, & z_{uc}<z<z_{lc}, \\ 0, & z>z_{lc}, \end{cases} \tag{4.4}$$

where B_{lc} is the magnetic field strength at $z=z_{lc}$ and H_c is the magnetically modified scale height.

This choice of profile for $B_o(z)$ leads to an Alfvén speed v_{ac} which is a constant within the layer:

$$v_{ac}^2=\frac{B_o^2(z)}{\mu\rho_o(z)}=\frac{B_{lc}^2}{\mu\rho_{lc}}, \tag{4.5}$$

where ρ_{lc} is the plasma density at $z=z_{lc}$. The magnetically modified scale height H_c is then given as

$$H_c=\frac{c_c^2}{g\Gamma_c}, \tag{4.6}$$

where c_c $(=(\gamma RT_c)^{\frac{1}{2}})$ is the speed of sound in the magnetic layer and Γ_c is the magnetically modified exponent denoted by

$$\Gamma_c=\frac{2\beta\gamma}{2\beta+\gamma}; \tag{4.7}$$

here β is the ratio of the sound speed to Alfvén speed squared in the magnetic layer,

$$\beta=\frac{c_c^2}{v_{ac}^2}. \tag{4.8}$$

Within the magnetic layer the plasma density and pressure both vary exponentially with depth. Outside the magnetic layer, where $B_o(z) = 0$, the magnetostatic pressure balance (Equation (4.2)) reduces to hydrostatic balance

$$\frac{dP_o(z)}{dz} = g\rho_o(z) \tag{4.9}$$

which, combined with the gas law and the assumption of a linear temperature profile, leads to power-law distributions for the pressure and density profiles. Specifically, for the complete medium, we have an equilibrium pressure

$$P_o(z) = \begin{cases} P_s(1+\frac{z}{z_{ou}})^{m+1}, & 0 < z < z_{uc}, \\ P_{lc}e^{\frac{z-z_{lc}}{H_c}}, & z_{uc} < z < z_{lc}, \\ P_L(1+\frac{z-z_{lc}}{z_{ou}+z_{uc}})^{m+1}, & z > z_{lc}, \end{cases} \tag{4.10}$$

and equilibrium density

$$\rho_o(z) = \begin{cases} \rho_s(1+\frac{z}{z_{ou}})^{m}, & 0 < z < z_{uc}, \\ \rho_{lc}e^{\frac{z-z_{lc}}{H_c}}, & z_{uc} < z < z_{lc}, \\ \rho_L(1+\frac{z-z_{lc}}{z_{ou}+z_{uc}})^{m}, & z > z_{lc}, \end{cases} \tag{4.11}$$

where P_L and ρ_L are the plasma pressure and density as $z \to z_{lc}^+$. The parameter m appearing in Equations (4.10) and (4.11) is the polytropic index of the gas (see Chapters 2 and 3).

Across the interfaces at $z = z_{uc}$ and $z = z_{lc}$ we require, consistent with Equation (4.2), that the total pressure is continuous, so that at $z = z_{lc}$

$$P_L = P_{lc} + \frac{B_{lc}^2}{2\mu}. \tag{4.12}$$

We use this relation to fix the value P_{lc} of the plasma pressure at $z = z_{lc}$:

$$P_{lc} = P_L - \frac{B_{lc}^2}{2\mu}. \tag{4.13}$$

Evidently, pressure balance places a constraint on the maximum allowable field strength B_{lc} at which the magnetic layer is completely evacuated. For the parameters used later (see Section 4.5, Table 4.1), the maximum field strength at which the plasma pressure within the magnetic field falls to zero is approximately 36 MG.

Finally, we note that across each interface $z = z_{uc}$ and $z = z_{lc}$ there is a density jump. Denoting the density immediately within the field as ρ_{mag} and the density immediately across the interface in the non-magnetic region by ρ_{nonmag}, we obtain

$$\frac{\rho_{mag}}{\rho_{nonmag}} = \frac{\Gamma_c}{\gamma}. \tag{4.14}$$

Notice that this density jump is the same at both interfaces, $z = z_{uc}$ and $z = z_{lc}$, even though the values of ρ_{mag} and ρ_{nonmag} are themselves different at these two locations.

4.3 Velocity Disturbances

As in previous chapters, we employ the following equations:
the equation of mass continuity

$$\frac{\partial \rho}{\partial t} + \nabla \cdot (\rho \mathbf{u}) = 0; \tag{4.15}$$

the momentum equation

$$\rho \frac{D\mathbf{u}}{Dt} = -\nabla P + \rho \mathbf{g} + \mathbf{j} \times \mathbf{B}; \tag{4.16}$$

an adiabatic energy equation

$$\frac{DP}{Dt} = \frac{\gamma P}{\rho} \frac{D\rho}{Dt}; \tag{4.17}$$

and an induction equation with no diffusion,

$$\frac{\partial \mathbf{B}}{\partial t} = \nabla \times (\mathbf{u} \times \mathbf{B}). \tag{4.18}$$

The current density $\mathbf{j}$ is given by

$$\mu \mathbf{j} = \nabla \times \mathbf{B}, \tag{4.19}$$

and the advective derivative is denoted by

$$\frac{D}{Dt} \equiv \frac{\partial}{\partial t} + \mathbf{u} \cdot \nabla. \tag{4.20}$$

Finally, the magnetic field is governed by the constraint

$$\nabla \cdot \mathbf{B} = 0. \tag{4.21}$$

We perturb the equilibrium of Section 4.2 with a two-dimensional velocity perturbation of the form

$$\mathbf{u} = (u_x(z), 0, u_z(z)) \exp\left[i(\omega t - k_x x)\right], \tag{4.22}$$

where ω is the angular frequency of the disturbance and k_x the horizontal wavenumber. We apply the perturbation given by Equation (4.22) to the system of Equation (4.15)-(4.21) to obtain the governing differential equations for the velocity disturbance. We consider each layer separately.

4.3.1 The field-free layers

In the two field-free layers of the model, the perturbation given by Equation (4.22) applied to Equations (4.15)-(4.21) gives the relations between the vertical velocity u_z and the compressibility $\triangle$ ($\equiv \nabla \cdot \mathbf{u}$):

$$\frac{du_z}{dz} + \frac{gk_x^2}{\omega^2} u_z = \left[1 - \frac{k_x^2 c_s^2(z)}{\omega^2}\right] \triangle \tag{4.23}$$

and

$$(\omega^4 - g^2 k_x^2) u_z = g[k_x^2 c_s^2(z) - \gamma\omega^2]\triangle - \omega^2 c_s^2(z) \frac{d\triangle}{dz}. \tag{4.24}$$

We assume that $\omega^2 \neq gk_x$ and eliminate u_z from Equations (4.23) and (4.24) to obtain the governing differential equation for $\triangle$ (Lamb 1932; see also Chapter 3), namely

$$c_s^2(z)\frac{d^2\triangle}{dz^2} + \left[g\gamma + c_s^2(z)'\right]\frac{d\triangle}{dz} + \left\{\omega^2 - k_x^2 c_s^2(z) + \frac{gk_x^2}{\omega^2}\left[(\gamma - 1)g - c_s^2(z)'\right]\right\}\triangle = 0. \tag{4.25}$$

The prime $'$ denotes the derivative with respect to depth z.

To solve Equation (4.25) in each of the field-free layers, we set

$$\triangle = e^{-k_x z_i} f(z), \tag{4.26}$$

where $f(z)$ is to be found and $z_i = z + z_{ou}$ for $0 < z < z_{uc}$ and $z_i = z + z_{ou} - z_c$ for $z > z_{lc}$; here $z_c = z_{lc} - z_{uc}$.

Applying Equation (4.26) to Equation (4.25), with the form for $c_s^2(z)$ in each region, we obtain the solution for $\triangle$ in the field-free layers:

$$\triangle(z) = \begin{cases} e^{-k_x(z+z_{ou})}\left[\alpha_1 M(-a, m+2, 2k_x(z+z_{ou})) \right. \\ \qquad \left. +\beta_1 U(-a, m+2, 2k_x(z+z_{ou}))\right], \qquad 0 < z < z_{uc}, \\ e^{-k_x(z+z_{ou}-z_c)}\left[\alpha_2 M(-a, m+2, 2k_x(z+z_{ou}-z_c)) \right. \\ \qquad \left. +\beta_2 U(-a, m+2, 2k_x(z+z_{ou}-z_c))\right], \qquad z > z_{lc}. \end{cases} \tag{4.27}$$

The functions M and U are the confluent hypergeometric functions (Abramowitz and Stegun 1965; Chapter 13) and α_1, α_2, β_1 and β_2 are arbitrary constants. The parameter a is determined by

$$2a = m\Omega^2 - (m+2), \tag{4.28}$$

where we have again introduced the dimensionless quantity Ω, given by

$$\Omega^2 = \frac{\omega^2}{gk_x}. \tag{4.29}$$

It is then possible to determine u_z from Equation (4.24).

4.3.2 The magnetic layer

In the isothermal magnetic layer it is found to be easier to work directly in terms of u_z. The velocity perturbation u_z satisfies the differential equation (Goedbloed 1971; Adam 1977; Roberts 1985; Chapter 3):

$$\frac{d}{dz}\left[\frac{\rho_o(c_s^2+v_a^2)(\omega^2-k_x^2c_T^2)}{(\omega^2-k_x^2c_s^2)}\frac{du_z}{dz}\right]$$
$$= \left[\frac{\rho_o g^2 k_x^2}{(\omega^2-k_x^2c_s^2)} - \rho_o(\omega^2-k_x^2v_a^2) - gk_x^2\frac{d}{dz}\left(\frac{\rho_o c_s^2}{(\omega^2-k_x^2c_s^2)}\right)\right]u_z. \tag{4.30}$$

In Equation (4.30) we have introduced the magnetohydrodynamic cusp speed, $c_T(z)$, defined by

$$c_T(z) = \frac{c_s v_a}{(c_s^2+v_a^2)^{\frac{1}{2}}}. \tag{4.31}$$

Under the assumptions of constant sound speed and Alfvén speeds within the magnetic layer, Equation (4.30) reduces to

$$\frac{d^2u_z}{dz^2} + \frac{1}{H_c}\frac{du_z}{dz} + Au_z = 0, \tag{4.32}$$

where

$$A = \frac{k_x[g^2(\Gamma_c-1) + (g\Omega^2-k_xv_{ac}^2)(g\Omega^2-k_xc_c^2)]}{(c_c^2+v_{ac}^2)(g\Omega^2-k_xc_{Tc}^2)}. \tag{4.33}$$

In order to solve Equation (4.32), we set

$$u_z = \alpha_3 e^{\lambda z}, \tag{4.34}$$

where α_3 is an arbitrary constant and λ is to be found. Application of Equation (4.34) to Equation (4.32) provides us with an expression for λ:

$$2H_c\lambda = -1 \pm (1-4AH_c^2)^{\frac{1}{2}}. \tag{4.35}$$

The square root term in Equation (4.35) indicates the behaviour of the modes within the interior. If $4AH_c^2 < 1$, the modes become evanescent at the depth of the magnetic

layer; if $4AH_c^2 > 1$, the modes are oscillatory in nature at this depth. Hence the square root term in Equation (4.35) does not describe a cutoff frequency as such; it is simply an indication of the depth of penetration of the modes for specific degree l and frequency ω. As a result, it is convenient to present two separate solutions for u_z in the magnetic layer, depending on whether $4AH_c^2 < 1$ or $4AH_c^2 > 1$. For modes satisfying the condition $4AH_c^2 < 1$,

$$u_z = C_1 e^{\lambda_+(z-z_{uc})} + D_1 e^{\lambda_-(z-z_{uc})}, \tag{4.36}$$

where

$$2H_c\lambda_+ = -1 + (1 - 4AH_c^2)^{\frac{1}{2}}, \qquad 2H_c\lambda_- = -1 - (1 - 4AH_c^2)^{\frac{1}{2}}. \tag{4.37}$$

Alternatively, if the mode frequency and wavenumber combination are such that $4AH_c^2 > 1$, then we may write

$$2H_c\kappa = (4AH_c^2 - 1)^{\frac{1}{2}}, \tag{4.38}$$

and u_z is then given by

$$u_z = e^{-\frac{(z-z_{uc})}{2H_c}} \left[C_2 \sin\{\kappa(z - z_{uc})\} + D_2 \cos\{\kappa(z - z_{uc})\}\right]. \tag{4.39}$$

In Equations (4.36) and (4.39), C_1, C_2, D_1 and D_2 are arbitrary constants.

4.4 The Dispersion Relation

In order to obtain the dispersion relation for the model, six boundary conditions are required. Firstly, we impose the condition that the kinetic energy density of the disturbances, $1/2\rho_o u_z^2$, should vanish as $z \to +\infty$. An inspection of the behaviour of the confluent hypergeometric equations as z becomes large indicates that only if $\alpha_2 = 0$ in Equation (4.27) is this condition satisfied.

Two other conditions are that the vertical velocity perturbation u_z is continuous across each interface, i.e.

$$u_z \quad \text{is} \quad \text{continuous} \quad \text{at} \quad z = z_{uc} \quad \text{and} \quad z = z_{lc}. \tag{4.40}$$

The total Lagrangian pressure perturbation must also be continuous at $z = z_{uc}$ and $z = z_{lc}$. This implies that (see Chapter 3)

$$\frac{\rho_o(c_s^2 + v_a^2)(\omega^2 - k_x^2 c_T^2)}{(\omega^2 - k_x^2 c_s^2)} \frac{du_z}{dz} + \left(\frac{\rho_o g k_x^2 c_s^2}{\omega^2 - k_x^2 c_s^2}\right) u_z \tag{4.41}$$

is continuous at $z = z_{uc}$ and $z = z_{lc}$.

Finally, due to the rigid wall at $z = 0$, we have the simple condition that

$$u_z = 0 \qquad \text{at} \qquad z = 0. \tag{4.42}$$

Application of Equations (4.40)-(4.42) leads to the dispersion relation for the model. The dispersion relation takes on two forms, depending on whether $4AH_c^2 < 1$ or $4AH_c^2 > 1$. The dispersion relation reads

$$\alpha\Psi = \eta\Phi, \tag{4.43}$$

where

$$\alpha = k_x c_s^2(\Omega^2 + 1) - g\gamma\Omega^2, \qquad \eta = 2ak_x\Omega^2 c_s^2, \tag{4.44}$$

$$\Psi = \epsilon M(-a, m+2, 2k_x z_{ou}) + \delta U(-a, m+2, 2k_x z_{ou}), \tag{4.45}$$

$$\Phi = \delta U(1-a, m+3, 2k_x z_{ou}) - \frac{\epsilon}{m+2} M(1-a, m+3, 2k_x z_{ou}), \tag{4.46}$$

$$\delta = \Lambda_7 M(-a, m+2, 2k_x(z_{uc}+z_{ou})) + \frac{\Lambda_8}{m+2} M(1-a, m+3, 2k_x(z_{uc}+z_{ou})), \tag{4.47}$$

$$\epsilon = \Lambda_8 U(1-a, m+3, 2k_x(z_{uc}+z_{ou})) - \Lambda_7 U(-a, m+2, 2k_x(z_{uc}+z_{ou})), \tag{4.48}$$

$$\Lambda_8 = \Gamma_c \Lambda_5 \tau, \qquad \Lambda_7 = \Gamma_c \sigma \Lambda_5 - \Lambda_6, \tag{4.49}$$

$$\tau = 2ak_x\Omega^2 c_c^2 \qquad \text{and} \qquad \sigma = k_x c_c^2(\Omega^2+1) - g\gamma\Omega^2. \tag{4.50}$$

If $4AH_c^2 < 1$, then Λ_5 and Λ_6 appearing in Equation (4.49) are given by

$$\Lambda_6 = \frac{\gamma(g\Omega^2 - k_x c_c^2)(\Omega^4 - 1)\Lambda_4(\Theta_- + I_-)}{\Lambda_2}, \tag{4.51}$$

and

$$\Lambda_5 = (1+\beta)(g\Omega^2 - k_x c_{Tc}^2)(\lambda_+\Theta_- + \lambda_- I_-) + \frac{\Lambda_4}{\Lambda_2}(\Theta_- + I_-), \tag{4.52}$$

where

$$I_- = e^{(\lambda_+ - \lambda_-)z_c}[\Lambda_4 - \lambda_+\Lambda_3] \qquad \text{and} \qquad \Theta_- = \Lambda_3\lambda_- - \Lambda_4. \tag{4.53}$$

When $4AH_c^2 > 1$, then Λ_5 and Λ_6 are given by

$$\Lambda_5 = (1+\beta)(g\Omega^2 - k_x c_{Tc}^2)(\Theta_+\kappa - \frac{I_+}{2H_c}) + gk_x\beta I_+, \tag{4.54}$$

and

$$\Lambda_6 = \frac{\gamma(\Omega^4 - 1)(g\Omega^2 - k_x c_c^2)\Lambda_4}{\Lambda_2} I_+, \tag{4.55}$$

where

$$I_+ = \Lambda_3 \left[\kappa \cos \kappa z_c - \frac{1}{2H_c} \sin \kappa z_c\right] - \Lambda_4 \sin \kappa z_c \tag{4.56}$$

and

$$\Theta_+ = \Lambda_3 \left[\kappa \sin \kappa z_c + \frac{1}{2H_c} \cos \kappa z_c\right] + \Lambda_4 \cos \kappa z_c. \tag{4.57}$$

For both cases,

$$\Lambda_4 = g k_x \beta \Lambda_2, \qquad \Lambda_3 = \Gamma_c(1 + \beta)(g\Omega^2 - k_x c_{Tc}^2)\Lambda_1, \tag{4.58}$$

$$\Lambda_2 = \gamma(g\Omega^2 - k_x c_c^2)(\Omega^4 - 1)U(-a, m + 2, 2k_x(z_{uc} + z_{ou})) - \Gamma_c \Lambda_1, \tag{4.59}$$

and

$$\Lambda_1 = \sigma U(-a, m + 2, 2k_x(z_{uc} + z_{ou})) - \tau U(1 - a, m + 3, 2k_x(z_{uc} + z_{ou})). \tag{4.60}$$

Equation (4.43) is the dispersion relation for the modes of oscillation of an adiabatically stratified three layer system. The outermost layers of fluid are assumed to be field-free. Between the two field-free regions resides a thin isothermal layer with an embedded horizontal magnetic field that is structured in such a way so as to maintain a constant Alfvén speed. Not only are the $p-$modes contained in Equation (4.43) but also the magnetoacoustic surface and body modes associated with the magnetic layer. In the next section we numerically examine the behaviour of the $p-$modes, determining how the frequencies of the modes respond to changes in the magnetic layer. A consideration of the magnetoacoustic surface and body modes is presented in Chapter 5.

4.5 Frequency Shifts Brought About by Changes in the Magnetic Layer

We wish to examine the possibility that the observed variation in the frequencies of the $p-$modes is a consequence of the evolution of the internal magnetic field over the course of the solar cycle. We do this by allowing the strength of the magnetic field in the convective

Parameter	*Value*
P_L	5.25855×10^{12} kg m^{-1} s^{-2}
T_L $(= T_c)$	2,234,410°K
R	9787.633326 m^{2}s^{-2}K^{-1}
T_s	17245°K
P_s	2.1418×10^{7} kg m^{-1} s^{-2}
z_{uc}	198,000 km
z_{lc}	218,000 km
m	3/2
γ	5/3
c_c	191 km s^{-1}
H_c $(B_{lc} = 0)$	79816 km

Table 4.1: Parameters used in the solution of Equation (4.43). The values of T_L and P_L are taken from the solar model of Guenther *et al.* (1992) in order to set conditions as close as possible to those at the base of the convection zone.

overshoot region to change over the solar cycle. Accordingly, we fix the parameters at this depth to be roughly equal to conditions at the base of the convection zone. To do this, we have referred to the model of Guenther *et al.* (1992) to set the temperature and pressure at the base of the sub-convective magnetic field. These are presented along with the other parameters used, in Table 4.1. The value of R $(=\hat{R}/\hat{\mu}$, where $\hat{R}$ is the universal gas constant and $\hat{\mu}$ is the mean molecular weight of the plasma) that we have used has been obtained by averaging $\hat{\mu}$ over the convection zone, using the model of Guenther *et al.* (1992). From the linear temperature profile of the model we may then obtain the surface temperature T_s and pressure P_s, given in Table 4.1. The parameters T_s and P_s fit reasonably well with conditions near the top of the convection zone when compared to the model of Guenther *et al.* (1992), and we have chosen the reference level $z = 0$ to be at this depth to avoid the superadiabatic layer above the convection zone where the temperature gradient departs strongly from the adiabatic value.

We are attempting to place bounds on the strength of the internal toroidal magnetic field of the Sun by using the observed variation in the $p-$mode frequencies over the solar cycle. To do this, we choose a range of base field strengths to represent solar minimum and allow the field to increase above this value. For simplicity, and to remain within the expected range for the strength of this field, we choose base field strengths of 10^4G, 10^5G

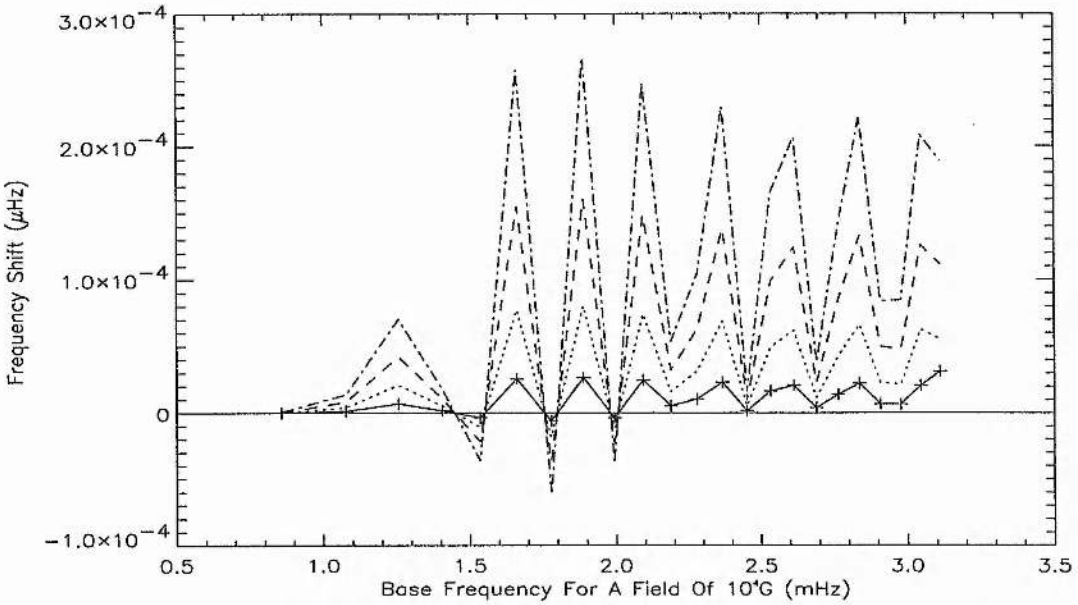

Figure 4.1: The changes in mode frequency (in μHz) given by Equation (4.61) plotted against mode frequencies for a sub-convective field strength of 10^4G. The degree $l = 30$ and the curves correspond to increased field strengths B_{lc} of 3.10^4G (solid curve), 5.10^4G (dotted curve), 7.10^4G (dashed curve) and 9.10^4G (dot-dashed curve). The crosses (+) show the first 23 modes of oscillation.

and 10^6G. The first frequency difference which we then calculate is $\Delta\nu$, given by

$$\Delta\nu = \nu(B_{lc}) - \nu(B_{lc} = 10^4\text{G}). \tag{4.61}$$

The frequency $\nu(B_{lc} = 10^4\text{G})$ is the frequency calculated for a field strength of 10^4G and $\nu(B_{lc})$ is the corresponding mode frequency for a raised internal magnetic field strength B_{lc}. The results of this procedure are shown in Figure 4.1 for modes of degree $l = 30$, plotted against $\nu(B_{lc} = 10^4\text{G})$. We have chosen $l = 30$ to display modes which penetrate to the depth of the magnetic layer and below. Figure 4.1 presents the frequency differences induced by field strengths of 3.10^4G (solid curve), 5.10^4G (dotted curve), 7.10^4G (dashed curve) and 9.10^4G (dot-dashed curve). The crosses (+) on the solid curve indicate the first 23 modes of oscillation of the system. Figure 4.1 provides us with some surprising results. There appears to be an almost oscillatory trend in the frequency shifts, with some modes exhibiting a frequency increase while others show a decrease. The magnitude of the frequency shifts increases with larger applied magnetic field strengths. Also, the $n = 1$ $p-$mode for $l = 30$ (the far left +) is the only mode to give $\Delta\nu = 0$ exactly. This is simply

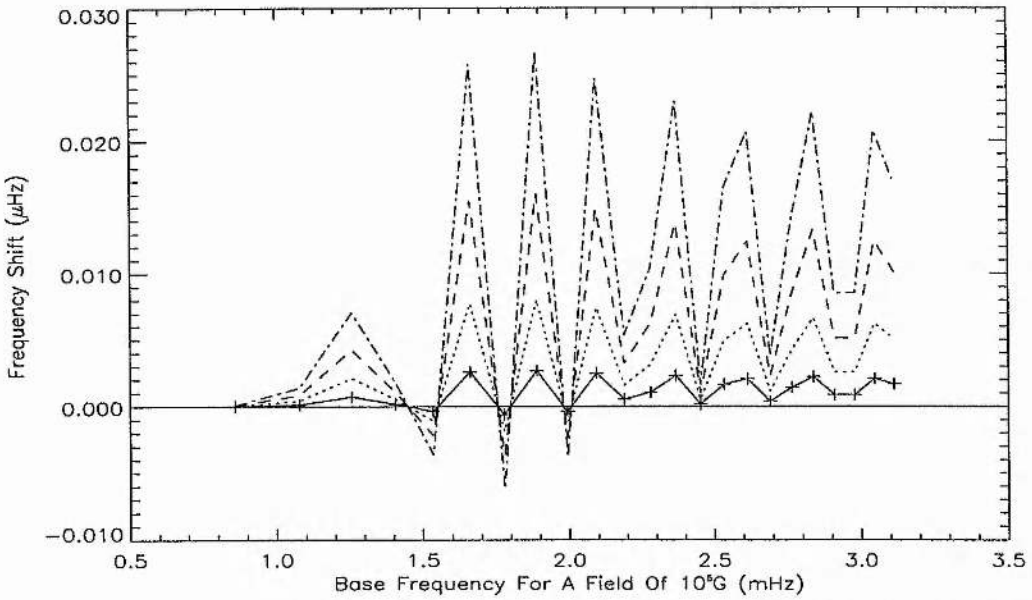

Figure 4.2: The frequency shift $\triangle\nu$ as a function of base $p-$mode frequency as determined by Equation (4.62). The magnetic field strengths chosen are 3.10^5G (solid curve), 5.10^5G (dotted curve), 7.10^5G (dashed curve) and 9.10^5G (dot-dashed curve). Again, $l = 30$ and the crosses (+) show the first 23 modes.

because the phase speed of the mode, $c_{ph} = \omega/k_x$, is less than the speed of sound in the magnetic layer. The turning point of a mode is approximately where the phase speed equals the local sound speed and, as such, the $n = 1$ mode has a turning point above the magnetic layer. Hence the $n = 1$ mode does not penetrate the magnetic layer and is unaffected by changes within it. Finally, the zeros of $\triangle\nu$ all fall at the same base frequency for all changes of B_{lc}. We have no explanation for this.

Repeating the calculation of $\triangle\nu$ for base field strengths of 10^5G and 10^6G yields qualitatively similar results to those presented in Figure 4.1. In Figure 4.2 we show the results of calculating

$$\triangle\nu = \nu(B_{lc}) - \nu(B_{lc} = 10^5\text{G}), \tag{4.62}$$

plotted against the base frequencies for a field strength of 10^5G. Increased field strengths of 3.10^5G (solid curve), 5.10^5G (dotted curve), 7.10^5G (dashed curve) and 9.10^5G (dot-dashed curve) are shown. Again, $l = 30$. In Figure 4.3 we have calculated

$$\triangle\nu = \nu(B_{lc}) - \nu(B_{lc} = 10^6\text{G}), \tag{4.63}$$

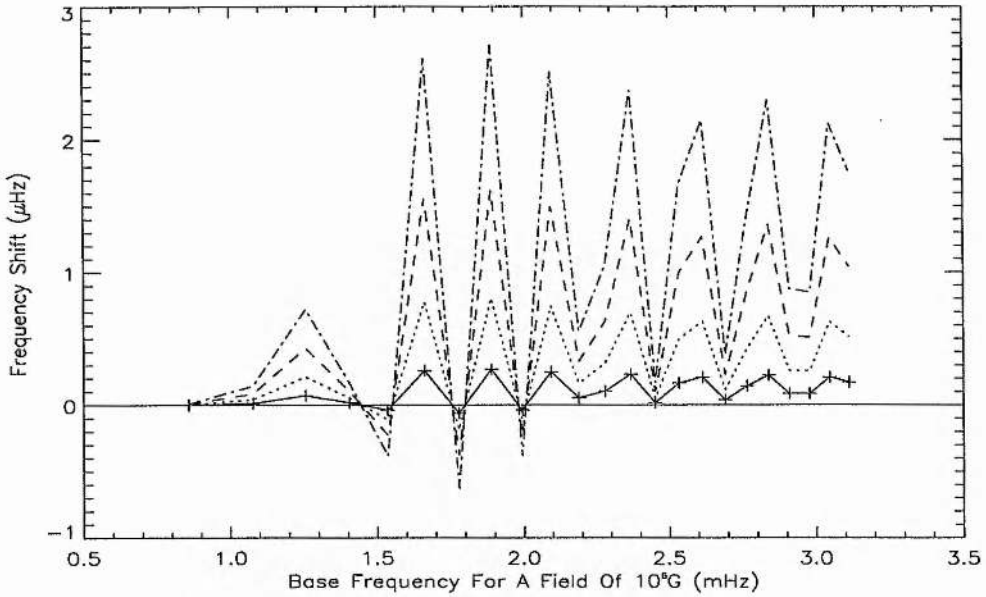

Figure 4.3: The results of Equation (4.63) plotted against base frequencies for B_{lc}=10^6G. The magnetic field strengths used to calculate frequency changes are 3.10^6G (solid curve), 5.10^6G (dotted curve), 7.10^6G (dashed curve) and 9.10^6G (dot-dashed curve) and $l = 30$.

and field strengths of 3.10^6G (solid curve), 5.10^6G (dotted curve), 7.10^6G (dashed curve) and 9.10^6G (dot-dashed curve) have been applied.

In Figures 4.2 and 4.3 we see the same oscillatory spread in the frequency shifts, with some modes showing an increase in frequency while others exhibit a frequency decrease. However, for the $n = 4$ $p-$mode we see an increase of 0.0004 μHz for a change in field strength from 10^4G to 7.10^4G from Figure 4.1, an increase of 0.04 μHz in Figure 4.2 when the field increases to 7.10^5G from 10^5G, and finally from Figure 4.3 we see a frequency increase of 0.4 μHz when the field grows from 10^6G to 7.10^6G. These results show an increase by a factor of 100, indicating that $\triangle\nu \propto B_{lc}^2$.

In Figures 4.1-4.3 we have seen that the $n = 1$ $p-$mode, with degree $l = 30$, exhibits no change in frequency whatsoever due to its turning point being above the magnetic layer. As remarked above, the turning point of a mode occurs roughly when its phase speed is equal to the local sound speed. To illustrate this, we repeat the calculation of Equation (4.62) but set the degree $l = 100$. The results of this calculation are shown in Figure 4.4 and once again field strengths of 3.10^5G (solid curve), 5.10^5G (dotted curve), 7.10^5G (dashed curve) and 9.10^5G (dot-dashed curve) are taken. For modes which show a change

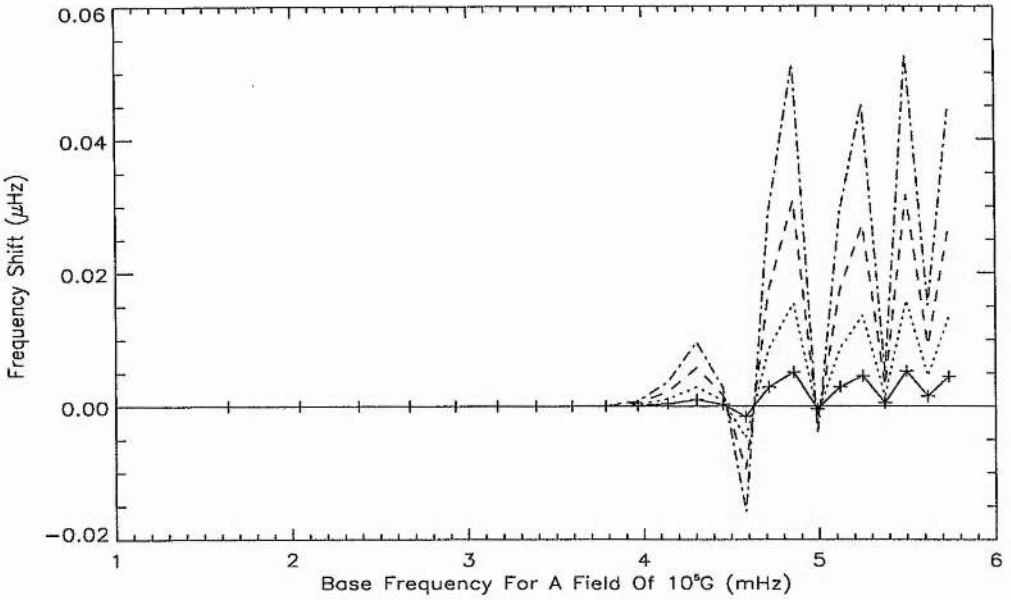

Figure 4.4: As in Figure 4.2 showing the results of Equation (4.62) but with the degree of the modes now set equal to 100. Field strengths used are 3.10^5G (solid curve), 5.10^5G (dotted curve), 7.10^5G (dashed curve) and 9.10^5G (dot-dashed curve).

in frequency, the curves are qualitatively similar to those of Figures 4.1-4.3 but now we see many more modes showing no change in frequency. In fact, now all modes up to radial order $n = 9$ suffer no change in frequency in Figure 4.4, which is to be expected with the $l = 100$ modes being confined much closer to the surface of the model.

We have been unable to explain satisfactorily the results presented in Figures 4.1-4.4. They do not reproduce the observed behaviour of the $p-$modes over the solar cycle. As far as we have been able to confirm, the dispersion relation and the code used to solve it are correct, and the modes have all been identified correctly. We shall present a possible simple explanation for these somewhat confusing results in Section 4.6.

Before we move on, we consider briefly the situation where the magnetic field strength at the base of the layer remains fixed, but the thickness z_c of the magnetic layer is allowed to vary, so increasing the magnetic flux. For this possibility we calculate $\triangle\nu$, now defined by

$$\triangle\nu = \nu(B_{lc} = 10^5\mathrm{G}, z_c = 15000\mathrm{km}) - \nu(B_{lc} = 10^5\mathrm{G}, z_c = 20000\mathrm{km}), \tag{4.64}$$

where $\nu(B_{lc} = 10^5\mathrm{G}, z_c = 20000\mathrm{km})$ is the frequency of a mode for a field strength of 10^5G and a thickness of the magnetic layer of 20000 km, and $\nu(B_{lc} = 10^5\mathrm{G}, z_c = 15000\mathrm{km})$ is the

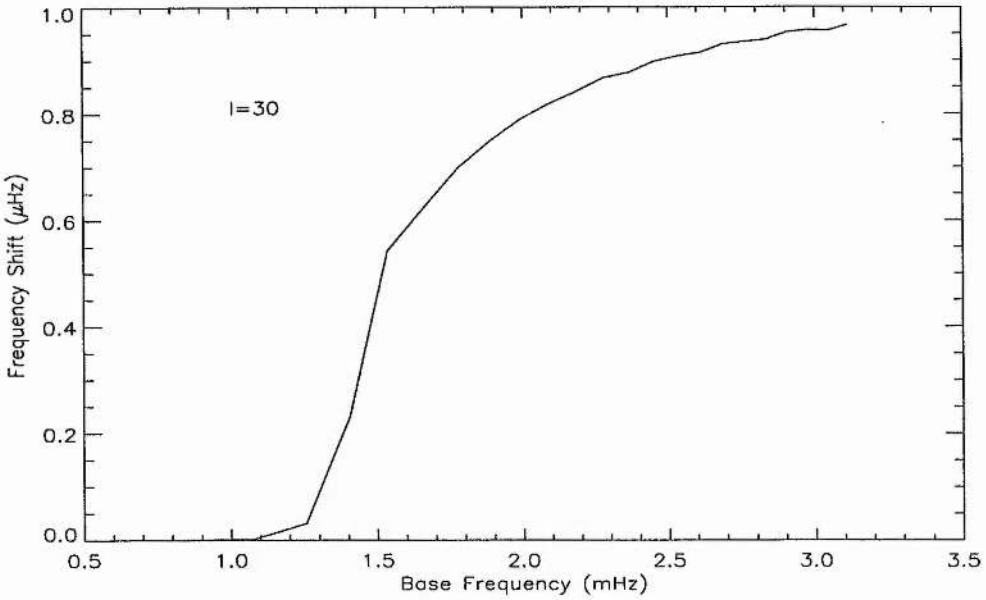

Figure 4.5: Changes in $p-$mode frequency calculated by Equation (4.64) for a reduction of 5000 km in the thickness of the magnetic layer. The results are plotted against mode frequencies for a field strength of 10^5G and a thickness of 20000 km. The degree $l = 30$.

corresponding mode for a magnetic layer that has narrowed by 5000 km. The results are shown in Figure 4.5, with $\triangle\nu$ plotted against $\nu(B_{lc} = 10^5\text{G}, z_c = 20000\text{km})$. The degree of the modes has been set equal to 30. From Figure 4.5 we see a more systematic change to the mode frequencies in that all modes show a frequency increase, with a steep increase at modes of low frequency followed by a levelling off of the curve as higher frequencies are reached. Again the $n = 1$ $p-$mode, which does not penetrate as far as the magnetic layer, is unaffected by changing the parameters of the magnetic layer.

4.6 A Possible Explanation for the Results of Section 4.5

The results presented in Section 4.5 are not consistent with the observed solar cycle behaviour of the $p-$modes. We are unable to pinpoint the reason why some modes should show an increase in frequency with an increase in magnetic field strength while others show a decrease. Unfortunately, the dispersion relation given by Equation (4.43) is not amenable to an analytical investigation but we may shed some light on the results of Section 4.5 if we consider the transit time τ_T of the modes across their cavity (the frequency of the mode

$\nu \propto 1/\tau_T$). The transit time τ_T is given by

$$\tau_T = \int_0^{z_{cav}} \frac{dz}{c_f(z)}, \tag{4.65}$$

where z_{cav} is the depth of the mode cavity. For this three layer model,

$$\tau_T = \tau_{T1} + \tau_{T2} + \tau_{T3}, \tag{4.66}$$

where τ_{T1} is the transit time across the uppermost field-free layer, τ_{T2} is the transit time across the magnetic layer and τ_{T3} the transit time across the lower field-free layer to the depth of the cavity. Hence, if we integrate across each layer in turn,

$$\tau_{T1} = \int_0^{z_{uc}} \frac{dz}{c_s(1+\frac{z}{z_{ou}})^{\frac{1}{2}}} \tag{4.67}$$

$$= \frac{2z_{ou}}{c_s}\left[\left(1+\frac{z_{uc}}{z_{ou}}\right)^{\frac{1}{2}} - 1\right], \tag{4.68}$$

$$\tau_{T2} = \int_{z_{uc}}^{z_{lc}} \frac{dz}{(c_c^2+v_{ac}^2)^{\frac{1}{2}}} = \frac{z_c}{(c_c^2+v_{ac}^2)^{\frac{1}{2}}}, \tag{4.69}$$

and

$$\tau_{T3} = \int_{z_{lc}}^{z_{cav}} \frac{dz}{c_c\left(1+\frac{z-z_c}{(z_{ou}+z_{uc})}\right)^{\frac{1}{2}}} \tag{4.70}$$

$$= \frac{2(z_{ou}+z_{uc})}{c_c}\left[\left(1+\frac{z_{cv}}{(z_{ou}+z_{uc})}\right)^{\frac{1}{2}} - 1\right], \tag{4.71}$$

where $z_{cv} = z_{cav} - z_{lc}$. Note that if we fix z_{uc}, the upper boundary of the magnetic layer, τ_{T1} is a constant and hence any variations in τ_T come from τ_{T2} and τ_{T3}.

As a first example, let us hold the cavity depth z_{cav} and the Alfvén speed v_{ac} fixed and allow the thickness of the magnetic layer to vary. We do this by varying z_{lc}, to z'_{lc} say. This then results in new travel times τ'_{T2} and τ'_{T3} of the modes, given by

$$\tau'_{T2} = \frac{z'_c}{(c_c^2+v_{ac}^2)^{\frac{1}{2}}}, \qquad z'_c = z'_{lc} - z_{lc} \tag{4.72}$$

and

$$\tau'_{T3} = \frac{2(z_{ou}+z_{uc})}{c_c}\left[\left(1+\frac{z'_{cv}}{(z_{ou}+z_{uc})}\right)^{\frac{1}{2}} - 1\right], \tag{4.73}$$

where $z'_{cv} = z_{cav} - z'_{lc}$. The differences in travel times $\triangle\tau_{T2}$ and $\triangle\tau_{T3}$ are then given by

$$\triangle\tau_{T2} = \tau'_{T2} - \tau_{T2} = \frac{\triangle z_{lc}}{(c_c^2 + v_{ac}^2)^{\frac{1}{2}}}, \tag{4.74}$$

where $\triangle z_{lc} = z'_{lc} - z_{lc}$, and

$$\triangle\tau_{T3} = \tau'_{T3} - \tau_{T3}, \tag{4.75}$$

$$= \frac{2(z_{ou} + z_{uc})}{c_c}\left[\left(1 + \frac{z'_{cv}}{(z_{ou} + z_{uc})}\right)^{\frac{1}{2}} - \left(1 + \frac{z_{cv}}{(z_{ou} + z_{uc})}\right)^{\frac{1}{2}}\right], \tag{4.76}$$

$$= \frac{2(z_{ou} + z_{uc})}{c_c}\triangle z_{cv}, \tag{4.77}$$

where

$$\triangle z_{cv} = \left(1 + \frac{z'_{cv}}{(z_{ou} + z_{uc})}\right)^{\frac{1}{2}} - \left(1 + \frac{z_{cv}}{(z_{ou} + z_{uc})}\right)^{\frac{1}{2}}. \tag{4.78}$$

The total difference in travel time, $\triangle\tau_T$, is then given by

$$\triangle\tau_T = \triangle\tau_{T2} + \triangle\tau_{T3}, \tag{4.79}$$

$$= \frac{\triangle z_{lc}}{(c_c^2 + v_{ac}^2)^{\frac{1}{2}}} + \frac{2(z_{ou} + z_{uc})}{c_c}\triangle z_{cv}. \tag{4.80}$$

From Equation (4.80) we see that if z_{lc} is decreased, i.e. if the magnetic layer narrows, then $\triangle z_{lc}$ is negative (hence $\triangle\tau_{T2} < 0$, which serves to increase mode frequencies ($\nu \propto 1/\tau$)) and vice versa. However, $\triangle z_{cv}$ is positive for a decrease in z_{lc} which increases the transit time and thus decreases mode frequencies. The dominant effect on mode frequencies comes from $\triangle\tau_{T2}$, however, as $\triangle z_{lc} >> \triangle z_{cv}$, for all z'_{lc}. This goes some way to explaining the results of Figure 4.5.

Turning now to a consideration of the magnetic parameters, we firstly investigate the consequences of increasing the magnetic field strength while z_{lc} and z_{cav} are held fixed. Inspection of Equation (4.70) shows that τ_{T3} is unaffected by these changes, but with a new magnetoacoustic fast speed, $c'_{fc}(= (c_c^2 + v_{ac}'^2)^{\frac{1}{2}})$, τ_{T2} changes by an amount

$$\triangle\tau_{T2} = \triangle\tau_T = \frac{z_c}{c'_{fc}} - \frac{z_c}{c_{fc}}, \tag{4.81}$$

$$= -z_c\triangle c_{fc} \tag{4.82}$$

where

$$\triangle c_{fc} = \frac{c'_{fc} - c_{fc}}{c_{fc} c'_{fc}}. \tag{4.83}$$

Hence, if we increase the magnetic field strength, $\triangle c_{fc}$ is positive, but with the minus sign appearing in Equation (4.82) the travel time is decreased, imposing a frequency increase. However, in Section 4.5 some modes exhibited a frequency decrease with an increase in B_{lc}, inconsistent with Equation (4.82).

In Section 4.5 the thickness of the magnetic layer was kept fixed while varying B_{lc}, so the only other possible variation that may occur is an associated change in the cavity depth z_{cav}. Then, the overall change in transit time in the lower region is

$$\triangle \tau_{T3} = \frac{2(z_{ou} + z_{uc})}{c_c} \left[\left(1 + \frac{z'_{ca}}{(z_{ou} + z_{uc})} \right)^{\frac{1}{2}} - \left(1 + \frac{z_{ca}}{(z_{ou} + z_{uc})} \right)^{\frac{1}{2}} \right], \tag{4.84}$$

where $z'_{ca} = z'_{cav} - z_{lc}$ and $z_{ca} = z_{cav} - z_{lc}$. Hence we write

$$\triangle \tau_{T3} = \frac{2(z_{ou} + z_{uc})}{c_c} \triangle z_{ca}, \tag{4.85}$$

where

$$\triangle z_{ca} = \left[\left(1 + \frac{z'_{ca}}{(z_{ou} + z_{uc})} \right)^{\frac{1}{2}} - \left(1 + \frac{z_{ca}}{(z_{ou} + z_{uc})} \right)^{\frac{1}{2}} \right]. \tag{4.86}$$

The overall change in travel time is then given by

$$\triangle \tau_T = -z_c \triangle c_{fc} + \frac{2(z_{ou} + z_{uc})}{c_c} \triangle z_{ca}. \tag{4.87}$$

If the cavity depth is decreased along with a rise in magnetic field strength, then $\triangle z_{ca} < 0$ and $\triangle \tau_T < 0$, for all z'_{cav}. However, if z_{cav} is increased then $\triangle z_{ca} > 0$. Large changes in magnetic field strength are necessary for small changes to c_{fc} at the base of the convection zone, owing to the high gas pressure; therefore $\triangle c_{fc}$ is not always sufficiently large to counteract the negative effect of increasing the cavity depth.

4.7 How does the Magnetic Layer Modify the Eigenfunctions of the Modes?

As a final study for the p–modes of general degree l, we look at the behaviour of the eigenfunctions of the modes, concentrating our attention on the region around the

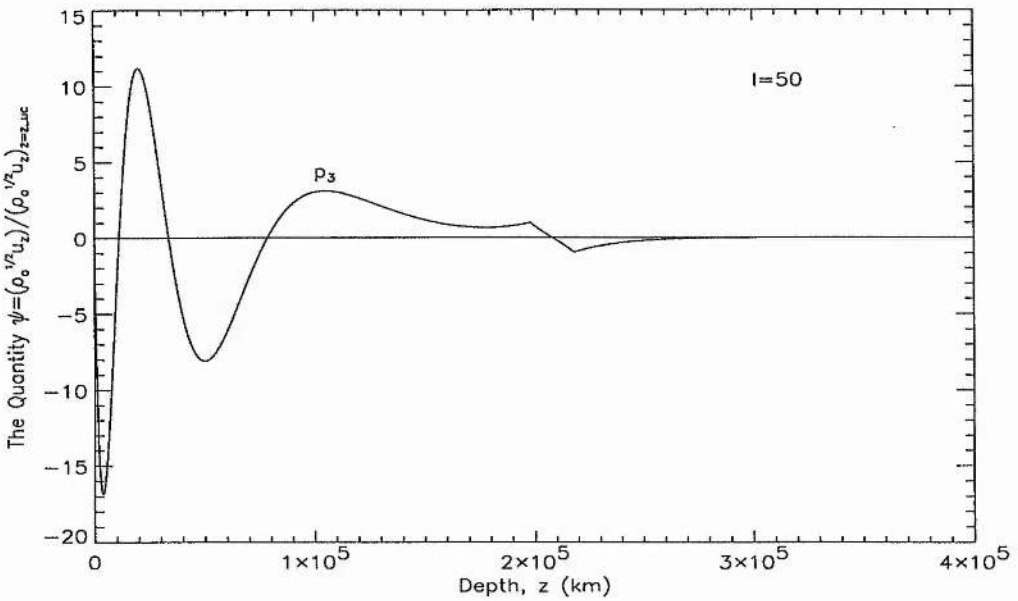

Figure 4.6: The parameter ψ, related to the kinetic energy density of vertical motions, plotted against depth z for the p_3 mode of degree $l = 50$. The magnetic field strength is set equal to 3.10^7G, close to the equipartition field strength, in order to display clearly the behaviour of the mode around the magnetic layer.

magnetic layer. In order to accomplish this, we calculate ψ, which is related to the energy density of the modes (see Chapter 3); specifically,

$$\psi(z) = \frac{\rho_o^{\frac{1}{2}} u_z}{(\rho_o^{\frac{1}{2}} u_z)_{z=z_{uc}}}, \tag{4.88}$$

where ψ is normalised relative to the depth $z = z_{uc}$. Also, to more clearly illustrate the behaviour of the modes as they encounter the magnetic layer, we set the strength of the magnetic field close to its equipartition value. We choose $B_{lc} = 3.10^7$G.

In Figure 4.6 we show ψ plotted against depth z for the p_3 mode of degree $l = 50$. For comparison, Figure 4.7 shows the equivalent mode when $B_{lc} = 0$. Note the different scales on ψ on the two figures. From Figures 4.6 and 4.7 the effect of the magnetic layer on ψ is obvious. In the convection zone ($0 < z < z_{uc}$) the same qualitative behaviour of ψ is seen in both figures, with the nodes of ψ all at the same depths. The difference in scales in the two figures is related to the depth $z = z_{uc}$ at which we have normalised ψ. The p_3 mode satisfies the condition that $4AH_c^2 < 1$ and as a result becomes evanescent at the depth of the magnetic layer. In fact, looking at Figure 4.7 we see that this mode begins to decay

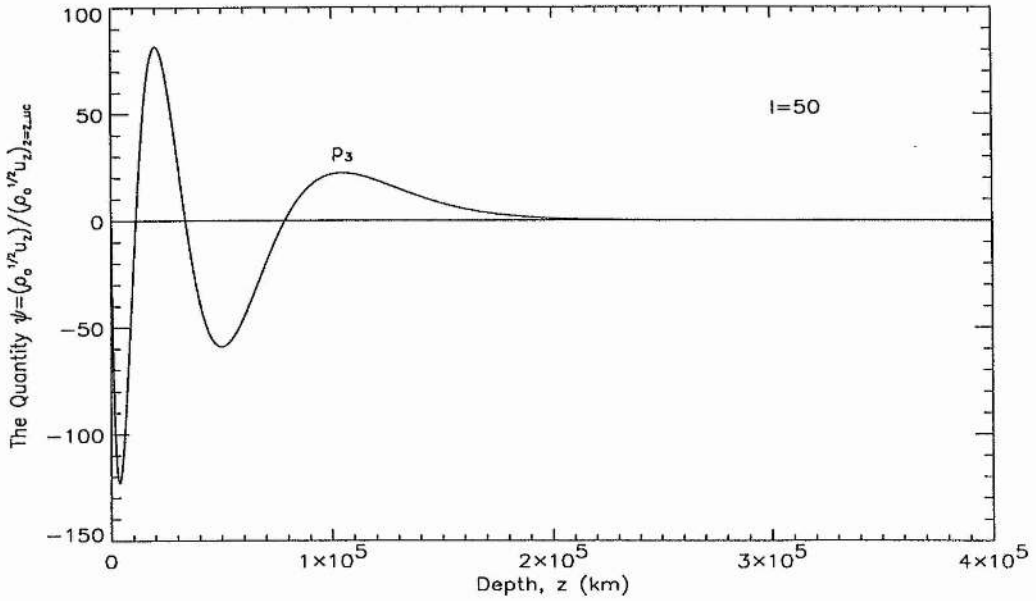

Figure 4.7: As in Figure 4.6 but with $B_{lc} = 0$.

way above $z = z_{uc}$. In the presence of a strong magnetic field, we see that ψ is actually increased as it approaches $z = z_{uc}$ and is no longer smoothly evanescent in Figure 4.6, as it is in Figure 4.7.

The magnetic interface at $z = z_{uc}$ gives rise to a sharp discontinuity in the gradient of ψ, and for the extremely strong field that we have chosen an extra node is produced in the standing wave pattern midway within the magnetic layer.

As a further example, Figure 4.8 shows ψ plotted against depth z for the p_8 mode of degree $l = 50$. This mode differs from the p_3 mode in that it satisfies the condition $4AH_c^2 > 1$, and the mode is oscillatory in nature throughout the magnetic layer. From Figure 4.8 we can see that the overall change in the behaviour of ψ around the magnetic layer is slight. A discontinuity in the gradient of ψ is present at $z = z_{uc}$ and $z = z_{lc}$ but the magnetic layer simply causes a steeper drop in ψ in the isothermal layer.

Finally, an interesting behaviour in ψ is seen in some of the higher order modes. Figure 4.9 displays ψ for the p_{22} mode plotted against depth z. The equivalent mode when $B_{lc} = 0$ is shown in Figure 4.10. Figures 4.9 and 4.10 both show an oscillatory decay of ψ throughout the convection zone but now the presence of a high magnetic field has an extreme effect on the mode. In Figure 4.9, ψ grows rapidly through the magnetic layer to values equivalent to those found in the upper convection zone. Below the magnetic layer

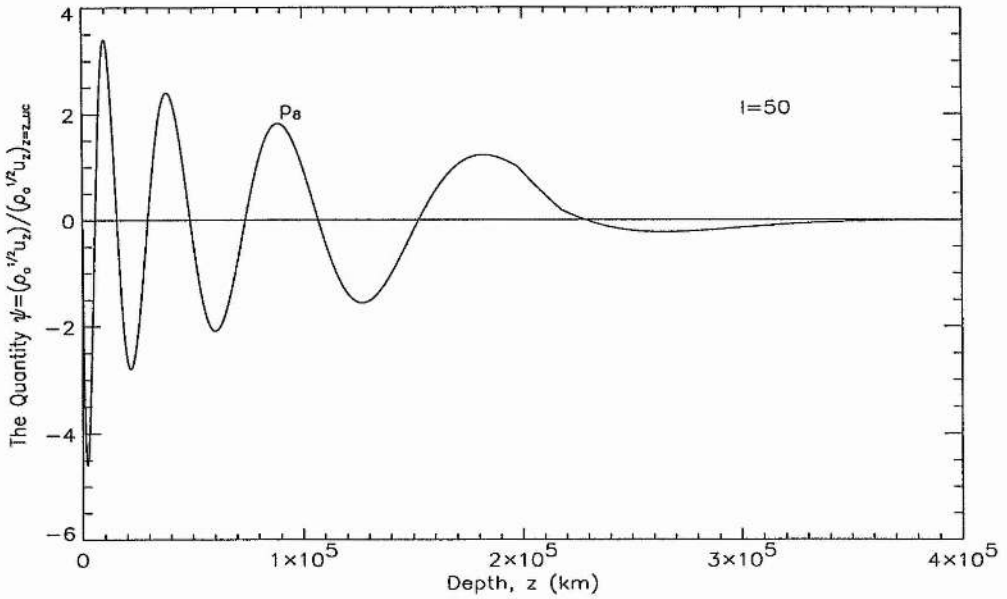

Figure 4.8: The normalised value of ψ plotted against depth z for the p_8 mode of degree $l = 50$. As in Figure 4.6, $B_{lc} = 3.10^7$G.

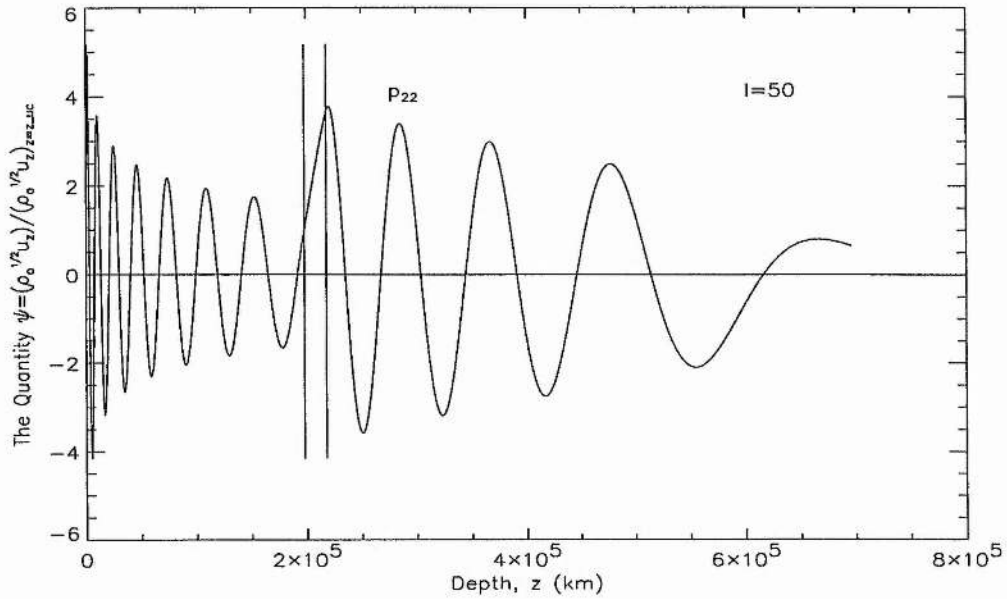

Figure 4.9: A plot of ψ calculated from Equation (4.88) for the p_{22} mode of degree $l = 50$, displaying an amplification of ψ through the magnetic layer. The vertical lines show the position of the magnetic layer. Note the change in horizontal scale compared to Figures 4.6-4.8.

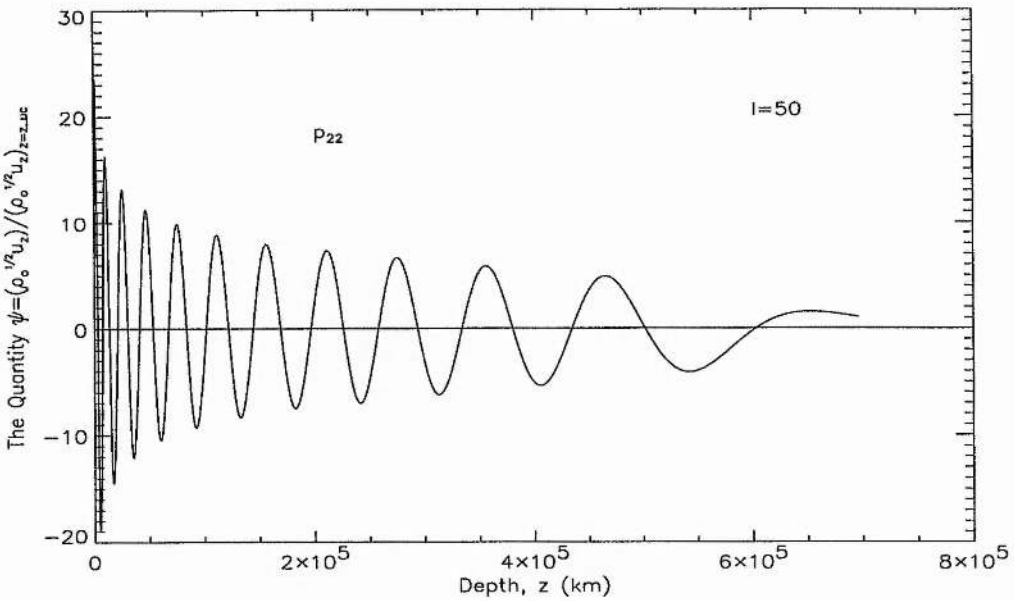

Figure 4.10: As in Figure 4.9 but with $B_{lc} = 0$.

ψ once again begins to decay in an oscillatory manner but its magnitude remains greatly enhanced compared to the non-magnetic case of Figure 4.10. In Figure 4.9 the vertical lines show the position of the magnetic interfaces at $z = z_{uc}$ and $z = z_{lc}$. We have been unable to offer a satisfactory explanation for this behaviour.

4.8 The Special Case $l = 0$

A special case that we may consider in the study of a buried magnetic layer is the radial modes of oscillation, i.e. modes of degree zero where $l = 0$ (see Chapter 2). The dispersion relation given by Equation (4.43) does not apply to these modes but we may modify the model of Chapter 2 to include a magnetic region at the base of the convection zone. The equilibrium of the model is simply that given in Section 4.2 but, as in Chapter 2, the fluid is taken to range in depth z from 0 to z_d, where z_d is taken to be the radius of the Sun, rather than being semi-infinite in extent. A fuller explanation of why we proceed in this way is given in Chapter 2.

4.8.1 The governing differential equations and their solutions

The equilibrium temperature, density and pressure profiles for this model are those of Section 4.2 but now we place a rigid wall at $z = z_d$. The equations governing plasma motions within the system are Equations (4.15)-(4.21). For modes of degree zero the velocity perturbation is

$$\mathbf{u} = (0, 0, u_z(z))e^{i\omega t}, \tag{4.89}$$

where ω is the angular frequency of the disturbance. The governing differential equation for the perturbation u_z is given by Equation (2.24) in Chapter 2, namely

$$\frac{d}{dz}\left[\rho_o(z)[c_s^2(z) + v_a^2(z)]\frac{du_z}{dz}\right] + \rho_o(z)\omega^2 u_z = 0. \tag{4.90}$$

The solution of Equation (4.90) proceeds much as described in Chapter 2, and so only a brief treatment is necessary here. The flow u_z is given by

$$u_z = r^{-m}\left[c_1 J_m(r) + c_2 Y_m(r)\right], \qquad 0 < z < z_{uc}, \tag{4.91}$$

with

$$r = \frac{2\omega z_o}{c_s}\left(1 + \frac{z}{z_{ou}}\right)^{\frac{1}{2}}. \tag{4.92}$$

For the lower polytropic region ($z_{uc} < z < z_{lc}$) the method of solution is analogous to that in obtaining Equation (4.91). The sound speed squared in this region is given by

$$c_s(z)^2 = c_c^2\left(1 + \frac{z - z_{lc}}{z_{ou} + z_{uc}}\right), \qquad z_{lc} < z < z_d. \tag{4.93}$$

Substituting this sound speed profile into Equation (4.90) with $v_a(z) = 0$ leads to

$$\left(1 + \frac{z - z_{lc}}{z_{ou} + z_{uc}}\right)\frac{d^2u_z}{dz^2} + \frac{m+1}{z_{ou} + z_{uc}}\frac{du_z}{dz} + \frac{\omega^2}{c_c^2}u_z = 0. \tag{4.94}$$

Setting

$$p = 1 + \frac{z - z_{lc}}{z_{ou} + z_{uc}} \tag{4.95}$$

yields

$$p\frac{d^2u_z}{dp^2} + (m+1)\frac{du_z}{dp} + \frac{\omega^2(z_{ou} + z_{uc})^2}{c_c^2}u_z = 0. \tag{4.96}$$

Putting

$$s = \frac{2\omega(z_{ou} + z_{uc})}{c_c}p^{\frac{1}{2}} \tag{4.97}$$

simplifies Equation (4.96) to

$$s^2\frac{d^2u_z}{ds^2}+(2m+1)s\frac{du_z}{ds}+s^2u_z=0. \tag{4.98}$$

Finally, setting

$$u_z=s^{-m}X, \tag{4.99}$$

leads to Bessel's equation for functions of order m (Abramowitz and Stegun 1965: 9.1.1):

$$s^2\frac{d^2X}{ds^2}+s\frac{dX}{ds}+(s^2-m^2)X=0. \tag{4.100}$$

The general solution to Equation (4.100) is

$$X=c_3J_m(s)+c_4Y_m(s), \tag{4.101}$$

where $J_m(s)$ and $Y_m(s)$ are Bessel functions of the first and second kind, and c_3 and c_4 are constants of integration.

The velocity perturbation $u_z(z)$ in $[z_{lc},z_d]$ is therefore given by

$$u_z(z)=s^{-m}[c_3J_m(s)+c_4Y_m(s)], \tag{4.102}$$

where

$$s=\frac{2\omega(z_{ou}+z_{uc})}{c_c}\left(1+\frac{z-z_{lc}}{z_{ou}+z_{uc}}\right)^{\frac{1}{2}}. \tag{4.103}$$

Turning now to the isothermal magnetic layer on $[z_{uc},z_{lc}]$, Equation (4.90), under the assumption of constant sound and Alfvén speeds, reduces to

$$\frac{d^2u_z}{dz^2}+\frac{1}{H_c}\frac{du_z}{dz}+\frac{\omega^2}{(c_c^2+v_{ac}^2)}u_z=0. \tag{4.104}$$

Equation (4.104) has solutions of the form

$$u_z(z)=\mathcal{A}e^{\mu_+z}+\mathcal{B}e^{\mu_-z}, \tag{4.105}$$

where

$$2H_c\mu_\pm=-1\pm\left(1-\frac{\omega^2}{\omega_{cmac}^2}\right)^{\frac{1}{2}}. \tag{4.106}$$

Note that both solutions to Equation (4.104) are retained in Equation (4.105). This is because there is no boundary condition on the total decay of the kinetic energy density applied in this region.

In Equation (4.106) we have introduced the cut-off frequency ω_{cmac} of the magnetic layer, defined by

$$\omega_{cmac}^2 = \frac{(c_c^2 + v_{ac}^2)}{4H_c^2}. \tag{4.107}$$

The square root in Equation (4.106) again defines whether the modes are either evanescent at the depth of the magnetic layer or are still oscillatory in nature (see Section 4.3.2), but now the condition is somewhat simpler with ω either satisfying $\omega^2 < \omega_{cmac}^2$ or $\omega^2 > \omega_{cmac}^2$. Because H_c is large in the submerged region, ω_{cmac} is generally very small. Hence, as ω is usually greater than ω_{cmac}, we write the parameter μ as

$$2H_c\mu_{\pm} = -1 \pm i\left(\frac{\omega^2}{\omega_{cmac}^2} - 1\right)^{\frac{1}{2}}, \tag{4.108}$$

and Equation (4.105) may be cast in the form

$$u_z(z) = e^{\frac{-z}{H_c}}[\mathcal{C}\sin\sigma z + \mathcal{D}\cos\sigma z], \tag{4.109}$$

where

$$2H_c\sigma = \left(\frac{\omega^2}{\omega_{cmac}^2} - 1\right)^{\frac{1}{2}}. \tag{4.110}$$

Overall, then, the vertical velocity disturbance $u_z(z)$ takes on different forms, depending on whether ω is less than or greater than ω_{cmac}: if $\omega < \omega_{cmac}$, the total velocity profile for the model is given by

$$u_z = \begin{cases} r^{-m}\left[c_1 J_m(r) + c_2 Y_m(r)\right], & 0 < z < z_{uc}, \\ \mathcal{A}e^{\mu+z} + \mathcal{B}e^{\mu-z}, & z_{uc} < z < z_{lc}, \\ s^{-m}\left[c_3 J_m(s) + c_4 Y_m(s)\right], & z_{lc} < z < z_d, \end{cases} \tag{4.111}$$

and if $\omega > \omega_{cmac}$ it is given by

$$u_z = \begin{cases} r^{-m}\left[c_1 J_m(r) + c_2 Y_m(r)\right], & 0 < z < z_{uc}, \\ e^{\frac{-z}{H_c}}[\mathcal{C}\sin\sigma z + \mathcal{D}\cos\sigma z], & z_{uc} < z < z_{lc}, \\ s^{-m}\left[c_3 J_m(s) + c_4 Y_m(s)\right], & z_{lc} < z < z_d. \end{cases} \tag{4.112}$$

Here

$$r = \frac{2\omega z_{ou}}{c_s}\left(1 + \frac{z}{z_{ou}}\right)^{\frac{1}{2}}, \tag{4.113}$$

$$2H_c\mu_{\pm} = -1 \pm \left(1 - \frac{\omega^2}{\omega_{cmac}^2}\right)^{\frac{1}{2}}, \tag{4.114}$$

$$2H_c\sigma = \left(\frac{\omega^2}{\omega_{cmac}^2} - 1\right)^{\frac{1}{2}}, \tag{4.115}$$

and

$$s = \frac{2\omega(z_{ou} + z_{uc})}{c_c}\left(1 + \frac{z - z_{lc}}{z_{ou} + z_{uc}}\right)^{\frac{1}{2}}. \tag{4.116}$$

The derivatives of u_z may be found quite easily, using Equations (2.42)-(2.43) and Equation (2.45) for the Bessel function solutions.

4.8.2 Dispersion relations and mode frequencies

With the inclusion of a magnetic layer into the model described in Chapter 2, two more boundary conditions must also be applied, additional to those of Chapter 2, to furnish us with the correct dispersion relation. The rigid walls at $z = 0$ and $z = z_d$ require that

$$u_z = 0 \quad \text{at} \quad z = 0 \quad \text{and} \quad z = z_d. \tag{4.117}$$

A further two conditions are simply that

$$u_z \quad \text{is} \quad \text{continuous} \quad \text{across} \quad z = z_{uc} \quad \text{and} \quad z = z_{lc}. \tag{4.118}$$

Finally, the Lagrangian pressure perturbation must be continuous across the magnetic interfaces. This requires that

$$\rho_o(z)(c_s^2(z) + v_a^2(z))\frac{du_z}{dz} \tag{4.119}$$

is continuous across $z = z_{uc}$ and $z = z_{lc}$ (see Chapter 2).

Application of the six boundary conditions (4.117)-(4.119) leads, after some algebra, to the dispersion relation of the model. For the case $\omega > \omega_{cmac}$, the dispersion relation is

$$\begin{aligned}\left[4H_c^2\sigma^2\alpha_1\alpha_2 + (\Psi\alpha_3 - \alpha_1)(\Psi\alpha_4 - \alpha_2)\right]\sin\sigma z_c \\ = 2H_c\sigma\Psi\left[\alpha_1\alpha_4 - \alpha_2\alpha_3\right]\cos\sigma z_c,\end{aligned} \tag{4.120}$$

where

$$\Psi = \frac{\gamma c_c\omega}{\Gamma_c c_{fc}\omega_{cmac}}, \tag{4.121}$$

$$\alpha_1 = J_m(r_{uc})Y_m(r_o) - Y_m(r_{uc})J_m(r_o), \tag{4.122}$$

$$\alpha_2 = J_m(s_{lc})Y_m(s_d) - Y_m(s_{lc})J_m(s_d), \tag{4.123}$$

$$\alpha_3 = J_{m+1}(r_{uc})Y_m(r_o) - Y_{m+1}(r_{uc})J_m(r_o), \tag{4.124}$$

and

$$\alpha_4 = J_{m+1}(s_{lc})Y_m(s_d) - Y_{m+1}(s_{lc})J_m(s_d). \tag{4.125}$$

The magnetoacoustic fast speed c_{fc} within the magnetic layer is

$$c_{fc} = (c_c^2 + v_{ac}^2)^{\frac{1}{2}}. \tag{4.126}$$

The parameters arising in the Bessel function combinations of Equations (4.122)-(4.125) are

$$r_o = \frac{2\omega z_{ou}}{c_s}, \qquad r_{uc} = \frac{2\omega z_{ou}}{c_s}\left(1 + \frac{z_{uc}}{z_{ou}}\right)^{\frac{1}{2}}, \tag{4.127}$$

and

$$s_{lc} = \frac{2\omega(z_o + z_{uc})}{c_c}, \qquad s_d = \frac{2\omega(z_{ou} + z_{uc})}{c_c}\left(1 + \frac{z_d - z_{lc}}{z_{ou} + z_{uc}}\right)^{\frac{1}{2}}. \tag{4.128}$$

When $\omega < \omega_{cmac}$ we may write

$$\sigma = i\kappa, \tag{4.129}$$

where

$$2H_c\kappa = \left(1 - \frac{\omega^2}{\omega_{cmac}^2}\right)^{\frac{1}{2}}. \tag{4.130}$$

Therefore, remembering that

$$\sin iz = i\sinh z \qquad \text{and} \qquad \cos iz = \cosh z, \tag{4.131}$$

Equation (4.120) becomes

$$\begin{aligned}\left[(\Psi\alpha_3 - \alpha_1)(\Psi\alpha_4 - \alpha_2) - 4H_c^2\kappa^2\alpha_1\alpha_2\right]\sinh\kappa z_c \\ = 2H_c\kappa\Psi\left[\alpha_1\alpha_4 - \alpha_2\alpha_3\right]\cosh\kappa z_c.\end{aligned} \tag{4.132}$$

Equation (4.120) or (4.132) provides the dispersion relation for a model consisting of three layers of fluid confined at $z = 0$ and $z = z_d$ by rigid boundaries. The outer two layers of the model are polytropic in nature, whilst the middle layer contains a magnetic field structured in such a way so as to give a constant Alfvén speed. It is specifically derived for

Parameter	Value
z_{uc}	200,000 km
z_c	15,000 km
T_c	$3,415,212^o$ K
P_{uc}	1.666×10^9 kg m^{-1} s^{-2}
c_c	191.25 km s^{-1}
$H_c(B_{uc} = 0)$	80,000 km

Table 4.2: The parameters for the isothermal layer used in solving Equations (4.120) and (4.132) when B_{uc} is set to zero. The values at $z = 0$ correspond to those at the temperature minimum given in Table 2.1 of Chapter 2.

modes of degree zero and cannot be reproduced analytically by letting $k_x \rightarrow 0$ in Equation (4.43).

Before we solve the dispersion relation numerically, note that Equations (4.120) and (4.132) have ω_{cmac} as a solution. For this frequency, both σ and κ are zero and it can be shown that the only solution for u_z is the trivial one. All of the constants on $[z_{uc}, z_{lc}]$ are zero for this case, except C, which tends to infinity. However, as it appears in the combination $C \sin \sigma z$ it is easy to show that

$$\lim_{\sigma \rightarrow 0} [C \sin \sigma z] = 0. \tag{4.133}$$

Using this, we may show that the constants of integration in the other two layers, $c_1 - c_4$, are also zero. Hence, for disturbances with the frequency $\omega = \omega_{cmac}$ then $u_z = 0$.

To test the dispersion relation given by Equations (4.120) and (4.132), let us first set $B_{uc} = 0$ and choose the thickness of the magnetic layer to be $z_c = 1.5 \times 10^4$ km. Also, we set the parameters of the model relative to $z = 0$ and use the parameters given by Table 2.1. This is simply an exercise in checking the dispersion relation of this section by comparing it to the model of Chapter 2. The dispersion relation is simplified somewhat by setting $v_{ac} = 0$, for which the magnetoacoustic cut-off frequency $\omega_{cmac} \rightarrow \omega_{cac}$, where ω_{cac} is the acoustic cut-off frequency of the now field-free layer defined by

$$\omega_{cac} = \frac{c_c^2}{g\gamma}, \tag{4.134}$$

and the parameter Ψ becomes

$$\Psi = \frac{\omega}{\omega_{cac}}. \tag{4.135}$$

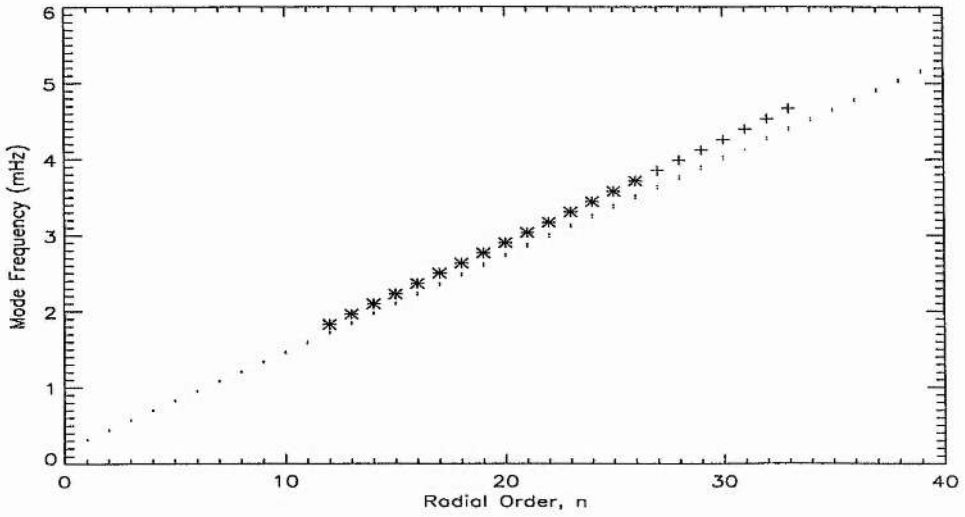

Figure 4.11: Mode Frequencies (in mHz) plotted against radial order n for the case when $B_{lc} = 0$ and $z_c = 15000$ km, shown as the lower line of dots (...). The crosses (+) are the observed frequencies of Libbrecht *et al.* (1990) and the stars (*) those of Elsworth *et al.* (1994). The upper row of dots show the calculated frequencies displayed in Figure 2.1 of Chapter 2.

The typical solar values given in Table 2.1 are used again for conditions at $z = 0$ in the numerical solutions of Equations (4.120) and (4.132). The values given at the depth of the upper boundary of the magnetic layer and the temperature and sound speed within the magnetic layer are then as given in Table 4.2.

From Equations (4.120) and (4.132) with the cut-off frequency given by Equation (4.134) and Ψ given by Equation (4.135), we are able to reproduce the linear dependence of mode frequency on radial order, n. The sequence of solutions calculated from the dispersion relation are displayed in Figure 4.11 as the lower line of dots (....). Figure 4.11 shows mode frequency ν ($\equiv \omega/2\pi$) in mHz plotted against radial order, n ranging from 0 to 40.

For comparison with observational results and the findings of Chapter 2 we have re-plotted the results of Figure 2.1 in Figure 4.11. As in Figure 2.1, the crosses (+ + +) are taken from the observations of Libbrecht *et al.* (1990) and the stars (* * *) from the observations of Elsworth *et al.* (1994). The upper line of dots (...) are the base mode frequencies of Chapter 2, calculated from Equation (2.64).

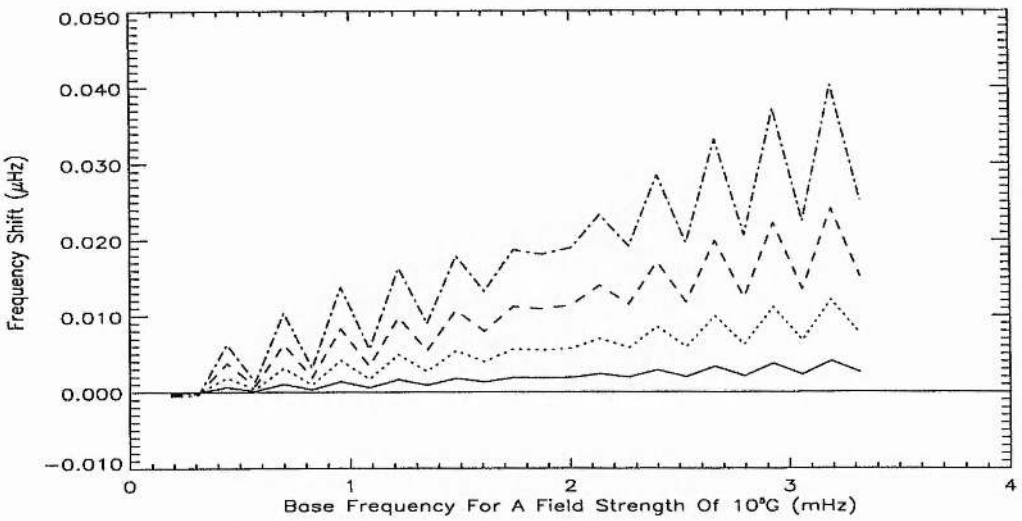

Figure 4.12: The changes in mode frequency found from Equation (4.136) for modes of degree zero. The results are plotted against the frequencies for a field strength of 10^5G. Increases in magnetic field strength to 3.10^5G (solid curve), 5.10^5G (dotted curve), 7.10^5G (dashed curve) and 9.10^5G (dot-dashed curve) are used.

From Figure 4.11 we may see that the resultant mode frequencies for a model with a submerged isothermal layer are somewhat less than their purely polytropic counterparts. This result is not difficult to understand. In the three layer model, the range of z taken is on the range $[0, z_d]$, the same as that in Chapter 2. However, the temperature at the lower interface ($z = z_{lc}$) is the same as that at the upper interface ($z = z_{uc}$). As a result there is a lower temperature at $z = z_d$ in the model of this chapter. Hence the inclusion of the isothermal layer leads to an increased transit time for the modes which serves to *decrease* their frequency.

To see if the region of magnetic field below the convection zone has any bearing on the solar cycle behaviour of $p-$modes, the strength of the field will be allowed to vary, as in Section 4.5, and the resultant changes in mode frequency calculated. In order to compare results, we now set the parameters for this model equal to those given in Table 4.1.

4.8.3 The effect of variations of the magnetic layer on oscillation frequencies

The procedure that we shall follow for determining frequency changes within the model will be analogous to that used in Section 4.5. Again, we set a base strength for the magnetic field within the isothermal layer to represent conditions at solar minimum. In this section, we use base field strengths of 10^5G and 10^6G and then allow the field to grow above these values. The first frequency difference that we calculate is given by

$$\triangle\nu = \nu(B_{lc}) - \nu(B_{lc} = 10^5\text{G}), \tag{4.136}$$

where $\nu(B_{lc} = 10^5\text{G})$ is the base frequency of a radial mode in the presence of a 10^5G magnetic field and $\nu(B_{lc})$ is a mode of equivalent radial order for an increase in B_{lc}. The frequency shifts $\triangle\nu$ of Equation (4.136) are shown in Figure 4.12 plotted against $\nu(B_{lc} = 10^5\text{G})$. Figure 4.12 displays the frequency changes brought about by field strengths of 3.10^5G (solid curve), 5.10^5G (dotted curve), 7.10^5G (dashed curve) and 9.10^5G (dot-dashed curve).

In Figure 4.12 the frequency shifts incurred by raising the internal magnetic field strength show a scatter, but now they are different to the results of Section 4.5 and there is a positive gradient overall to $\triangle\nu$ as ν increases, with the frequency shifts scattered about this gradient. As in Section 4.5 the magnitude of the frequency shifts increases as B_{lc} is raised. Note also that the magnitude of the frequency differences are comparable in Figures 4.12 and 4.2, indicating that the frequency shifts are not highly dependent on the degree of the modes. The scatter in frequency changes around a generally increasing trend may be explained by the rigid walls we have placed at $z = 0$ and $z = z_d$. The fixed range in depth z of the model tends to force preferred wavelengths on to the system, which do not change when varying B_{lc}. As a result this leads to a discretisation of the modes with the frequencies being forced to fit these wavelengths.

Finally, we raise the internal base field strength to 10^6G and calculate the frequency difference $\triangle\nu$ given by

$$\triangle\nu = \nu(B_{lc}) - \nu(B_{lc} = 10^6\text{G}), \tag{4.137}$$

where $\nu(B_{lc} = 10^6\text{G})$ is the frequency of a mode at the base field strength and $\nu(B_{lc})$ is the equivalent mode for a higher value of B_{lc}. The results of Equation (4.137), with $\triangle\nu$ plotted against $\nu(B_{lc} = 10^6\text{G})$, are shown in Figure 4.13. The same trend in $\triangle\nu$ is seen in Figure

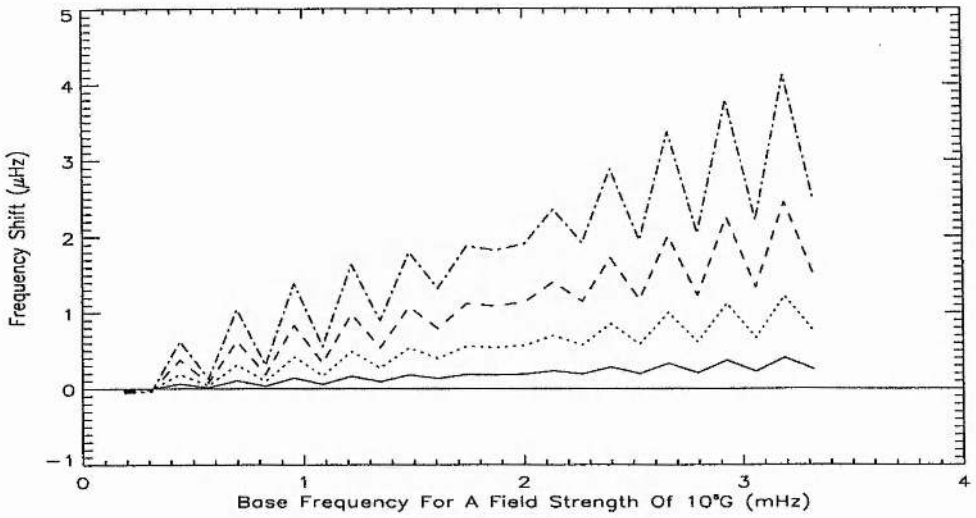

Figure 4.13: The results of Equation (4.137) plotted against the base frequencies for a field of 10^6G. The curves shown correspond to increases in magnetic field strength to 3.10^6G (solid curve), 5.10^6G (dotted curve), 7.10^6G (dashed curve) and 9.10^6G (dot-dashed curve) are used.

4.13 but as expected the magnitude of $\triangle\nu$ is much greater than seen in Figure 4.12. Again, as in Section 4.5, Figures 4.12 and 4.13 point to $\triangle\nu$ being proportional to B_{lc}^2.

4.9 Discussion

In this chapter, a three layer model has been used to assess the influence of an internal, sub-convective, magnetic field on $p-$mode frequencies. The two field-free layers contain linear equilibrium temperature profiles stratified in such a way so as to maintain stability to convective motions. Between these two layers we have a thin isothermal layer permeated by a horizontal magnetic field, the equilibrium structure of which is taken to be such that a constant Alfvén speed is present in the layer. A rigid wall is placed at $z = 0$.

Variations in the strength of the buried magnetic layer will lead to corresponding variations in the frequencies of the $p-$modes whose cavities extend to or below the depth of the magnetic region. Through this, we hope to place bounds on the highly controversial question of the strength of the sub-convective zone magnetic field (see Section 4.1) by

attempting to match the frequency changes imposed on the $p-$modes of this model with the observed solar cycle variation.

The results that we have found from this model have not reproduced the observed variation of the $p-$mode frequencies with the solar cycle. By choosing base field strengths of 10^4G, 10^5G or 10^6G (Section 4.5), modes of degree $l = 30$ showed no systematic trend to frequency changes when the field strength was increased above these values (Figures 4.1-4.3). Some modes showed an increase in frequency while others exhibited a decrease. The presence of a magnetic layer at the base of the convection zone varied the frequencies of the $p-$modes by an amount proportional to the square of the magnetic field strength. For example, raising the strength of the magnetic field from 10^4G to 5.10^4G increased the frequency of the p_6 mode by 7.10^{-5} μHz. The same mode under a rise in B_{lc} from 10^5G to 5.10^5G showed a 0.007 μHz increase, and when the field was increased from 10^6G to 5.10^6G it suffered a 0.7 μHz increase. Making a tentative comparison with the observations, Figure 4.3 would appear to indicate that a base field strength of 10^6G is most likely; it is very unlikely that the field would increase to strengths of 3.10^6G-5.10^6G over the course of the solar cycle. This is comparable to (though somewhat higher than) the result found by Campbell and Roberts (1986) who predict a peak field strength of 5.10^5G-10^6G as necessary to produce the required frequency shifts. We are not claiming that this large increase in the strength of the sub-convective magnetic field is actually present in the Sun.

We compared the results of Figure 4.2 with the same changes in magnetic field strength but for higher degree modes (specifically $l = 100$; see Figure 4.4). As expected, more modes in Figure 4.4 showed no change in mode frequency. However a similar, apparently random, spread in $\triangle\nu$ was seen for $l = 100$ modes that penetrate the magnetic layer as we saw for modes with $l = 30$. Also, the frequency changes for $l = 100$ modes were only approximately twice those of the $l = 30$ modes, indicating that the frequency changes are only weakly dependent on l in this model.

Finally, for modes of general l, we examined the effect of varying the thickness of the magnetic layer. From this, we saw that a decrease in the thickness of the magnetic layer of 5000 km, while the magnetic field strength remained fixed at 10^5G, led to a steep rise in mode frequencies in the frequency range 1-2 mHz, with the shift curve becoming more shallow at higher frequencies. Although through this we were not able to reproduce a downturn at higher frequencies, the actual magnitude of the frequency variations was not too far away from the observed values, with frequency shifts up to 1 μHz being seen.

As a limiting case for this study, we have looked at the model that specifically describes the radial modes of the Sun for which $l = 0$ (Section 4.8). Figures 4.12 and 4.13 would again appear to indicate that frequency changes brought about by the magnetic layer are $\propto B_{lc}^2$, but we cannot reproduce the observed frequency variations by altering B_{lc} alone. However, for the modes of degree zero, there is a trend to the frequency shifts in that the $n = 0$ and $n = 1$ modes show a frequency decrease, while all others show an increase, and that on average, there is a systematic increase in the magnitude of $\triangle\nu$ as ν increases.

This model has been unable to reproduce the observed solar cycle variation in the $p-$mode frequencies. However, this does not discount the possibility that it may in fact be variations in the sub-convective magnetic field that are responsible for the observed shifts. Our model takes no account of the stability aspects of such a magnetic field (since we are using a plane-parallel model with the magnetic field being horizontal and infinite in extent). Also of importance is the very simple and basic assumption that the magnetic layer is isothermal; a more complex thermal structure may produce significant differences. However, our wish has been to examine an analytical model and the model presented here permits such an approach whereas a more complicated model would require a fully numerical approach. Therefore, we may conclude that although this model sheds no further light on the position within the Sun responsible for varying $p-$mode frequencies over the course of the solar cycle, the influence of the region at the base of the convection zone cannot be ruled out and it may take a model utilising more sophisticated physics to study the effects of this layer on mode frequencies in greater detail.

Chapter 5

The Surface and Body Waves Associated with the Magnetic Layer at the Base of the Convection Zone

5.1 Introduction

Magnetoacoustic surface waves exist wherever there is an abrupt change in the magnetic field strength, or plasma density, pressure, or temperature. In the Sun, rapid changes in magnetic field strength and plasma density are seen in structures such as sunspots, coronal loops and prominences, to name but a few.

In an attempt to understand the waves such objects may support, various structures have been used: the step function, where the magnetic field changes discontinuously from one place to another; an isolated slab or cylinder of magnetic flux; and an embedded slab or cylinder of magnetic flux. The solar atmosphere shows a number of objects that may be described approximately by these simple structures although in reality the objects themselves are far more complex. For example, the isolated tube is seen in the photosphere, and embedded tubes of flux are akin to coronal loops in the magnetically filled corona. Such objects may be viewed as containing step functions as, for example, the interface between the field-free photosphere and the horizontal canopy field of the chromosphere.

Many studies of magnetohydrodynamic waves have been made for the case of a

single magnetic interface in an incompressible medium (see the discussion in Chandrasekhar 1961). The surface waves arising for this case are seen to have a phase speed c_{ph} given by

$$c_{ph} = \left(\frac{\rho_o v_{ao}^2 + \rho_e v_{ae}^2}{\rho_o + \rho_e} \right)^{\frac{1}{2}}, \tag{5.1}$$

where ρ_o and v_{ao} are the plasma density and the Alfvén speed, respectively, on one side of the interface, and ρ_e and v_{ae} are the equivalent values on the other side of the interface. The phase speed given in Equation (5.1) has also arisen in studies of surface waves in magnetic flux tubes (see, for example, Spruit 1983; Spruit and Roberts 1983; Ryutova 1990).

Models of surface waves in compressible media have also been studied. The case of a single magnetic interface has been studied by, for example, Wentzel (1979), Roberts (1981*a*) and Miles and Roberts (1989). The effect of compressibility showed an extra mode in the work of Roberts (1981*a*) over the simple incompressible case.

One major candidate for a magnetoacoustic surface wave is the running penumbral wave observed to propagate outwards from the umbrae of sunspots. They were suggested to be magnetoacoustic-gravity modes by Nye and Thomas (1974; 1976*b*) and to be fast magnetoacoustic surface modes by Small and Roberts (1984).

Finally, Roberts (1981*b*) has considered the modes of oscillation of an isolated slab of magnetic flux in the absence of gravity. The properties of the plasma within and outside the slab are assumed to be uniform, but not necessarily equal. His analysis showed that *slow* ($c_{ph} < \min[c_o, v_a]$, where c_o is the speed of sound within the slab) surface and body modes are always able to propagate. However, if the surroundings are *hotter* than the slab, i.e. $c_e > c_o$ where c_e is the speed of sound in the surrounding media, *fast* waves may also propagate. Their nature is dependent on the field strength within the slab. If the field strength is such that $c_e > c_o > v_a$, where v_a is the Alfvén speed in the magnetic slab, the wave propagates as a fast body wave with $c_e < c_{ph} < c_o$. If $v_a > c_e > c_o$ then the mode takes on the form of a fast surface wave.

As yet there exists no study of the fully compressible modes of an isolated slab in the presence of gravity where the temperatures of the field-free regions are not isothermal, but contain linear temperature profiles. The model of Chapter 4 provides the ideal situation for studying surface waves under these conditions. To recap, the model equilibrium consists of a semi-infinite region of fluid contained by a rigid wall at $z = 0$. Within this region, there are two field-free layers of fluid, each containing linear temperature profiles which increase

with depth. Between these two layers resides a slab of magnetic flux structured in such a way as to maintain a constant Alfvén speed. In this chapter we are interested in the surface and body modes this slab may support.

In Section 5.2 we recap on the model of Chapter 4 and present the dispersion relation. The dispersion relation is solved numerically to find the surface and body modes of the magnetic layer. In Section 5.3 we examine the behaviour of the modes in and around the magnetic layer, and we discuss the results in Section 5.4.

5.2 The Dispersion Relation and Mode Frequencies

We wish to examine the surface and body waves associated with the sub-convective magnetic field. The model used is that of Chapter 4. The interior of the Sun is modelled as a semi-infinite region of fluid, ranging from $z = 0$ to $z = +\infty$ and containing three layers of plasma. In the field-free regions, the equilibrium temperature profile is taken to be linear in z with the gradient chosen such that the plasma is marginally stable to convective motions. In $z_{uc} < z < z_{lc}$, between the two field-free layers, there is an isothermal layer of magnetic flux. A rigid wall is placed at $z = 0$ and the entire medium is gravitationally stratified in depth z. The temperature profile is structured so as to give a continuous profile at $z = z_{uc}$ and $z = z_{lc}$. For mathematical simplicity we have assumed a magnetic field profile that provides us with a constant Alfvén speed in the magnetic layer.

In Chapter 4 we were concerned with the variation in the frequencies of the $p-$modes as the magnetic field strength within the layer changed. However, the presence of a magnetic layer in $z_{uc} < z < z_{lc}$ leads to a discontinuity in the plasma density profile at $z = z_{uc}$ and $z = z_{lc}$. If we denote the plasma density immediately within the field as ρ_{mag} and the plasma density immediately across the interface as ρ_{nonmag}, we saw in Chapter 4 that

$$\frac{\rho_{mag}}{\rho_{nonmag}} = \frac{\Gamma_c}{\gamma}, \tag{5.2}$$

where γ is the adiabatic index and Γ_c is the magnetically modified index. This ratio is the same at both interfaces, even though ρ_{mag} and ρ_{nonmag} are themselves different at these two depths. From Equation (5.2) we therefore see that the magnetic field causes a decrease in the plasma density within the layer in order to maintain pressure balance.

The discontinuity in the equilibrium plasma density profile allows surface waves

to occur. The magnetic slab will also contain body modes, motions of the whole layer, of course.

As derived in Chapter 4, a velocity perturbation of the form

$$\mathbf{u} = (u_x(z), 0, u_z(z))\exp\left[i(\omega t - k_x x)\right], \tag{5.3}$$

applied to the above equilibrium (see Equations (4.15)-(4.21)) provides us, after much algebra, with the dispersion relation for the model:

$$\alpha\Psi = \eta\Phi, \tag{5.4}$$

where

$$\alpha = k_x c_s^2(\Omega^2 + 1) - g\gamma\Omega^2, \qquad \eta = 2ak_x\Omega^2 c_s^2, \tag{5.5}$$

$$\Psi = \epsilon M(-a, m+2, 2k_x z_{ou}) + \delta U(-a, m+2, 2k_x z_{ou}), \tag{5.6}$$

$$\Phi = \delta U(1-a, m+3, 2k_x z_{ou}) - \frac{\epsilon}{m+2} M(1-a, m+3, 2k_x z_{ou}), \tag{5.7}$$

$$\delta = \Lambda_7 M(-a, m+2, 2k_x(z_{uc} + z_{ou})) + \frac{\Lambda_8}{m+2} M(1-a, m+3, 2k_x(z_{uc} + z_{ou})), \tag{5.8}$$

$$\epsilon = \Lambda_8 U(1-a, m+3, 2k_x(z_{uc} + z_{ou})) - \Lambda_7 U(-a, m+2, 2k_x(z_{uc} + z_{ou})), \tag{5.9}$$

$$\Lambda_8 = \Gamma_c \Lambda_5 \tau, \qquad \Lambda_7 = \Gamma_c \sigma \Lambda_5 - \Lambda_6, \tag{5.10}$$

$$\tau = 2ak_x\Omega^2 c_c^2 \qquad \text{and} \qquad \sigma = k_x c_c^2(\Omega^2 + 1) - g\gamma\Omega^2. \tag{5.11}$$

If $4AH_c^2 < 1$, then Λ_5 and Λ_6 appearing in Equation (5.10) are given by

$$\Lambda_6 = \frac{\gamma(g\Omega^2 - k_x c_c^2)(\Omega^4 - 1)\Lambda_4(\Theta_- + I_-)}{\Lambda_2}, \tag{5.12}$$

and

$$\Lambda_5 = (1+\beta)(g\Omega^2 - k_x c_{Tc}^2)(\lambda_+\Theta_- + \lambda_- I_-) + \frac{\Lambda_4}{\Lambda_2}(\Theta_- + I_-), \tag{5.13}$$

where

$$I_- = e^{(\lambda_+ - \lambda_-)z_c}\left[\Lambda_4 - \lambda_+\Lambda_3\right] \qquad \text{and} \qquad \Theta_- = \Lambda_3\lambda_- - \Lambda_4. \tag{5.14}$$

For the condition $4AH_c^2 > 1$,

$$\Lambda_6 = \frac{\gamma(\Omega^4 - 1)(g\Omega^2 - k_x c_c^2)\Lambda_4}{\Lambda_2} I_+, \tag{5.15}$$

and

$$\Lambda_5 = (1+\beta)(g\Omega^2 - k_x c_{Tc}^2)(\Theta_+ \kappa - \frac{I_+}{2H_c}) + g k_x \beta I_+, \tag{5.16}$$

where

$$I_+ = \Lambda_3 \left[\kappa \cos \kappa z_c - \frac{1}{2H_c} \sin \kappa z_c\right] - \Lambda_4 \sin \kappa z_c \tag{5.17}$$

and

$$\Theta_+ = \Lambda_3 \left[\kappa \sin \kappa z_c + \frac{1}{2H_c} \cos \kappa z_c\right] + \Lambda_4 \cos \kappa z_c. \tag{5.18}$$

For both cases,

$$\Lambda_4 = g k_x \beta \Lambda_2, \qquad \Lambda_3 = \Gamma_c (1+\beta)(g\Omega^2 - k_x c_{Tc}^2)\Lambda_1, \tag{5.19}$$

$$\Lambda_2 = \gamma(g\Omega^2 - k_x c_c^2)(\Omega^4 - 1) U(-a, m+2, 2k_x(z_{uc} + z_{ou})) - \Gamma_c \Lambda_1, \tag{5.20}$$

and

$$\Lambda_1 = \sigma U(-a, m+2, 2k_x(z_{uc} + z_{ou})) - \tau U(1-a, m+3, 2k_x(z_{uc} + z_{ou})). \tag{5.21}$$

The identification of the surface and body modes from Equation (5.4) is straightforward. The energy density of a surface wave decays exponentially from both sides of the interfaces at $z = z_{uc}$ and $z = z_{lc}$, whereas the body modes show an oscillatory kinetic energy density within the magnetic layer and become evanescent in the field-free regions. This behaviour is governed by the form of the velocity perturbation u_z given by Equations (4.36) and (4.39), and is reflected in the dispersion relation given above. Simply, the magnetoacoustic surface modes satisfy the condition $4AH_c^2 < 1$ while for the magnetoacoustic body modes $4AH_c^2 > 1$.

The surface and body modes we obtain fall into one of two categories. Firstly, disturbances within the magnetic layer may be symmetrical about the centre of the slab. These modes are characterised in the zero gravity case by having a zero in u_z at the centre of the slab (a condition that we have not demanded here), and u_z being an odd function of z. The modes may therefore be viewed as a succession of symmetric compressions and rarefactions travelling along the slab, and are called *sausage modes* after their obvious appearance. Secondly, there is a class of modes representing an anti-symmetric disturbance of the slab or its edges. For these modes, the centre of the slab is usually a maximum

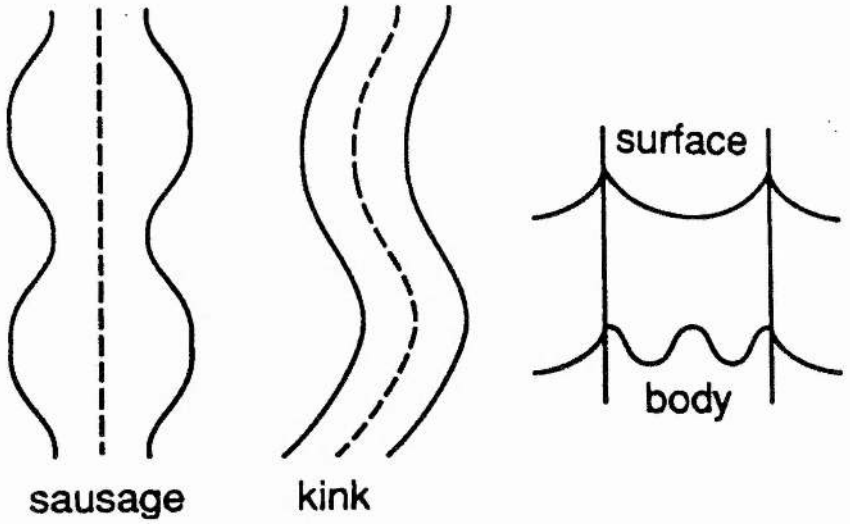

Figure 5.1: A pictorial representation of the surface and body modes of a magnetic slab, along with the disturbances classified as sausage and kink modes (taken from Roberts 1990).

or a minimum of the perturbed velocity, and u_z is represented by an even function of z. The modes of this type follow a pattern along the tube which is analogous to the motions of a snake's body as it moves forward; these are termed *kink modes*. Figure 5.1 displays what we understand by the terms surface and body waves, and depicts the mode structure formed by sausage modes and kink modes.

5.2.1 A diagnostic diagram

The surface and body waves contained in Equation (5.4) are quite difficult to resolve numerically because of the overbearing dominance of the $p-$modes in the numerical code. We therefore found it convenient to use a very high magnetic field strength in the numerical solution of Equation (5.4) as this makes the modes much easier to pick up. As in Section 4.7 of Chapter 4, we choose $B_{lc} = 3.10^7$G, which is close to the equipartition field strength. The values that this field strength gives to the relevant physical parameters that we require are displayed in Table 5.1. The other parameters that we shall use, such as the temperature and pressure at the base of the convection zone, are displayed in Table 4.1.

Figure 5.2 shows the results of solving the dispersion relation (5.4). The horizontal phase speed c_{ph} ($\equiv \omega/k_x$) of the modes is plotted against $k_x H_c$. The sausage modes

Parameter	*Value*
c_c	191 km s^{-1}
v_{ac}	306 km s^{-1}
c_{fc}	360 km s^{-1}
c_{Tc}	161 km s^{-1}
H_c	250194 km
Γ_c	0.532

Table 5.1: The parameters used in the numerical solution of Equation (5.4). They are calculated for magnetic field strength of 3.10^7G.

are shown as a solid line (——) and the kink modes as dashed curves (- - -). The curves appearing in Figure 5.2 cover a range of k_xH_c from 3.75 to 18.15 (corresponding to horizontal wavelengths of 416960 km to 86600 km, respectively). We have not calculated mode frequencies for modes with $k_xH_c < 3.15$ because, as we have said in previous chapters, the application of the model becomes less valid for modes which feel the spherical nature of the Sun. We do not extend the range in k_xH_c beyond 18.15 simply for numerical reasons; the modes become more and more difficult to extract as k_x increases. The two horizontal dotted lines display the tube speed c_{Tc} and the sound speed c_c. Finally, note that the vertical axis does not extend up to such values as the Alfvén speed v_{ac} and the fast speed c_{fc}; this is simply to display more clearly the modes that we have found.

The modes presented in Figure 5.2 are the *slow* magnetoacoustic surface modes and slow magnetoacoustic body modes of a magnetic layer at the base of the convection zone. There are no fast modes present in this model because the slab is not cooler than its immediate surroundings, a condition necessary for them to occur in an unstratified slab (Roberts 1981*b*). The slow magnetoacoustic surface modes satisfy the condition $c_{ph} < c_{Tc}$, with $c_{ph} \to 0$ as $k_x \to 0$ for the kink surface mode and $c_{ph} \to c_{Tc}$ as $k_x \to 0$ for the sausage surface mode. These modes are principally acoustic in nature with $c_{Tc} \approx c_c$ ($\ll v_{ac}$). The slow body modes, on the other hand, have phase speeds in the range $c_{Tc} < c_{ph} < c_c$. For clarity, we have shown only the first two body modes of the slab. There are, of course, an infinite number of slow body modes consisting of the fundamental mode and its overtones. These are categorised by the number of nodes, n, that the mode has across the slab. The kink modes have an even number of nodes, $n = 0, 2, 4, ...$; while the sausage modes contain an odd number of nodes, $n = 1, 3, 5, ...$ In Figure 5.2 the kink mode shown is the fundamental

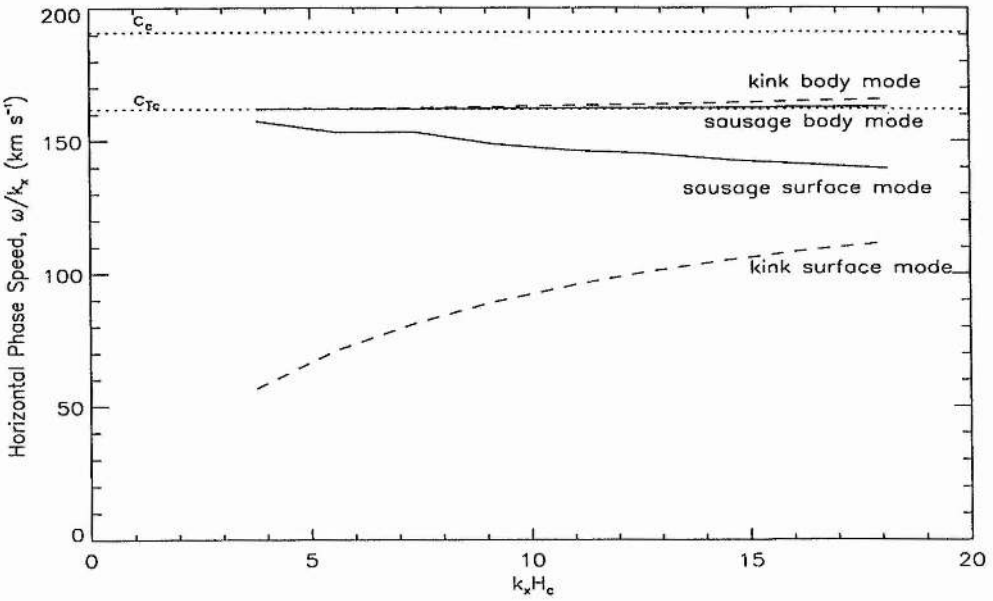

Figure 5.2: The phase speed $c_{ph}(=\omega/k_x)$ of the surface and body modes of the magnetic layer, plotted against k_xH_c. The kink (anti-symmetric) modes are plotted as dashed curves (- - -) and the sausage (symmetric) modes are shown as solid curves. The horizontal dotted lines indicate the tube speed c_{Tc} and sound speed c_c within the magnetic slab. The surface modes have phase speeds such that $c_{ph} < c_{Tc}$ and the body modes are confined to the range $c_{Tc} < c_{ph} < c_c$.

body oscillation of the layer with $n = 0$, and the sausage mode is the first harmonic with $n = 1$. The whole continuous spectrum of body modes form an anti-Sturmian sequence with c_{ph} decreasing as n increases for a specific horizontal wavenumber k_x. From Figure 5.2, we can also see that $c_{ph} \to c_{Tc}$ as $k_x \to 0$, for all n.

5.3 The Behaviour of the Modes in and around the Magnetic Layer

In this brief initial investigation into the compressible magnetoacoustic-gravity surface and body modes of a sub-convective magnetic field, we round off the numerical study by considering the structure of the modes in and around the magnetic layer. To do this, we follow the approach of Chapters 3 and 4 and calculate the normalised square root

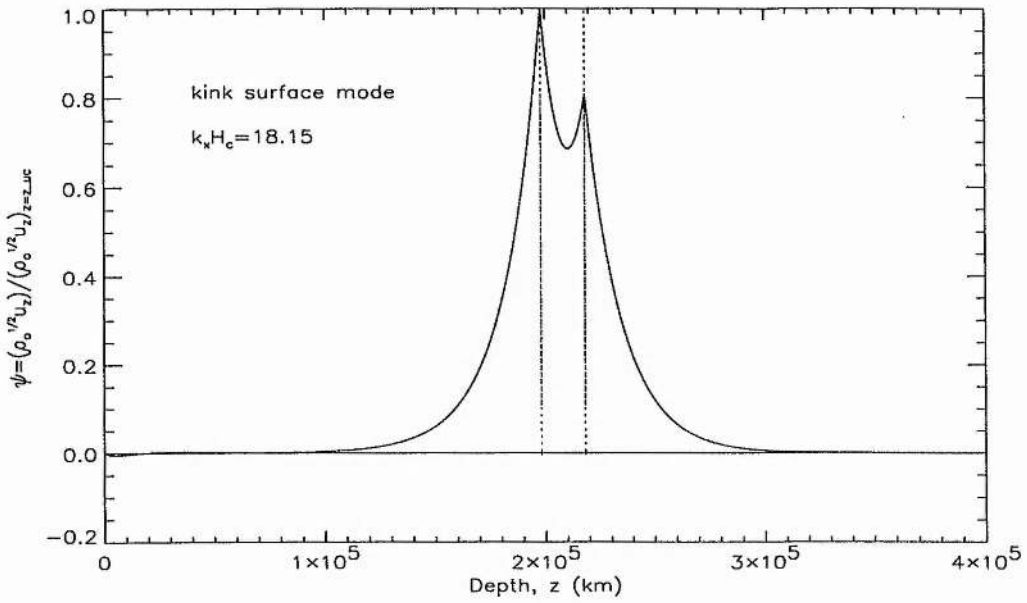

Figure 5.3: The normalised square root of the energy density, ψ, plotted against depth z for the kink surface mode with $k_xH_c = 18.15$. The vertical dotted lines show the position of the magnetic layer. The mode is highly localised on the magnetic interfaces.

of the kinetic energy density of vertical motions. This quantity is denoted by ψ, given by

$$\psi = \frac{\rho_o^{\frac{1}{2}} u_z}{(\rho_o^{\frac{1}{2}} u_z)_{z_{uc}}}, \tag{5.22}$$

where $z = z_{uc}$ is the depth at which ψ is normalised.

In Figure 5.3 we have plotted ψ against depth z for the kink magnetoacoustic surface mode with $k_xH_c = 18.15$ and $B_{lc} = 3.10^7$G. The two vertical dotted lines indicate the position of the magnetic layer. From Figure 5.3 we can see that the disturbance is highly localised on the interfaces at $z = z_{uc}$ and $z = z_{lc}$. The value of ψ decreases exponentially into the magnetic layer, exhibiting a minimum at a depth just below the centre of the layer. In the field-free region beneath the magnetic layer, ψ rapidly decays exponentially and any indication of the disturbance has disappeared by a depth of 3.3×10^5 km. In the layer above the magnetic slab, the behaviour of ψ is somewhat different. There is still an exponential decay present, but ψ becomes oscillatory in nature as the surface layers are approached. For the kink mode pictured in Figure 5.3 this behaviour is almost negligible. A decay in ψ that is not entirely exponential throughout the upper field-free layer is understandable because no boundary condition has been placed on the kinetic energy density in this layer. The

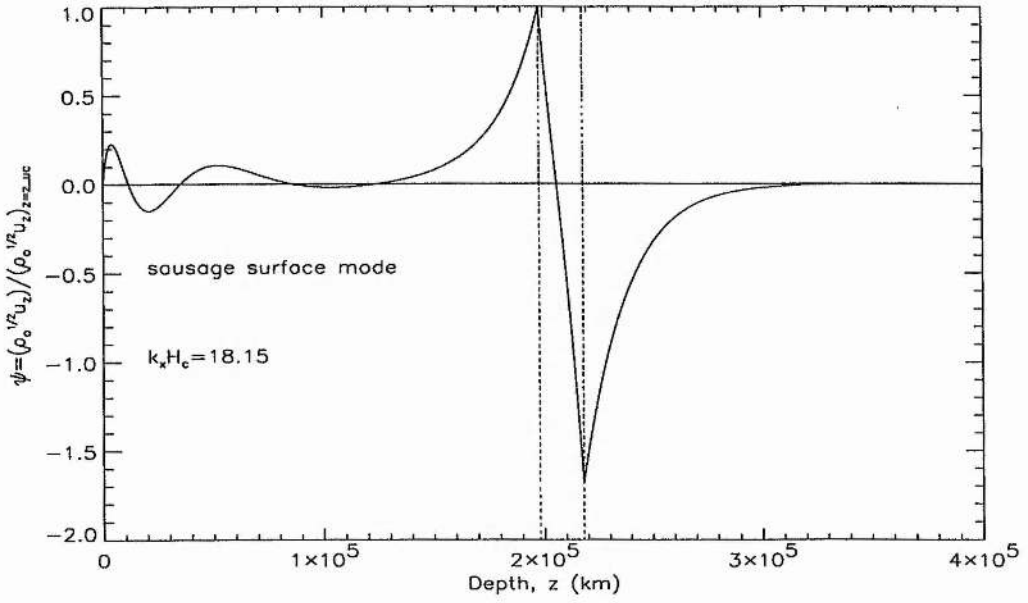

Figure 5.4: As in Figure 5.3 but for the sausage surface mode with k_xH_c=18.15. Note the change of scale on the vertical axis.

onset of an oscillatory motion in the near surface layers is less clearly understood, however. One suggestion may be that a low frequency disturbance such as the kink surface mode is unable to drive an oscillation outside of the magnetic layer in the deep convection zone where the plasma density is high, but carries enough energy to disturb the upper, rarefied, layers. As it is, this consideration is purely academic because the motions that the kink mode drives at the near surface are hardly likely to be measured above the vastly larger motions of the $p-$modes.

Finally, what do the different magnitudes of ψ on each interface tell us about the nature of the modes? In a zero gravity situation, with uniform plasma densities, we would expect the amplitude of the disturbance to be equal at $z = z_{uc}$ and $z = z_{lc}$. In Figure 5.3, ψ is greater at the upper interface. From an inspection of Equation (5.22) we see that this implies a much greater value of u_z at $z = z_{uc}$ than at $z = z_{lc}$, because the plasma density $\rho_o(z)$ grows exponentially through the magnetic layer. The effect of gravitational stratification of the atmosphere seems therefore to diminish the mode energy ($\propto \psi^2$) at the lower interface. This seems acceptable when we consider that a disturbance has to work against much more dense plasma as we move deeper into the model, a direct consequence of stratification. The implication that this has for the slab itself is that as the mode propagates

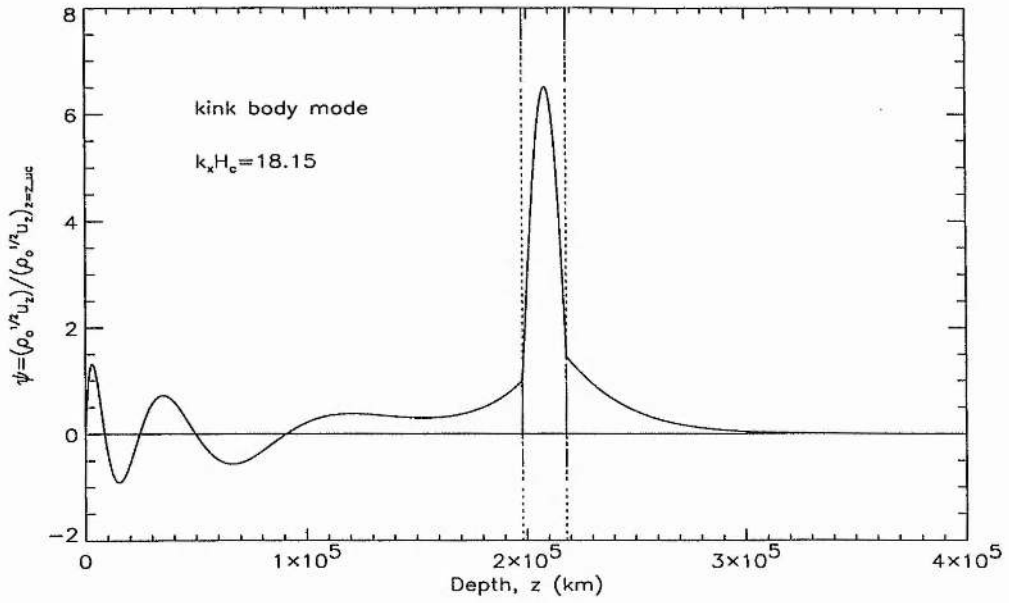

Figure 5.5: The quantity $\psi(z)$ plotted against depth, z, for the kink body mode with k_xH_c=18.15, and $\kappa = 0$. Note the larger scale on the vertical axis here than in Figures 5.3 and 5.4 indicating that the relative disturbances of the body modes are far greater than the surface modes.

along the slab it displaces the upper interface more than the lower one. This leads to a small expansion of slab in areas where the mode is moving the surfaces slightly towards the model surface and a slight compression of the layer at places where the surfaces are being perturbed downwards.

In Figure 5.4 we have plotted ψ against depth z for the sausage surface mode, again with $k_xH_c = 18.15$. This mode is the symmetric partner of the antisymmetric kink mode shown in Figure 5.3. In Figure 5.4 we see that the sausage surface mode, similar to the kink mode, is highly localised on the interfaces at $z = z_{uc}$ and $z = z_{lc}$. As expected for a surface mode, ψ decreases exponentially from each interface as we move into the magnetic layer and the deeper field-free layer. Again, ψ decreases exponentially into the upper field-free layer, with the sausage mode showing similar behaviour to the kink mode in that ψ becomes oscillatory as we move upwards from the layer. This oscillatory behaviour begins at much deeper depths for the sausage surface mode than the kink surface mode however. From the numerical code used to evaluate Equation (5.22) we find that the velocity node within the magnetic layer is about 200 km above the centre of the slab. Different to Figure

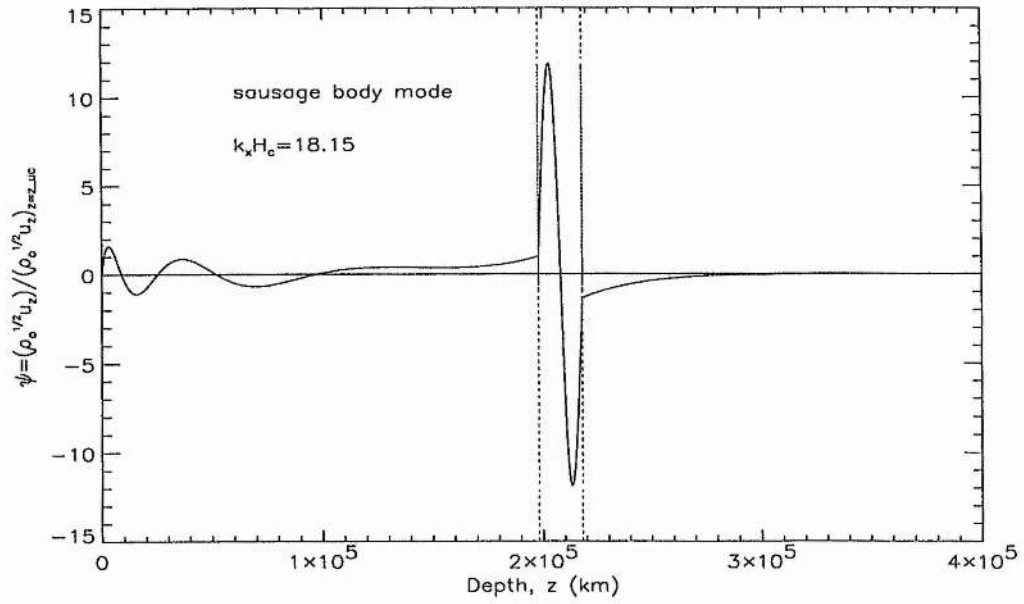

Figure 5.6: As in Figure 5.5 but for the first overtone ($n = 1$) sausage body mode with k_xH_c=18.15. Note the change of scale on the vertical axis.

5.3, the lower interface shows a greater magnitude of ψ than the upper one for the sausage surface mode. This does not necessarily imply a greater velocity perturbation u_z at the lower interface for the sausage mode, because we must remember that the plasma density is significantly larger at $z = z_{uc}$ than it is at $z = z_{lc}$.

Finally, we show the fundamental ($n = 0$) kink body mode in Figure 5.5 and the first overtone ($n = 1$) sausage body mode in Figure 5.6. For both figures, k_xH_c=18.15. As we would expect, ψ decays exponentially away from the magnetic slab into the field-free regions, showing an oscillatory behaviour in the upper field-free layer in both Figure 5.5 and Figure 5.6. The magnitude of ψ is far greater for both the kink body mode and sausage body mode within the magnetic layer than it is for the surface modes, however. For the kink body mode in Figure 5.5, ψ is approximately seven times larger at the centre of the slab than it is at the interfaces, while for the sausage mode in Figure 5.6 the maximum of ψ is approximately twelve times the value it takes at the interfaces.

5.4 Discussion

In this chapter we have studied the modes of oscillation of the magnetic layer believed to reside at the base of the convection zone. The model used is the one presented in Chapter 4 where we considered the influence of the magnetic layer on the frequencies of the $p-$modes. To recap, a semi-infinite three layer model has been used. The outer two, field-free, layers contain linear temperature profiles, the gradients of which are chosen to maintain plasma stability to convective motions. Between these layers resides a layer of magnetic field, the equilibrium profile of which provides a constant Alfvén speed in the layer. The magnetic layer is assumed to be isothermal. A rigid wall is placed at $z = 0$ and the entire medium is stratified under gravity.

We have seen that the magnetic slab embedded in a compressible field-free plasma sustains a variety of modes of oscillation (see Figure 5.2). The slab does not support fast magnetoacoustic waves because there is no discontinuity in the temperature profile at the edges of the slab at $z = z_{tc}$ and $z = z_{lc}$ (see Roberts 1981*b* for the conditions for fast wave propagation in a magnetic slab). However, the slow magnetoacoustic waves may exist either as surface waves or as body waves in the form of harmonics of the slab. The slow surface waves propagate with phase speeds $c_{ph} < c_{Tc}$, whereas the slow body waves propagate with phase speeds in the narrow region $c_{Tc} < c_{ph} < c_c$.

As far as we are aware, there have been no other attempts as yet to study the modes of an isolated magnetic slab in the presence of gravity. The case when gravity is absent has been studied by Roberts (1981*b*). There are similarities and differences between the work presented here and Roberts (1981*b*). Comparing Figure 5.2 to Figure 1(b) of Roberts (1981*b*) we see that both studies show the slow surface modes to possess phase speeds which are less than the tube speed of the slab, and the body modes to have phase speeds between the tube speed and the sound speed within the slab. However, in Roberts (1981*b*) the phase speeds of the body modes increases rapidly to the sound speed in the slab as k_x increases. In Figure 5.2, however, the phase speed of the body modes shows only a slight increase over the range of k_x chosen. Comparison between the two figures is difficult because Roberts (1981*b*) provides only a schematic of the modes and does not indicate the range of k_x taken in his study. By visually comparing the two Figures though we may see the difference. In Figure 5.2 note the difference in phase speeds between the kink surface mode and sausage surface mode when $k_x H_c$=10. At this point the kink and

sausage body modes have $c_{ph} \approx c_{Tc}$ in Figure 5.2. From Figure 1(b) of Roberts (1981*b*), if we approximate the same gap between the phase speeds of the kink and sausage surface modes, the body modes of his model already have phase speeds approaching the sound speed within the magnetic slab.

There are several possible explanations. Firstly, it may be the fact that we have included gravity that causes a shallower gradient in the phase speeds of the body modes. Also, it may be that in this chapter the field-free regions are not isothermal, as they were in the work of Roberts (1981*b*), but contain linear temperature profiles. Also, it must be remembered that we have used an exceptionally large and unrealistic value for the strength of the magnetic field at the base of the magnetic layer in order to pick out the modes more easily. This leads to the slow modes being principally acoustic in nature ($c_o \approx c_{Tc}$). However, this study has been necessarily brief and we have not been able to fully investigate these modes. More detailed studies into their properties may shed further light on the behaviour reported in this chapter.

Chapter 6

Conclusions and Suggestions For Further Work

In this thesis we have examined, through a magnetohydrodynamic formalism, the effect that various layers of the solar atmosphere and interior have on the frequencies of the global solar oscillations ($p-$modes). The investigations have been concerned, either independently or jointly, with thermal and magnetic field strength variations in the chromosphere, the thin superadiabatic layer at the upper extremes of the convection zone, and the magnetic field believed to reside at the base of the convection zone. Each individual study has attempted to model the basic structure of the solar atmosphere and interior to allow an analytical investigation; an undoubtedly simple approach, but one which allows us to single out the physical changes that may be responsible for the variations in $p-$mode frequencies over the course of the solar cycle.

6.1 Conclusions

In Chapter 2, we focussed our attention on the radial modes of oscillation of the Sun, modes for which the degree $l = 0$. The role of a magnetic chromosphere in influencing the frequencies of the modes was investigated. For a field-free atmosphere we found that an *increase* in chromospheric temperature led to a *decrease* in frequency for all modes, a result also shown by Johnston (1994) for $l = 0$ modes, and for modes of non-zero degree by Evans (1990), Evans and Roberts (1990, 1991, 1992), Jain (1994), and Jain and Roberts (1994, 1996). A magnetic field permeating the chromosphere that is structured in such a

way so as to give a constant Alfvén speed produced qualitatively similar results to the field-free case when the strength of the magnetic field was increased. However, the magnitude of the frequency shift was considerably less for magnetic changes than for thermal variations in the field-free case. Finally, for a uniform magnetic field, simply *raising* the strength of the magnetic field led to an *increase* in the frequencies of the modes. Combining magnetic field strength increases with a simultaneous increase in chromospheric temperature led to frequency shift curves which displayed an increase in frequency for all modes, but ones which exhibited a peak in frequency shift for frequencies of around 3.8 mHz with a turnover and subsequent downturn for frequencies above this value. This result is in good agreement with observations, especially the results of Chaplin *et al.* (1998) which indicate that from solar minimum to maximum, the $l = 0$ modes exhibit a rise in mode frequency up to frequencies of around 3.7-3.9 mHz, followed by a sharp downturn in the frequency increase at frequencies above this value. This observational feature detected in the low degree modes is similar but less pronounced to that observed in intermediate degree modes by Libbrecht and Woodard (1990).

The model presented in Chapter 3 investigated the influence that the superadiabatic layer of the upper convection zone may have on the frequencies of the $p-$modes. The superadiabatic layer is unstable to convective motions and as a result may give rise to convective modes (g^--modes). In Chapter 3, we have also investigated their properties and the variations that they may experience over the solar cycle.

For the $p-$modes, it was found that by *increasing* the temperature gradient of the superadiabatic layer, the frequencies of the $p-$modes were *increased* over their base values. The frequency shift curves for these conditions displayed a steep increase in the low frequency range (2-3) mHz, followed by a levelling off at frequencies above this value. The effect of steepening the temperature gradient of the superadiabatic layer was seen to be more pronounced as l increased; a result we would expect because modes of higher l sample more of this layer than modes of lower l. When the above variation was combined with a rise in atmospheric temperature we found that we were able to reproduce qualitatively the observed solar cycle variation in the $p-$mode frequencies. Relatively small temperature increases were required ($\triangle T_{at} \approx 10 - 50^o$K) compared with the changes $\triangle T_{at} \approx 1500^o$K that Jain and Roberts (1994) found necessary to produce a turnover.

In the presence of a magnetic atmosphere the $p-$modes showed an *increase* in frequency for an *increase* in magnetic field strength. The magnitude of the frequency increases

was less than those reported by Evans and Roberts (1990), a result we have understood by the fact that our reference level has a much higher gas pressure than the reference level used in Evans and Roberts (1990), leading to a greater domination of the plasma over the magnetic field for our model (i.e. β is higher for this model for an equal magnetic field strength). As before, we have been able to produce a downturn in the frequency shifts by simultaneously increasing the temperature gradient of the superadiabatic layer and raising the atmospheric temperature along with increases to the magnetic field strength. However, we have found that much larger increases ($\triangle T_{at} \approx 100-250°\mathrm{K}$) in atmospheric temperature are required to produce the observed peak and subsequent downturn.

The convective modes (g^-−modes) have been studied by investigating the sensitivity of their growth times to the same changes that have been applied to the p−modes. By steepening the temperature gradient of the superadiabatic layer, the g_1^-−mode showed a decrease in its growth time while the overtones were suppressed (i.e. their growth times increased). When the atmospheric temperature was simultaneously increased with the decrease in m_u, the decrease in the growth time of the g_1^-−mode was lessened for higher temperatures, while the overtones were further suppressed. For a magnetic atmosphere, an increase in magnetic field strength led to an increase in the growth time of all modes, but the g_1^-−mode still displayed a decrease in its growth time when an increase in magnetic field strength was coupled with a steeper temperature gradient in the superadiabatic layer.

In Chapter 4 we introduced a model that included a thin magnetic layer taken to represent the stored magnetic field believed to reside at the base of the convection zone. By increasing the magnetic field strength at the base of this layer, some rather interesting, but confusing, results were found. There appeared to be no systematic (monotonic) trend to the changes in mode frequency with some modes showing a decrease in frequency with an increase in magnetic field strength while others displayed an increase. However, by decreasing the thickness of the magnetic layer while the field strength was kept fixed, the frequency shifts show a smooth behaviour, exhibiting a steep rise in frequency for frequencies between 1-1.5 mHz followed by a levelling off for frequencies above this value.

The magnetic layer at the base of the convection zone was also incorporated into a model similar to that used in Chapter 2, to analyse its effect on modes of degree zero. Again the distinctive frequency changes that are observed could not be reproduced by increasing the magnetic field strength alone. However, frequency shifts are more orderly than for modes of general degree, with an average positive gradient to the changes in frequency.

Finally, in Chapter 5 we made a brief study of the surface and body modes of the magnetic layer at the base of the convection zone. We presented a diagnostic diagram showing the surface modes to have phase speeds c_{ph} such that $c_{ph} < c_{Tc}$, where c_{Tc} is the tube speed within the magnetic slab; the body modes are seen to be confined to the range $c_{Tc} < c_{ph} < c_c$, where c_c is the speed of sound in the magnetic layer.

6.2 Suggestions For Further Work

The radial modes of oscillation of the Sun are of interest because the mathematics required to study their behaviour is relatively simple. This allows for a deeper analytical investigation, especially through some asymptotic expansions of the alternative form of the dispersion relation, given in Section 2.6. Also, the assumption of an isothermal chromosphere should be discarded. However, as far as we are aware there is not yet an analytical equilibrium solution for a linear temperature profile threaded by a uniform horizontal magnetic field. However, it may be the more subtle influence of a change in the temperature gradient of the chromosphere, rather than the extreme changes we apply, that are responsible for the downturn in the observed frequency shifts. Combining the chromospheric effects that we have investigated with the influence of the magnetic field at the base of the convection zone could also prove instructive.

Better models of the thin superadiabatic shell of the upper convection zone would seem to be required following the results of Chapter 3. Our assumption of a simple linear temperature profile for this region is crude, but it does provide us with some rather encouraging results for determining the location of the layer responsible for solar cycle variations. To be more realistic a purely numerical approach is necessary. Also, it would be of interest to discard the assumption of isothermality in the overlying atmosphere, and maybe to include the additional effects of vertical fields through the superadiabatic layer.

The magnetic layer at the base of the convection zone is little understood. Even the field strength there is not known. For simplicity, we have assumed that this layer is isothermal and that the magnetic field is structured so as to give a constant Alfvén speed. This layer needs to be investigated further, especially as it is still unresolved whether there is an alternative to either neutral buoyancy or thermal equilibrium that holds the layer in place.

Finally, the surface and body modes of a magnetic slab in the presence of gravity

need to be studied further. The modes of an unstratified magnetic slab are well known, but stratification introduces a number of complications and there have been very few investigations in this area. We hope that our brief study prompts further investigations into these modes.

REFERENCES

Abramowitz, M., & Stegun, I. A. 1965, *Handbook of Mathematical Functions* (New York: Dover).

Adam, J. A. 1975, *PhD thesis*, University of London.

Adam, J. A. 1977, *Solar Physics* **52**, 293.

Anguera Gubau, M. ,Pallé, P. L., Pérez Hernández, F., Régulo, C., & Roca Cortés, T. 1992, *Astron. & Astrophys.* **255**, 363.

Bachmann, K. T., Duvall, T. L., Harvey, J. W., and Hill, F. 1994, in Gong '94: *Helio– and Asteroseismology from Earth and Space*, ed. R. Ulrich, E. J.Rhodes and W. Däppen, (San Francisco: ASP), p.280.

Basu, S. 1997, *Mon. Not. Royal Astron. Soc.* **288**, 572.

Campbell, W. R., and Roberts, B. 1986, in IAU Symposium 123, *Advances in Helio– and Asteroseismology*, ed. J. Christensen-Dalsgaard and S. Frandsen (Dordrecht: Reidel), p.161.

Bogdan, T. J., and Cattaneo, F. 1989, *ApJ* **342**, 545.

Bogdan, T. J., and Zweibel, E. G. 1985, *ApJ* **298**, 867.

Campbell, W. R., & Roberts, B. 1989, *ApJ* **338**, 538.

Chandrasekhar, S. 1961, in *Hydrodynamic and Hydromagnetic Stability*, Carenden Press, Oxford, Section 97.

Chaplin, W. J., Elsworth, Y., Isaak, G. R., Lines, R., McLeod, C. P., Miller, B. A., & New, R. 1998, *Mon. Not. Royal Ast. Soc.*, in press.

Christensen-Dalsgaard, J. 1986, in IAU Symposium 123, *Advances in Helio– and Asteroseismology*, ed. J. Christensen-Dalsgaard and S. Frandsen (Dordrecht: Reidel), p.3.

Christensen-Dalsgaard, J., Gough, D. O., and Thompson, M. J. 1991, *ApJ* **378**, 413.

Claverie, A., Isaak, G. R., McLeod, C. P., and van der Raay, H. B. 1979

Nature **282**, 591.

Cowling, T. G. 1941, *Mon. Not. Royal Astron. Soc.* **101**, 367.

Dearborn, D. S. P., and Blake, J. B. 1980, *ApJ* **237**, 616.

Demarque, P., Guenther, D. B., and Kim, Y. -C. 1997, *ApJ* **474**, 790.

Deubner, F. -L. 1975, *Astron. & Astrophys.* **44**, 371.

Deubner, F. -L., and Gough, D. O. 1994, *Ann. Rev Astron. Astrophys.* **22**, 593.

D'Silva, S. 1993, *ApJ* **407**, 385.

D'Silva, S., and Choudhuri, A. R. 1993, *ApJ* **272**, 621.

Duvall, T. L., Harvey, J. W., and Pomerantz, M. A. 1987, in *The Internal Solar Angular Velocity*, ed. B. R. Durney and S. Sofia, D. Reidel, p.19.

Dziembowski, W. A., and Goode, P. R. 1989, *ApJ* **347**, 540.

Elsworth, Y., Howe, R., Isaak, G. R., McLeod, C. P., & New, R. 1990, *Nature* **345**, 322.

Elsworth, Y., Howe, R., Isaak, G. R., McLeod, C. P., Miller, B. A., New, R., Speake, C. C., & Wheeler, S. J. 1994, *ApJ* **434**, 801.

Endal, A. S., Sofia, S., and Twigg, L. W. 1985, *ApJ* **290**, 748.

Evans, D. J., & Roberts, B. 1990, *ApJ* **356**, 704.

Evans, D. J., & Roberts, B. 1991, *ApJ* **371**, 387.

Evans, D. J., & Roberts, B. 1992, *Nature* **355**, 230.

Evans, J. W., and Michard, R. 1962, *ApJ* **136**, 493.

Fossat, E., Gelly, B., Grec, G., & Roca Cortés, T. 1989, *Astron. & Astrophys.* **177**, L47.

Galloway, D. J., and Weiss, N. O. 1981, *ApJ* **243**, 945.

Gingerich, O., Noyes, R. W., Kalkofen, W., and Cuny, Y. 1971, *Solar Phys.* **18**, 347.

Giovanelli, R. G. 1980, *Solar Physics* **68**, 49.

Giovanelli, R. G., & Jones, H. P. 1982, *Solar Physics* **79**, 267.

Goedbloed, J. P. 1971, *Physica* **53**, 412.

Goldreich, P., Murray, N., Willette, G., and Kumar, P. 1991, *ApJ* **370**, 752.

Guenther, D. B., Demarque, P., Kim, Y. -C., and Pinsonneault, M. H. 1992, *ApJ* **387**, 372.

Hale, G. E., Ellerman, F., Nicholson, S. B., and Joy, A. H. 1919,

ApJ **49**, 153.

Isaak, G. R., Jefferies, S. M., McLeod, C. P., New, R., van der Raay, H. B., Pallé, P. L., Régulo, C., and Roca Cortés, T. 1986, in IAU Symposium 123, *Advances in Helio– and Asteroseismology*, ed. J. Christensen-Dalsgaard and S. Frandsen (Dordrecht: Reidel), p.201.

Jain, R. 1994, *PhD Thesis*, University of St. Andrews.

Jain, R., & Roberts, B. 1994, *ApJ* **414**, 898.

Jain, R., & Roberts, B. 1996, *ApJ* **456**, 399.

Jefferies, S. M., Pallé, P. L., van der Raay, H. B, Régulo, C., and Roca-cortés, T. 1988, *Nature* **333**, 646.

Johnston, A. 1994, *PhD Thesis*, University of St. Andrews.

Johnston, A., Roberts, B. and Wright, A. N. 1994, in Gong '94: *Helio– and Asteroseismology from Earth and Space*, ed. R. Ulrich, E. J. Rhodes and W. Däppen, (San Francisco: ASP), p.264.

Jones, H. P., and Giovanelli, R. G. 1983, *Solar Physics* **87**, 37.

Kim, Y. -C., Fox, P. A., Sofia, S., and Demarque, P. 1995, *ApJ* **442**, 422.

Kim, Y. -C., Fox, P. A., Demarque, P., and Sofia, S. 1996, *ApJ* **461**, 506.

Kosovichev, A. G. 1996*a*, *ApJ* **461**, L55.

Kosovichev, A. G. 1996*b*, *ApJ* **469**, L61.

Lamb, H. 1908, *Hydrodynamics* (Cambridge: CUP).

Lamb, H. 1932, *Hydrodynamics* (Cambridge: CUP).

Leibacher, J. W., & Stein, R. F. 1971, *Astrophys. Lett.* **7**, 191.

Leighton, R. B. 1960, Proceedings of IAU Symposium, **12**, 321.

Leighton, R. B., Noyes, R. W., and Simon, G. W. 1962, *ApJ* **135**, 474.

Libbrecht, K. G. 1988, *ApJ* **334**, 510.

Libbrecht, K. G., Woodard, M. F., & Kaufmann, J. M. 1990, *ApJ Suppl.* **74**, 1129.

Libbrecht, K. G., & Woodard, M. F. 1990, *Nature* **345**, 779.

Libbrecht, K. G., & Woodard, M. F. 1991, *Science* **253**, 152.

Livingston, W. C. 1978, *Nature* **272**, 340.

Lydon, T. J., Guenther, D. B. and Sofia, S. 1996, *ApJ* **456**, L127.

Miles, A. J., and Roberts, B. 1989, *Solar Physics* **119**, 257.

Monteiro, M. J. P. F. G., Christensen-Dalsgaard, J., and Thompson, M. J. 1996, *Astron. & Astrophys.* **307**, 624.

Nishizawa, Y., and Shibahashi, H. 1994, in Gong '94: *Helio– and Asteroseismology from Earth and Space*, ed. R. Ulrich, E. J. Rhodes and W. Däppen, (San Francisco: ASP), p.280.

Nye, A. H., & Thomas, J. H. 1974, *Solar Physics* **38**, 399.

Nye, A. H., & Thomas, J. H. 1976a, *ApJ* **204**, 573.

Nye, A. H., & Thomas, J. H. 1976b, *ApJ* **204**, 582.

Pallé, P. L. 1994, in Gong '94: *Helio– and Asteroseismology from Earth and Space*, ed. R. Ulrich, E. J. Rhodes and W. Däppen, (San Francisco: ASP), p.239.

Pallé, P. L., Peréz, J. C., Régulo, C., Roca-cortés, T., Isaak, G. R., Mcleod, C. P., and van der Raay, H. B. 1986, *Astron. & Astrophys.* **170**, 114.

Pallé, P. L., Régulo, C., and Roca Cortés, T. 1989, *Astron. & Astrophys.* **224**, 253.

Parker, E. N. 1979, *Cosmical Magnetic Fields* (Oxford: Clarendon).

Parker, E. N. 1975, *ApJ* **198**, 205.

Priest, E. R. 1982 *Solar Magnetohydrodynamics*, D. Reidel Publ.

Régulo, C., Jiménez, A., Pallé, P. L., Pérez Hernández, F., and Roca Cortés, T. 1994, *ApJ* **434**, 384.

Rhodes, E. J., Woodard, M. F., Cacciani, A., Tomczyk, S., Korzennik, S. G., & Ulrich, R. K. 1988, *ApJ* **326**, 479.

Rhodes, E. J., Johnson, N. M., Rose, P. J., Korzennik, S. G., and Cacciani, A. 1994, in Gong '94: *Helio– and Asteroseismology from Earth and Space*, ed. R. Ulrich, E. J. Rhodes and W. Däppen, (San Francisco: ASP), p.227.

Roberts, B. 1981*a*, *Solar Physics* **69**, 27.

Roberts, B. 1981*b*, *Solar Physics* **69**, 39.

Roberts, B. 1985, in *Solar System Magnetic Fields*, ed. E. R.

Priest (Dordrecht: Reidel), Chapter 3.

Roberts, B. 1988, in *Symp. on the Physics of Ionised Gases, Sarajevo*, ed. L. Tanović, p. 687.

Roberts, B., and Campbell, W. R. 1986, *Nature* **323**, 603.

Rosenthal, C. S. 1995, *ApJ* **438**, 434.

Rüdiger, G., and Brandenberg, A. 1995, *Astron. & Astrophys.* **296**, 557.

Ryutova, M. P. 1990, in *Solar Photosphere: Structure, Convection and Magnetic Fields*, ed. J. O. Stenflo, IAU Symposium **138**, p.229.

Schou, J., and Brown, T. M. 1994, *ApJ* **434**, 378.

Shibahashi, H. 1991, in *Progress of Seismology of The Sun and Stars*, ed. Y. Osaki and H. Shibahashi (New York: Springer-Verlag).

Smeyers, P. 1970, *Astron. & Astrophys.* **7**, 204.

Small, L. M., and Roberts, B. 1984, in *The Hydromagnetics of the Sun*, ESA SP-200, p.257.

Speigel, E. A., and Weiss, N. O. 1980, *Nature* **287**, 616.

Spruit, H. C. 1974, *Solar Phys.* **34**, 291.

Spruit, H. C. 1983, in *Solar and Stellar Magnetic Fields: Origins and Coronal Effects*, ed. J. O. Stenflo, (Dordrecht: Reidel), p.41.

Spruit, H. C., and Roberts, B. 1984, *Nature* **304**, 401.

Thomas, J. H. 1983, *Ann. Rev. Fluid Mechanics* **15**, 321.

Ulrich, R. K. 1970, *ApJ* **162**, 993.

van Ballegooijen, A. A. 1982*a*, *Astron. & Astrophys.* **106**, 43.

van Ballegooijen, A. A. 1982*b*, *Astron. & Astrophys.* **113**, 99.

Vanlommel, P., and Cadez, V. M. 1998, *Solar Physics*, in press.

Wentzel, D. G. 1979, *ApJ* **227**, 319.

Weiss, N. O. 1994, in Proctor, M. R. E., and Gilbert, A. D. eds., *Lectures on Solar and Planetary Dynamo.* CUP, p.59.

Willson, R. C., & Hudson, H. S. 1988, *Nature* **332**, 810.

Woodard, M. F. 1987, *Solar Phys.* **114**, 21.

Woodard, M. F., and Noyes, R. W. 1985, *Nature* **318**, 419.

Woodard, M. F., and Libbrecht, K. G. 1991, *ApJ* **374**, L61.

Woodard, M. F., Kuhn, J. R., Murray, N., and Libbrecht, K. G.
1991, *ApJ* **373**, L81.

Yu, C. P. 1965, *Phys. Fluids* **8**, 650.

Zweibel, E. G., and Bogdan, T. J. 1986, *ApJ* **308**, 401.

Zweibel, E. G., and Däppen, W. 1989, *ApJ* **343**, 994.